DRES

DEFENCE RESEARCH ESTABLISHMENT SUFFIELD

CR 98-30

UNCLASSIFIED

Blast Focussing Hazard Assessment

BY:

Combustion Dynamics Ltd.

SUBMITTED TO:
SCIENTIFIC AUTHORITY

John Slater
Defence Research Establishment Suffield
Box 4000, Medicine Hat, Alberta, T1A 8K6

June 1998

WARNING

"The use of this information is permitted subject to recognition of proprietary and patent rights."

CRAD

National Defence Défense nationale

Canada

CDL

BLAST FOCUSSING HAZARD ASSESSMENT

Contract No. W7702-0-R202/01-XSG

June 1998

Combustion Dynamics Ltd.

Blast Focussing Hazard Assessment

W7702-R0-202

Final Report

30 June 1998

Combustion Dynamics Ltd.

1. Introduction

The DRES range has a long history of large scale explosion trials designed to evaluate the blast effects of condensed and fuel-air explosives. Sites commonly used for such trials include the HOB and FAE pads near Currie junction. These sites are approximately 13 km from the nearest residence, 22 km from Redcliff and 27 km from Medicine Hat. Under "normal" and "ideal" atmospheric conditions, thousands of kilograms of explosives may be detonated without any major disturbances to the neighbouring population. Unfortunately, unfavourable weather conditions such as thermal inversions and strong winds can drastically reduce the allowable explosive yield due to shock enhancement and focussing effects. From an operational point of view, this can result in the costly postponement and cancellation of trials and introduce a great deal of uncertainty in trial schedules particularly during the fall and winter seasons when focussing conditions become more frequent. The difficult task of protecting the local population, while accommodating DRES researchers, requires accurate weather information and reliable blast predictions to determine the allowable explosive weights that can be detonated at a given time. The purpose of this contract is to address the latter issue by providing DRES with blast prediction and detection methods. This report summarizes the following work performed under this contract:

- Review of methods to predict atmospheric blast propagation,
- Evaluation of selected methods based on specific weather data profiles,
- Blast noise monitoring,
- Recommendations for blast noise monitoring and prediction,
- Improvements to the IFSAS software,
- Purchase of computer software and hardware, and materials for DRES experiments.

2. Atmospheric Blast Propagation Prediction

2.1 General Blast Wave Properties

The blast wave decay from an explosive may be divided into different regimes depending on the distance of the target from the explosive. For short distances from the charge, the rate of blast decay depends not only on the weight and chemical composition of the explosive but also on the shape of the charge and on the location of detonation initiation. A correct prediction of the blast propagation in this regime requires the use of a CFD code to predict the two- and three-dimensional flows involved. The height of burst (HOB) of the explosive is also very important since reflected shock waves and Mach stems can result in a significant enhancement of blast loading. As the shock propagates further away from ground zero, it gradually "spheres" up at which point it can be modelled using simpler one-dimensional modelling techniques. The analysis is simplified considerably when the shock enters the "far-field" regime due to the so-called "energy equivalency" which allows one to predict the shock pressure, duration and impulse in terms of a distance which is scaled with the energy of the explosive. This approach has been successfully used to characterize the blast waves generated by a wide variety of explosives ranging from condensed explosives such as TNT [1] and low density explosives involving fuel-air mixtures [2].

As the shock propagates further into the "long distance" regime, it becomes affected by local nonuniformities in the ambient sound speed and wind velocity. These nonuniformities tend to destroy the well defined and predictable pressure profiles observed closer to the charge. In this regime, the signatures become much more irregular and are more easily characterized in terms of their peak to peak amplitude rather than their shock overpressures [3] (Figure 1).

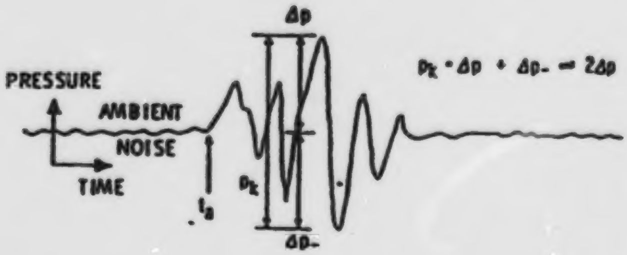

Figure 1 Typical Pressure-Time History at Long Range (From Ref. 3)

The presence of thermal and wind velocity gradients above the ground also destroys the spherical symmetry of the wave and can either accelerate or impede the rate of shock decay in the direction of the target [4]. For example, a decrease of temperature (and sound velocity) will bend the ray-paths upwards, thereby increasing the rate of shock decay along the ground (Figure 2a). An increase in temperature with height, on the other hand, will bend the shock wave towards the surface, thereby reducing its rate of decay (Figure 2b). This condition, usually referred to as a "thermal inversion", commonly occurs in the evening when the surface temperature cools down due to radiation or when a mass of warm air flows over a cold air mass [3]. Such conditions become even more hazardous when the wind velocity increases with height in the direction of the target, which further bends the ray-paths towards the ground. Another unfavourable weather pattern occurs when a negative thermal gradient bending the shock upwards is followed by a positive gradient which redirects the ray-paths towards the ground. This "dog leg" configuration (Figure 2 c) results in a "silent zone" of shock attenuation followed by a shock focussing zone where paths converge back onto the ground. Depending on the severity of the path convergence, this can lead to either a low rumbling noise or a sharp shock that is much much stronger than the sound wave observed in a more "normal" weather pattern. Sonic boom experiments carried out in

France have shown that the shock overpressure may increase by as much as 9.6 times in extreme focussing conditions [3,5].

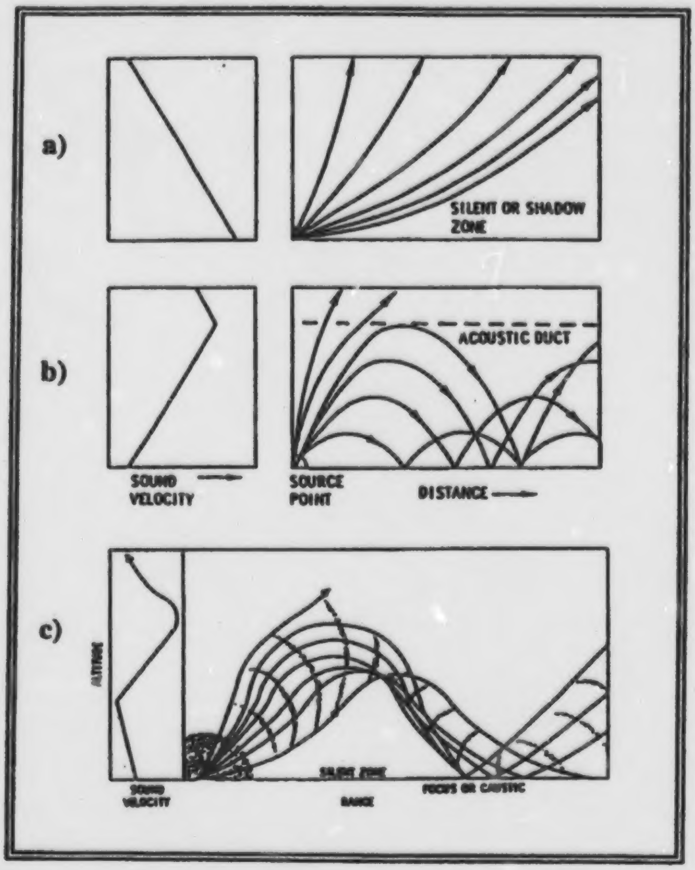
a)
SILENT OR SHADOW ZONE
b)
ACOUSTIC DUCT
SOUND VELOCITY
SOURCE POINT
DISTANCE
c)
ALTITUDE
SOUND VELOCITY
SILENT ZONE
RANGE
FOCUS OR CAUSTIC

Figure 2 Atmospheric Ray Bending for Gradient, Inversion and Focussing Conditions (From Ref. 4)

2.2 Blast Prediction Methods

Computational methods for atmospheric wave propagation vary greatly in terms of their level of complexity and the atmospheric data required to perform the calculations. This section summarizes the most commonly used methods for atmospheric noise propagation modelling.

2.2.1 ANSI Standard

In 1983, the American Institute of Physics published a report which has been approved as an American standard by the American National Standards Institute [3].

This standard is based on one-dimensional CFD calculations by Needham [6] and on large scale nuclear trials performed in Nevada during the 1950's. For window damage, the ANSI standard uses the "distant" correlation for overpressure

$$\Delta p = 0.05309 M_{TNT}^{0.3667} R^{-1.1} (p / p_o)^{0.633} kPa$$

where M_{TNT} is the equivalent TNT mass (kg), R is the distance (km) from the charge and p_o is the standard pressure at sea level.

Since pressure histories observed in the far-field tend to be oscillatory in nature, they are usually characterized by the peak to peak pressure, p_k, which is approximately 1.35 times the incident overpressure. In the event of thermal inversion or atmospheric conditions leading to focussing, the above predicted incident pressure should be increased by an enhancement factor. In the case where no accurate atmospheric data is available, the ANSI standard recommends an enhancement factor of 5.

Given the incident peak to peak pressure, p_k, and the local population, N, the ANSI standard provides an estimate of the number of broken windows based on the simple correlation:

$$C = 2.46x10^{-9} N(K_r p_k)^{2.78}$$

where K_r denotes a reflection factor which is usually assumed to equal 2. This equation assumes 19 window panes per capita and a "typical" distribution of window sizes and orientations. In the case where safety requirements call for no window damage, the standard provides the following restriction on the explosive charge M_{TNT}:

$$M_{TNT} < 328 R^3 / N$$

For rural areas with no concentrated populations, the maximum charge mass is given by:

$$M_{TNT} < 40 R^3$$

In the absence of detailed meteorological data, the ANSI standard can be quite restrictive in terms of the trials that can be performed near populated areas. As a case in point, Moen [7] considered the population of Medicine Hat located at approximately 25 km from the FAE test site, and computed a maximum allowable charge of approximately 145 kg. This is approximately half the TNT equivalent charge in DRES JUGFAE charges (250 kg TNT equivalent) and 35 times smaller than that used for FALCON trials (5,000 kg TNT equivalent).

The conservative nature of the ANSI Standard is mostly the result of the probabilistic nature of glass breakage which imposes more stringent charge restrictions for larger populations. For example, the maximum allowed incident blast overpressure for a city of the size of Medicine Hat is approximately 44 Pa. This corresponds to a peak to peak pressure, p_k, of 60 pa which is much smaller than that usually required for glass breakage (400 Pa [3]). The factor of 5 assumed for focussing enhancement also has a strong effect on the maximum charge restriction. Without focussing, the maximum allowable charge at the FAE site for no window damage in Medicine Hat would be approximately 11,329 kg which is more than twice the yield of the 200m FALCON charge.

The advantages and disadvantages of the ANSI standard are as follows:

Advantages:

1. Ease of use: This standard is very easy to apply given the population of the area of interest.
2. No need of weather data: Because the standard assumes the worst case focusing conditions, it does not require local temperature and velocity profiles.

2.2.2 Semi-Empirical Atmospheric Effect Model (Reed)

A blast prediction method taking into account local meteorological conditions has been developed by Reed [8,9]. The method is based on a series of empirical peak to peak pressure curves versus distance. These are presented for different weather conditions which are categorized according to the vertical profile of the directed sound speed (Figure 3). This speed is the sum of the local sound speed and the wind velocity component in the direction of the target. The gradient of the directed sound velocity may either be zero in the case of a "standard" atmosphere, negative in the case of gradient conditions, or positive in the case of inversions. Gradient conditions will lead to an upward bending of ray paths which results in faster shock decay and very favourable conditions for explosive trials. Inversion conditions, on the other hand, will bend the ray paths back towards the ground and reduce the shock decay. Finally, gradient reversal from negative to positive will create a "silent" zone followed by shock focussing which represents the least favourable conditions. If gradient or inversion conditions are observed, the peak to peak pressure, p_k, at the target may be estimated using the maximum difference in the directed sound speed, ΔV, as the characteristic weather indicator. Knowing the charge weight and the target distance, p_k may then be calculated using Figure 3 which is normalized for a free-field blast from a 1 kg charge. For example, consider the 11,390 charge which produces an ANSI acceptable p_k value of 60 Pa in Medicine Hat for a "Standard" atmospheric condition. The same charge would result in a value of 200 Pa for an inversion condition with $\Delta V = 10 m/s$ and 11 Pa for a gradient condition of

$\Delta V = -10 m/s$. For such conditions, the acceptable charges would change to approximately 670 kg and 110,000 kg respectively.

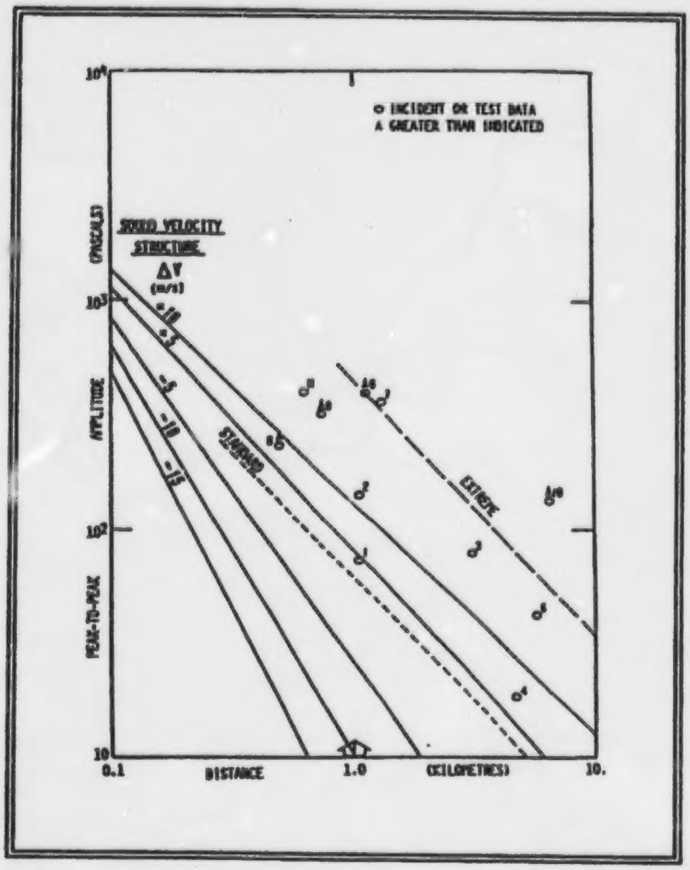

Figure 3: Explosion Pressure Amplitude Versus Distance, Yield-Scaled to 1 kg HE (from Ref. 4)

The above methodology has been automated by Reed [8,9] using a program called BLASTO which allows the user to enter meteorological data and obtain the blast overpressures at selected target positions.

The advantages and disadvantages of the Jack Reed approach are as follows:

Advantages:

1. Ease of use: Due to the relatively simple description of the blast decay as a function of the local directed velocity profile category, this method is relatively easy to implement and use.

2. Short Run Times: The simple implementation results in very short run times on a personal computer.

3. Limited Weather Data Requirements: Due to the simple classification of directed sound speed profiles, this method does not require very high resolution profile measurements.

4. Extension Capabilities: Due to its empirical nature, the method can accommodate a wide variety of explosion types (surface burst, HOB, underground explosions etc.).

Disadvantages:

1. Wave decay law applies to entire radial: Based on the directed sound velocity profile, this method applies the same pressure decay law along the entire radial for a given direction. This is a serious limitation when focussing is predicted since it is assumed that worst case focussing conditions apply along the entire radial whereas, in reality, the wave focussing may be limited to a small area that may be distant from the populated area of interest.

2. Simple profile classification: The BLASTO method reduces the description of the directed sound speed profile to a simple linear gradient or to a focussing condition. This oversimplification can lead to inaccuracies in the predicted overpressure.

2.2.3 Ray-Tracing Method

The semi-empirical approach of Reed is useful in relaxing the strict ANSI standard when meteorological data indicates favourable weather conditions. One limitation of this method, however, is that the directed sound velocity profile must be sufficiently smooth to indicate a clear gradient or inversion condition. Furthermore, in the case of focussing conditions, this approach does not provide the location and exact intensity of the focussing effect.

In order to obtain this added information, one must resort to ray-tracing algorithms which can determine the areas of ray-path convergence. This method essentially involves tracing the path of a sound wave through the atmosphere based on the local directed velocity V + c. The simplest codes of this type trace the ray-paths that are emanated in different azimuth directions and elevation angles from the charge. The code then determines the position where the rays return to the ground. Conditions are considered very favourable if ray-paths do not return to the ground at the location of interest. Conditions are considered very unfavourable if different ray-paths emanating from different elevation angles converge on a populated area. The Sound-Ray code [10] developed by DRES uses this approach and has been applied for many years to assist safety officers in making Go or No Go decisions for trials involving large amounts of explosives during possible inversion and focussing conditions.

One limitation of the simple raytracing code described above is that it does not predict peak pressures and pressure histories. This limitation can be addressed by assuming that energy is conserved within a ray tube propagating away from the charge. This approach is used by Smith [11], Sauvel and Vermorel et al. [12] and in the ASOPRAT code developed by the University of Mississippi [13]. The intensity of the pressure wave is then obtained from the fact that the energy density decreases with the cross-sectional area of the ray tube. The expressions for the cross-sectional area are given by:

$$dA_o = R_o^2 \cos\theta_o d\theta_o d\phi$$

and

$$dA = \Delta r r' \sin\theta_f d\theta_o d\phi$$

for non-refractive and refractive atmospheres respectively.

The range of applicability of the raytracing approach is determined by the focus factor

$$f = \frac{dA_o}{dA} = \frac{R_o^2 \cos\theta_o}{\Delta r r' \sin\theta_f}$$

For $|f| << 1$ or $|f| >> 1$, the raytracer method no longer applies and must be replaced by a more accurate wave solver described below.

The advantages and disadvantages of raytracer methods are as follows:

Advantages:

1. Easy implementation: Due to their simple geometrical basis, raytracer methods are relatively simple to implement.

2. Short run times: Raytracing calculations involve relatively short run times compared with more complex wave equation solutions discussed below.

3. Good prediction of inversion and focussing conditions: The raytracing method is particularly useful for weather patterns leading to wave funnelling (inversion profile) or wave focussing (dog-leg profile).

4. Accommodates possible extensions: This method is relatively flexible and can accommodate different ground reflection properties and the wave attenuation due to viscous effects.

Disadvantages:

1. Limiting Assumptions: This method is not valid when the focus factor, f, is much larger or much smaller than unity. The approach fails to predict pressures for regions where no ray-paths return to the ground. This includes silent zones associated with gradient conditions and skip zones for focussing conditions.
2. Linear Accoustics: Since the raytracing approach is based on linear acoustics where the flow velocity and sound speed are not affected by the blast wave, the raytracing calculations will not be accurate in the close vicinity of the charge.
3. Low Frequencies: Raytracing methods are not accurate in modelling the propagation of low frequency components in the blast signal [12].
4. Limited Number of Rebounds: Most Raytracer codes only calculate the first ground rebound of a specific ray-path. This may be a serious limitation for inversion and focussing conditions where multiple rebounds of a ray-path may take place before reaching a distant target.
5. Terrain Contours: Although the raytracer method can "in principle" deal with terrain contours, the implementation becomes complex if backward reflected rays must be calculated.

2.2.4 Wave Equation Solver

Another approach to the sound propagation problem is to solve the wave equation [13]:

$$\nabla^2 p(r,z,t) - \frac{1}{c^2}\frac{\partial^2 p(r,z,t)}{\partial t^2} = -\frac{2}{r}\delta(r)\delta(z-z_s)$$

The above equation may be solved using a method of characteristics. Strictly speaking, a complete solution to the wave equation must consider both forward and backward characteristics. Due to the difficulties involved in following both sets of characteristics, some wave equation solvers limit the analysis to the forward characteristics, thereby reducing the original hyperbolic wave equation to a simpler parabolic equation. Codes using the PE (Parabolic Equation) method have been developed by the US Army [14] and Penn State University. Another approach to the solution of the wave equation is the FFP (Fast Field Program) method. This solver was originally developed for underwater acoustics and was later applied by Franke and Swenson [15] for atmospheric noise propagation. Details of the FFP method can be found in the Franke and Swenson paper and the ASOPRAT User manual [13]. The first step in the FFP approach involves the decomposition of the source signal into harmonic components of the form $e^{i\omega t}$. Substituting into to the wave equation, each harmonic component can then be described by the Helmholtz equation:

$$\frac{\partial^2 p}{\partial r^2}+\frac{1}{r}\frac{\partial p}{\partial r}+\frac{\partial^2 p}{\partial z^2}+k^2 p=-\frac{2}{r}\delta(r)\delta(z-z_s)$$

where k is the wave number. The partial differential Helmholtz can be reduced to an ordinary differential equation:

$$\frac{d^2 P}{dz^2}+\left(k^2+K^2\right)P=-2\delta(z-z_s)$$

using the Hankel transform:

$$P(K,z)=\int_0^\infty p(r,z)J_o(Kr)rdr$$

where J_o is the zeroth order Bessel function.

Further transformations can reduce the ordinary differential equation to the so-called "Telegrapher" equations which are used to describe signal propagation in non-uniform transmission lines. The acoustic wave propagation between a sound source and a receptor is therefore reduced to a relatively simple electrical analog.

The main advantages and disadvantages of wave equations solvers using PE or FFP methods are as follows:

Advantages:

Pressure Prediction: Using harmonic wave decomposition, these methods can be used to predict pressure histories at any given point. Furthermore, unlike raytracing methods, PE and FFP methods can predict pressures in gradient conditions.

Includes Frequency Dependence: These methods account for the frequency dependence of wave propagation. This is particularly important for low frequency signals that are not correctly modelled using a ray-tracer approach.

Disadvantages:

Large Computer Resources: These methods generally involve relatively long run times for each frequency component. Depending on the computer resources available, this could pose a problem for blast waves generated by explosives which involve a large spectrum of frequencies. It should be noted, however, that this limitation will soon disappear due to the recent improvements in the efficiency of wave equation solvers and the continuing advances in computer speed and memory.

Effects of Turbulence: Wave equation solvers are capable of predicting pressures diffracted into silent (or shadow) zones that occur in gradient conditions. However, it is also known that the energy penetration in shadow zones is also highly dependent on sound scattering from turbulence. Consequently, predictions in these zones should account for stochastic fluctuations of the directed sound speed [16].

Limitations in Topography: Due to their neglect of backward propagating characteristics, Parabolic Equation (PE) solvers cannot account for the reflection of waves off hills. Although this does not appear to be an intrinsic limitation to FFP solvers, FFP codes developed for atmospheric sound propagation do not usually account for terrain contours.

2.2.5 Hybrid Method

Due to the relative advantages and disadvantages of raytracer methods and wave equation solvers, the ASOPRAT code developed by the University of Mississipi uses both methods for different regions of the computational domain. The much faster raytracer method is applied in areas of inversion and focussing where rays return to the ground. Silent zones associated with gradient weather profiles and skip zones in focussing conditions are solved using the slower FFP method.

2.3 Comparison of Raytracing and Semi-Empirical Method

As part of this contract, CDL compared the results predicted by the raytracing Sound-Ray [10] code and the Jack Reed BLASTO code [8,9] for the same weather profile. Comparisons were made with idealized and actual weather profiles recorded at DRES. As an illustrative example, Figure 4 displays BLASTO results for targets located at a distance of 40 km at azimuth angles of 145° and 325°. Based on the weather profile classification used in the code, BLASTO predicts focussing conditions for both directions This is due to the fact that the directed sound velocity crosses the base velocity line from left to right for both directions. The focussing prediction results in a calculated overpressure of 55 Pa which is approximately four times higher than that for a "standard" weather profile. Figure 5 shows the calculated return locations calculated using the DRES Sound-Ray code for ray-paths emanating from different azimuth and elevation angles. It can be seen that this weather pattern results in inversion or focussing conditions for all azimuth angles. The "cross over" of ray-paths at 145° and 325° appears to be consistent with the focussing predicted by BLASTO. However, it has been found that for some weather profiles, the BLASTO code does not detect focussing conditions predicted by SoundRay. This is due to the fact that BLASTO is not a raytracing code and uses a very simple profile categorization to predict gradient, inversion and focussing conditions.

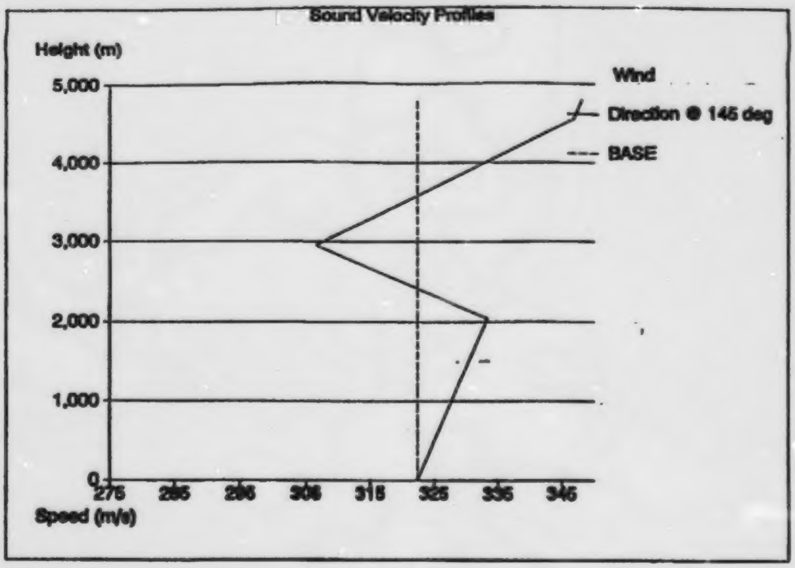

```
           WEATHER-DEPENDENT OVERPRESSURES (PASCALS) AT TARGET LOCATIONS

                                      OVERPRESSURES (PASCALS)               CAUS-
                   DIR    DIST   <<- - - WEATHER CATEGORIES - - ->>   RAOB  TIC
    TARGET        (DEG)    (M)   STND  +10    +5    -5   -10  CADET WEATHER  ?
*********************************************************************************
4
 10 NO. 10        145.  39998.   14.   46.   22.    3.    1.   55.     55. YES
```

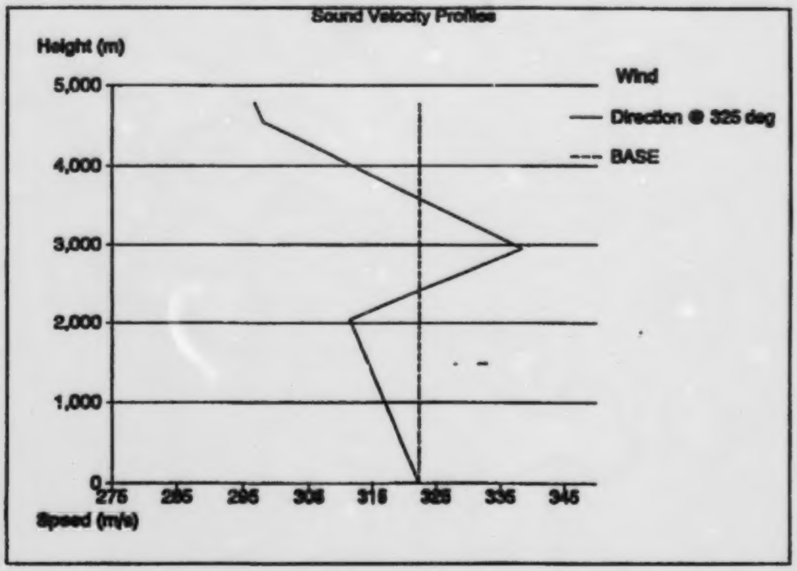

```
           WEATHER-DEPENDENT OVERPRESSURES (PASCALS) AT TARGET LOCATIONS

                                      OVERPRESSURES (PASCALS)               CAUS-
                   DIR    DIST   <<- - - WEATHER CATEGORIES - - ->>   RAOB  TIC
    TARGET        (DEG)    (M)   STND  +10    +5    -5   -10  CADET WEATHER  ?
*********************************************************************************
4
 22 NO. 22        325.  39998.   14.   46.   22.    3.    1.   55.     55. YES
```

Figure 4. Focusing Conditions Predicted by BLASTO for Double Dog-Leg Weather Profile

```
Radius of source:        .0 ft.

                                  ELEVATION ANGLES (Degrees)
AZIMUTH   1.0   2.0   3.0   4.0   5.0   7.0   9.0  11.0  13.0  15.0  17.0  19.0  21.0  23.0
(Deg.)  ----- ----- ----- ----- ----- ----- ----- ----- ----- ----- ----- ----- ----- -----
   0. |  23.6  22.3  21.0  19.9  18.9  17.3  16.1  15.1  14.5  14.1
   5. |  24.4  22.9  21.6  20.5  19.4  17.7  16.4  15.5  14.9  14.5
  10. |  25.3  23.8  22.4  21.1  20.0  18.3  16.9  16.0  15.4
  15. |  26.5  24.8  23.3  21.9  20.8  18.9  17.5  16.6  16.0
  20. |  27.9  26.1  24.4  22.9  21.7  19.7  18.3  17.3  16.7
  25. |  29.8  27.6  25.8  24.2  22.8  20.7  19.2  18.3
  30. |  32.2  29.7  27.6  25.8  24.2  21.9  20.5  19.6
  35. |  35.4  32.5  29.9  27.9  26.2  23.7  22.2
  40. |  40.1  36.4  33.3  30.8  28.9  26.3
  45. |  47.7  42.6  38.6  35.5  33.3  30.7
  50. |  59.8  53.7  48.7  45.3
  55. |
  60. |  16.8  38.0  54.4  68.6  74.6
  65. |   7.9  22.0  26.2  34.3  40.7  53.7  48.0
  70. |   5.2  10.4  15.7  20.9  26.1  36.7  41.6  36.4
  75. |   3.9   7.8  11.7  15.7  19.6  27.5  43.7  34.4  39.5
  80. |   3.1   6.3   9.5  12.6  15.8  22.0  28.5  34.0  29.6
  85. |   2.7   5.3   8.0  10.6  13.3  18.6  24.0  35.3  28.9  26.3
  90. |   2.3   4.6   6.9   9.2  11.5  16.2  20.8  25.6  28.7  25.5
  95. |   2.1   4.1   6.2   8.2  10.3  14.4  18.5  22.8  29.0  25.0  23.2
 100. |   1.9   3.7   5.6   7.5   9.3  13.1  16.8  20.6  30.0  24.8  22.7
 105. |   1.7   3.4   5.2   6.9   8.6  12.1  15.5  19.0  32.4  24.8  22.3  22.7
 110. |   1.6   3.2   4.8   6.4   8.0  11.3  14.5  17.7  21.2  24.9  22.0  20.6
 115. |   1.5   3.0   4.6   6.1   7.6  10.7  13.7  16.8  20.0  25.1  21.9  20.3
 120. |   1.4   2.9   4.4   5.8   7.3  10.2  13.1  16.0  19.1  25.4  21.8  20.1  24.2
 125. |   1.4   2.8   4.2   5.6   7.0   9.8  12.6  15.4  18.4  25.8  21.8  19.9  21.1
 130. |   1.4   2.7   4.1   5.4   6.8   9.5  12.3  15.0  17.8  26.2  21.7  19.8  18.8
 135. |   1.3   2.7   4.0   5.3   6.7   9.4  12.1  14.7  17.5  26.6  21.7  19.8  18.7
 140. |   1.3   2.6   4.0   5.3   6.6   9.2  11.9  14.5  17.3  26.9  21.7  19.7  18.6
 145. |   1.3   2.6   3.9   5.3   6.6   9.2  11.9  14.5  17.2  27.0  21.7  19.7  18.6
 150. |   1.3   2.6   4.0   5.3   6.6   9.2  11.9  14.5  17.3  26.9  21.7  19.7  18.6
 155. |   1.3   2.7   4.0   5.3   6.7   9.4  12.1  14.7  17.5  26.6  21.7  19.8  18.7
 160. |   1.4   2.7   4.1   5.4   6.8   9.5  12.3  15.0  17.8  26.2  21.7  19.8  18.8
 165. |   1.4   2.8   4.2   5.6   7.0   9.8  12.6  15.4  18.4  25.8  21.8  19.9  21.1
 170. |   1.4   2.9   4.4   5.8   7.3  10.2  13.1  16.0  19.1  25.4  21.8  20.1  24.2
 175. |   1.5   3.0   4.6   6.1   7.6  10.7  13.7  16.8  20.0  25.1  21.9  20.3
 180. |   1.6   3.2   4.8   6.4   8.0  11.3  14.5  17.7  21.2  24.9  22.0  20.6
 185. |   1.7   3.4   5.2   6.9   8.6  12.1  15.5  19.0  32.4  24.8  22.3  22.7
 190. |   1.9   3.7   5.6   7.5   9.3  13.1  16.8  20.6  30.0  24.8  22.7
 195. |   2.1   4.1   6.2   8.2  10.3  14.4  18.5  22.8  29.0  25.0  23.2
 200. |   2.3   4.6   6.9   9.2  11.5  16.2  20.8  25.6  28.7  25.5
 205. |   2.7   5.3   8.0  10.6  13.3  18.6  24.0  35.3  28.9  26.3
 210. |   3.1   6.3   9.5  12.6  15.8  22.0  28.5  34.0  29.6
 215. |   3.9   7.8  11.7  15.7  19.6  27.5  43.7  34.4  39.5
 220. |   5.2  10.4  15.7  20.9  26.1  36.7  41.6  36.4
 225. |   7.9  22.0  26.2  34.3  40.7  53.7  48.0
 230. |  16.8  38.0  54.4  68.6  74.6
 235. |
 240. |  59.8  53.7  48.7  45.3
 245. |  47.7  42.6  38.6  35.5  33.3  30.7
 250. |  40.1  36.4  33.3  30.8  28.9  26.3
 255. |  35.4  32.5  29.9  27.9  26.2  23.7  22.2
 260. |  32.2  29.7  27.6  25.8  24.2  21.9  20.5  19.6
 265. |  29.8  27.6  25.8  24.2  22.8  20.7  19.2  18.3
 270. |  27.9  26.1  24.4  22.9  21.7  19.7  18.3  17.3  16.7
 275. |  26.5  24.8  23.3  21.9  20.8  18.9  17.5  16.6  16.0
 280. |  25.3  23.8  22.4  21.1  20.0  18.3  16.9  16.0  15.4
 285. |  24.4  22.9  21.6  20.5  19.4  17.7  16.4  15.5  14.9  14.5
 290. |  23.6  22.3  21.0  19.9  18.9  17.3  16.1  15.1  14.5  14.1
 295. |  23.0  21.7  20.5  19.5  18.5  17.0  15.7  14.8  14.2  13.7
 300. |  22.5  21.3  20.2  19.1  18.2  16.7  15.5  14.6  13.9  13.5
 305. |  22.1  20.9  19.8  18.9  18.0  16.5  15.3  14.4  13.7  13.3  13.0
 310. |  21.9  20.7  19.6  18.6  17.8  16.3  15.1  14.2  13.6  13.1  12.9
 315. |  21.7  20.5  19.4  18.5  17.6  16.2  15.0  14.1  13.5  13.0  12.8
 320. |  21.5  20.4  19.4  18.4  17.6  16.1  15.0  14.1  13.4  13.0  12.7
 325. |  21.5  20.4  19.3  18.4  17.5  16.1  14.9  14.1  13.4  13.0  12.7
 330. |  21.5  20.4  19.4  18.4  17.6  16.1  15.0  14.1  13.4  13.0  12.7
 335. |  21.7  20.5  19.4  18.5  17.6  16.2  15.0  14.1  13.5  13.0  12.8
 340. |  21.9  20.7  19.6  18.6  17.8  16.3  15.1  14.2  13.6  13.1  12.9
 345. |  22.1  20.9  19.8  18.9  18.0  16.5  15.3  14.4  13.7  13.3  13.0
 350. |  22.5  21.3  20.2  19.1  18.2  16.7  15.5  14.6  13.9  13.5
 355. |  23.0  21.7  20.5  19.5  18.5  17.0  15.7  14.8  14.2  13.7
```

Figure 5. Ray Path Return Positions Calculated by DRES Sound-Ray Code for Double Dog-Leg Weather Profile

3. Weather Monitoring

Measurements of the directed sound speed require the simultaneous measurement of wind velocity and temperature as a function of elevation. Although the local sound speed also depends on the local humidity, this is a secondary effect which is usually not considered for atmospheric blast propagation prediction [5]. Methods currently available to measure wind and sound velocity include meteorological balloons, wind/temperature profilers and satellite measurements. Meteorological balloons measure the local temperature which is transmitted back to a ground station. The position of the balloon can be measured using optical methods, radar or GPS.

Profilers usually use UHF radar for wind speed measurements combined with a Radar Acoustic Sounding System (RASS) for temperature measurements [17,18]. The latter method uses a variable-frequency acoustic source and the temperature is determined from the frequency producing the strongest radar return. Literature provided by Radian Corporation is included with this report. Combined wind/temperature profilers are currently being used in the USA as part of the NOAA (National Oceanic and Atmospheric Administration) program. Unfortunately, due to the high cost of the hardware and software (approx. $400,000), very limited wind/temperature profile data is available in Canada. Although meteorological balloon data is available from Stony Plain and Great Falls, these sites are far too distant from Suffield to be used for blast propagation predictions. Currently DRES uses a meteorological balloon with a radio transmitter to record temperature profiles [19]. The balloon elevation is obtained by assuming a constant rise rate of 500 ft/min. Wind velocity data is obtained from computer weather predictions for Empress. The weather profile is used by the DRES Sound-Ray program to determine possible blast focussing conditions for trials involving more than 200 lbs of explosives.

4. Sound Monitoring Equipment and Testing

The vulnerability of a specific area to the blast produced by a distant explosion event can also be determined by detonating a small "test" charge just prior to the actual "trial" charge. As indicated by Spivey and Baker [20], this method, which has been used in White Sands New Mexico [21], can be relatively inexpensive and easy to implement.

As part of this contract, CDL searched for suitable sound sensors and communication hardware to relay the sound levels back to the DRES test site. The hand-held Sound Level Meter Type 2236 developed by Bruel & Kjaer [22] consists of a microphone with electronics to extract a wide variety of noise parameters. Tests were performed by DRES and CDL to compare the pressure traces recorded by this sensor with that detected by a PCB pressure transducer [23]. These tests indicated that the peak pressures and wave profiles were significantly different for the two sensors. B&K have indicated that the main difference for profile shapes are due to the frequency-dependent phase shift of the B&K microphone. The peak pressure difference is due to the limited low frequency response of the microphone. These limitations could be reduced by using a different B&K level meter (eg. 2231) that would give better low frequency response [24]. The B&K microphone did exhibit an excellent signal to noise ratio which was further enhanced by a highly effective windscreen. In spite of their current limitations, B&K sound level meters could probably be calibrated to meet DRES requirements for monitoring the sound produced by a preliminary "test" charge and a subsequent "trial" charge. One advantage of these noise level meters is that they can store the noise data and send the data back to the test site by modem via a conventional phone line or a cellular phone network.

5. Recommendations

DRES currently uses the raytracer Sound-Ray program in conjunction with weather data to determine if weather conditions are favourable for detonating charges over 200 lbs. The main limitations of the current approach are:

1. The Sound-Ray program does not predict the pressures produced by the ray rebound on the ground. The qualitative nature of the output also results in a certain level of subjective interpretation.

2. The wind data is not directly measured but obtained from computer predictions for the area.

3. The temperature profile assumes a constant rise rate of the meteorological balloon.

Since the main concern involves the detonation of charges for inversion and focussing conditions, more quantitative predictions could be made using a raytracing code of the type used in ASOPRAT. However, since raytracing codes are usually limited to the first rebound and cannot model silent zones, the more accurate wave equation solvers should be seriously considered. This is particularly true considering continuing advances in computer performance and recent improvements in FFP and PE wave equation solvers. The ASOPRAT code includes both raytracer and FFP solvers and has been delivered to CDL by the National Research of Canada Council (Dr. Gilles Daigle) under the terms of reference of NATO AC/243 Panel 3 RSG. 11. It is anticipated that DRES could acquire the latest version of this code through the same agreement. PE and FFP codes are also available from the Army Research Laboratory [14].

It should be stressed that any quantitative predictive code requires validation before being used as a Go/No-Go decision tool for trials involving large quantities of explosive. In collaboration with the National Research Council of Canada, the NATO Panel 3 Research Study Group 11 compared the performance of various codes using raytracing, FFP and PE methods [25]. This study, which was based on benchmark comparisons with analytical solutions, involved 11 research laboratories in North America and Europe. The results of this study indicated that the FFP and PE codes were capable of reproducing the analytical solutions with a high degree of accuracy. The accuracy of raytracing codes was limited by the inherent assumptions in the method discussed in Section 2.2.3. The above NATO study did not perform comparisons with actual experiments where factors such as turbulence can play an important role in the sound propagation in shadow zones. An experimental database has been made available, however, through a separate NATO study (JAPE-91) [26]. Finally code/experiment comparisons have been performed by Havelock et al. [16] using a PE solver that accounts for directed sound speed fluctuations in the atmosphere.

Improved wind velocity and temperature profiles could be obtained using satellite monitoring [19] or profilers. Unfortunately, the relatively high cost associated with these methods may make them unfeasible in the very near future. In the interim, improved profile measurements could be obtained by monitoring the balloon position using conventional visual methods, radar or GPS.

For specific rural areas with histories of noise complaints, a B&K noise monitoring and reporting system described in Section 4 could be used to monitor small "test" charge explosions before the larger "trial" charge. It should be noted, however, that a single noise monitoring sensor is not capable of representing the overall weather conditions. The reliability of this approach clearly increases with the number of sensors distributed around the test site.

6. Initial Development on the BWS (IFSAS)

This contract contributed to significant IFSAS software developments. In particular, the internal explosion raytracing code that was initially developed by CDL for a PC environment was partly re-written and integrated into IFSAS for a UNIX operating system. Substantial improvements were also made to the CFD input and output modules and the State module.

7.0 Hardware/Software Purchases

The following hardware and software was purchased under this contract to support DRES experimental and computational projects:

1.	BLASTO Program	$1,170.10
2.	2 Rockets from Brome Laboratories	$7,223.07
3.	Minefield clearance hoses	$26,947.83
4.	Livingston broker fees	$2,528.67
5.	486 Computer	$9,807.50
6.	Workstation software	$1,192.50
7.	Motif environment	$456.55
8.	Interactive Systems Software	$230.00
9.	Literature Search (NRC)	$74.80
		$49,631.02

8. References

1. Baker, W.E., Cox, P.A., Westine, P.S., Kulesz, J.J. and Strehlow, R.A.: "A Short Course on Explosion Hazards Evaluation', Southwest Research Institute, San Antonio, Texas, 1978.
2. Moen, I.O, Thibault, P.A. and Funk, J.W., "Blast Waves from Non-Spherical Fuel-Air Explosions", Proceedings of the 8th International Symposium on Military Application of Blast Simulation, Spiez, Switzerland, I7-1 - I.7-24, 1983.
3. "American National Standard: Estimating Airblast Characteristics for Single Point Explosions in Air, With a Guide to Evaluation of Atmospheric Propagation Effects", ANSI S2.20-1983 (ASA 20-1983), Published by the American Institute of Physics for the Acoustical Society of America.
4. Reed, J.W.: "Blast Predictions for Coyote Canyon Explosions", Presented at the DOD 20th Explosives Safety Seminar, Norfolk, Virginia, 26-28 August 1982.
5. Wanner, J.L., Vallee, J., Vivier, C. and Thery, C.: "Theoretical and Experimental Studies of Focus of Sonic Booms", J. Acoust. Soc. Amer., Vol. 52, July, 1972.
6. Needham, C.E., Havens, M.L. and Knauth, C.S.: "Nuclear Blast Standard (1kt)", Report AFWL-TR-732-55(rev), Air Force Weapons Laboratory, Kirkland Air Force Base, NM, April 1975.
7. Moen, I.O.: "Blast Focussing from Explosion Tests at Currie Junction", DRES Memorandum, 1987.
8. Reed, J.W.: "Explosion Airblast Predictions on a Personal Computer and Application to the Henderson, Nevada, Incident" SAND88-0681C, Presented at the 23rd DOD Explosive Safety Seminar, Atlanta, GA, August 8-11, 1988.
9. Reed, J.: "BLASTO – Airblast Prediction Program for IBM-PC Compatible Computers. Vesrion 9 for MS-DOS 5 or Above", March 1997.
10. Clink, W.L. and McKay, D.J.: "Sound-Ray Tracing by Digital Computer Techniques", Suffield Technical Note No. 65, 11 December, 1961.
11. Smith, G.: "Prediction of Acoustic Focussing Hazard in the Atmosphere", Twenty Fourth DOD Explosives Safety Seminar, 28-31 August Saint Louis, USA, pp. 2347-2358, 28-31 August, 1990.
12. Sauvel, J. and Vermorel, J.: "An Operation Prediction for Far-Field Airblast Effects", Twenty Fourth DOD Explosives Safety Seminar, 28-31 August Saint Louis, USA, pp. 2359-2379, 28-31 August, 1990.
13. "Advanced Sound Propagation in the Atmosphere (ASOPRAT), User's Guide, Version 3.0", University of Mississippi, 1991.
14. White, M., Department of the Army, Correspondence to Paul Thibault, December, 1991.
15. Franke, S.J. and Swenson, G.W.: "A Brief Tutorial on the Fast Field Program (FFP) as Applied to Sound Propagation in Air", Applied Acoustics, Vol. 27, pp. 203-215, 1989.
16. Havelock, D.I, Di, X., Daigle, G and Stinson: "Spatial Coherence of a Sound Field in a Refractive Shadow: Comparison of Simulation and Experiment", J. Acoust. Soc, Am., Vol. 98, No. 4, pp. 2289-2302, 1995.

17. Currier, P.E., Exklund, W.L., Carter, D.A., Warnock, J.A. and Balsley, B.B.:"Temperature Profiling using a UHF Wind Profiler and an Acoustic Source", Presented at the Symposium on Lower Tropospheric Profiling: Needs and Technologies, Boulder, Colorado, May 31-June 3, 1988.
18. "LAP-3000 System Lower Atmosphere Profiler", Radian International Electronics Division.
19. Hansen, T., Private Communication, June 1998.
20. Spivey, K.H. and Baker, W.E.: "Noise Abatement at FMC Hollister Site", Twenty Fourth DOD Explosives Safety Seminar, 28-31 August Saint Louis, USA, pp. 2333-2345, 28-31 August, 1990.
21. Baker, Q., Private Communication, June 1998.
22. "A Personalised SLM to Match Your Needs, Environmental- and Industrial-Noise Measurements Using Precision Integrating Sound Level Meter Type 2236", Bruel & Kjaer.
23. Ritzel, D.V. and Rude, G.: "Comparative SLM Data from Trials at DRES, 26 April 1994", Communication between DRES and B&K, 16 May 1994.
24. Ulicki, J: Reply to communication from D. Ritzel and G. Rude, 29 July, 1994.
25. Attenborough, K., Taherzadeh, S., Bass, H.E., Di, X., Raspet, R., Becker, G.R., Gudesen, A., Chrestman, A., Daigle, G.A., L'Esperance, A., Gabillet, Y., Gilbert, K.E., Li, Y.L., White, M.J., Naz, P., Noble, J.M. and van Hoof, H.A.J.M:"Benchmark Cases for Outdoor Sound Propagation Models", J. Acoust. Soc. Am. Vol. 97, No. 1, pp. 173-191, 1995.
26. Wilshire, W.L. and Chesnutt, D.: "Joint Acoustic Propagation Experiment (JAPE-91) Workshop", NASA Conference Publication 3231, 1993.

Appendix

NASA Conference Publication 3231

Joint Acoustic Propagation Experiment (JAPE-91) Workshop

Compiled by
William L. Willshire
and David Chestnutt
Langley Research Center
Hampton, Virginia

Proceedings of a workshop jointly sponsored by
the National Aeronautics and Space Administration,
Washington, D.C., and the University of Mississippi,
Oxford, Mississippi, and held in
Hampton, Virginia
April 28, 1993

NASA
National Aeronautics and
Space Administration
Office of Management
Scientific and Technical
Information Program
1993

Preface

In theory the sound a vehicle emits can be used to detect, track and identify the vehicle. In fact, in the case of underwater acoustics the navies of the world have used passive sonar techniques as a primary means of gathering target information. In principle, the sound airborne vehicles emit can also be used for these purposes and, in fact, artillery ranging has been used in one form or another for many years. Acoustic propagation in air differs from that in water in a few major ways. The sound propagation speed in air is much slower than in water while the vehicle speeds are much greater in air than in water. Therefore, vehicle Mach numbers are much greater in air than in water. Additionally, the time constants under which propagation conditions can radically change are generally much shorter in air than in water. The potentially rapid changes in propagation conditions in air make acoustic system performance estimation difficult, particularly within any practical confidence bounds.

As in underwater applications, in air the major thrust of research is in developing validated propagation models. The Joint Acoustic Propagation Experiment (JAPE), performed under the auspices of the NATO AC/243, Panel 3, Research Study Group 11 (RSG 11) on Automatic Pattern Recognition in Battlefield Surveillance with Mechanical Waves, was conducted to obtain a comprehensive set of acoustic propagation data to validate outdoor, long range propagation models. Of primary importance in the performance of this experiment was the extensive characterization of the atmosphere, including turbulence measurements during the tests. The quality and quantity of the meteorological data collected make this experiment unique.

The JAPE-91 workshop was held in Hampton, Virginia, USA on April 28, 1993. The purpose of the meeting was to exchange information and results from the experiment. The hosts would like to express their appreciation to the participants for attending and for sharing their knowledge and expertise.

Henry E. Bass
Professor of Physics
The University of Mississippi
Oxford, Mississippi

William L. Willshire, Jr.
Research Engineer
Applied Acoustics Branch
NASA Langley Research Center
Hampton, Virginia

David Chestnutt
Head, Applied Acoustics Branch
NASA Langley Research Center
Hampton, Virginia

CONTENTS

Preface iii

Joint Acoustic Propagation Experiment (JAPE) 1
Benny L. Carnes, Robert O. Olsen, and Bruce W. Kennedy

Some Results Gained From JAPE—An Overview 19
Gunnar R. Becker

Intercomparison of Remote and Balloon-Borne Sensors Operated at JAPE-91 31
Richard J. Okrasinski, Greg J. Cook, and Robert O. Olsen

Effects of Atmospheric Variations on Acoustic System Performance 41
Robert Nation, Stephen Lang, Robert Olsen, and Prasan Chintawongvanich

Comparison of Measured and Predicted Pure Tone Propagation Levels from JAPE-1: An Evaluation of the Performance of ASOPRAT 55
Carl K. Frederickson, Henry E. Bass, Richard Raspet, and John Messer

Ground Characterization for JAPE 65
Keith Attenborough and Shahram Taherzadeh

JAPE 91: Influence of Terrain Masking on the Acoustic Propagation of Helicopter Noise 79
P. Naz

Comparisons of Calculated and Measured Helicopter Noise Near Instrument Hill 87
Henry E. Bass and Chulsoo You

Preliminary Analysis of Amplitude and Phase Fluctuations in the JAPE Multiple Tone Data to Distances of 500 Meters 93
James Rogers, Radomir Sokolov, Daniel Hicks, and Lloyd Cartwright

Dimensional Analysis of Acoustically Propagated Signals 107
Scott D. Hansen and Dennis W. Thomson

Comparison Between 1-Minute and 15-Minute Averages of Turbulence Parameters . . . 119
John M. Noble

Beamforming in an Acoustic Shadow 129
David Havelock, Michael Stinson, and Gilles Daigle

Analysis of Passive Acoustic Ranging of Helicopters from the Joint Acoustic Propagation Experiment 131
Benny L. Carnes and John C. Morgan

Acoustic Target Detection and Classification Using Neural Networks 171
James A. Robertson and Mark Conlon

Preliminary Analysis of the JAPE Ground Vehicle Test Data With an Artificial Neural Network Classifier 181
Nathan F. Larsen and Ben L. Carnes

JAPE-91 Workshop
Participant List

NAME	Organization & Address	Telephone
Erik A. Andersen	Danish Defence Research Establishment	(45)39272233
Keith Attenborough	The Open University, Milton Keynes, UK	(908) 652766
Henry E. Bass	Univ. of Mississippi, University, MS 38677	(601)232-5840
Gunnar R. Becker	Atlas Elektronik, POB 448545, D 28 Bremen 44	+49-421-457-3275
Ben L. Carnes	USAE WES, Vicksburg, MS	(601) 634-2231
David Chestnutt	NASA Langley Research Center, MS 460, Hampton, VA 23681	(804) 864-5263
Prasan Chintawongvanich	Physical Science Lab, Las Cruces, NM 88003	(505) 522-9142
Mark Conlon	IIT Research Institute, Las Cruces, NM	(505) 521-3014
David A. Dadley	Defence Research Agency U.K.	0959 532222
Idar Dyrdal	Norwegian Defence Research Establishment	(47) 63807513
Bernard F. Engebos	US Army Research Lab, AMSRL-BE-M, White Sands Missle Range, NM 88003	(505) 678-1489
Carl Frederickson	Univ. of Mississippi, University, MS 38677	(601) 232-5768
Georges R. Garinther	US Army Research Lab, HRED, APG. MD 21005-5425	(410) 278-5984
Scott Hansen	Penn State University, University Park, PA	(814) 865-2859
David I. Havelock	NRC, Canada	(613) 993-7661
Joel T. Kalb	US Army Research Lab, HRED AMSR L-HR-SD, Aberdeen Proving Grounds, MD 21005-5425	(410) 278-5983
Geoff Kerry	University of Salford, UK	061 745 5582
Richard Lacoss	MIT Lincoln Lab 02173	(617) 981-7212
Claude Lahaze	Defence Research Establishment, Valcartier	(418) 844-4684
Tom Landers	Northrop Corporation	(213) 600-5727
Stephen W. Lang	Lockheed-Sanders, Nashua, NH	(603) 885-9067
Nathan Larsen	US Army Waterways Exp. Station	(601) 634-3504
Philip Le Masurier	Sikorsky Aircraft, Stratford, CT 06601	(203) 383-3499
Jerry R. Lundien	USACE/CERD-M	(202) 272-1847
Cyril Maillet	DGA/DAT/SEFT (French MOD)	(33)-1-4095-3480
Arnold Mueller	NASA Langley Research Center, MS 460, Hampton, VA 23681	(804) 864-5277
Robert Nation	Lockheed Sanders, Nashua, NH	(603) 885-9815
Pierre Naz	French German Research Institute of St. Louis	(33) 89695098

JAPE-91 Workshop
Participant List
(continued)

NAME	Organization & Address	Telephone
John M. Noble	US Army Research Lab, AMSRL-BE-M, White Sands Missile Range, NM 88002	(505) 678-3751
Richard Okrasinski	Physical Science Lab, Box 30002 Las Cruces, NM 88003	(505) 522-9496
William A. Peterson	US Army Research Lab, AMSRL-BE-A, White Sands Missle Range, NM 88002	(505) 678-1465
Jim Robertson	IIT Research Institute, Dayton, OH	(513) 252-9969
Jim Rogers	Michigan Tech, KRC	(906) 487-2750
Peter J. Soilleux	DRA (Malvern), St. Andrews Rd., Malvern, Worcs UK (WR143PS)	0684 894841
Huub van Hoof	Physics & Electronics Lab, FEL-TND, The Hague, Netherlands	3170 326 4221
Klemens Vattrodt	Fraunhofen-Gesellschaft, Karlsruhe, GE	49-721-6091-252
Michael J. White	US Army Constr. Eng. Res. Lab	(217) 352-6511
William L. Willshire	NASA Langley Research Center, MS 460, Hampton, VA 23681	(804) 864-5270

ANSI S2.20-1983
(ASA 20-1983)

Standards Secretariat
Acoustical Society of America
335 East 45th Street
New York, New York 10017

AMERICAN NATIONAL STANDARD
Estimating Airblast Characteristics for Single Point Explosions in Air, With a Guide to Evaluation of Atmospheric Propagation and Effects

ABSTRACT

This standard provides consensus quantitative definitions of explosion characteristics for a single point explosion in air, along with methodologies for scaling these characteristics for a wide range of yield and ambient air conditions. Factors for use with common solid explosives are also included. Methods are provided for predictions of long range propagation under atmospheric refractive influences. Target damage estimation procedures are provided for use in explosion operation planning and evaluation.

DEFENCE RESEARCH
ESTABLISHMENT SUFFIELD
Date Recd. 3 Jan 84
From PS 5696
Reg No. 25816

Published by the American Institute of Physics for the Acoustical Society of America

AMERICAN NATIONAL STANDARDS ON ACOUSTICS

The Acoustical Society of America is the Secretariat for American National Standards Committees S1 on Acoustics, S2 on Mechanical Shock and Vibration, S3 on Bioacoustics, and S12 on Noise. Standards developed by these committees, which have wide representation from the technical community (manufacturers, consumers, and general-interest representatives), are published by the Acoustical Society of America as American National Standards after approval by their respective standards committees.

These standards are developed as a public service to provide standards useful to the public, industry, and consumers, and to Federal, State, and local governments.

This standard was approved by the American National Standards Institute as ANSI S2.20-1983 on 1 March 1983.

An American National Standard implies a consensus of those substantially concerned with its scope and provisions. An American National Standard is intended as a guide to aid the manufacturer, the consumer, and the general public. The existence of an American National Standard does not in any respect preclude anyone, whether he has approved the standard or not, from manufacturing, marketing, purchasing, or using products, processes, or procedures not conforming to the standard. American National Standards are subject to periodic review and users are cautioned to obtain the latest editions.

Caution Notice: An American National Standard may be revised or withdrawn at any time. The procedures of the American National Standards Institute require that action be taken to reaffirm, revise, or withdraw this standard no later than five years from the date of publication.

Copyright © 1983 by the Acoustical Society of America. No portion of this publication
may be quoted or reproduced in any form without permission of the
Acoustical Society of America.

FOREWORD

[This Foreword is not a part of American National Standard Estimating Airblast Characteristics for Single Point Explosions in Air, with a Guide to Evaluation of Atmospheric Propagation and Effects, S2.20-1983 (ASA Catalog No. 20-1983).]

This standard is the first in a planned series of definitions, standards, and specifications for use in airblast acoustics. It has been developed under the American National Standards Institute by the Standards Committee Method of Procedure under the American National Standards Committee S2, whose Secretariat is held by the Acoustical Society of America.

American National Standards Committee S2, under whose jurisdiction this standard was developed, has the following scope:

> Standards, specifications, methods of measurement and test, and terminology, in the fields of mechanical shock and vibration, but excluding those aspects which pertain to biological safety, tolerance, and comfort.

At the time this standard was submitted to Standards Committee S2 for approval, the membership was as follows:

P. H. Maedel, Jr., *Chairman*
S. Feldman, *Vice-Chairman*
A. Brenig, *Secretary*

Acoustical Society of America • P. H. Maedel, Jr.
American Iron & Steel Institute • E. H. Toothman, P. A. Hernandez *(Alt)*
American Mining Congress • G. R. Coonan, H. B. Johnson *(Alt)*
American Society of Heating, Refrigerating and Air Conditioning Engineers • P. K. Baade, P. Ostergaard *(1st Alt)*,, G. F. Hohn *(2nd Alt)*
Anti-Friction Bearing Manufacturers Association • J. C. Morrison
Institute of Electrical & Electronics Engineers • R. G. Bartheld
Institute of Environmental Sciences • H. Pusey
National Bureau of Standards • M. R. Serbyn, D. R. Flynn *(Alt)*
National Council of Acoustical Consultants • G. C. Tocci, D D. Reynolds *(Alt)*
National Electrical Manufacturers Association • D. V. Wright, J. R. Keinz *(Alt)*
Naval Biodynamics Laboratory • J. Guignard, C. L. Ewing *(Alt)*
Naval Ship Research & Development Center • A. Zaloumis
Schenck Trebel Corporation • D. G. Stadelbauer
U.S. Department of the Air Force • N. Bingman, R. F. Wilkus *(1st Alt)*, J. P. Henderson *(2nd Alt)*
U.S. Department of Defense • H. Pusey, R. J. Volin *(Alt)*
U.S. Department of the Navy–Naval Sea Systems Command • L. Herstein, K. Hartman *(Alt)*

Individual members of the S2 Committee were

R. G. Bartheld
L. Batchelder
G. Booth
R. A. DiTaranto
K. M. Eldred
S. Feldman
D. Johnson
D. Muster
H. L. Rich
A. O. Sykes
H. E. von Gierke

Working Group S2-54, on Atmospheric Blast Effects, which assisted the Committee in preparing the standard, had the following members:

Jack W. Reed, *Chairman*

John A. Blume
Everett F. Cox *(deceased)*
Robert E. Fuss
John H. Keefer
Joseph E. Minor
Donald N. Montan
James F. Moulton, Jr.
Donald R. Richmond
Leonard Rudlin *(deceased)*
John H. Wiggins, Jr.

Suggestions for improvements in this standard will be welcomed. They should be sent to the Standards Secretariat, Acoustical Society of America, 335 East 45th Street, New York, NY 10017.

CONTENTS

1 SCOPE 1
2 DEFINITIONS OF SYMBOLS AND ABBREVIATIONS 1
2.1 Quantity Symbols 1
2.2 Unit Symbols 1
2.3 Abbreviations 2
2.4 Common Conversion Factors 2
3 INTRODUCTION 2
3.1 Purpose 2
3.2 Applicability 2
3.3 Background 2
4 SOURCE DEFINITIONS 3
4.1 Point Explosions 3
4.2 Chemical Explosives 8
4.3 Empiricisms 10
5 REFRACTED ATMOSPHERIC PROPAGATION 12
5.1 Refractive Distortion of Waves by Inhomogeneous Atmospheres 12
5.2 Atmospheric Parameters 12
5.3 Propagation Climatology 14
6 STRUCTURAL RESPONSE 15
6.1 Strong Shock Effects 15
6.2 Intermediate Strength Shocks 18
6.3 Nuisance Level Airblasts 18
7 REFERENCES 21

APPENDICES

APPENDIX A: EVOLUTION OF EXPLOSION AIRBLAST MODELS 22
APPENDIX B: CALCULATION EXAMPLES 24
APPENDIX REFERENCES 24

FIGURES

FIG. 1 Typical explosion wave pressure-time signature 4
FIG. 2 AFWL 4.2 TJ (1 kiloton) standard overpressure versus radius, high pressures 5
FIG. 3 AFWL 4.2 TJ (1 kiloton) standard overpressure versus radius, low pressures 5
FIG. 4 AFWL 4.2 TJ (1 kiloton) standard overpressure impulse versus radius 5
FIG. 5 AFWL 4.2 TJ (1 kiloton) standard radius versus time 5
FIG. 6 Yield scaling factors for surface and air burst explosions 6
FIG. 7 Standard atmosphere pressure altitude 6
FIG. 8 Altitude scaling factors for explosion times and distances 7
FIG. 9 Mach stem formation for above ground burst 7
FIG. 10 Airblast HOB effect on apparent yield 8
FIG. 11 Peak overpressure versus radius, 1 kg HE surface burst 8
FIG. 12 Summary of troposphere propagations from Nevada nuclear tests 9
FIG. 13 Long range airblast data scaled to distances from 4.2 TJ (1 kton) 10
FIG. 14 Typical explosion wave pressure-time signature at long range 11
FIG. 15 Standard explosion overpressure-distance curves for NE and HE yields 11
FIG. 16 Shock wave distortion by layered atmospheric temperature and wind structure 12

FIG. 17 Typical explosion ray paths........13
FIG. 18 United States Standard Atmosphere, 1962........13
FIG. 19 Measured overpressures scaled to 84 TJ (20 kton) surface burst (2W), Nevada and Pacific test troposphere propagations........14
FIG. 20 Atmospheric focus factor probability distribution near a caustic........15
FIG. 21 Ozonosphere signal amplitudes from Nevada nuclear tests........16
FIG. 22 Distribution of atmospheric focus factors........17
FIG. 23 Stages in the diffraction of a blast wave by a structure........17
FIG. 24 Airblast damage to residential structures........17
FIG. 25 Window breakage from airblast, theory and data........19
FIG. 26 No damage yield limits for surface burst HE explosions versus distance and population........20
FIG. 27 No damage yield limits for surface burst HE explosions for rural areas........20
FIG. A1 Overpressure-distance decay exponent, AWFL 4.2 TJ (1 kton) NE at sea level........23

TABLES

TABLE I Standard 4.2 TJ (1 kton) NE airblast parameters versus distance........4
TABLE II Equivalent explosive weight approximations (based on TNT)........8
TABLE III Metric low overpressure coefficients for various yield and distance units........11
TABLE IV Minimum overpressures which cause vehicle damages........18
TABLE V Damaging overpressures for structures on cargo ships........18

American National Standard
Estimating Airblast Characteristics for Single Point Explosions in Air, With a Guide to Evaluation of Atmospheric Propagation and Effects

1 SCOPE

This standard is intended to provide methods for determining blast wave characteristics for single point or spherical explosions, estimating the variations of characteristics caused by the atmospheric medium of propagation, and predicting the expected effects on populations and structures. It applies to chemical or nuclear explosions, of yields ranging from about 1 kg to many megatons, at burst heights to at least 50 km altitude, and to distances where wave pressure amplitudes drop below 1 Pa. The phenomenology is less well defined for many practical explosions of distributed charges or shapes, wholly or partially confined explosions, either underground or underwater. In many cases, however, these effects may be normalized and an equivalent point explosion used for evaluation.

2 DEFINITIONS OF SYMBOLS AND ABBREVIATIONS

2.1 Quantity Symbols

A_i = constant coefficients ($i = 1, 2, 3$)

c = sound speed in air

C = cost of damage repairs

F = atmospheric blast focus factor, or magnification, referenced to spherical wave expansion

$\overline{F}$ = geometric average blast focus factor

h = height above ground

I = blast overpressure impulse

I_d = dynamic-pressure impulse

K = proportionality constant

K_r = airblast overpressure reflection factor

N = population (human)

p = ambient air pressure

p_0 = sea level standard air pressure

p_k = peak-to-peak pressure amplitude in the blast wave

Δp = peak blast overpressure, or maximum positive deviation from ambient pressure in the blast wave

Δp_- = negative peak blast pressure

$\Delta p/p$ = shock strength

$\Delta p(P)$ = overpressure causing P precent probability of window damage

P = probability of damage

Q = number or quantity

R = slant range from the center of explosion

R_1 = slant range to nearest vulnerable residence

t = time

t_a = blast wave arrival time after detonation

t_r = compression rise time

t_+ = positive phase duration in explosion wave

t_- = negative phase duration in explosion wave

T_C = temperature (Celsius)

T_K = temperature (Kelvin)

V = sound velocity (directed)

W = explosion energy yield

W_a = apparent airblast yield

x, y = Cartesian horizontal coordinates

θ = blast ray incidence angle, measured from the horizontal

σ_G = geometric standard deviation

2.2 Unit symbols

Pa = pascal (N/m^2)

K = kelvin

kg = kilogram

m/s = meters per second

2.3 Abbreviations

HE = chemical high explosives

NE = nuclear explosives

MSL = mean sea level

HOB = height of burst

STP = standard sea level pressure (101.325 kPa) and temperature (288.15 K)

SD = standard deviation

AFWL = Air Force Weapons Laboratory

NSWC = Naval Surface Weapons Center

2.4 Common Conversion Factors

100 kPa = 1000 mbar = 14.504 $\mathrm{lb}_f/\mathrm{in.}^2$ (psi)

$T_K = T_C + 273.15$

1 m/s = 3.2808 ft/s = 2.2369 mph = 1.9438 knots

1 kton (NE) = 4.2×10^{12} J (equivalent explosion yield)

1 Mton (NE) = 4.2×10^{15} J (equivalent explosion yield)

3 INTRODUCTION

3.1 Purpose

The purpose of this standard is to provide, where possible, consensus quantitative methods for estimating explosion characteristics, effects of atmospheric propagation, and typical responses to explosion waves. Published literature gives a wide variety of results from a multitude of experiments dealing with some or all of these three major categories in explosion phenomenology. It now appears that some of the most important complexities, which have confused explosion evaluation in the past, are fairly well understood. Various interactions have been identified, their effects removed from the data, and a satisfactory evaluation and prediction system has finally been assembled in one published standard.

3.2 Applicability

3.2.1 Potential Users

This standard will help explosives operators to design adequate and safe systems, predict troublesome conditions that may occur, prepare environmental impact statements, and evaluate damages that are caused by intentional or accidental explosions, as well as assess the credibility of damage claims which may arise. It will also allow more realistic public evaluation of proposed projects, with consideration of credible costs as well as benefits, so that decision makers are able to delineate between the physical and political factors.

3.2.2 Methodologies

For strong shock regions, airblast characteristics are defined by the source model, in terms of yield and distance, in 4.1.3. Responses of idealized target structures are briefly described in 6.1. Details are adequately treated in several textbooks, following common physical principles. Distant propagations, more influenced by meteorology and thus less generally understood and less reproducible, are stressed in 5.3 to aid prediction of nuisance level effects (6.3) on target populations that are likely unassociated with the explosion operators.

3.3 Background

3.3.1 Explosions

An explosion is defined by Webster as "a violent expansion or bursting that is accompanied by noise and is caused by a sudden release of energy from a very rapid chemical reaction, from a nuclear reaction, or from an escape of gases or vapors under pressure." Because of its destructive nature it has been difficult to adequately measure precisely what happens in an explosion as well as how it affects its nearby environment, including structural or biological systems that might be exposed. Many important data collections have relied on after-the-fact evaluations from both wars and accidents. Laboratory and experimental determinations have often been limited by safety or expense. In consequence, conflicting and confusing results have been reported, from a variety of sources. This has led to many divergences of predictions. It now appears, however, that enough is known to explain most of these phenomena, at least those associated with the simplest case, of an explosion in air.

3.3.2 Source, Propagation, and Effects

3.3.2.1 Chronological Order

Predictions of explosion phenomena are conveniently divided into three phases. The historical, or chronological approach used in Secs. 4, 5, and 6 considers source, propagation, and effects phases in that order, as they occur. Some users may first wish to understand something about immediate causes for concern, nuisance noise, or blast damage as examples. They would then want to learn about how these conditions developed and how to ameliorate them. In this case they could begin by skipping from 3.3.3 to 6.1.

3.3.2.2 Airblast Source

Source definition (Sec. 4) depends on the kind and amount or yield of energy release, its timing, and the dimensions over which it is rapidly spread. This standard only addresses the airblast wave which is emitted by an explosion. Included are the air compression, subsequent decompression, and eventual return to ambient pressure that radiates from an explosion. It will not treat special emissions from particular kinds of explosions such as electromagnetic or particulate radiations from nuclear explosions or contaminants from chemical explosions.

3.3.2.3 Atmospheric Propagation

Propagation of the airblast wave at close ranges in air depends primarily on ambient temperature and pressure. Waves traveling to long distances, however, may be refracted by an atmospheric acoustic lens effect, which is dependent on temperatures and winds as described in Sec. 5. Refracted waves may be considerably focused in some cases, or diverged to negligible magnitude in others.

3.3.2.4 Target Response

Effects which result from blast wave interaction with an exposed body, either structural (Sec. 6) or biological may depend on the strength, the compression rate, and sometimes the duration of the wave, as well as response characteristics of the target body.

3.3.3 Limitations and Uncertainties

3.3.3.1 Explosion Yield

Conditions within or near a specified explosion yield may generally be stated, but, for a variety of reasons, there is usually a significant uncertainty about yield. Two apparently identical samples, such as TNT, may indeed differ in internal local density and crystal structure. Such differences may affect detonation to give partial low order yield, or there may be locally intensified detonation emitting strong shock jets. Error ranges are not generally known and specified, but at least 10%–20% variations in airblast characteristics may be expected, even for nuclear explosions.

3.3.3.2 Atmospheric Conditions

Airblast propagation through the atmosphere encounters air turbulence, wind gusts, and convective plumes and bubbles of air, all of various scales and strengths that are practically never known in detail, particularly over large distances. The result is an acoustic analogy to optical heat shimmer and star twinkle. Such variability limits predictability so that errors of a factor of two in airblast overpressure are commonplace, even for repeated explosions shot only minutes apart.

3.3.3.3 Target Response

Finally, the response of targets is often governed by nonideal conditions of particular installations. There is variance in material strength, and, of course, natural differences between biological targets.

3.3.3.4 Statistical Approaches

In consequence, statistical probability estimation is essential in designing for or evaluating explosion effects. There will be surprises, both good and bad. This standard sets forth prediction principles as well as the uncertainties, so that explosions can be used without harmful surprises, but also without excessive costly controls.

4 SOURCE DEFINITIONS

4.1 Point Explosions

4.1.1 Nuclear Explosions

Since a nuclear explosion is the closest thing presently available to the ideal hypothetical point source of an instantaneous energy pulse, it is used as the standard reference explosion. At moderate to large distances an airborne shock wave has little memory of its origin. Thus, for many applications, other explosions may be related to nuclear equivalents.

4.1.2 Point-Explosion Scaling Laws

Atmospheric explosion waves, in the absence of reflections, are known to obey the following three simultaneous relationships[1] (numbered references are found in Sec. 7) known as Sach's scaling,[2] for comparing two similar explosions of different yields (volumes) at different ambient pressures (altitudes):

$$\frac{\Delta p_1}{p_1} = \frac{\Delta p_0}{p_0}, \tag{1}$$

$$\frac{R_1}{R_0} = \left(\frac{W_1 p_0}{W_0 p_1}\right)^{1/3}, \tag{2}$$

$$\frac{t_1}{t_0} = \left(\frac{W_1 p_0}{W_0 p_1}\right)^{1/3}\left(\frac{c_0}{c_1}\right). \tag{3}$$

Subscripts 0 and 1 distinguish the variables that are associated with the two different explosions. Note that time scaling is quite general, applying equally to t_a, t_+, and t_-. It does not apply to compression rise time, however, which is one result of nonscalable attenuation (see 4.1.5). Also, for bursts below about 20 km altitude, the scaling pressure, p_1, is ambient at the gauge or target rather than at burst altitude. As most often used, these scaling laws state that shock strength is conserved at distances which are scaled for yield and ambient pressure.

4.1.3 Standard Explosion Characteristics

4.1.3.1 Hydrodynamic Models

One dimension hydrodynamic calculations[3] have provided good estimates of blast wave characteristics for free air explosions of nuclear devices in a homogeneous, calm atmosphere (with constant temperature and pressure throughout), out to ranges and down to peak overpressures where numerical integration became either unreliable or prohibitively expensive. The most recent and sophisticated AFWL calculation for 4.2 TJ (1 kton NE) at STP conditions,[4] has been adopted for this standard. Comparison with other important models is described in Appendix A.

NOTE: In practice, the type of "ton" is not important, since short tons, long tons, and metric tons vary at most by 12%. Scaled blast effects would only vary by the cube root of the difference, or 4%.

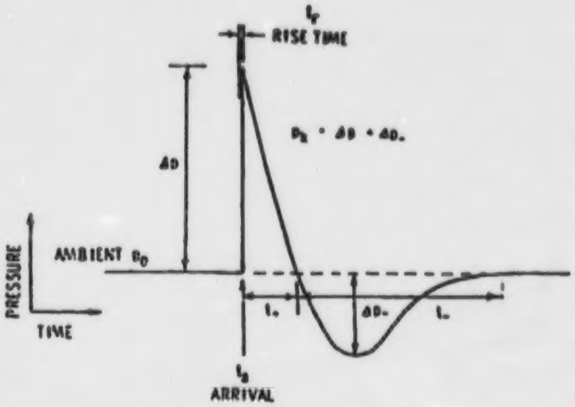

FIG. 1. Typical explosion wave pressure–time signature.

4.1.3.2 AFWL Model Characteristics

Basic airblast wave characteristics are shown in Fig. 1 for a typical pressure versus time signature, as recorded by a gauge. The standard incident overpressure versus distance curve for strong shock waves is shown in Fig. 2, and the curve at long range and low overpressure is shown in Fig. 3. Positive phase pressure impulse versus distance, or radius, is shown in Fig. 4. Time of arrival, positive phase duration, and negative phase duration (at recovery to 80% of ambient) are shown versus radius in Fig. 5. Numerical values at regular logarithmic distance intervals are shown in Table I to aid scaling calculations for other explosions. Analytical equations for producing the standard overpressure, overpressure impulse, and phase duration curves are included with some history of their development in Appendix A. Ambient conditions for the standard explosion are STP, that is $p_0 = 101.325$ kPa and $T_0 = 288.15$ K, where $c_0 = 340.294$ m/s.

TABLE I. Standard 4.2 TJ (1 kton) NE airblast parameters versus distance.

R (m)	t_a (s)	Δp (Pa)	t_+ (s)	I (Pa-s)
10	2×10^{-4}	3.289×10^{6}	0.12	1.2×10^{5}
10^2	6×10^{-2}	5.069×10^{5}	0.097	9.5×10^{3}
10^3	2.4	8.917×10^{3}	0.34	1.2×10^{3}
10^4	30	518.3	0.52	1.1×10^{2}
10^5	—	38.78	0.93	—
10^6	—	3.241	1.33	—
10^7	—	0.2843	1.73	—

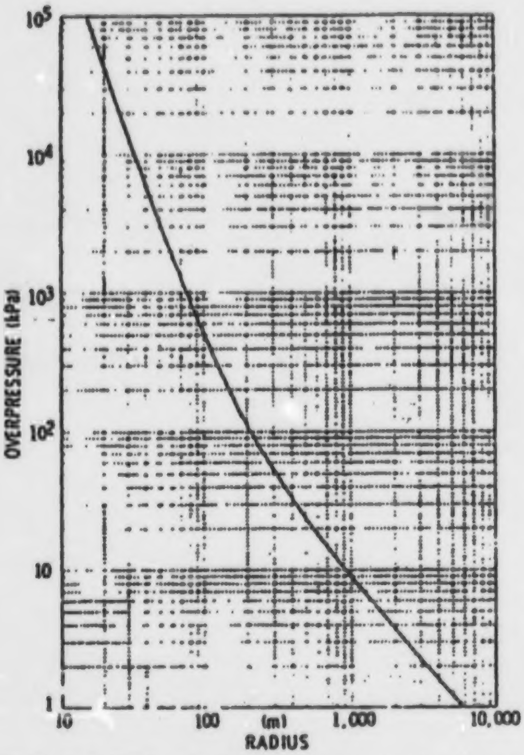

FIG. 2. AFWL 4.2 TJ (1 kiloton) standard overpressure versus radius, high pressures.[4]

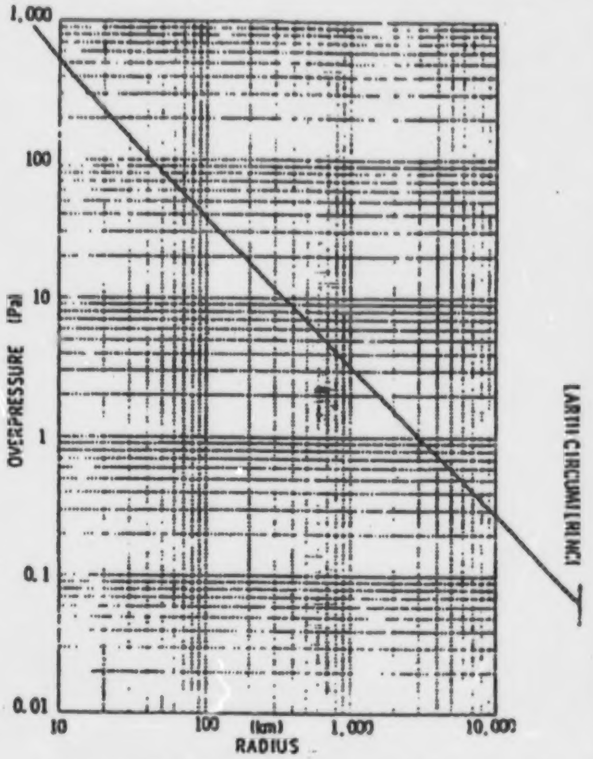

FIG. 3. AFWL 4.2 TJ (1 kiloton) standard overpressure versus radius, low pressures.[4]

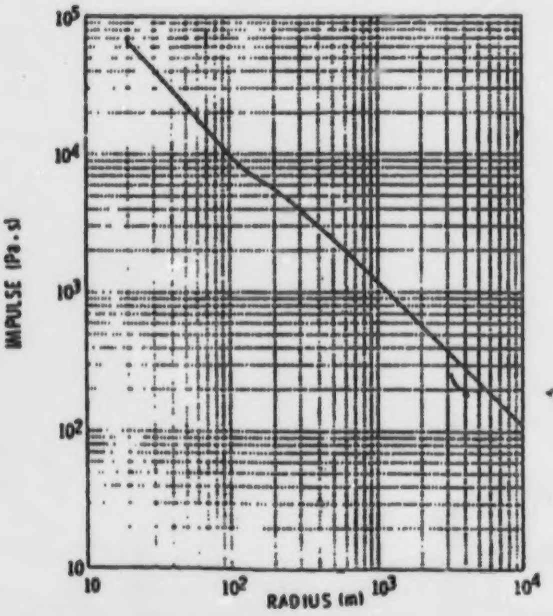

FIG. 4. AFWL 4.2 TJ (1 kiloton) standard overpressure impulse versus radius.[4]

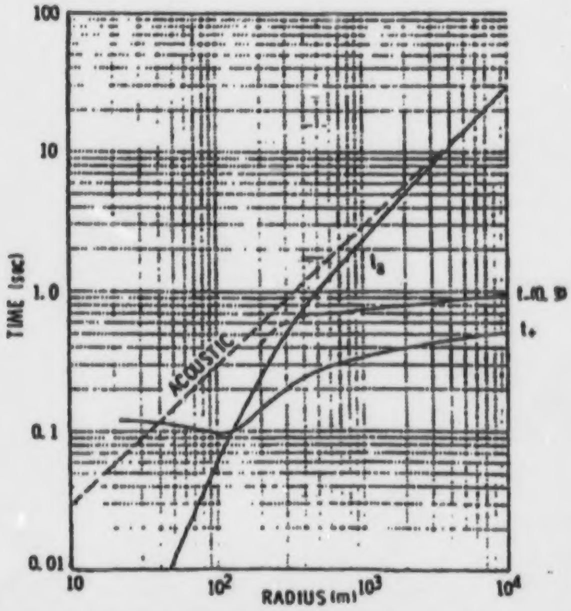

FIG. 5. AFW 4.2 TJ (1 kiloton) standard radius versus time.[4]

4.1.3.3 Scaling to Other Explosions

Yield scaling is accomplished by cube root calculation in Eq. (2) or from Fig. 6. The TNT scale is explained in 4.2.1. Atmospheric pressure depends on altitude and temperature. Average pressure-altitude is given by the U. S. Standard Atmosphere[5] shown in Fig. 7. Altitude-dependent scaling factors for distance from Eq. (2) and for time from Eq. (3) are shown in Fig. 8 for standard atmosphere conditions. Some numerical examples of applying the scaling laws to specific explosions are given in Appendix B.1.

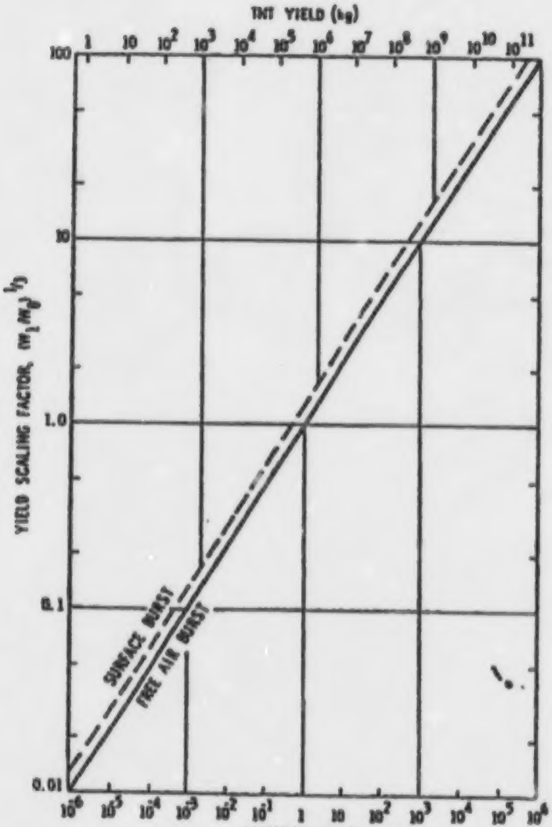

FIG. 6. Yield scaling factors for surface and air burst explosions.

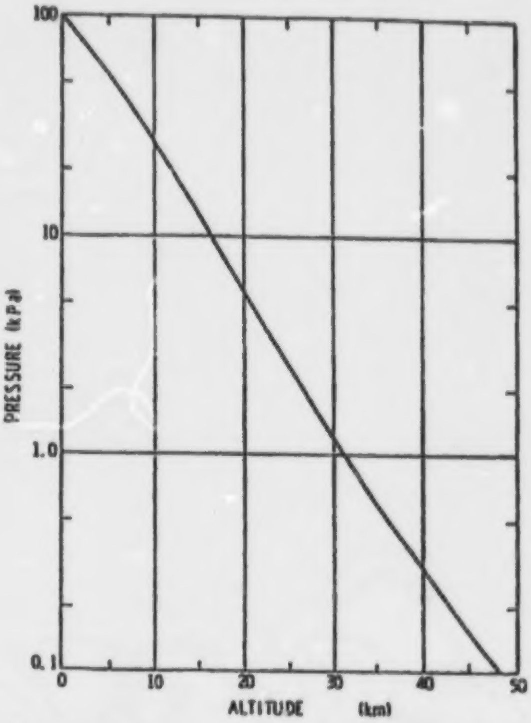

FIG. 7. Standard atmosphere pressure—altitude.

4.1.4 Effects of Nearby Reflectors (HOB)

Many explosions are detonated near reflectors, for example, as ground level surface bursts. A true surface burst of a point source explosion on a perfect reflector would create a hemispherical wave in the atmosphere with blast characteristics for a yield (2*W*) double that of a free air burst with nominal yield *W*. Bursts above such a surface may cause incident and reflected shocks to fuse into a Mach wave[1] as shown by Fig. 9. This shock merging results in wave characteristics which depend on incident shock strength and angle and properties of the reflecting surface. The Mach stem expands approximately as an annulus centered at the surface point nearest the detonation, and acquires characteristics which are determined for an equivalent free air burst of enhanced yield. The HOB yield factor as a function of scaled HOB[6] is shown in Fig. 10, for a typical flat, smooth earth surface, based on measurements made near the 14 kPa overpressure level.[7] It was found to be generally applicable to larger distances and lower pressures.[8] An example of calculating HOB effects is shown in Appendix B.1.3. Specialized curves may be obtained for effects at shorter ranges.[1] Experimental data for nuclear explosion bursts below about 75 m/kt$^{1/3}$ are not generally repeatable because of complex interactions between the fireball and the ground. In consequence, the 2*W* assumption should be made and the resulting bias is seldom distinguishable

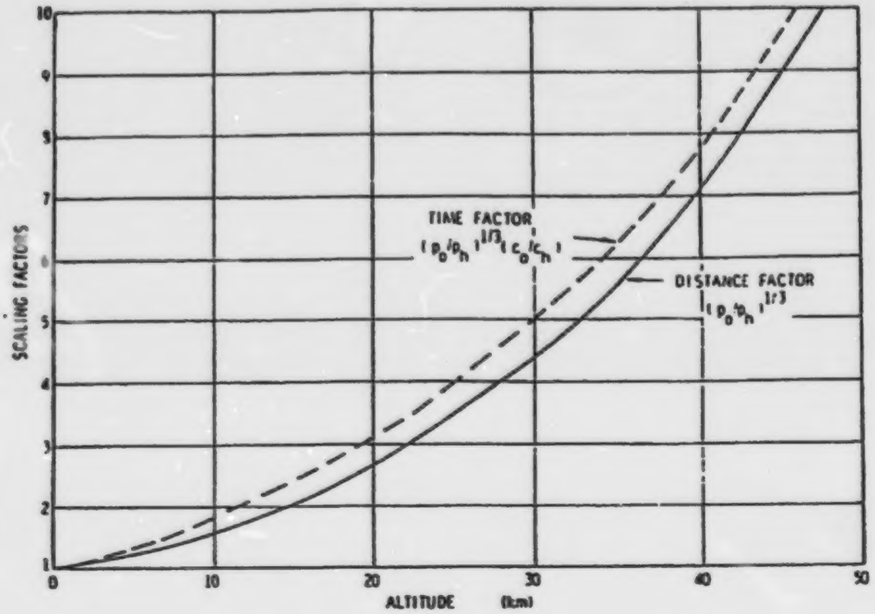

FIG. 8. Altitude scaling factors for explosion times and distances.

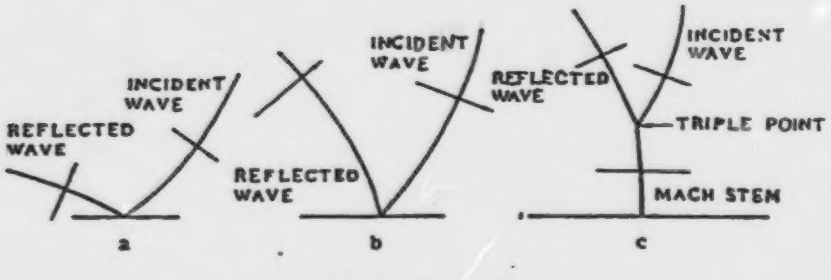
REFLECTED WAVE
INCIDENT WAVE
a
REFLECTED WAVE
INCIDENT WAVE
b
REFLECTED WAVE
INCIDENT WAVE
TRIPLE POINT
MACH STEM
c

Fusion of Incident and Reflected Waves

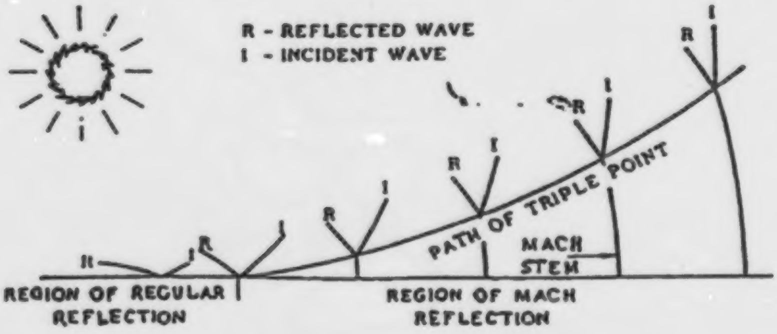
R - REFLECTED WAVE
I - INCIDENT WAVE
R
I
PATH OF TRIPLE POINT
MACH STEM
REGION OF REGULAR REFLECTION
REGION OF MACH REFLECTION

Blast Wave Motion in the Mach Region

FIG. 9. Mach stem formation for above ground bursts.[1]

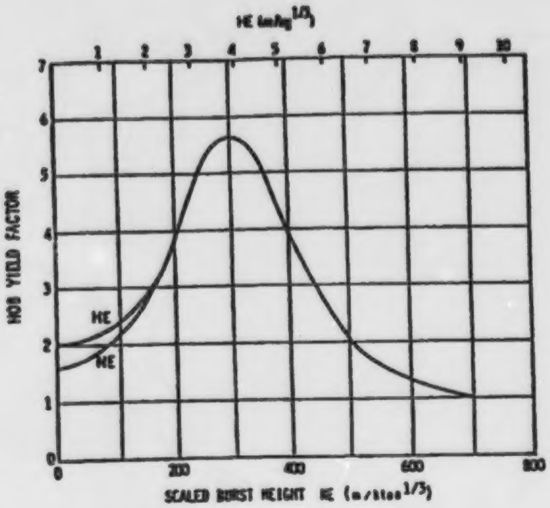

FIG. 10. Airblast HOB effect on apparent yield.

from the noise of experimental measurements. In practice, measurements and calculations of HOB effects have not always shown agreement, because of frequent nonideal conditions. Fireball jets have contributed considerable scatter on occasion. Also, in nuclear tests, intense surface heating sometimes led to "precursor" formation of a very fast moving shock in the warmed surface air layer.

4.1.5 Absorption and Dispersive Losses

Low frequency waves from most explosions are not ordinarily affected in any significant degree by atmospheric attenuation factors.[9] Corrections for attenuation only appear necessary to prediction of amplitudes for very small (grams) explosives, or for bursts above about 60 km altitude,[10] where atmospheric density is very low. Propagation at such high altitude is carried particle by particle and may involve complex species interactions. Attenuation is important at all altitudes, however, if compression rise time calculations are needed for particular applications. A state of the art method for evaluating atmospheric absorption of low amplitude (sonic) pressure waves is available.[11]

4.2 Chemical Explosives

4.2.1 Chemical Solid and Liquid Explosives

These high explosives have relatively large initial dimensions and detonate at lower temperatures and

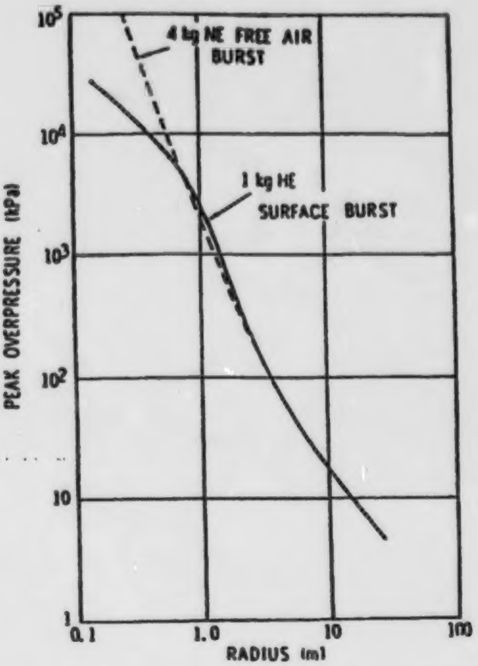

FIG. 11. Peak overpressure versus radius, 1 kg HE surface burst.

TABLE II. Equivalent explosive weight approximations (based on TNT).[a] (Averaged values in regions where $35 < \Delta p < 700$ kPa[15].)

Explosive	Equivalent weight (Δp)	Equivalent weight (I)	Relative energy[b]	Reference
TNT	1.00	1.00	1.00	14, 15
Tritonal	1.07	0.96	1.03	15
Composition B	1.11	0.98	1.09	15
HBX-1	1.17	1.16	1.36	15
HBX-3	1.14	0.97	1.11	15
TNETB	1.36	1.10	1.50	15
Composition C-4	1.37	1.19	1.63	15
H-6	1.38	1.15	1.59	15
Pentolite	1.42	1.00	1.42	15
PETN	1.27	—	1.80	14, 15
Nitroglycerine	1.23	—	1.86	14
RDX-Cyclonite	1.17	—	1.60	14
Nitromethane	1.00	—	1.01	14
Ammonium nitrate	0.84	—	0.60	14
Black powder	0.46	—	0.10	14
Nuclear explosives (0.5W in thermal and radiation)	0.79	—	0.50	1

[a] Example: At a given distance from 1 kg of Pentolite, the same overpressure would result from using 1.42 kg TNT.

[b] Obtained from equivalent weights EW(Δp) × EW(I) from data.[15]

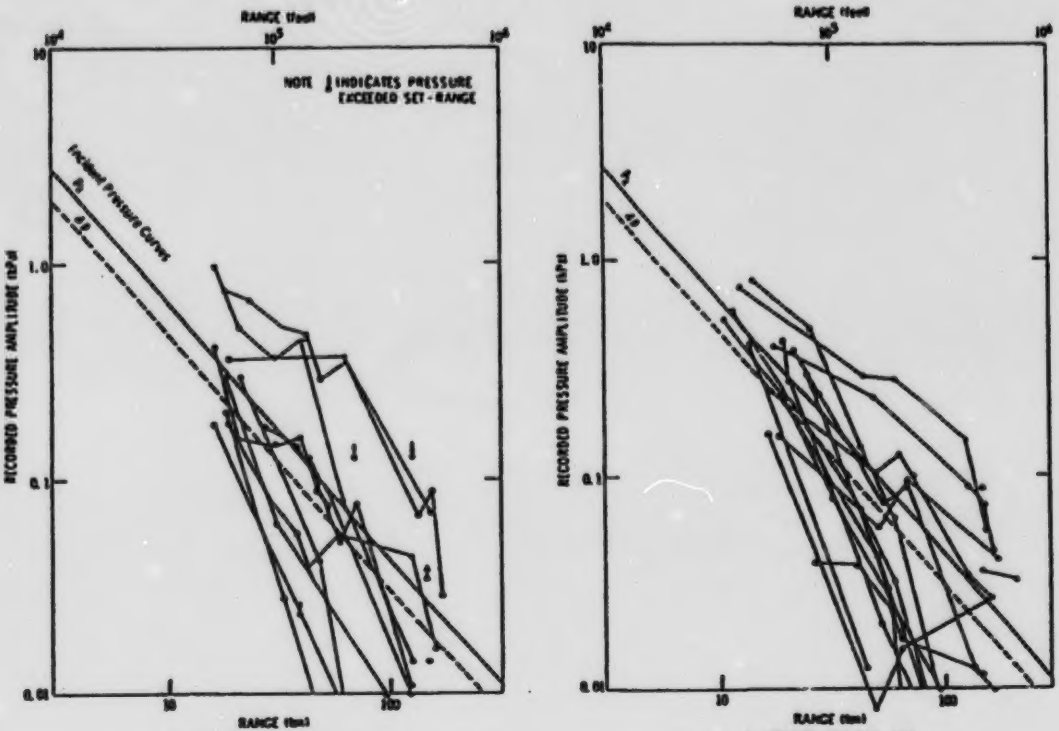

a. UPSHOT-KNOTHOLE, 3/17-6/4, 1953.

b. TEAPOT, 2/18-5/15, 1955.

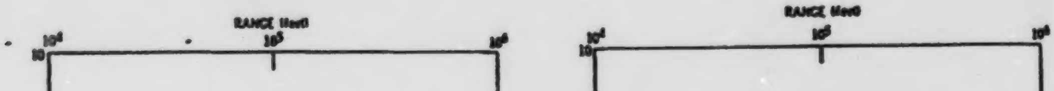

c. PLUMBBOB, 5/28-10/7, 1957.

d. HARDTACK II, 9/19-10/29, 1958.

FIG. 12. Summary of troposphere propagations for Nevada nuclear tests.[6]

pressures than nuclear explosions. For several reasons HE does not lose its energy as fast as NE.[1] The result is, at overpressures below about 1.4 MPa, a typical HE yield gives airblast approximately equivalent to a doubled yield of NE. This equivalence was used in calculating the upper scale in Fig. 6. A calculated theoretical overpressure versus distance curve at short distances scaled for a 1 kg TNT sphere[12] is shown in Fig. 11, and has been well verified by experimental data.[13] At large distances, a blast wave acquires characteristics primarily defined by the propagation medium, air, and a nuclear equivalent yield or energy. Energy outputs for some common chemical high explosives[14,15] are shown in Table II. Strictly speaking, equivalent weights given for various explosives vary as a function of distance from the charge,[15] but at scaled distances beyond 1–3 m from 1 kg HE it is sufficient to cite a single equivalent weight number.

4.2.2 Gaseous Explosives

No data on gas explosions are supplied in this standard because their characteristics have not yet been well defined. With their low initial density and very large relative dimensions, detonating gases take relatively long times and large distances to acquire standard propagating waveforms. Approximate characteristics could be defined for equivalent nuclear yields but with rather different weight equivalences than are obtained for solid HE. Minimum distances for applying simplified procedures would also differ from values for solid HE.

4.3 Empiricisms

4.3.1 Close-In Experimental Data

A number of measured overpressures and overpressure versus distance curves from various nuclear test explosions,[6,16,17] scaled to standard explosion conditions, are shown in Fig. 12. These curves show the variance which may be expected for a wide variety of yields and sources. Much of this variance can be attributed to inhomogeneities in the real atmosphere, which cause nonradial expansions, particularly at large distances.

4.3.2 Long Range Propagation

The range of possible results widens at large distances. A few experimental data have been obtained from vertical propagations from high altitude bursts,[18–20] relatively unaffected by refraction in the horizontally stratified atmosphere. Measurements at low pressures from very small charges are likewise little distorted by atmospheric refraction[21] because of the short distance of travel. Some unrefracted overpressure data ranges are shown in Fig. 13 to show the level of agreement with the standard curve. In addition, a data set from Operation Prairie Flat[22] is shown, with records from 1.1 Mg and 454 Mg HE explosions, ten minutes apart, which were analyzed to remove an assumed constant atmospheric refraction effect. Note that standard incident overpressures, Δp, were doubled to give standard recorded (reflected) overpressures, $K_r \Delta p$, in both Figs. 12 and 13. With either vertical propagation or typical atmospheric refraction, distant waves strike ground at some appreciable incidence angle, often up to 30° with refractive ducting. In result, recorded pressures are about doubled by acoustic reflection from the ground. Of course, measurement well above ground would show separate incident and reflected wave arrivals with nearly equal amplitudes.

4.3.3 Waveforms and Durations

No comparable studies of signature shapes or durations versus large scaled distances have been attempted. At 200 km ranges, observed blast wavelengths do appear to be increased by factors of two to five beyond

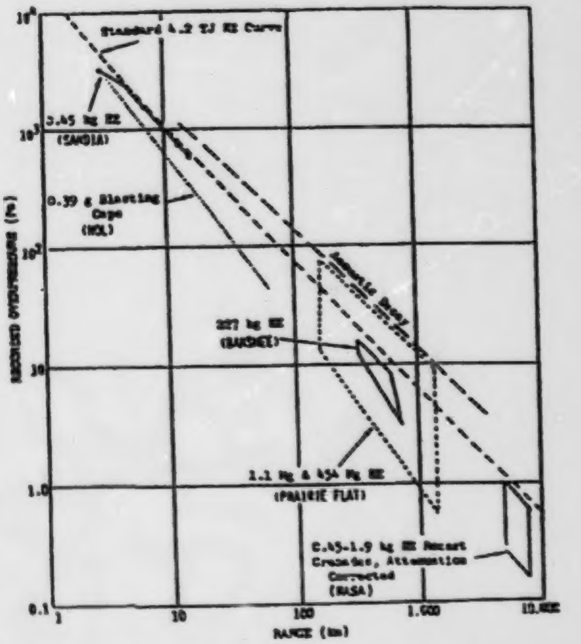

FIG. 13. Long-range airblast data scaled to distances from 4.2 TJ (1 kiloton).

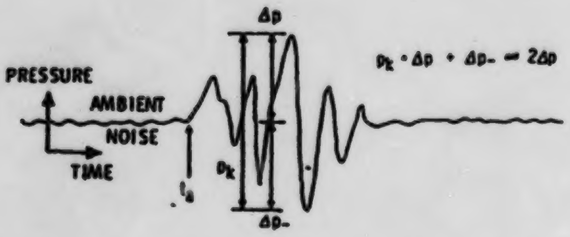

FIG. 14. Typical explosion wave pressure–time signature at long range.

standard values at 10 km shown in Fig. 5. Also, the classical explosion pressure-time signature of Fig. 1 usually becomes distorted by multi-path propagation to long distances,[9] as shown in Fig. 14.

4.3.4 Power Law Standard Overpressure Approximations

At very short distances and high pressures from a nuclear explosion, overpressure decreases inversely with distance cubed.[4] At distances less than 16 m in the standard calculation shown in Fig. 2, approximate extension thus follows:

4.2 TJ (1 kton) CLOSE-IN: $\Delta p = 3.18 \times 10^5\ R^{-3}$ MPa (4)

for R in meters. An example of the application of Eq. (4) is given in Appendix B.2.

At long range, shown by Fig. 3, the calculated standard curve near 100 km range closely follows $R^{-1.1}$ (see Fig. A1), so that extension beyond 10 km can be approximated by

4.2 TJ (1 kton) DISTANT: $\Delta p = 6.526\ R^{-1.1}$ kPa for R in km. (5)

A consequence of this simplified power law relationship is that the scaling laws, Eqs. (1) and (2), have been used to derive a single equation for overpressure in terms of yield, distance, and ambient pressure, applicable at low amplitudes, that

DISTANT: $\Delta p = 6.526 W_A^{0.3667}\ R^{-1.1}\ (p/p_0)^{0.6333}$ kPa (6)

for W_A in kilotons NE, and R in km. For convenience, alternative coefficients for use with other units of yield and distance are shown in Table III. Examples of the application of Eq. (6) are given in Appendix B.3. Figure 15 shows this long range approximation for a wide

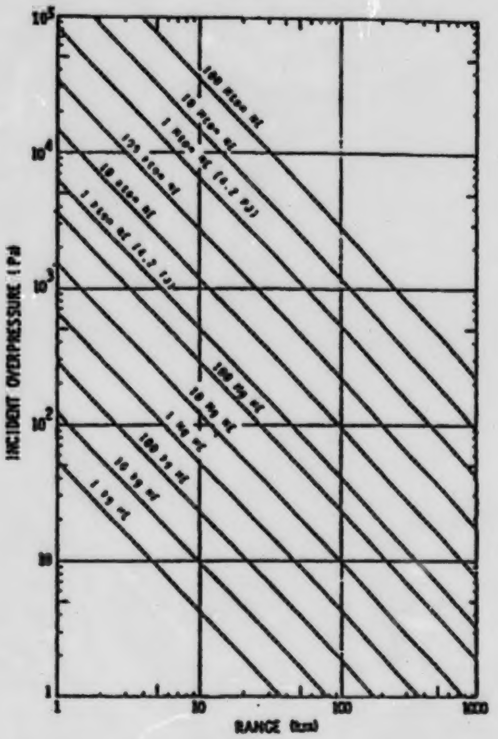

FIG. 15. Standard explosion overpressure–distance curves for NE and HE yields.

TABLE III. Metric (kPa) low-overpressure equation coefficients for various yield and distance units in Eq. (6).

Yield units	Distance units Kilometers	Meters	Kilofeet	Feet	Miles
metric kiloton NE (10^6 kg)	6.763	1.349×10^4	24.989	4.986×10^4	4.007
kiloton NE (2×10^6 lb)	6.526	1.302×10^4	24.112	4.811×10^4	3.866
metric kiloton HE (10^6 kg)	8.720	1.740×10^4	32.221	6.429×10^4	5.167
kiloton HE (2×10^6 lb)	8.414	1.679×10^4	31.089	6.203×10^4	4.986
kg NE	0.04267	82.157	0.1521	303.55	0.02440
kg HE	0.05309	105.93	0.1962	391.39	0.03146
lb HE	0.03973	79.27	0.1468	292.90	0.02354

variety of yields. Extension to 100 megaton NE is included for estimating airblast equivalents for volcanic or meteoritic explosions.

5 REFRACTED ATMOSPHERIC PROPAGATION

5.1 Refractive Distortion of Waves by Inhomogeneous Atmospheres

5.1.1 Plane Wave Refraction

When a plane acoustic wave moves horizontally through an atmosphere which has varying sound velocity strata, it becomes distorted as shown in Fig. 16. Wave front normals, or rays, are turned up (down) away from (toward) ground in layers where sound velocity decreases (increases) with altitude.

5.1.2 Spherical Wave Refraction

Ray bending similarily affects spherical explosion waves as shown in Fig. 17. Atmospheric strata with a succession of decreasing and increasing sound velocity gradients can cause complex wave front distortions and even occasional focusing or caustic formation.

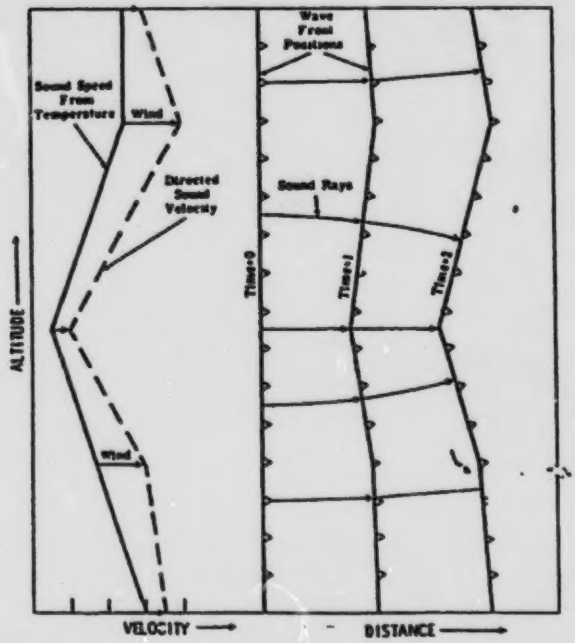

FIG. 16. Shock wave distortion by layered atmospheric temperature and wind structure.

5.1.3 Ray Path Calculations

Fermat's "Principle of Least Time," minimizing the integral of dR/V, is applied, using Snell's Law for refraction that $V \sec \theta = \text{constant}$, to obtain the incremental ray path equation $dx = \cot \theta \, dh$. Path coordinates, $x(h)$, may thus be calculated from any of several numerical or computer methods.[9,23,24] Sound velocity is the isotropic sound speed modified by the superposition of the directed wind vector, and differences between most ray path computer codes lie in how exact a solution is desired, thus how these two components are combined into the integration to provide $x(h)$.

5.2 Atmospheric Parameters

5.2.1 Temperature Effects

5.2.1.1 Sound Speed

Sound speed in air depends on temperature, following[5]

$$c = 1087.53\,(T/273.15)^{1/2}\ \text{ft/s}$$
$$= 331.48\,(T/273.15)^{1/2}\ \text{m/s}. \qquad (7)$$

5.2.1.2 Standard Atmosphere

In the lower "weather" atmosphere, called the troposphere, temperature usually decreases with altitude at an average lapse rate of about −6.5 K/km (−2 K/1000 ft) shown by the U.S. Standard Atmosphere[5] curve in Fig. 18. The top of the troposphere occurs at 8 km to 15 km (25 000–50 000 ft) altitude, depending on location and season. Above this boundary, or tropopause, and in the stratosphere, temperature is relatively constant for a few kilometers, then increases to almost 272 K near 50 km. Above this height, called the mesopeak, there is another decrease in temperature to a minimum near 85 km followed by a monotonic increase with altitude through the ionosphere and out toward space. This single standard atmosphere curve does not show the range of conditions that may be encountered, depending on season, location, and, for very high altitudes, sunspot index. These variations may be obtained from the U.S. Standard Atmosphere Supplements.[25]

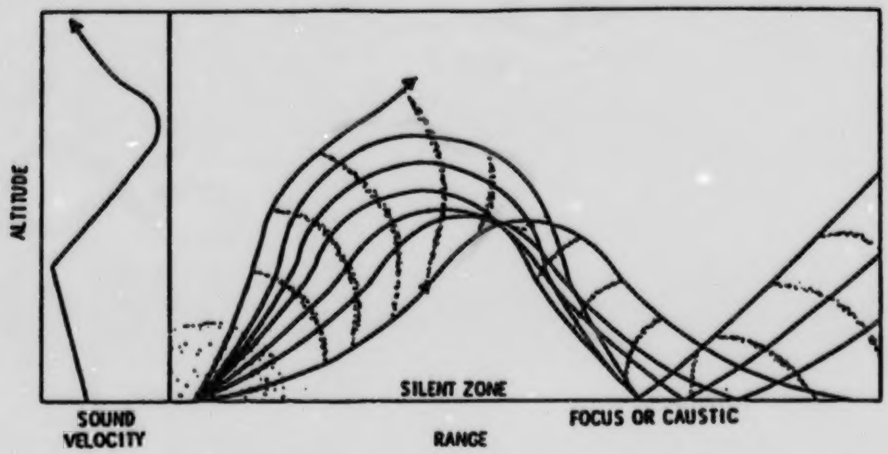

FIG. 17. Typical explosive ray paths.

5.2.1.3 Temperature Inversions

In specific weather conditions, temperature and sound speed may increase with altitude, as in a stable *inversion*, caused by ground cooling at night or by warm air overrunning a cold surface air mass. This could cause blast wave ducting, restricting a portion of the wave to propagation along the ground. In the limit it would allow only cylindrical wave-front expansion and a reduced rate of decrease of overpressure with distance for an explosion wave.

5.2.1.4 Temperature Gradients

Buoyancy and adiabatic gas expansion relations usually limit the temperature decrease with altitude to neutral stability at about − 10 K/km, or certainly not more than the autoconvective lapse rate of − 34.2 K/km. With any common gradient, and in the absence of wind, blast rays would thus be turned up away from ground. Only scattered or diffracted noise would be propagated to ground level at large distances from an explosion under such gradient conditions.

5.2.1.5 High Altitude Temperatures

High temperatures above 40 km altitude may also duct blast waves but they usually give returns to ground at 110 km to 210 km ranges. These blast receptions have been called "ozonosphere waves," being reflected (refracted) from the warm layer caused by ozone photosynthesis. Very high temperatures in the ionosphere above 100 km altitude also duct blast waves so that, in fact, little explosion energy ever actu-

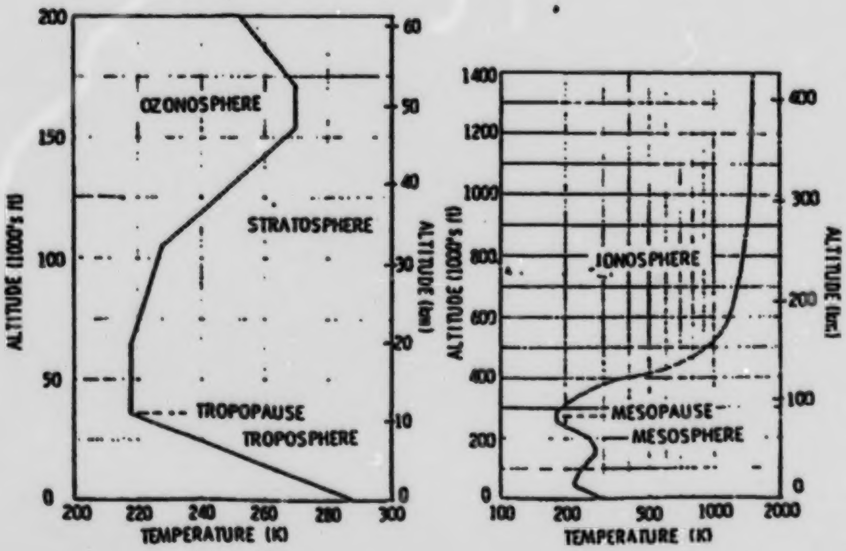

FIG. 18. United States Standard atmosphere, 1962.[3]

ally escapes to space. These ionosphere-returned waves are the infrasonic waves often recorded around the world by various monitoring stations after very large explosions.

5.2.2 Wind Effects

5.2.2.1 Wave Convection

Acoustic or blast waves are further carried by the wind so that they travel at sound speed, based on temperature, plus a directed component of the wind speed, which is usually regarded as a horizontal vector. Wind variations with height do not generally correlate with temperature gradient, so ray-path calculations must be made for specified atmospheric conditions and propagation azimuths. Three special wind effects need consideration in blast prediction.

5.2.2.2 Downwind

Wind speed usually increases with height above the ground since surface flow is retarded by friction. Averaged measurements of wind speed versus height have shown a speed increase that is proportional to the one-seventh power of height above ground.[26] This relation yields a boundary layer sound duct during conditions of neutral adiabatic stability that is over 100 m deep downwind of only 5-m/s wind speed. Thus enhanced downwind propagation would usually be expected unless it were broken up by hills or terrain irregularities. Over rough terrain or built-up cities, however, the greater frictional drag causes a more rapid wind speed increase with height than over flat terrain, and thus more downwind ducting than if surface wind speed (normally observed at 10-m height above ground) criteria are used alone. There could also be appreciable turbulence attenuation of the blast wave.

5.2.2.3 Jet Streams

Winds aloft may reach 90-m/s to 135-m/s (200–300 mph) speeds near 10-km altitude in winter storm situations. Such strong winds can clearly overwhelm the effect of cold temperature and low sound speed near the tropopause, and cause downwind blast ducting and focusing. Blast pressure magnifications from jet stream ducting usually center around 60-km to 80-km ranges, according to ray-path calculations.[27]

5.2.2.4 Monsoon Ozonosphere Ducting

In temperate latitudes near 50-km altitudes, summer winds usually blow from east to west while winter winds blow from west to east. Since temperature and sound speed near 50-km altitude are rather close to surface values, the result is downwind blast ducting that gives a sound "ring" (actually an arc sector) located near 200-km range.[9]

5.3 Propagation Climatology

5.3.1 Boundary Layer Ducting

Available experimental data are not adequate to give separable groups that distinguish between frictional wind ducting and surface temperature inversion ducting of explosion waves. It appears, as shown in Figs. 12 and 19, that incident pressure amplitudes may be enhanced above standard values by factors of two to three for propagations of 30 km to 50 km under sound velocity inversion conditions.[6]

5.3.2 Jet Stream Ducting and Focusing

Also from Fig. 12, an approximate upper bound may be estimated for pressure amplitudes where jet stream ducting caused relatively strong propagations out to 150-km range.[6] Experimental HE data, gathered near a calculated focus or caustic, appear to have a lognormal statistical distribution[27] as shown in Fig. 20. There was concern that surplus depth charge ex-

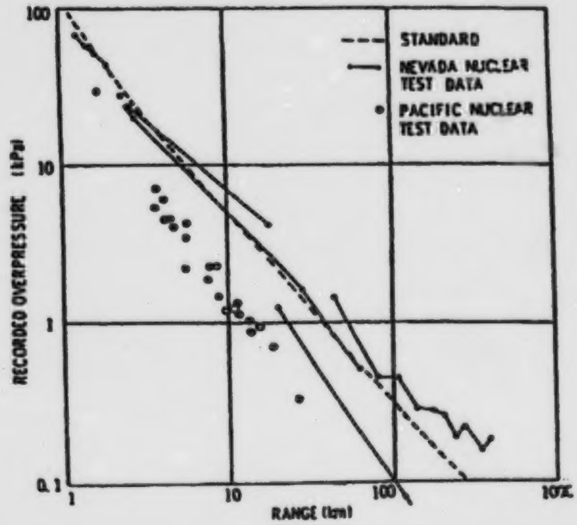

FIG. 19. Measured overpressures scaled to 84 TJ (20 kton) surface burst (2W), Nevada and Pacific test troposphere propagations.

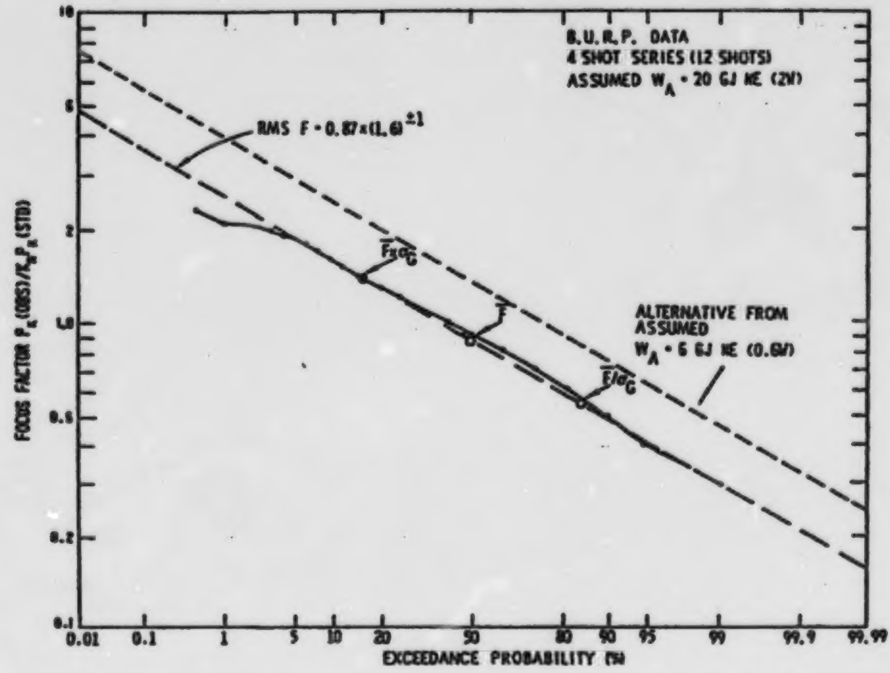

FIG. 20. Atmospheric focus factor probability distribution near a caustic.[17]

plosion sources used in this experiment did not act as point sources (2*W*). The true focus factor distribution may have followed the alternate curve shown, with the geometric average $\overline{F} = 1.36$ for a 0.6-*W* source rather than $\overline{F} = 0.87$ for a 2-*W* source. Data scattered with a geometric standard deviation factor of 1.6 for either assumed source.

5.3.3 Downwind Ozonosphere Propagations

Nuclear test data, scaled for yield and HOB, display seasonal monsoon wave characteristics[6] shown in Fig. 21. Downwind data have been assembled to give the amplitude probability distribution shown in Fig. 22.

5.3.4 Gradient Propagation

Explosion data from recording stations with sound velocity gradients observed for their direction, and no calculated ducting, show an approximate R^{-2} average amplitude decay with distance.[6] This slope was evident in Fig. 12 because most distant ducting at low altitudes was blocked by rough terrain and upper air gradients controlled propagation. In Fig. 19, Pacific nuclear test data show reduced propagation[16,17] caused by predominant thermal gradients in tropical air masses.

6 STRUCTURAL RESPONSE

6.1 Strong Shock Effects

6.1.1 Overpressure Range

Strong shocks may be defined as having more than 6.9 kPa (1 psi) overpressure, and a capability for causing considerable damage to many exposed structures.

6.1.2 Diffraction Loading

When a blast wave front strikes a structural face it will be reflected, and that face will experience at least twice the incident overpressure. When strong shocks reflect at certain incidence angles, the reflected overpressure may be as much as eight times the incident overpressure (see Ref. 14 for derivation and details). As the pressure wave passes the structure it bends or "diffracts" around it. When this structure is eventually engulfed by a blast wave of sufficiently long duration (large yield), pressures exerted on all sides may be nearly equal except for blast wind pressures on the front face. This is illustrated in Fig. 23, for both normal (Fig. 23 a–e) and oblique (Fig. 23 f–i) incident wave fronts. The pressure differential between front and back faces of a structure will be maximized while the wave has not completely surrounded it. This diffraction loading may cause the structure to deflect or

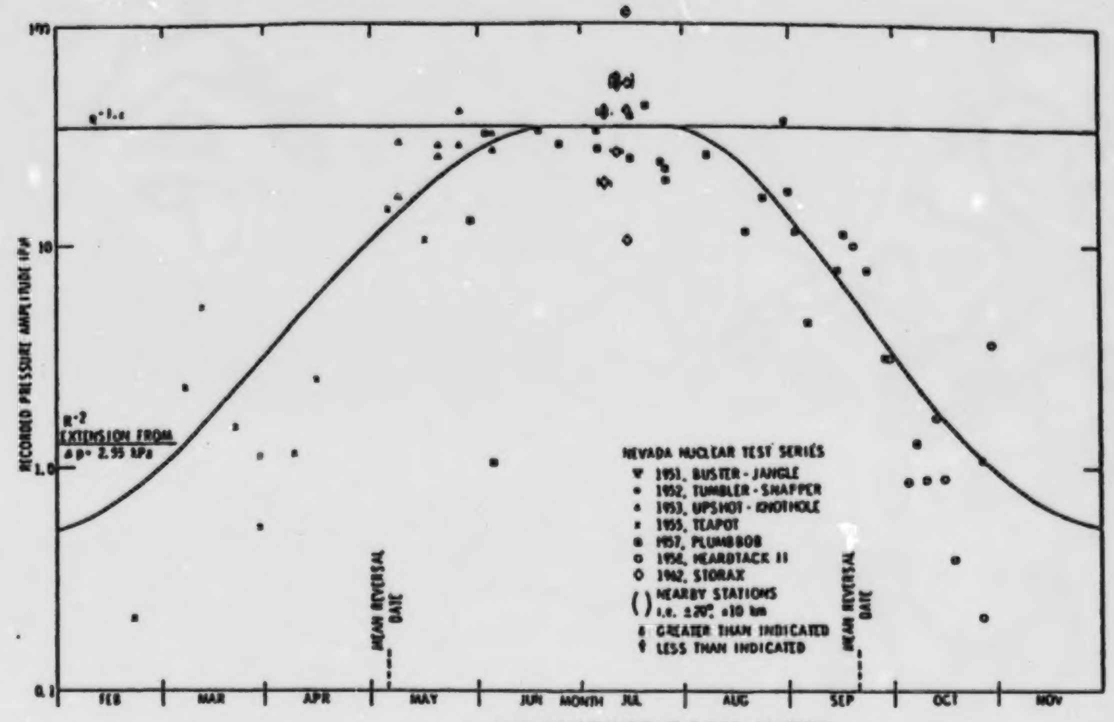

A. WESTWARD PROPAGATION TO BISHOP, CALIFORNIA

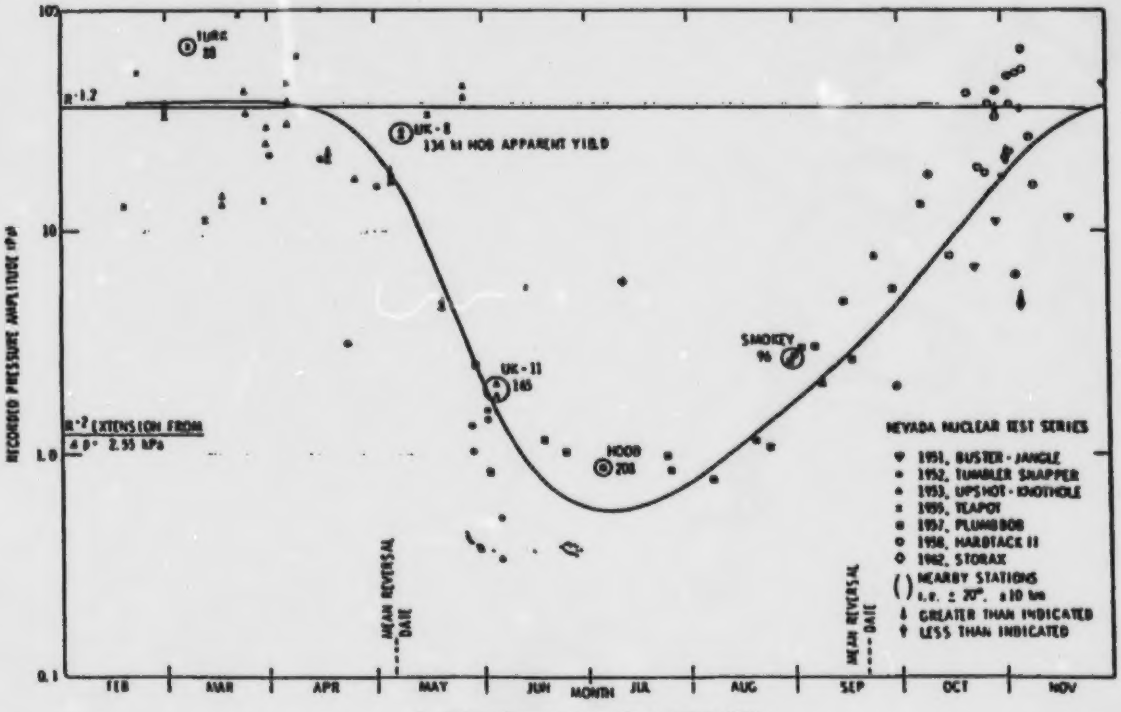

B EASTWARD PROPAGATION TO ST GEORGE, UTAH

FIG. 21. Ozonosphere signal amplitudes from Nevada nuclear tests.[6]

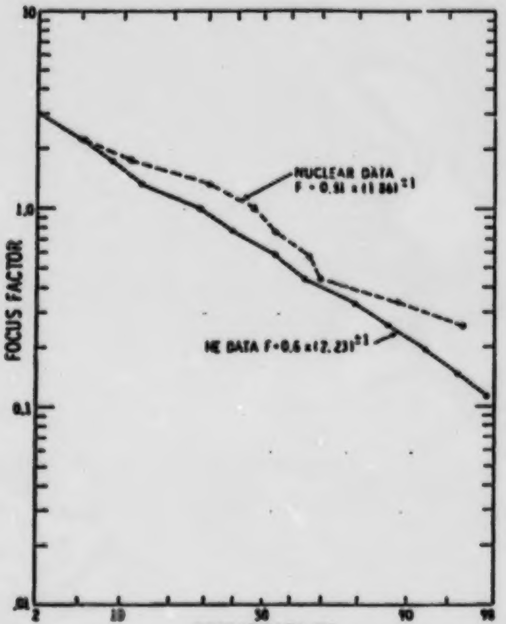

FIG. 22. Distribution of atmospheric focus factors, St. George, Utah, winter data (Nov.–Mar.), downwind ozonosphere propagations.[6]

move, or the faces may fail. The diffraction period depends on structure size, and is seldom greater than a small fraction of a second. Thin structures may have such short diffraction periods that this loading is negligible. Also, if there is panel failure, there will be rapid equalization of exterior and interior pressures, tending to reduce diffraction loading on the total structures.

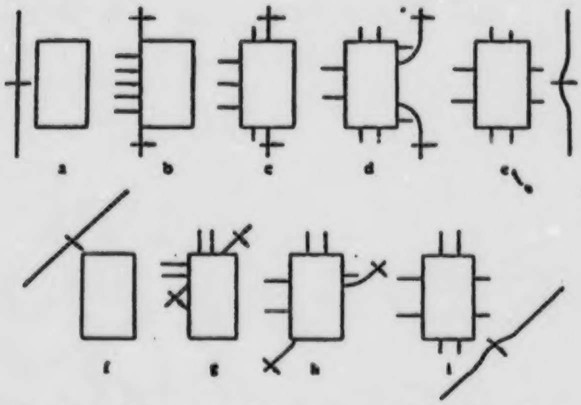

FIG. 23. Stages in the diffraction of a blast wave by a structure.

6.1.3 Drag Loading

During the positive pressure phase duration a structure will be exposed to a lateral drag or dynamic pressure loading by the air movement following the blast wave front. For large yields and long positive pressure phases, this drag force may persist much longer than the diffraction loading. It lasts about one second at one kilometer from a megaton yield burst. Dynamic pressures at the front face are smaller than incident and reflected overpressures for incident overpressures below about 400 kPa, where blast wind speed reaches 470 m/s. Some typical drag-sensitive targets are smokestacks, utility poles, and communications towers.

6.1.4 Residential Structure Damage

Damages, in terms of needed repair costs as a percentage of complete replacement construction costs, vary with incident overpressure as shown by test data for wood-frame housing[28,29] in Fig. 24. As indicated, extrapolation to near the damage threshold shows tha:

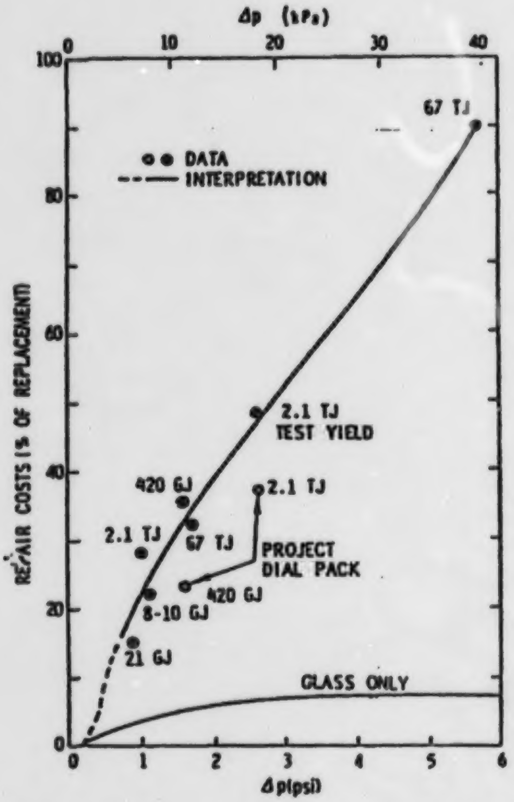

FIG. 24. Airblast damage to residential structures.

minor damage increases rapidly with increasing overpressures, but it appears to be independent of yield and wavelength. Estimation of such cosmetic damage, particularly to window glass, is described in 6.3.2. Though often spectacular in failure under airblast loading, total glass replacement would only average 7.5% of total structural replacement cost. Masonry structures, of brick, concrete block, or stone, would have different responses but there are no comparable test data for such buildings.

6.1.5 Vehicle Damages

Flight hazards and damage may occur to vehicles from overpressures larger than indicated[1] in Table IV.

6.1.6 Ships and Craft Damage

Ships and craft are susceptible to structural damage and overturning by an airblast wave. Loaded cargo ships tend to sit low in the water and are not in danger of being capsized. Damage to different types of structures on cargo ships will initiate at different overpressure ranges as shown in Table V. For lightweight craft, capsizing and structural damage can result. Capsizing will depend on the particular type craft and the duration of the shock wave, and can occur at overpressures less than 7 kPa. The onset of structural damage may also occur at overpressures below 7 kPa, with moderate to severe structural damage occurring at 20 to 40 kPa overpressures.

6.2 Intermediate Strength Shocks

6.2.1 Overpressure Range

Intermediate strength shocks may be defined between 0.7 kPa and 7 kPa (0.1–1.0 psi). With large yields, such as nuclear kilotons, these pressures propagate far enough to be strongly affected by atmospheric refractive distortion. Effects from small yields, in megagrams or kilograms of HE, at shorter ranges are not so much perturbed by atmospheric refraction.

TABLE IV. Minimum overpressures which cause vehicle damages, in kilopascals (psi in parentheses).

Vehicle	Flight hazard	Damage light	Damage moderate	Damage severe
Light aircraft and helicopters	1.38 (0.20)	3.45 (0.5)	6.89 (1.0)	13.8 (2)
Transport aircraft	1.72 (0.25)	6.89 (1.0)	13.8 (2.0)	20.7 (3)
Automobiles	—	13.8 (2.0)	100 (15)	150 (22)

TABLE V. Damaging overpressures for structures on cargo ships.

Structure	Overpressure (kPa)	Overpressure (psi)
Navigation equipment	7–21	1–3
Large windows	7–21	1–3
Superstructure	28–41	4–6
Hull	34–138	5–20

6.2.2 Cosmetic Building Damage

Damage consists mostly of window pane breakage, possible door damage, disturbed knickknacks and wall hangings, and cracked plaster wall finishes. In these lower pressure ranges, such damages are usually not predicted by standard engineering design considerations.[30] They are often aggravated by improper installation, prestressing, aging or weathering, or precarious positioning, so that failure might soon be expected even without blast wave insult. Much damage reduction is possible, if warning is given, by opening doors, and securing bric-a-brac and fluorescent ceiling light bulbs. Boarding over window glass may be effective, but panes may still be broken by total building racking under diffractive blast wave stress.

6.3 Nuisance Level Airblasts

6.3.1 Recorded Amplitudes

Recorded peak-to-peak amplitude is often used to describe blast waves with less than 0.7 kPa (0.1 psi) incident overpressure. Often these waves do not have ideal explosion waveforms or pressure signatures because they have been distorted by atmospheric refraction, turbulent scattering, and multi-path transmission and interference (see 4.3.3). Use of peak-to-peak values helps to average these variable, non-repeatable waveforms so that amplitude values are more predictable and reproducible. Also, they are about doubled by acoustic reflection as they strike the ground. Peak-to-peak amplitude in a classical explosion waveform[3] is about 1.35 Δp; recorded, and doubled amplitude is thus 2.7 Δp. This category of amplitudes thus falls below about 1.9 kPa recorded peak-to-peak.

6.3.2 Window Glass Breakage

6.3.2.1 Experimental Results

Experimental data that are available from limited laboratory tests[31] do not give strong confidence in extreme value statistics which are necessary for engineering analysis of relatively rare incidents. Recordings from nuclear tests, however, indicate that amplitudes of about 400 Pa correspond in practice to the threshold level at which claims for window damage begin. Claims become quite numerous at 500-Pa recorded amplitude. Interpretations of damage patterns from an accidental explosion incident at Medina Facility (near San Antonio, Texas), in November 1963,[32] showed that costs and damage could be roughly related to wave amplitude and impacted population.

6.3.2.2 Power Law Prediction Model

By assuming an average unit pane repair cost ($15.40 per pane[32] in 1963 dollars) and an empirical relation between population, pane counts, and pane dimension distribution (total of 19 panes per capita), broken pane costs, *C* in dollars, can be described by

$$C = 2.46\times10^{-9}N(K_r p_k)^{2.78} \tag{8}$$

for p_k in Pa (the coefficient is 8.94×10^{-4} for p_k in mbar). The quantity of broken panes can be estimated from

$$Q = 1.56\times10^{-10}N(K_r p_k)^{2.78} \tag{9}$$

for p_k in Pa (this coefficient is 5.66×10^{-5} for p_k in mbar). This relation is shown in probability form by the dashed line in Fig. 25. Various spot applications of these equations to small scale damaging wave incidents have shown that the number of broken panes, thus calculated, usually agrees with claims reports within a factor of two.

Such a power law response obviously cannot be used for damage prediction from large amplitude waves. As shown by Fig. 25, total window breakage is predicted for an incident overpressure of 8 kPa ($K_r p_k$ = 22 kPa). Full scale tests of typical residential structures exposed to large explosions[33] showed that two to five times this pressure was required to break all installed glass panes. On the other hand, this simple empiricism works surprisingly well for small amplitude waves when compared to some other estimates[30] commonly used by engineers and architects.

6.3.2.3 Lognormal Probability Model

A more satisfactory probabalistic model has been defined by connecting damage probabilities from the Medina incident with explosion test data by a lognormal failure distribution,[34] shown by a solid line curve in Fig. 25. At intermediate overpressures this probability relation predicts greater damage than the power law in 6.3.2.2. There was, however, a paucity of verification data in this zone until Redpath's survey of damages[35] from an accidental explosion of 45.5 m³ of monomethylamine nitrate in Wenatchee, Washington, in August 1974. His results appear to somewhat exceed even the probabilistic prediction. The lognormal relationship states that 50% of window panes in an "average typical" community should be broken by an incident wave of 7.5-kPa overpressure, with a logarithmic standard deviation of ±0.916.[36] In equation form, use of the geometric (logarithmic) average and lognormal distribution of pane-breaking overpressures,

$$\Delta p = 7.5\times(2.5)^{\pm 1}\ \text{kPa} \tag{10}$$

shows that 84% (+1 SD) of panes would be broken by $\Delta p = 7.5\times2.5 = 18.75$ kPa, 16% (−1 SD) by $\Delta p = 7.5/2.5 = 3$ kPa. This empirical model has shown reasonable agreement with a theoretical derivation

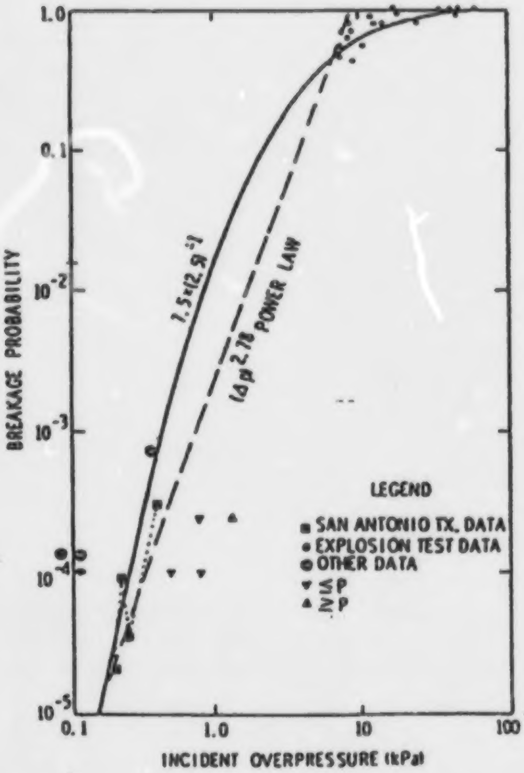

FIG. 25. Window breakage from airblast, theory and data.

that is based on a combination of variance in glass strength from laboratory experiments[32] with the variance of atmospheric acoustic propagation,[27] a randomized direction of exposure that gives reflected doubling on front windows and halved overpressures on rear windows,[37] and a weathering factor.[38] Details have not been completely resolved but an interesting feature is that edge defects and installation variance, including prestressing from building settling or warping, apparently make little contribution to breakage from airblast pressure loading, a result predicted by plate theory.[39] This model needs further development, but, meanwhile, use of Eqs. (8) and (9) can be applied with reasonable confidence.

6.3.2.4 Yield Limits for No Breakage

6.3.2.4.1 Concentrated Populations. The overpressure relation of Eq. (6) has been combined with the power law window breakage relation of Eq. (9) to give estimates for nondamaging separation distances from explosions.[40] A safe conservative assumption was made that there could be extreme $F = 5$ blast focusing unless it was avoided by a weather-watch. In result, there should be no window damage, $Q < \frac{1}{2}$, when

$$W < 328\, R^3/N, \qquad (11)$$

for a surface burst of W in kg HE at distance R in km from a concentration of N people. For a single exposed residence, it may be assumed that $N = 4$. Census statistics are used to estimate populations of vulnerable communities. "Worst case" analysis for focusing, rather than a probability analysis, gives a smaller coefficient of 114. Yield limit estimates for no damage to communities may be made from Fig. 26.

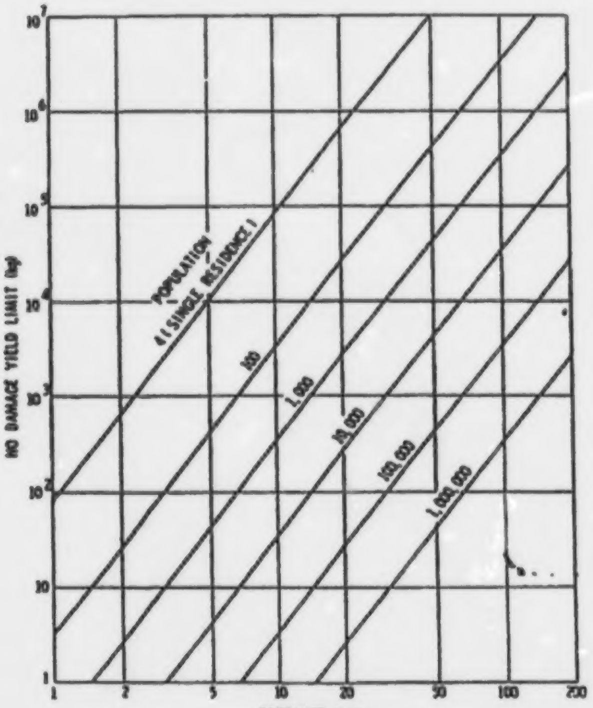

FIG. 26. No damage yield limits for surface burst HE explosions versus distance and population.

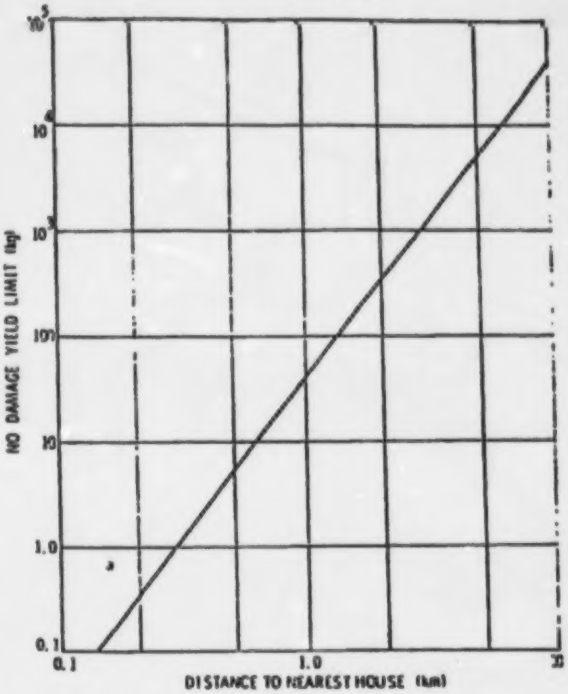

FIG. 27. No damage yield limits for surface burst HE explosion for rural areas.

6.3.2.4.2 Uniform Population Distributions. Evaluations for rural areas, without population concentrations, are based on the distance to the nearest house, R_1, and a probability analysis of a random areal distribution for succeeding houses. To limit damage over the entire area of assumed uniform population density to $Q < \frac{1}{2}$, an approximate yield limit results that

$$W < 40 R_1^3 \qquad (12)$$

for a surface burst of W in kg and distance R_1 in km, as shown in Fig. 27.

6.3.3 Other Damages

Experience with plaster damage claims is varied. At Medina, paid claims for plaster cracks and other miscellany amounted to almost 50% of paid glass claims.[41] In certain other blast wave cases plaster claims considerably exceed window claims.[42] This reflects local construction practice, the general state of building repair and age, and publicity given to the incident. With all the variability inherent in window glazing practices, glass panes are still simpler, more uniform and ideal targets than plastered interior walls. Similarly, miscellaneous damage, such as broken mirrors or bric-a-brac, seems practically unpredictable. It is usually clear, however, that claims for damages such as cracked concrete foundations or broken pipes are invalid.

6.3.4 Blast Repetition

There are contrary opinions about cumulative effects from repeated airblast insults on structures. In structures, repeated impacts might cause accelerated deterioration of a component, and eventual failure. On the other hand, the "weak-sister theory" reasonably postulates that nearly all imminent failure will be brought out by a first blast wave, and there would be reduced damages and costs from subsequent blasts. Counter to this, variability of amplitude in an apparently uniform field, particularly from farfield atmospheric distorted waves, may not allow much assurance that all "weak-sisters" were broken by a first event. Also, local reflective acoustic amplifications may contribute to many of the actual breakages. These amplifications would not be exactly repeated by successive waves, unless not only the experiment or operation but also the meteorology and wave incidence angle were repeated exactly. There are no firm data available for exploring these conflicting intuitive views on the influence of repetition.

7 REFERENCES

[1] S. Glasstone (Editor), *The Effects of Nuclear Weapons*, Rev. Ed. (Government Printing Office, Washington, DC, 1962), pp. 6–557.

[2] R. G. Sachs, "The Dependence Of Blast On Ambient Pressure and Temperature," BRL Report No. 472, Army Ballistic Research Laboratories, Aberdeen Proving Ground, MD, 1944.

[3] H. A. Bethe (Editor), "Blast Wave," Report LA-1020, Los Alamos Scientific Laboratory, Los Alamos, NM, Aug. 1947.

[4] C. E. Needham, M. L. Havens, and C. S. Knauth, "Nuclear Blast Standard (1 kt)," Report AFWL-TR-73-55 (Rev.), Air Force Weapons Laboratory, Kirtland Air Force Base, NM, Apr. 1975.

[5] *U.S. Standard Atmosphere*, 1962 (Government Printing Office, Washington, DC, 1962), pp. 113–147.

[6] J. W. Reed "Climatology of Airblast Propagations from Nevada Test Site Nuclear Airbursts," Report SC-RR-69-572, Sandia Laboratories, Albuquerque, NM, Dec. 1969.

[7] L. J. Vortman and J. D. Shreve, Jr., "The Effect of Height of Explosion on Blast Parameters," Report SC-3858 (TR), Sandia Laboratories, Albuquerque, NM, Jan. 1956.

[8] H. W. Church, "Height-of-Burst Effects on Long-Range Propagated Blast Pressures," Report SC-4687 (RR), Sandia Laboratories, Albuquerque, NM, May 1962.

[9] E. F. Cox, "Sound Propagation in Air," *Handbuch der Physik* (Springer-Verlag, Berlin, 1958), Vol. 48, Chap. 22, pp. 455–461.

[10] J. W. Reed, "Attenuation of Blast Waves by the Atmosphere," J. Geophys. Res. 77, 1616–1622 (1972).

[11] *American National Standard Method for the Calculation of the Absorption of Sound by the Atmosphere*, S1.26–78 (American National Standards Institute, New York, 1978).

[12] C. E. Needham, "Theoretical Airblast Calculations—Project LN103," in "Operation Prairie Flat Preliminary Report," DASA-2228-I, Defense Atomic Support Agency Information and Analysis Center, Santa Barbara, CA, Jan. 1969.

[13] L. Giglio-tos, "Fundamental Air Blast Measurements—Project LN101," in "Event Dial Pack Symposium Report," Defence Research Board of Canada, Ottawa, Mar. 1971.

[14] G. F. Kinney, *Explosive Shocks in Air* (MacMillan, New York, 1962), pp. 66–170.

[15] M. M. Suisdak, Jr., (Editor), "Explosion Effects and Properties," Report NSWC/NOL/TR-75-116, Naval Surface Weapons Center, Silver Spring, MD, Oct. 1975.

[16] J. J. Meszaros, R. E. Reisler, and R. C. Wise, Personal communication, Ballistic Research Laboratories, Aberdeen Proving Ground, MD, July 1962.

[17] E. J. Bryant and J. H. Keefer, Personal communication, Ballistic Research Laboratories, Aberdeen Proving Ground, MD, Jan. 1962.

[18] J. W. Reed, "Airblast Overpressure Decay at Long Range," J. Geophys. Res. 77, 1623–1629 (1972).

[19] J. R. Kelso, G. Stalk, and C. C. Clifford, Jr., "Project Banshee Field Operations (1961 and 1962)," in Preliminary Report DASA-543, Defense Atomic Support Agency, Washington, DC, May 1963.

[20] D. J. Ramsdale, "Calculations of the Properties of Finite-Amplitude Waves Propagating from High-Altitude Grenade Explosions," *79th Meeting, Acoustical Society of America*, Atlantic City, NJ, Apr. 1970.

[21] L. D. Sadwin and E. A. Christian, "Characteristics of the Shock Wave Generated in Air by a Blasting Cap," Report NOLTR 71–105, Naval Ordnance Laboratory, Silver Spring, MD, June 1971.

[22] J. W. Reed, "Distribution of Airblast Amplitudes in the Ozonosphere Sound Rings," Report SC-M-69-33, Sandia Laboratories, Albuquerque, NM, Feb. 1969.

[23] E. F. Cox, H. J. Plagge, and J. W. Reed, "Meteorology Directs Where Blast Will Strike," Bull. Am. Meteorol. Soc. 35, 95–103 (1954).

[24] R. J. Thompson, "Ray Theory For an Inhomogeneous Moving Medium," J. Acoust. Soc. Am. 51, 1675–1682 (1972).

[25] *U. S. Standard Atmosphere Supplements*, 1966 (Government Printing Office, Washington, DC, 1966), pp. 3–289.

[26] *American National Standard Building Code Requirements for Minimum Design Loads in Buildings and Other Structures*, A58.1-1972 (American National Standards Institute, New York, 1972).

[27] J. W. Reed, "Explosion Wave Amplitude Statistics for a Caustic at Ranges of 30 to 45 Miles," Report SC-RR-67-860, Sandia Laboratories, Albuquerque, NM, Feb. 1968.

[28] C. Wilton, "Building Damage Surveys from Explosion Tests," in "Minutes of the Twelfth Explosives Safety Seminar, Armed Services Explosives Safety Board," Washington, DC, Aug. 1970, pp. 267–286.

[29] C. Wilton, "Assessments of House Damage from Event DIAL PACK and 100 ton AN/FO Test," Interim Report DNA 27291, URS Research Corporation, San Mateo, CA, Mar. 1972.

[30] "Glass Product Recommendations, Structural," Report 101, Pittsburgh Plate Glass Company, Pittsburgh, PA (undated).

[31] R. W. Ansevin, "Correlation of the DSR with the Strength of Glass of Different Compositions and Configurations," Report ML TDR 64-180, Pittsburgh Plate Glass Company, Harmar Township, PA, Aug. 1964.

[32] J. W. Reed, B. J. Pape, J. E. Minor, and R. C. DeHart, "Evaluation of Window Pane Damage Intensity in San Antonio Resulting from Medina Facility Explosion on November 13, 1963," Ann. N.Y. Acad. Sci. 152, 565–584 (1968).

[33] C. Wilton and B. Gabrielsen, "House Damage Assessment," Summary Report DNA-2906F (Defense Nuclear Agency), URS Research Corporation, San Mateo, CA, Jan. 1973.

[34] J. W. Reed, "Wind Damage to Windows as Estimated from Explosion Tests," in *Proceedings, 2nd National Conference on Wind Engineering Research* (Colorado State University, Fort Collins, CO, 1975), pp. II-22-1,2.

[35] B. B. Redpath, personal communication, URS/J. A. Blume and Associates, San Francisco, CA, Jan. 1976.

[36] J. Aitchison and J. A. C. Brown, *The Lognormal Distribution* (University Press, Cambridge, England, 1969), pp. 7–14.

[37] J. A. Blume, R. L. Sharpe, E. G. Kost, and J. Proulx, "Response of Structures to Sonic Booms Produced by XB-70, B-58, and F-104 Aircraft," J. A. Blume and Associates, San Francisco, CA, July 1967.

[38] R. W. McKinley, "Response of Glass in Windows to Sonic Booms," Mater. Res. Stand. 4, 594–600 (1964).

[39] L. Orr, "Practical Analysis of Fractures in Glass Windows," Mater. Res. Stand. 12, 21–23 (1972).

[40] "Guidelines for Preparing Environmental Impact Statements on Noise," Report of National Academy of Sciences Committee on Hearing and Bioacoustics Working Group 69, Washington, DC, Mar. 1977.

[41] B. J. Pape, J. E. Minor, and R. C. DeHart, "Evaluation of Window Pane Damage Intensity in San Antonio Resulting from Medina Facility Explosion on 13 November 1963," Report 03-1716, Southwest Research Institute, San Antonio, TX, Jan. 1966.

[42] J. H. Wiggins, Jr., *Effects of Sonic Boom* (J. H. Wiggins, Palos Verdes Estates, CA, 1969), pp. 83–95.

APPENDIX A: EVOLUTION OF EXPLOSION AIRBLAST MODELS

[This Appendix is not part of American National Standard Estimating Airblast Characteristics for Single Point Explosions in Air, With a Guide to Evaluation of Atmospheric Propagation and Effects S2.20-1983, but is included for information purposes only.]

A.1 IBM Problem M

Prior to World War II, studies of explosion wave phenomena were relatively few and far between, although the basic principles involved in detonation, yield scaling, and shock propagation were understood. During that war, considerable research was done under security wraps, and only a small part of it was later published in scientific periodicals after restrictions were lifted. Probably the earliest one-dimension sphere hydrodynamic blast calculation[3] was produced on the early Manhattan Project electronic computer. It was later refined, detailed, and released as "IBM Problem M".[A1,A2] Experimental data generally verified its reliability, but certain theoretical reservations delayed its general acceptance. More sophisticated calculations were continuingly being developed in later years for solution by increasingly powerful computers. The physics and mathematics have now been well explained.[A3]

A.2 AFWL Explosion Model

One shortcoming of IBM Problem M was that it ended at 2.7 km, where overpressure was 2.5 kPa, because of computational instability in handling very small quantitites. Extension to lower pressures and longer ranges, for use in a variety of problems, has been the subject of extensive discussion until recently when adequate computer treatments became available. Meanwhile, some favored simple acoustic extension, that $\Delta p \sim R^{-1}$, and no further change of wave shape. Early study of shock waves from bullets[A4] led to the well known asymptotic farfield solution that $\Delta p \sim 1/R(\ln KR)^{1/2}$, but there was difficulty in determining an appropriate value for the constant, K. Further analytical refinements proceeded[A5,A6,A7] until an agreeable standard calculation for a kiloton nuclear free air burst was obtained by AFWL,[4] which reasonably fits the important theoretical and experimental results. The analytical expression for overpressure, is

$$\Delta p = \frac{A_1}{R^3} + \frac{A_2}{R^2} + \frac{A_3}{R\{\ln[(R/R_0) + 3\exp(-(R/R_0)^{1/2}/3)]\}^{1/2}}, \tag{A1}$$

where $A_1 = 3.18 \times 10^{11}$, $A_2 = 10^9$, $A_3 = 9 \times 10^6$, and $R_0 = 445.5$ m for Δp in pascals and R in meters. Quadratic curves were fitted to logarithmic overpressure impulse and positive phase duration curves, over a limited range from $10^2 < R < 10^4$ m, to give

$$I = 2.406 \times 10^{-9} R^{-2.872 + 0.3491 \ln R}, \tag{A2}$$

and

$$t_+ = 5.041 \times 10^{-4} R^{1.518 - 0.08255 \ln R} \tag{A3}$$

for overpressure impulse in pascal-seconds and duration in seconds, respectively. These approximations are only accurate to about ± 20%. Other characteristics have also been described in analytical form[4] but are not repeated here.

A.3 Distant Non-Acoustic Propagations

A.3.1 Finite Amplitude Effects

Several experiments have also shown that blast propagation does not necessarily approach acoustic expansion, $\Delta p \sim R^{-1}$, at small wave amplitude and very long range, even when distorting atmospheric refraction effects are removed.[18–22] Finite amplitude effects, though small, are compounded over long times and distances and thus cause observable excess attenuations from the expected acoustic expansion conditions. Likewise, pressure signature times are not fixed as required by infinitesimal acoustics theory. There are energy losses in the shock front and there is some supersonic lengthening of even small, finite amplitude pulses.

A.3.2 Model Comparisons

Empirical data that were shown in Fig. 13 were approximated by an extension from IBM Problem M that followed $\Delta p \sim R^{-1.2}$. This simplified model has been used extensively to estimate atmospheric focusing or divergence factors operative on various test explosions.[6,27] By comparison to the new standard overpressure curve, it slightly underpredicts nonrefracted wave amplitudes, and thus overrates the atmospheric modification. This discrepancy is not serious, however, and amounts to only 12% at 100 km from 4.2 TJ (1 kton) NE. This certainly cannot be significant when the uncertainty noise level exceeds 50% at such ranges where atmospheric magnification may cause nuisance damage.

A.3.3 Overpressure-Distance Decay Rates

The exponent, or logarithmic slope, of the standard overpressure curve has been evaluated by differentiation of Eq. (A1). Results of numerical evaluation are shown in Fig. A1, which indicates that $a = -1.1$ near

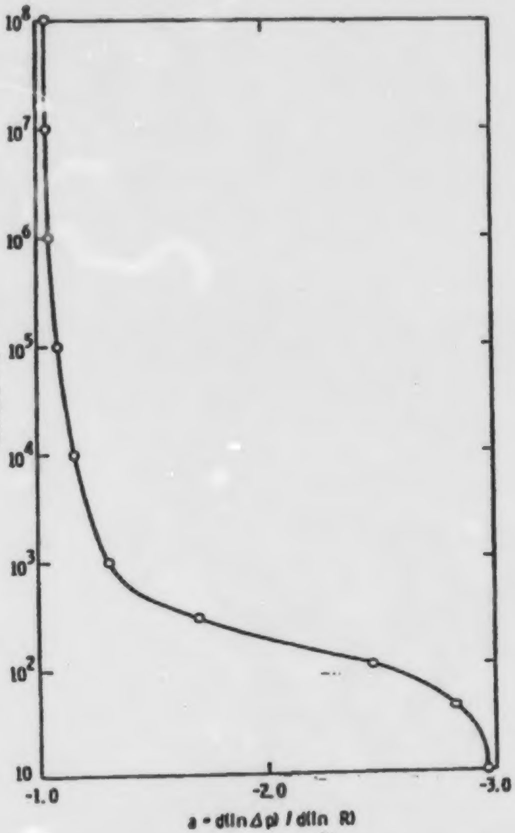

FIG. A1. Overpressure–distance decay exponent, AWFL 4.2 TJ (1 kton) NE at sea level.

$R = 100$ km may be appropriately used for simplified predictions of nuisance damage levels.

A.3.4 Farfield Slope Assumption

A rule-of-thumb for window-damaging propagations, derived from results of atmospheric nuclear tests, was that recorded peak-to-peak pressures of less than about 4 mbar ($\Delta p = 148$ Pa) would not create any damage claims from impacted communities. This pressure level occurs at 55 km from a 4.2 TJ (1 kton) NE free air burst under standard conditions of Fig. 3. Figure A1 shows the pressure-distance slope is -1.11 at that range. Thus, $a = -1.1$ appears suitable for use in defining the very small probabilities of damage in many environmental impact analyses.

APPENDIX B: CALCULATION EXAMPLES

[This Appendix is not part of American National Standard Estimating Airblast Characteristics for Single Point Explosions in Air, With a Guide to Evaluation of Atmospheric Propagation and Effects S2.20-1983, but is included for information purposes only.]

B.1 Examples of Scaling Law Applications

B.1.1 10 kton NE at 3 km Altitude

Ambient pressure altitude is 70.1 kPa from Fig. 7 or Table V. A scaled overpressure $\Delta p = (70.1/101.3)\,\Delta p_0$ reaches a scaled distance $R_1 = R_0(10/1)^{1/3}\,(101.3/70.1)^{1/3} = 2.436\,R_0$ from Eq. (2) or Figs. 6 and 8. At that scale distance and overpressure, all scaled times would be $t_1 = t_0\,(2.436)\,(288.15/268.7)^{1/2} = 2.525\,t_0$ for 268.7 K temperature.[5] The scaled HOB, $3000/(10)^{1/3} = 1392$ m, indicates a free air burst per Fig. 10.

B.1.2 1000 kg HE Surface Burst at Sea Level

This source would be an equivalent airblast generator to 2000 kg NE surface burst, 4000 kg NE free air burst, or 4.4×10^{-3} kton NE free air burst. The yield scaling factor would be $(4.4\times10^{-3}/1)^{1/3} = 0.164$, as shown in Fig. 6. The 100 kPa overpressure level, from Fig. 2, would reach $R_1 = (210)\,(0.164) = 34.4$ m. At that distance the positive phase duration, from Fig. 5, would be $t_+ = (0.15)\,(0.164) = 24.6$ ms. At long range, beyond $R_1 = 10^4(0.164) = 1640$ m, the total wave duration would be $t_+ + t_- = (0.96 + 0.52)(0.164) = 0.243$ s.

B.1.3 100 kg HE at 20 m HOB

The scaled HOB is $20/(100)^{1/3} = 4.3$ m, where the HOB yield factor, from Fig. 10, is 5.5. The equivalent airblast yield is thus 550 kg HE, or 1.213×10^{-3} kton NE. The yield scaling factor would be 0.107. At 1-km distance, $R_0 = 9138$ km, and the incident overpressure would be 550 Pa from Fig. 3.

B.2 Close-In Approximations

The overpressure at 15-m radius from a 10-kton NE source is required. The yield scaling factor is 2.15 so the scaled distance $R_0 = 15/2.15 = 6.96$ m. Overpressure, from Eq. (4), would be $\Delta p_1 = \Delta p_0 R_0^{-3} = (3.18 \times 10^5)\,(6.96)^{-3} = 942$ MPa, or 9300 atmospheres.

B.3 Long Range Propagations

B.3.1 60 km from 100-Mg HE Surface Burst

Assume standard conditions and the coefficient 8.720 from Table III for use in Eq. (6). Then $p = (8.72 \cdot (0.1)^{0.3667}\ (60)^{-1.1} = 41.5$ Pa. Recorded amplitude would be $K_r p_k = (2)\,(1.35)\,(41.5) = 112$ Pa, and this airblast amplitude would be easily audible.

B.3.2 1 ton HE at 200 km

Assume standard conditions and the coefficient 0.05309 from Table III for 1000 kg HE, to give $\Delta p = (0.05309)\,(10^3)^{0.3667}\,(200)^{-1.1} = 1.97$ Pa. The recorded amplitude of 5.3 Pa could be recorded with light wind conditions. Downwind of ozonosphere monsoon winds even higher pressures might be recorded (see Fig. 22) but in the upwind direction considerably smaller amplitudes (see Fig. 21) would not be detectable.

APPENDIX REFERENCES

[A1] C. D. Broyles, "IBM Problem M Curves," Report SC-TM-268-56(51), Sandia Laboratories, Albuquerque, NM, Dec. 1956.

[A2] D. D. Eilers, "A Numerical Integration of a 97-kt Explosion in Sea Level Air," Report LAMS-2985, Los Alamos Scientific Laboratory, Los Alamos, NM, Dec. 1963.

[A3] W. E. Baker, *Explosions in Air* (University of Texas P., Austin, 1973), pp. 27–162.

[A4] J. W. M., Dumond, E. R. Cohen, W. K. H. Panofsky, and E. Deeds, "A Determination of the Wave Forms and Laws of Propagation and Dissipation of Ballistic Shock Waves," J. Acoust. Soc. Am. 18, 97–118 (1946).

[A5] H. L. Brode, "Numerical Solutions of Spherical Blast Waves," J. Appl. Phys. 26, 766–775 (1955).

[A6] W. A. Whitaker, "Theoretical Calculations of the Phenomenology of HE Detonations," Report AFWL-TR-66-141, Air Force Weapons Laboratory, Kirtland Air Force Base, NM, Nov. 1966.

[A7] D. L. Lehto and R. A. Larson, "Long Range Propagation of Spherical Shock Waves from Explosions in Air," Report NOL-TR-69-88, Naval Ordnance Laboratory, Silver Spring, MD, July, 1969.

Benchmark cases for outdoor sound propagation models

K. Attenborough and S. Taherzadeh
The Open University, Milton Keynes MK7 6AA, England, United Kingdom

H. E. Bass, X. Di,[a] and R. Raspet
The University of Mississippi, University, Mississippi 38677

G. R. Becker and A. Güdesen
Atlas Elektronik GmbH, D-2800 Bremen 44, Germany

A. Chrestman
USAE Waterways Experiment Station, Vicksburg, Mississippi 39180-6199

G. A. Daigle and A. L'Espérance[b]
National Research Council of Canada, Ottawa, Ontario K1A 0R6, Canada

Y. Gabillet
Centre Scientifique et Technique du Bâtiment, 38400 Saint-Martin-d'Hères, France

K. E. Gilbert
Pennsylvania State University, State College, Pennsylvania 16804

Y. L. Li and M. J. White
U.S. Army Construction Engineering Research Laboratory, Champaign, Illinois 61826-9005

P. Naz
French-German Institute of Research of Saint Louis, 68301 Saint Louis, France

J. M. Noble
U.S. Army Research Lab, White Sands Missile Range, New Mexico 88002-5501

H. A. J. M. van Hoof
Physics and Electronics Lab/TNO, 2509 J.G. The Hague, The Netherlands

(Received 15 June 1993; revised 12 May 1994; accepted 22 August 1994)

The computational tools available for prediction of sound propagation through the atmosphere have increased dramatically during the past decade. The numerical techniques include analytical solutions for selected index of refraction profiles, ray trace techniques which include interaction with a complex impedance boundary, a Gaussian beam ray trace algorithm, and more sophisticated approximate solutions to the full wave equation; the fast field program (FFP) and the parabolic equation (PE) solutions. This large array of computational approaches raises questions concerning under what conditions the various approaches are reliable and concerns about possible errors in specific implementations. This paper presents comparisons of predictions from the several models assuming a complex impedance ground and four atmospheric conditions. For the cases studied, it was found that the FFP and PE algorithms agree to within numerical accuracy over the full range of conditions and agree with the analytical solutions where available. Comparisons to ray solutions define regimes where ray approaches can be used. There is no attempt to compare calculated transmission losses to measurements.

PACS numbers: 43.28.Fp, 43.20.Bi

INTRODUCTION

Propagation of sound outdoors involves a number of physical phenomena including geometric spreading, molecular absorption, reflection from a complex impedance boundary, refraction, diffraction, and scattering.[1] Accurate predictions of sound transmission loss (TL) from a source to a receiver must somehow account for all of these phenomena simultaneously. Although this goal is beyond current capabilities, a great deal of progress has been made in the past decade. Specifically, numerical techniques originally developed for applications in underwater acoustics have been modified for atmospheric predictions and new analytical results provide solutions for more realistic conditions. Some progress has been made toward including turbulence and terrain in the propagation models, but research on these aspects is still in progress.

Ray tracing has been a standard approach extensively used to predict outdoor sound levels in the presence of speed of sound gradients even though the mathematical conditions for ray solutions are seldom met outdoors. Recent analytical solutions include a refractive atmosphere and a complex impedance boundary[2,3] but are only applicable to cases where the speed of sound varies with altitude in a specific functional form. Numerical solutions to the wave equation include the diffraction effects which limit the applicability of ray solutions and can be applied to arbitrary speed of sound profiles.[4,5] For this reason, the development of numerical algorithms to predict transmission loss through the atmosphere is being pursued by a number of groups throughout the world.

---

[a] Also with National Research Council of Canada, Ottawa, Ontario K1A 0R6, Canada.

[b] Also with Université de Sherbrooke, Sherbrooke, Quebec J1K 2R1, Canada.

Research groups in many countries have developed propagation models to predict transmission loss. The models can be generally classified as analytic (such as normal mode models), ray trace, a variation of the fast field program (FFP), or a form of the parabolic equation (PE). Though many of the groups involved share results at international meetings, the codes were generally developed independently. Members of NATO Panel 3 Research Study Group 11 (RSG-11) began an effort in 1990 to compare predictions of the various models and different implementations of the same model. The goals of this effort were to identify any differences and sources of those differences and to provide a set of results which future researchers can use to check new models and codes.

Thus the objective of this paper to look for consensus between models or, more accurately, significant differences, to investigate regimes of validity and to examine artifacts. We have chosen not to evaluate accuracy in any systematic way nor computational requirements since these change rapidly.

Assessing the quality of numerical computation schemes is an issue that has recently received considerable attention in underwater acoustics.[6] At technical meetings it became common to find numerical results presented in profusion that differed for the same problem. Researchers in underwater acoustics therefore explored the utility of benchmark solutions as standards against which numerical codes could be tested. The success of their efforts inspired the members of RSG-11 to also develop benchmarks.

We define a "benchmark" throughout this paper as a well-defined environment given in terms of a set of numerical parameters. This set of parameters represents the input data for model runs.

Comparison of different codes and models requires selection of suitable atmospheric conditions, ground surface, frequencies, and ranges. These were limited, in many cases, by the current state of development of the different approaches. Since most models do not include turbulence, quiet atmospheres were assumed. Similar reasons led the group to consider only flat terrain. Even with these limitations, however, much of the physics is included.

The absence of turbulence or real terrain in the calculations severely limits comparison to experimental data. In fact, no such comparisons are made here. There are limited comparisons of data to individual models in many of the references cited. In those cases, however, differences are often attributed to atmospheric inhomogeneities. That may well be the reason, but it involves an assumption not necessary to meet the goals of this study. If predictions based upon tl same set of assumptions do not agree, the reason for tl difference should provide guidance as to the applicability (the models.

In the case of the underwater acoustic benchmarks r sults of individual contributions were published in *The Jou nal of the Acoustical Society of America* following the form presented in Ref. 6. In the present case members of RSG-l concluded that much of the material used in the atmospher benchmarks could be found in existing archival papers ar that it would be more expedient to publish the results as single summary paper.

The next section explains in more detail the propagatic conditions assumed for the benchmark calculations. The co ditions selected represent cases where there is no refractio downward refraction, upward refraction (including shado zones), and ducted propagation. The exact profiles are n realistic but these conditions should provide good tests predictive abilities of the different approaches. Further, tl exact profiles were chosen because there are analytical sol tions for the first three cases. Section II describes the diffe ent models. In some cases, differences in implementatio are also described. Although the issue of CPU time is di cussed, a comprehensive comparison is beyond the scope this paper and is not considered in detail here. In the fou section, results are given and interpreted for selected cases. complete set of results is given only for the FFP/PE calcul tions (these two approaches are usually in agreement within about 0.5 dB) since it is these two methods that a pear most accurate and versatile.

I. DEFINITION OF BENCHMARK CASES

The aim of the benchmark cases outlined in this secti is to create a set of well-defined test cases for which co puter codes for airborne sound propagation, of any orig may be compared with respect to computational effort a numerical accuracy. It is intended to check numerical perf mance of computer codes by comparing their outputs w test cases for which analytical solutions exist. Researchers other laboratories are invited to use the standard test ca and to compare their results with examples discussed in S III.

A. General considerations

Benchmark cases for numerical tests of propagat codes should be defined in such a way as to cover the ra between "simple" cases for which analytical solutions mi be available and relevant cases with boundary conditi close to real world situations. Due to the large variation propagation conditions of the real world, cases must be i alized; e.g. simplified in such a way as to allow for compl analytical solutions or at least piecewise analytical solutic This is also motivated by the need to study typical numer limitations such as

(1) discretizing sound profiles,
(2) truncation of numerical approximations,
(3) capping of profiles at a certain height.

Aside from the "simple" case or cases which can se as the basis for computing a numerical reference it is v difficult to define other cases which are both realistic and few in number and still possibly rewarding to overcome the problems of complexity due to all possible variations of parameters. Another problem area is the types of outputs one needs to compare the outputs of various codes; e.g., whether one cares for the details in the interference nulls or just for the average level. Again a compromise has to be found in order to keep the number of graphs as low as possible without neglecting essential features of the codes. A description of the benchmark cases is given below.

B. Common parameters for benchmark cases

1. Basic parameters

All comparisons rely on a model geometry of two infinite half-spaces, the airspace and the groundspace. Unless otherwise noted the interface between both spaces is regarded as a smooth infinite plane. There is an acoustic point source at source height h_s above the interface and a receiving microphone at a horizontal range R and receiver height h_r. The source emits a constant tone of frequency f.

The following quantities were chosen for calculations:

$h_s = 5$ m (source height),

$h_r = 1$ m (receiver height),

$R = 200$ m; 10 000 m

(horizontal range to receiver),

$f = 10;100;1000$ Hz (frequency).

The transmission loss (TL) was considered to be the most useful quantity to be used for comparison purposes. The following definition is used:

$$\mathrm{TL} = -20 \log \frac{(\text{total acoustic pressure at a field point})}{(\text{acoustic pressure of direct sound field at 1 m from source})}. \tag{1}$$

2. Plot parameters

For ease of quantitative comparison the graphical outputs of the various propagation codes are standardized by using the following three types of output graphs:

1. TL versus horizontal range.
2. TL versus frequency at $R = 200$ m and $R = 10\,000$ m.
3. Contour plot: Height versus range with TL contours at 6-dB increments, maximum height being 1000 m.

C. Characterization of the ground

Ground impedance plays a major role in airborne sound propagation near the surface. Typically outdoor ground surfaces are uneven and their character will vary with range but here it is assumed

(a) that the ground is transversely uniform and its properties do not vary with range,

(b) that all interfaces are flat and horizontal.

The properties of the ground surface that have the most influence on outdoor propagation below 1000 Hz are its flow resistivity and any near surface layering. Typically the ground surface may be treated as an impedance boundary. At higher frequencies the tortuosity and porosity will be important. Moreover in predicting the response of a buried geophone to acoustic sources above the surface the elasticity of the ground is important as well as its porosity and flow resistivity (see, for example, Ref. 23). The seismic profile of the ground is required as input to the SAFARI code,[21] originally developed for use in underwater acoustics. It has been found necessary to specify sufficient parameters to allow inputs to any of the codes that are compared in this paper even though the resulting complication may not be needed simply for predicting sound in the atmosphere. A series of careful and comprehensive measurements have been carried out by various authors on a site at Wezep, The Netherlands[7] revealing a homogeneous and isotropic layer of porous sand, 2-m deep, above a nonporous substrate. The resulting values are given in Table I. For those codes that require input only of surface impedance, a four parameter model[8] has been used. The specific characteristic impedance of the ground, and hence the specific surface impedance where the ground is acoustically homogeneous, may be calculated from

$$Z_c = \omega \rho_b(\omega)/(k_b \rho_0 c_0), \tag{2}$$

where

TABLE I. Parameters used to characterize the ground and air at surface.

Parameters	Value
Flow resistivity (σ)	366 000 Pa s m^{-2}
Porosity (Ω)	0.27
Pore shape factor (s_p)	0.25
Grain shape factor (n')	0.5
(N.B. tortuosity $q^2 = \Omega^{-n'}$)	(tortuosity = 1.925)
N_{Pr} (Prandtl number)	0.724
γ (ratio of specific heats)	1.4
ρ_0 (air density at 20 °C)	1.205 kg m^{-3}
c_0 (speed of sound at 20 °C)	343.23 m s^{-1}
Upper p velocity	270 m s^{-1}
Upper s velocity	190 m s^{-1}
Lower p velocity	500 m s^{-1}
Lower s velocity	330 m s^{-1}
Solid bulk modulus	4.6×10^{11} Pa
Upper layer thickness	2 m
Bulk density	1700 kg m^{-3}
p,s damping	0.02 dB per wavelength

$$k_b^2=(q\omega/c_0)^2[1-2(\lambda\sqrt{i})^{-1}T(\lambda\sqrt{i})]^{-1}[1+2(\gamma-1)$$

$$\times(N_{\mathrm{Pr}}{}^{1/2}\lambda\sqrt{i})^{-1}T(N_{\mathrm{Pr}}{}^{1/2}\lambda\sqrt{i})],$$

$$\rho_b(\omega)=(q^2/\Omega)\rho_0[1-2(\lambda\sqrt{i})^{-1}T(\lambda\sqrt{i})]^{-1},$$

$$q^2=\Omega^{-n'},\quad T(x)=J_1(x)/J_0(x),$$

and

$$\lambda=(1/2s_p)[8\rho_0 q^2\omega/\Omega\sigma]^{1/2}.$$

Using the values in Table I, the real and imaginary parts of impedance given by Eq. (2) are (38,79,38.41), (12.81,11.62), and (5.96,2.46) at 10, 100, and 1000 Hz, respectively.

D. Speed of sound profiles

1. General

All test cases assume the following general boundary conditions:

i. Atmospheric density and pressure are assumed constant.

ii. The density ρ_0 of the air at ground level is 1.205 kg/m^3 at $T=20$ °C and $p=1$ atm.

iii. The attenuation coefficient, α for atmospheric absorption is taken at a relative humidity (RH) of 70% and at a temperature $T=20$ °C. The frequency dependence of α is as defined by ANSI S1.26.[9]

iv. Under the conditions as above the sound velocity c_0 at the surface will be $c_0=343.23\simeq343$ m/s.

2. Test cases

Illustrations of the test cases are depicted in Fig. 1.

Case 1 is the above mentioned "simple" case to study numerical effects of propagation codes. The profile simply consists of an isovelocity (homogeneous) medium with a constant sound speed c_0. For numerical reasons, the predictions for this case are sensitive to the numerical truncation of the medium to at a finite height.

Case 2 is a strong positive sound speed gradient as occurs under "downwind" conditions. The real world conditions were idealized to a linear profile with a constant gradient of 0.1 s^{-1}. No assumptions are made with respect to an upper boundary of the linear increase of sound speed. This case is intended to stimulate investigations on the effects of profile height on the sound field at a given range.

Case 3 depicts another idealized real world situation: Sound propagation under "upwind" conditions. For ease of systematic investigations only the sign of the gradient was changed from case 2. All other aspects discussed for case 2 apply to case 3 as well.

Case 4, as can be seen in Fig. 1, is a composite profile. This ducting type of sound profile is a rather typical observation in many real situations. To keep all cases systematic, case 4 includes only elements of earlier discussions. The profile starts at the surface with a positive gradient up to a height of 100 m. The gradient is constant at a rate of 0.1 s^{-1}. At a height of 100 m an inversion occurs yielding a constant negative gradient of -0.1 s^{-1}. The negative gradient continues to 300 m height. At this point the sound speed assumes a constant value to infinite height.

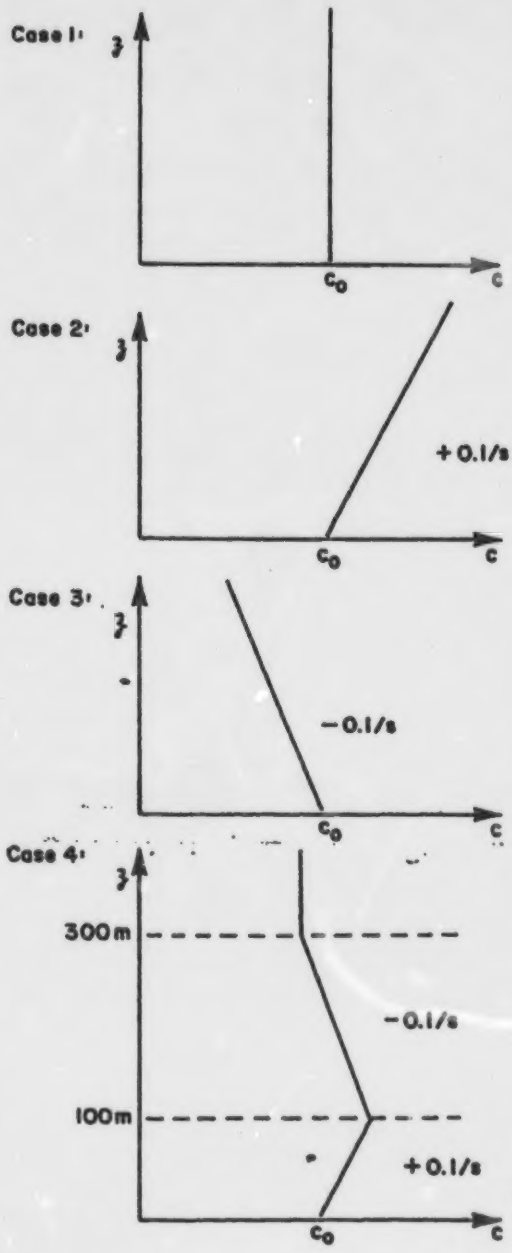

FIG. 1. Speed of sound profile for the four test cases.

3. Contour plots

Plots of height versus range with TL contours at 6-
increments, maximum height being 1000 m, were also p
duced for the four cases.

II. DESCRIPTION OF THE MODELS

In this section the different models and the differ
implementations of the same model used in the benchma
are briefly summarized. A complete and detailed descript
of each model can be found in the references cited in the t
below. The analytical solutions for cases 1, 2, and 3 are f

described. No analytical solution for case 4 is discussed. Ray tracing is extensively used in atmospheric sound propagation. Therefore, next, three ray tracing based models are described. Third, the numerical models are discussed. These include four implementations of the FFP and two implementations of the PE.

A. Analytical wave solutions

We start with the classical wave equation for the acoustic pressure:[10]

$$\left(\nabla^2-\frac{1}{c^2(z)}\frac{\partial^2}{\partial t^2}\right)p(r,z,t)=-4\pi\delta(x,y,z-z_s,t), \tag{3}$$

where δ represents a delta-function source of unit strength, $c(z)$ is the speed of sound, and z_s is the height coordinate of the source.

Assuming simple harmonic time dependence $\exp(-i\omega t)$, Eq. (3) becomes the Helmholtz equation

$$(\nabla^2+k^2)p(r,z)=-4\pi\delta(r,z-z_s), \tag{4}$$

where the wave number $k=\omega/c(z)$.

In cylindrical coordinates (r,θ,z) and for cylindrical symmetry so that there is no variation with θ, the Helmholtz equation becomes

$$\frac{\partial^2 p}{\partial r^2}+\frac{1}{r}\frac{\partial p}{\partial r}+\frac{\partial^2 p}{\partial z^2}+k^2 p=-\frac{2}{r}\,\delta(r)\delta(z-z_s), \tag{5}$$

where the source has been assumed to be at $r=0$.

Equation (5) can be solved with a zero-order Hankel transform[10]:

$$p(r,z)=-\int_{-\infty}^{\infty}H_0^1(Kr)P(K,z)K\,dK, \tag{6}$$

where H_0^1 is the Hankel function of the first kind and of order 0 and $P(K,z)$ satisfies

$$\frac{d^2P(K,z)}{dz^2}+[k^2(z)-K^2]P(K,z)=-\delta(z-z_s). \tag{7}$$

In Eq. (7), K represents the horizontal component of the wave number. The function $P(K,z)$ must satisfy an impedance boundary condition at the ground, must be continuous at the source, have a discontinuous derivative with height at the source and must satisfy a radiation boundary condition at large height.

Analytical solutions for $P(K,z)$ can be found when the sound-speed variation with height is approximated by

$$c(z)=\frac{c(0)}{\sqrt{1-2az}}\approx c(0)(1+az) \tag{8}$$

in the case of downward refraction and

$$c(z)=\frac{c(0)}{\sqrt{1+2az}}\approx c(0)(1-az) \tag{9}$$

in the case of upward refraction. In the above a is defined by

$$a=\frac{1}{c(0)}\left(\frac{dc}{dz}\right)_0,$$

and $c(0)=c_0$ is the sound speed at the ground surface. As noted, these profiles approximate linear variations near the ground.

If $k^2(z)$ is linear, $P(K,z)$ can be expressed in terms of Airy functions. Airy functions are desirable since they have no branch cuts in the complex plane, which simplifies the analysis and the search for poles. To obtain the acoustic pressure $p(r,z)$, the expression for $P(K,z)$ in terms of Airy functions is substituted into Eq. (6), the residue of the integrand is calculated at each pole of the integral, and the results summed to form the total solution. Note that the effect of the ground impedance on these solutions, as well as the effect of the ground impedance on the normal modes is discussed in detail in Refs. 2 and 3.

1. Normal modes solutions for downward refraction (case 2)

The normal mode solution[3] is the residue series for the acoustic pressure corresponding to downward refraction (case 2):

$$p(r,z)=\frac{i\pi}{l}\sum_n\frac{H_0^1(k_n r)\mathrm{Ai}(\tau_n+z_s/l)\mathrm{Ai}(\tau_n+z/l)}{\tau_n[\mathrm{Ai}(\tau_n)]^2-[\mathrm{Ai}'(\tau_n)]^2}, \tag{10}$$

where $\tau_n=(k_n^2-k_0^2)l^2$ are the zeros of $\mathrm{Ai}'(\tau_n)+\gamma\,\mathrm{Ai}(\tau_n)=0$, $k_0=\omega/c(0)$ and k_n is the wave number of the nth mode. The abbreviations are

$$\gamma=(ik_0 l\rho c)/Z,\quad l=(r_c/2k_0^2)^{1/3},$$

where Z is the acoustic impedance and r_c is the radius of curvature of the ray paths (which are arc of circles in the case of a linear profile). The downward refracting case does not converge rapidly since the poles mostly lie close to the real axis. The number of modes necessary to accurately evaluate the downward refraction integral may be approximated by

$$n_{\max}=\frac{2}{3}\left(f\bigg/\left|\frac{dc}{dz}\right|_0\right),$$

where f is the frequency. If the gradient expressed in Eq. (8) is truncated at a given height, the series will not contain modes which are reflected from the gradient above this height. In most cases, the nth mode height, h_n, may be approximated by $h_n\approx(3\pi n^{2/3}/2)l$. At long ranges, the largest contributions to the integral Eq. (6) result from poles of $P(K,z)$ which arise from the ground reflected term. Hence the solution is accurate at sufficient range for the direct wave to be negligible with respect to the sum of the residues of the integral.

2. Residue series for upward refraction (case 3)

The residue series for the acoustic pressure for upward refraction (case 3) is[10]

$$p(r,z)=\frac{\pi e^{i\pi/6}}{l}\sum_{n}\frac{H_0^1(k_n r)\mathrm{Ai}[b_n-(z_s/l)e^{2i\pi/3}]\mathrm{Ai}[b_n-(z/l)e^{2i\pi/3}]}{[\mathrm{Ai}'(b_n)]^2-b_n[\mathrm{Ai}(b_n)]^2},\qquad (1$$

where $b_n=(k_n^2-k_0^2)l^2\exp(2i\pi/3)$ are the zeros of $\mathrm{Ai}'(b_n)+\gamma e^{2i\pi/3}\,\mathrm{Ai}(b_n)=0$. The other quantities are the same. The upward refracting case converges rapidly since the absorption increases very rapidly for higher-order poles.

3. Homogeneous medium (case 1)

In the absence of refraction (case 1), the basic problem is described in Fig. 2. The sound emitted by a monopole source S travels to a receiver along a direct ray path and a ray path reflected from the ground with a grazing angle ψ. The ray paths are straight. In this case the solution to Eq. (3) for the acoustic pressure at the receiver can be written in the following form[11]

$$p(r)=[A(R_1)/R_1]\exp(ikR_1)+Q[A(R_2)/R_2]\exp(ikR_2), \tag{12}$$

where R_1 and R_2 are the path lengths of the direct and reflected paths respectively, and the amplitude $A(R)$ accounts for atmospheric absorption. The quantity Q is a reflection coefficient which has been modified for spherical waves reflecting from a complex plane boundary. A good approximation for Q is

$$Q=R_p(\psi)+B[1-R_p(\psi)]F(w), \tag{13}$$

where $R_p(\psi)$ is the plane-wave reflection coefficient and the boundary loss function $F(w)$ is defined in terms of the numerical distance w and complimentary error function:

$$F(w)=1+i(\pi)^{1/2}we^{-w}\ \mathrm{erfc}(-iw). \tag{14}$$

In Eqs. (13) and (14), $B\sim 1$ is a correction term close to unity which can be set to unity at near grazing incidence. Expressions for $R_p(\psi)$, B, and w in the general case of a ground of extended reaction can be found in Ref. 11.

For most purposes it is sufficient to assume locally reacting ground and to set $B=1$. In this case

$$R(\psi)=\frac{\sin\psi-1/Z}{\sin\psi+1/Z} \tag{15}$$

and

$$w^2=\tfrac{1}{2}ikR_2(\sin\psi+1/Z)^2, \tag{16}$$

where Z is the normalized acoustic impedance of the ground. We note that both R_p and w are functions of the grazing angle ψ and that $R_p\rightarrow-1$ when $\psi\rightarrow 0$. Further, for high f quencies $Q=R_p$.

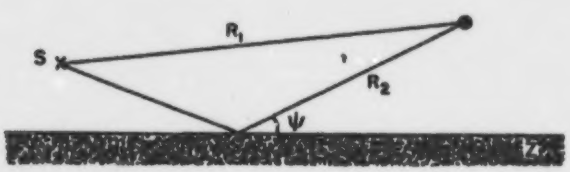

FIG. 2. Schematic showing geometrical definitions for direct and reflected ray paths in the absence of refraction (case 1).

B. Ray tracing and hybrid solutions

1. Inhomogeneous atmosphere

The effects of curved ray paths on the total sound fi can be described from general principles even for comp sound speed profiles. Figure 3 illustrates curved direct reflected ray paths for weak refraction in the case of dov ward and upward refraction, respectively. The total p lengths R_1 and R_2 are modified thus changing the path len difference between direct and reflected paths. More imp tantly, the effective grazing angle ψ for the reflected ra different. In the case of downward refraction, the graz angle for the reflected ray is greater than in the absence refraction. This has the consequence that the reflection c ficient $R(\psi)$ deviates further from -1, the destructive in ference between direct and reflected waves becomes complete and their geometrical interference is shifted higher frequencies. In the case of upward refraction, grazing angle for the reflected ray is smaller than in the sence of refraction. The reflection coefficient tends more ward -1, the destructive interference is enhanced and geometrical interference is shifted to lower frequencies.

In the cases of extreme downward refraction or at lon ranges, there are usually many ground reflected paths. Th is no general ray tracing solution for this case. In the cas upward refraction at long ranges, the receiver can be bey the shadow boundary and according to ray theory there i sound. In this situation, wave theory, or wave extension ray theory must be used.

The following describes three models based on theory. The first model is restricted to a single bounce assumes an arbitrary sound speed profile. This model designed to predict sound propagation from aircraft and

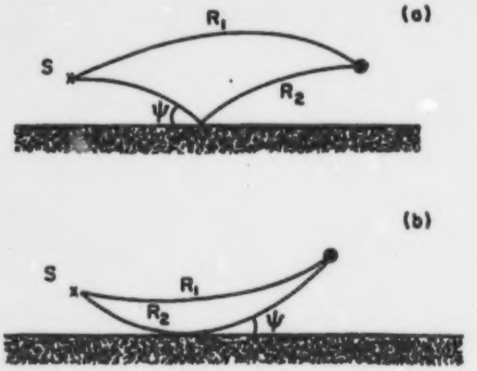

FIG. 3. Curved ray paths in the presence of a (a) downward refr atmosphere (case 2) and (b) upward refracting atmosphere (case 3).

not account for multiple reflections from the ground. The second model assumes a linear sound speed profile but can account for the effects of multiple bounces. The third model is an extension of ray theory to account for wave effects.

2. The single bounce arbitrary profile model

In the cases of mild downward or upward refraction, the model ASOPRAT[12] uses a raytrace program to obtain the total path lengths, R_1 and R_2, and the grazing angle. Also, propagation constant and attenuation coefficients are computed from the raytrace program information about the paths R_1 and R_2. These calculated total path lengths and modified grazing angle are then used in Eqs. (15) and (16) and the resulting numerical distance and reflection coefficient are used to calculate the total field using Eq. (12).

When there is strong downward refraction or at long ranges where there are multiple reflected ray paths, ASOPRAT only accounts for one reflected path. The shortest ground-reflected path for R_2 is chosen since it is usually strongest in amplitude. The reflected paths that strike the ground more than once are disallowed under the assumption that ground reflections produce a loss in amplitude and coherence and paths with fewer reflections usually have larger amplitudes.

In ASOPRAT, the atmosphere is divided into horizontal layers which have different values of sound speed. The sound speed and wind speed are assumed to vary linearly with height between interfaces. This assumption permits solution of the acoustic ray equation in closed form but can sometimes lead to false caustics caused by sound speed slope discontinuities. An image atmosphere has also been inserted so reflected eigenrays can be treated as direct eigenrays.

For horizontally stratified media, the ray paths are given by Snell's law,

$$\frac{\cos\theta(z)}{c_z}=\xi=\frac{\cos\theta_s}{c_s}, \qquad (17)$$

where c_s is the sound speed at the source and ξ is a constant. The initial angle measured from horizontal is θ_s with upward-sloping rays having positive launch angles. If the sound speed gradient is constant ($g=dc/dz$), the ray paths are arcs of circles with radius of curvature $r_c=1/\xi g$.

3. The multiple bounce linear profile model

This heuristic model[13] assumes that many realistic sound speed profiles can be approximated by a linear sound speed profile. The assumption of a linearly varying sound speed profile permits solutions of the acoustic ray equations in closed form. In the case of weak refraction there is the direct ray path and one reflected ray path (Fig. 3) and one can calculate the effective geometrical parameters of these two rays. In Eq. (12), the geometrical interference resulting from the path length difference between direct and reflected rays is represented by $k(R_2-R_1)$. However, because the sound speed varies with the height, the wave number k is not constant over all the rays. To consider such phenomena, the model uses the difference in the travel times between the rays instead of the difference in path lengths. Applying Eq. (12), the mean square sound pressure becomes

$$p^2(r)=\frac{A(R_1)^2}{R_1^2}+\frac{A(R_2)^2|Q|^2}{R_2^2}+\frac{2A(R_1)A(R_2)|Q|}{R_1R_2}\times\cos[2\pi f(\tau_2-\tau_1)+\mathrm{Arg}(Q)], \qquad (18)$$

where τ_1 and τ_2 are the effective travel times for R_1 and R_2 computed using equations found in Ref. 13.

In the presence of a strong positive sound speed gradient, and/or for larger propagation distances, additional rays that go through n reflections on the ground appear between the source and the receiver. These additional rays can be determined using the following 4th order equation

$$n(n+1)x^4-(2n+1)Rx^3+[b_r^2+(2n^2-1)b_s^2+R^2]x^2-(2n-1)b_s^2Rx+n(n-1)b_s^4=0, \qquad (19)$$

where $b_i^2=(z_i/a)(2+az_i)$ for $i=s$ or r and R is the horizontal distance between source and receiver. In Eq. (19), n is the number of reflections and the unknown x is the horizontal distance between the source and the first reflection on the ground. This equation must be solved successively from $n=0,1,2,3,\ldots$ (the number of reflections on the ground), until there is no real solution for x, i.e., as long as $0<x<R$. In presence of a positive gradient, there is at least one direct ray (for $n=0$) and one reflected ray (for $n=1$). When the receiver moves closer to the ground and further from the source, or when the gradient increases, the complex conjugate of the roots may become real, which means that additional reflected rays have to be considered. For $n=2$, two additional reflected rays may appear, and for $n>2$, four additional reflected rays may appear for each n.

Defining N as the total number of rays reaching the receiver (including the direct ray), the total sound pressure at the receiver can be calculated by summing up the contributions of all the N rays involved. This is done in the model using the following expression.

$$p^2(r)=\sum_{i=1}^{N}\frac{A_i^2|Q_i|^2}{R_i^2}+2\sum_{i=2}^{N}\sum_{j=1}^{i-1}\frac{A_i|Q_i|A_j|Q_j|}{R_iR_j}\times\cos\left[\omega(\tau_j-\tau_i)+\mathrm{Arg}\left(\frac{Q_j}{Q_i}\right)\right], \qquad (20)$$

where $i=1$ denotes the direct ray, and therefore $Q_1=1$. A_i represents the standard attenuation of a single ray due to atmospheric absorption, computed using the refracted length of the path, R_i. τ_i is the travel time of the ray, Q_i is the equivalent reflection coefficient on the ground of this ray calculated with

$$Q_i=Q(\psi_i)^{n_i}, \qquad (21)$$

where ψ_i is the angle of reflection on the ground, and n_i is the number of reflections.

The case of a weak sound speed gradient is therefore defined by putting $N=2$; in this case there is only one direct and one reflected ray, and Eq. (20) reduces to Eq. (18).

4. Gaussian beam approach

The basic concept of the theory is to launch a fan of beams from the source and to trace the propagation of these beams through the medium. The wave equation is solved in the immediate vicinity of each ray and the acoustic pressure at a receiver is obtained by summing the contribution of each of the individual beams. The solution is everywhere uniform thus removing the singularities at caustics found in the traditional ray tracing methods. The procedure is not sensitive to the exact details of the medium since, contrary to ray methods, the Gaussian beam provides a local averaging. It is not necessary to find the rays that exactly intercept the receiver, thus reducing computation time.

The first step of the Gaussian beam method is to solve the classical ray equations to obtain the central ray of the beam:

$$\frac{d\mathbf{r}}{dt}=\mathbf{V}_e+[\mathbf{k}/|k|]\cdot c \tag{22}$$

$$\frac{d\mathbf{k}}{dt}=-|k|\,\mathrm{grad}\,c-\sum k_i\,\mathrm{grad}\,V_e, \tag{23}$$

where $\mathbf{V}_e$ is the vector wind speed, k is the wave number, c is the speed of sound, r is the position vector along the ray, and d/dt is the derivative with respect to time. These equations can be solved by standard numerical techniques or analytically in the case of a linear profile.

The second step of the Gaussian beam method is to solve the wave equation locally in ray-centered coordinates using the parabolic approximation. The ray-centered coordinate system is an orthogonal curvilinear system that follows a particular ray. In a two-dimensional medium, the ray centered coordinates can be specified by the unit vector $\mathbf{t}$ tangent to the ray in the (x,z) plane and the unit vector $\mathbf{n}$ normal to the ray. In the case of a point source, the solution of the local parabolic equation (see Sec. II D) is[14]

$$u(s,n,\omega)=\left(\frac{c(0)q(0)}{c(s)q(s)}\right)^{1/2}\times\exp\{-i\omega[\tau(s)+\tfrac{1}{2}M(s)n^2]\}, \tag{24}$$

where s is the distance along the central ray from the source and n represents the length in a direction perpendicular to the ray at s, $c(s)$ is the sound speed, $\tau(s)$ is the travel time along the central ray, and the function $M(s)$ is given by

$$M(s)=p(s)/q(s), \tag{25}$$

where

$$p(s)=\epsilon p_1(s)+p_2(s), \tag{26}$$

$$q(s)=\epsilon q_1(s)+q_2(s), \tag{27}$$

and

$$\epsilon=\epsilon_1+i\epsilon_2,\quad \epsilon_2\geqslant 0. \tag{28}$$

The complex number ϵ is the Gaussian beam parameter and $\{p_i,\ q_i,\ i=1,2\}$ are the two real, independent solutions of the following ray tracing system

$$\frac{dp_i}{ds}=-[c_{nn}/c^2(s)]q_i(s) \qquad \text{(2}$$

and

$$\frac{dq_i}{ds}=c(s)p_i(s), \qquad \text{(3}$$

where $c_{nn}=\partial^2c(s)/\partial n^2$ denotes the second normal deri\ tive of the sound speed $c(s)$. The condition that $\epsilon_2\geqslant 0$ in I (28) guarantees that the energy is localized in the vicinity the central ray. Equations (29) and (30) are solved step step along each ray by standard numerical techniques in same way as the ray equations. The choice of the Gaussi beam parameter ϵ and the initial condition at $s=0$ in the c of atmospheric sound propagation are discussed in Ref. 1

The third step of the Gaussian beam method is a sup position of all Gaussian beams passing in the neighborh of the receiver. We designate α as the launch angle of a with respect to an arbitrary axis passing through the sour The total field at a point located at the receiver is

$$p(r,\omega)=\int \phi(\alpha,\omega)u(s,n,\omega)d\alpha, \qquad \text{(}$$

where $\varphi(\alpha,\omega)$ is the weight function determined by expa ing the wave field at the source and matching the high quency asymptotic behavior of the integral in Eq. (31) to exact solution for the source in a homogeneous medium.

C. FFP models

1. Introduction

The fast field program (FFP) technique was develo for the prediction of underwater sound propagation[16–18] has been adapted to propagation in the atmosphere by sev authors. Four such adaptations are called CERL-FF CFFP,[20] SAFARI,[21] and FFLAG.[23]

Full details of there adaptations will not be given h Descriptions will be limited to outlines of basic formulat and differences. Further information on standard FFP m ods may be found in two tutorial articles.[24,25] Fast field grams permit the prediction of sound-pressure level in a l zontally stratified atmosphere at an arbitrary point o above a flat continuous ground, with range-indepen properties, from a point source somewhere in the same space. They allow specification of effective sound spee arbitrary functions of height above the ground.

The basis of the FFP method is to work numeri from exact integral representations of the sound field w each layer in terms of coefficients that may be determ from boundary conditions. The method gets its name the discrete Fourier transform used to evaluate these grals.

2. Basic formulation

By taking the Hankel transform of Eq. (5) it is po to remove the r dependence. Writing the zero order H transform of p and its inverse as

$$p(r,z)=\int_0^\infty P(K,z)J_0(Kr)K\,dK$$

and

$$P(K,z)=\int_0^\infty p(r,z)J_0(Kr)r\,dr \tag{32}$$

it is possible to obtain

$$\frac{d^2P}{dz^2}+[k^2(z)-K^2]P=-2\delta(z-z_s), \tag{33}$$

where K is the horizontal wave number.

Equation (33), known as the height (or depth)-dependent transformed wave equation, reduces the problem to one that is one dimensional and forms the starting point of the FFP or Green's function method. The solution $(P(K,z))$ to Eq. (33) is the sum of a particular solution $(\hat{P}(K,z))$ and any linear combination of the two independent solutions $[P^-(K,z)$ and $P^+(K,z)]$ to the corresponding homogeneous equation (where the right-hand side is zero). Hence

$$P(K,z)=\hat{P}(K,z)+A^-(K)P^-(K,z)+A^+(K)P^+(K,z), \tag{34}$$

where $A^-(K)$ and $A^+(K)$ are arbitrary coefficients to be determined from the boundary conditions. The most convenient choice for the particular solution is the field produced by the source or sources in the absence of boundaries. When the unknown coefficients have been found, the total field at angular frequency ω is found at any range r by carrying out the inverse Hankel transform according to Eq. (32).

The various FFP methods differ initially according to whether the sound speed gradient within each layer is assumed to be zero (as in the CERL-FFP and FFLAGS) or constant (as in CFFP and SAFARI). The form assumed for the transformed pressure potential within homogeneous layers, $\phi(K,z)$,

$$\phi(K,z)=A^-e^{-\alpha_i z}+A^+e^{\alpha_i z} \tag{35}$$

and within constant gradient layers in which $c(z)=[1/\rho(az+b)]^{1/2}$,

$$\phi(K,z)=A^+\mathrm{Ai}(\zeta)+A^-\mathrm{Bi}(\zeta), \tag{36}$$

where Ai and Bi are Airy functions of the first and second kind, respectively, and ζ is a transformed height variable.

CERL-FFP and CFFP treat the ground surface as an impedance boundary, while SAFARI allows the ground to be layered and elastic and FFLAGS permits ground layering, elasticity and porosity. Consequently SAFARI introduces two potentials in the form of Eq. (36) in each elastic ground layer and FFLAGS introduces three potentials in the form of Eq. (35) in each porous and elastic ground layer. Boundary conditions are solved to determine the unknown coefficients. CERL-FFP and CFFP use a transmission line method[24] to do this whereas FFLAGS and SAFARI use a global matrix method.[21]

After application of the appropriate number of boundary conditions to determine the unknown coefficients it remains to evaluate the Hankel transform integrals of the form of Eq. (32). Typically the Bessel function is replaced by the sum of two Hankel functions and the outgoing wave Hankel function is replaced by its asymptotic form.

This results in integrals of the form

$$G(r,z)=\sqrt{\frac{1}{2\pi r}}\,e^{i\pi/4}\int_0^\infty g(K,z)e^{-ikr}\sqrt{K}\,dK. \tag{37}$$

The indefinite integrals are then replaced by finite sums using discrete Fourier transforms. If the maximum value of wave number in the sum is $K_{\max}$ and N discrete values of K are introduced, then the wave number intervals are given by $\Delta K=K_{\max}/(N-1)$ and correspond to range intervals $\Delta r=2\pi/N\Delta K$, so for example,

$$p(r_m,z)=2(1-i)\sqrt{\pi/r_m}\,\Delta K\sum_{n=0}^{N-1}P(K_n)\sqrt{K_n}e^{2i\pi nm/N}, \tag{38}$$

where $K_n=n\Delta K$ and $r_m=m\Delta r$ (or $r_0+m\Delta r$, where r_0 is the desired starting range). Various numerical difficulties follow from the truncation of the integral to a finite sum and from the behavior of the integrand. For a detailed discussion of these see Refs. 21 and 22.

Different methods of dealing with these difficulties are used in CERL-FFP and in SAFARI or FFLAGS. In the FFT implementations employed in CERL-FFP, SAFARI, and FFLAGS, the relationship $\Delta K\Delta r=2\pi/N$ must hold. This does not allow the user to specify the desired range points independently of the step sizes used for the horizontal wave number K (i.e., the frequency range). CFFP uses the following range intervals

$$\Delta r=2n\pi/K_{\max}, \tag{39}$$

where n is any real number and evaluates the sums in Eq. (38) by means of the chirp-z transform.[20] This allows freedom both to select the desired ranges and to decrease the ΔK adaptively for accurate evaluation of the integral transform without changing the output range values.

3. Execution times (CPU times)

It is beyond the scope and purpose of this paper to provide a detailed discussion of computational effort since each code has been run under different conditions on different machines. Nonetheless the following qualitative remarks can be made. The CPU time is directly proportional to the number of integration points and therefore the CPU time is almost proportional to the range. Increasing the frequency requires that the integration limit be increased and therefore one has to increase the number of integration points to obtain a given range. Thus in an indirect way the frequency also influences the CPU time. The CPU time also depends on the number of air layers (and ground layers for FFLAGS) used in the FFP. Increasing the number of layers requires more CPU time for evaluation of the height-dependent Green's function. Typically the codes takes minutes to run on a fast workstation.

D. PE models

1. Introduction

The parabolic equation (PE) method has been a very useful technique for solving a variety of wave propagation problems. It has been used in optics and electromagnetic studies,[26] seismic prediction problems,[27] underwater acoustics,[28] and more recently in atmospheric sound propagation.[5,29–31] The technique employs an assumption that wave motion for a particular problem is always directed away from the source or that there is very little backscattering. The advantage in making this assumption is that it reduces a boundary value problem to an *initial* boundary value problem that results in a differential equation that is often much easier to solve.

Several PE methods have been developed for outdoor sound propagation, with many similarities between them. Departures from the usual atmospheric model include sound propagation over ground whose impedance varies with range,[32] sound propagation over a large ridge,[33] propagation through large-scale turbulence[34] and through randomly inhomogeneous media.[35] In this paper, we compare results from two PE-type models for the four benchmark cases.

2. Basic formulation

Here we present some important steps in the derivation of the PE. Precise details of the derivation may be found in the many references cited above. The boundary condition at the ground surface (assuming flat ground) is the local reaction condition:

$$\left(\frac{\partial p}{\partial z}+ik\beta p\right)_{z=0}=0, \tag{40}$$

where β is the complex surface admittance, which has been normalized by the characteristic impedance (ρc) of the air just above the surface; i.e., $\beta=1/Z$ where Z is the specific acoustic impedance of the ground divided by ρc. Proceeding with Eq. (5), the change of variables $U=pr^{1/2}$ and the far-field assumption ($kr\gg 1$) lead to the well-known Helmholtz wave equation for the field U in two dimensions (r,z):

$$\frac{\partial^2 U}{\partial r^2}+\frac{\partial^2 U}{\partial z^2}+k^2U=0. \tag{41}$$

Let $\bar{Q}$ denote the operator in the last two terms of Eq. (41); that is

$$\bar{Q}=\frac{\partial^2}{\partial z^2}+k^2. \tag{42}$$

Assuming k to be independent of range, Eq. (41) can be written

$$\left(\frac{\partial}{\partial r}+i\sqrt{\bar{Q}}\right)\left(\frac{\partial}{\partial r}-i\sqrt{\bar{Q}}\right)U=0. \tag{43}$$

The factors represents propagation of incoming and outgoing waves respectively, if we use a time dependence $\exp(-i\omega t)$. Considering only the outgoing wave Eq. (43) reduces to

$$\frac{\partial U}{\partial r}=i\sqrt{\bar{Q}}U. \tag{44}$$

Most implementations of the PE can be traced back to (44). The approach for advancing the field in range is point of departure for the two PE methods we describe. T software implementation of the two approaches are called FINITE-PE[5,30] and FAST-PE,[31] respectively.

The FINITE-PE method numerically integrates the ferential equation using a Crank–Nicolson approach. T operator $\sqrt{\bar{Q}}$ is cast in the form of a rational P expansion[27] for small argument $\bar{q}$. That is, we write $\sqrt{\bar{Q}}$ $k_0\sqrt{1+\bar{q}}$, where $\bar{q}=(\bar{Q}/k_0^2-1)$, and

$$\sqrt{1+\bar{q}}\sim\frac{1+\frac{3}{4}\bar{q}}{1+\frac{1}{4}\bar{q}}.$$

The wave number k_0 is chosen as some constant, mean va of $k(z)$.

The FAST-PE uses a Green's function approach an split operation that factors propagation effects into an ope tor for a homogeneous medium and another operator propagation through the inhomogeneous perturbation. T operator $\sqrt{\bar{Q}}$ is evaluated using a spectral decompositi leading naturally to a Green's function implementat which, besides being relatively easy to compute, directly corporates boundary conditions such as finite ground imp ance. Defining $\bar{Q}_0=\bar{Q}-\delta k^2$, where $\delta k^2=k^2(z)-k_0^2$ and ing an expansion for $\sqrt{\bar{Q}_0}$ gives

$$\sqrt{\bar{Q}_0}=\sqrt{\bar{Q}}+\frac{\delta k^2}{2k_0}.$$

This results in the so-called split step approximation.

3. Notes on Implementation

The FINITE-PE uses a spacing between points of 1 on its computational grid in height and the same spacing range step intervals. A very small spacing was chosen the ground to correctly match the boundary conditions Gaussian-shaped amplitude function was used to model source and its image in the ground, as a starting field for model. The amplitude of the image Gaussian was modifie satisfy the reflection coefficient at the ground. The w number was made to be complex-valued to accommo loss in the media. An absorbing layer approximately wavelengths thick was used to attenuate reflections from upper boundary, and correctly simulate radiation boun conditions at infinity. The vertical grid height was fixe either 500 or 1000 m, to ensure that no unwanted sig would arrive at the receiver, following the 45-deg beamw of the wide-angle PE.

In the FAST-PE, all of the range-stepping is acc plished via an FFT algorithm applied to the vertical fiel each step. The computational grid must be of equal spa in height to satisfy constraints placed on the computatio the FFT. Since the boundary condition is modeled expli in the algorithm (there are explicit terms for the field flected from the ground), the grid size is not limited minimum spacing that might be needed to model the variation of the field close to the boundary. Thus, the step size may be considerably larger than the FINITE (however, to accurately track rapid deterministic spatial variations in the medium, the FAST-PE generally must use reduced range and height steps, as must the FINITE-PE). An absorbing layer of 30 wavelengths and fixed grid height was also used in the FAST-PE.

4. Execution time (CPU time)

On one computer we used, the finite-PE computational time rose according to the square of frequency and the square of the range of the most distant receiver. This was, of course, to be expected from the equal height and range spacing and the placement of the top boundary. The short-range, low-frequency cases usually ran faster with the finite-PE than with the CERL-FFP model we tested. On the other hand, there was generally not enough computational time available to complete the long-range high-frequency cases, using the finite-PE.

On another computer the FAST-PE and FINITE-PE were exercised on the test cases and the run times were logged.[31] For a constant sound speed (case 1) the FAST-PE calculation was 400, 90, and 80 times faster than the FINITE-PE at 1000, 100, and 10 Hz, respectively. The speed advantage was essentially the same for upward refraction (case 3): 450, 120, and 80 times faster, respectively, at 1000, 100, and 10 Hz. For downward refraction (case 2) and ducted propagation (case 4) the speed advantage was somewhat less. For case 2, at 1000, 100, and 10 Hz the FAST-PE speed advantage was 163, 40, and 86, respectively. For ducted propagation (case 4) and the same three frequencies the speed advantage was, respectively, 70, 44, and 81.

IV. RESULTS

From a practical point of view, downward refraction (case 2) represent propagation conditions for which large detection ranges are possible. Further, agreement between the various models and experimental data is generally good for downward refraction. On the other hand, although upward refraction (case 3) is as commonly occurring, detection ranges are shorter and the agreement of the models with experimental data is not good (for example, see the data in Ref. 30). There is no analytical solution for ducted propagation (case 4) and an isovelocity (homogeneous) medium (case 1) is rarely achieved. For these reasons, we only provide here a complete discussion of all the models for case 2. This is followed by a detailed discussion of all four cases for the FFP and PE.

A. Case 2; 200 m, 100 Hz

Case 2 for a horizontal propagation distance of 200 m and a frequency of 100 Hz has been selected for a detailed comparison of results. All the methods are applicable to this problem and all the wave solution equations perform best for lower frequencies. This case corresponds to propagation at a relatively short distance under downward refraction conditions. In the real world, this situation is expected to be relatively insensitive to atmospheric turbulence. Equation (19) predicts that there should only be one ground reflected ray.

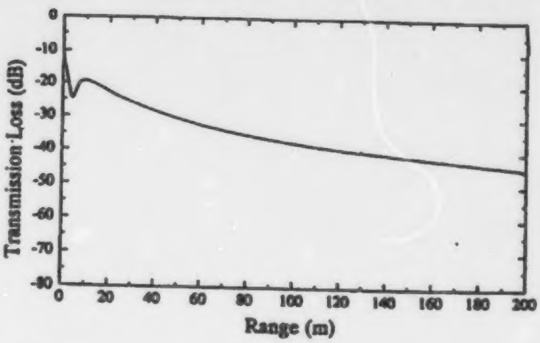

FIG. 4. Transmission loss versus range for case 2, 200 m, 100 Hz, obtained from all the models except SAFARI FFP.

1. Normal mode solution

The discrete normal mode solution [Sec. II A 1, Eq. (10)] for a sound speed gradient represented by Eq. (8) for the impedance of Eq. (2) is displayed in Fig. 4 for 100 Hz and ranges up to 200 m. Note that Eq. (8) represents a linear profile for az small, but becomes infinite at $z=1/2a$ and that the solution does not contain the direct wave. For this reason the discrete normal mode solution will not be accurate near the source. At long ranges, the direct wave decays spherically while the modes decay cylindrically so that the direct wave is negligible.

2. Ray tracing solutions

The same curve as Fig. 4 is also obtained from the single bounce ray tracing model (Sec. II B 2). The single bounce model is a hybrid that uses ray tracing to obtain the total path length of direct and reflected ray and the grazing angle. In general the ray tracing is not restricted to any particular form of atmospheric profile. The resulting grazing angle, when used in Eqs. (12)–(16), modifies the phase of the reflected ray and in turn modifies the transmission loss. The impedance was calculated using Eq. (2).

The same curve as in Fig. 4 is also obtained using the multiple bounce model [Sec. II B 3, Eq. (20)]. The multiple bounce model is also a hybrid model that assumes at the onset a linear sound speed profile and therefore derives the modified path lengths and grazing angle from analytical equations. For case 2, both hybrid models yield the same results since only one reflection occurs [$N=2$ in Eq. (20)].

The Gaussian beam solution [Sec. II B 4, Eq. (31)] yields a curve that is indistinguishable from the one in Fig. 4. This is expected since, in the case of a single reflection, there are no singularities where conventional ray tracing would fail.

3. CERL FFP

The curve in Fig. 4 is also obtained from the CERL FFP solution [Sec. II C 2, Eq. (35) with the ground surface as an impedance plane]. In using the CERL FFP, only the number and distribution of sound speed layers, the extra loss and the number of integration points were varied. Default values for other parameters (Kmax, layer cutoff tolerance, and number of points per FFT) were used. Sufficient layering to represent

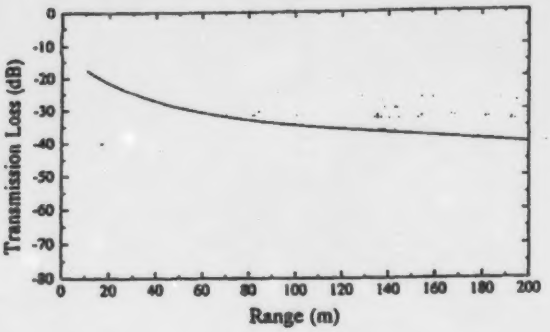

FIG. 5. Transmission loss versus range for case 2, 200 m, 100 Hz, obtained from SAFARI FFP.

the sound speed profile and sufficient number of sampling points to represent the integrand were provided. The number of layers and number of sampling points were continually adjusted where possible to achieve convergence of the TL within 0.5 dB. The run time for convergent solutions was minimized and, given convergence, the extra loss was minimized. Finally, the layer thickness was 2.5 m, with a 100 m isospeed cap.

4. CFFP

The CFFP solution [Sec. II C 2, Eq. (36) with the ground surface as an impedance plane] was implemented using 12 layers and a cap of 12 m. The artificial attenuation used to move poles off the integration path was 1×10^{-8} Np/m. For this case, 64 k points were required. The resulting curve is indistinguishable from the one in Fig. 4.

5. FFLAG FFP

For this implementation [Sec. II C 2, Eq. (35) for a poroelastic ground surface] the atmosphere is modeled by a 12 layer system each about 1 m thick. The air density is calculated by assuming that $\rho=\eta/c^2$ and the constant of proportionality η is calculated by substituting the surface values of ρ_0 and c_0.

The complete parameter set given in Table I is used to model the ground as a thick porous elastic layer over a porous elastic half-space. However, for this parameter set, the predictions are expected to be indistinguishable from those over a rigid porous half-space and the resulting curve is indistinguishable from the one in Fig. 4.

6. SAFARI FFP

This implementation [Sec. II C 2, Eq. (36) for an elastic surface, i.e., porosity is not included] characterizes the ground by compressional and shear wave velocities and compressional and shear wave attenuation from the relevant parameters listed in Table I. The result is the curve in Fig. 5. In the calculation the wave number spectrum is limited to a 4096 samples FFT length. The wave number resolution Δk and spatial resolution Δr are linked by minimum phase velocity: e.g., $\Delta k=2\pi f/c_{\min}M$ (m^{-1}), $\Delta r=c_{\min}/f$ (m) and $R_{\max}=M\Delta r$ (m), where f=frequency, $c_{\min}$=minimum phas velocity, M=number of range intervals and $R_{\max}$=maximu useable range.

As the range increases to 200 m, SAFARI predicts les transmission loss than the normal mode or ray tracing solu tions because SAFARI assumes a nonporous elastic soil. I fact for ranges less than 200 m, the transmission loss is clos to geometric spreading and the inversion does not affect th loss until larger distances at this frequency.

7. The FINITE PE

The result of the FINITE PE calculation [Sec. II D Eq. (45) with the ground surface as an impedance plane] indistinguishable from the curve in Fig. 4. The range a height step sizes were both 0.547 m (usually equal to $\frac{1}{4}$ wav length), the upper edge of the field array was equal to 400 and the total number of grid points needed in each field arr was 730.

8. FAST-PE

The numerical implementation of the FAST-PE [Se III D 2, Eq. (46) with the ground surface impedance plan on a computer requires the computation of a forward a inverse Fourier transform. For efficiency, a fast Fourier tra form (FFT) is used. A numerical Fourier transform requi finite limits on the integration. The lower end of the tra form is truncated at the ground while the upper limit is tru cated at a height which is defined as z_{top}. The calculat results are also indistinguishable from the curve in Fig. 4 b took less time to compute than the FINITE PE employin Crank Nicolson method. A complete discussion of the spe advantage of FAST PE is found in Ref. 31 where run ti were logged for the FAST-PE and FINITE-PE on the sa computer.

9. Summary

In summary, at this short range, all the models (exc SAFARI) agree to within the thickness of the line when same set of parameters are used as input data. The cu obtained from SAFARI, predicts less transmission loss t the other models because of the assumption of an elastic with no porosity. Finally, although FFLAG also assumes elastic soil, the addition assumption of porosity le FFLAG to agree with models that assume the ground surf as an impedance plane.

B. Case 2; 10 000 m, 100 Hz

1. Normal mode solution

The curve in Fig. 6 is obtained for case 2, $f=100$ H to a range of 10 000 using the normal mode solution, (10). Beyond about 500 m, the transmission loss sho complex feature of dips and peaks. These dips and peaks explained by the normal mode solutions in terms of m density. We note that there are approximately 667 modes this case.

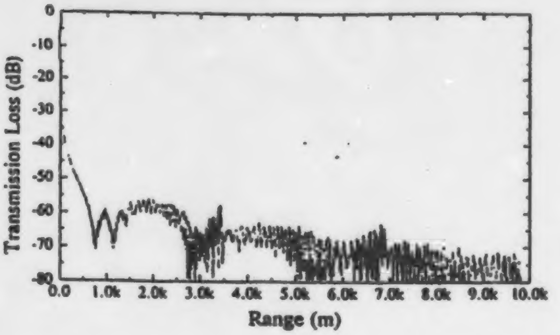

FIG. 6. Transmission loss versus range for case 2, 10 km, 100 Hz, obtained from the normal mode solution.

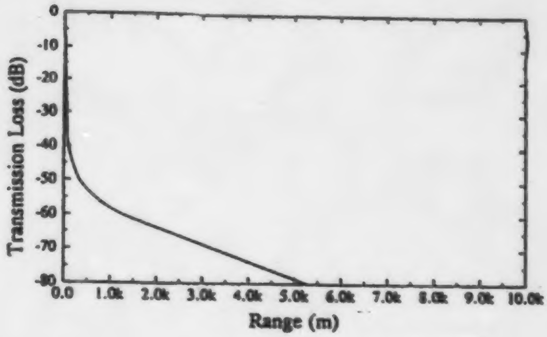

FIG. 8. Transmission loss versus range for case 2, 10 km, 100 Hz, obtained from the single bounce ray model.

2. Ray tracing solutions

At longer ranges, Eq. (19) predicts additional rays that go through multiple reflections on the ground. The curve in Fig. 7 is obtained using the multiple bounce ray model, Eq. (20). The discontinuity that appears at about 500 m corresponds to the sudden appearance of additional rays and is an artifact of the model. However the dip corresponds to physical reality and is explained by a ray model by interference between the various rays. As the range increases, more rays appear in the summation Eq. (20). The additional rays produce the interferences in the curve and contribute to reducing the transmission loss (increasing relative levels). At a range of about 10 km, Eq. (19) predicts up to 100 rays reflected from the ground.

The curve in Fig. 8 is the result of the single bounce ray model described in Sec. II B 2. Since the calculation is restricted to a single bounce, the dips corresponding to the additional rays are absent and at ranges beyond about 1500 m, the transmission loss is greater than the loss predicted when the additional rays are accounted for.

The curve in Fig. 9 was obtained from the Gaussian beam solution, Eq. (31). We note that the beam summation smooths the sharp discontinuity around 500 m that is produced by the multiple bound ray model.

It is interesting to note that on the whole the average TL predicted from the Gaussian beam solution agrees with the TL obtained from the multiple bounce ray model. Not surprisingly, though, the detailed fine structure in the dip and peaks differs due to the nature of the approximations inherent in the ray tracing solutions. The same comments apply to the comparison with the normal mode solution. We note, however, that in a real atmosphere, turbulence would smooth out most of the fine structure predicted by this test case.

3. FFP solutions

The curve calculated from three FFPs that assume a porous ground is shown in Fig. 10. The agreement between the three calculations is within the accuracy of implementation (typically 0.5 dB). The features, predicted as ray interferences according to ray theory and modal density according to the residue series, are reproduced by the numerical solution of the full wave equation.

The curve obtained from the FFLAG FFP is indistinguishable to within numerical implementation from the curves obtained from the CERL FFP and the CFFP. The FFLAG FFP allows for a layered porous and elastic ground using the full range of parameters in Table I. On the other hand the CERL FFP and the CFFP models the ground as a porous half-space. The agreement suggests that a complex impedance plane is a good approximation to the layered ground described in Table I for the benchmark cases. As expected, although not shown here, SAFARI yields a different result from the other FFPs.

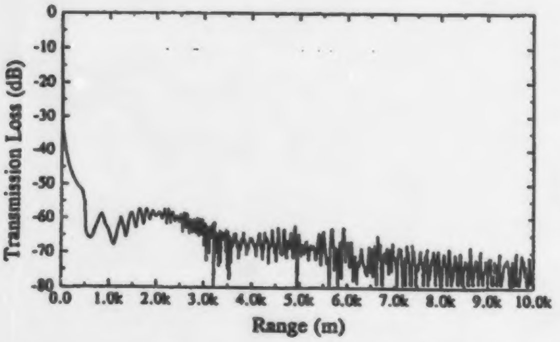

FIG. 7. Transmission loss versus range for case 2, 10 km, 100 Hz, obtained from the multiple bounce ray model.

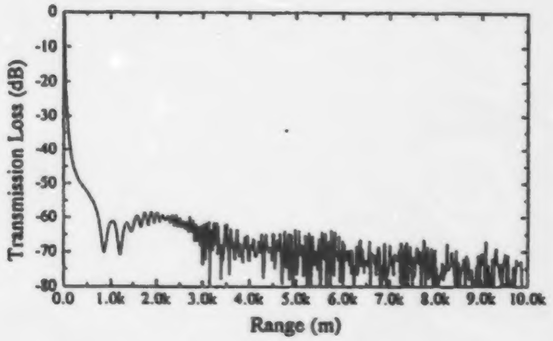

FIG. 9. Transmission loss versus range for case 2, 10 km, 100 Hz, obtained from the Gaussian beam model.

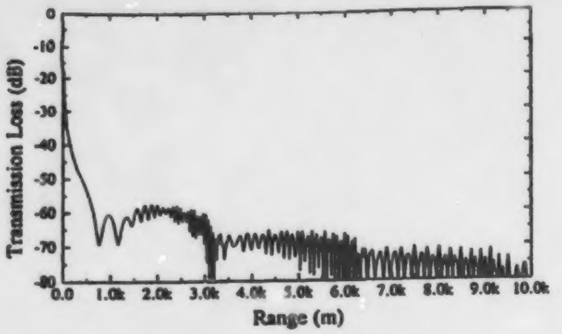

FIG. 10. Transmission loss versus range for case 2, 10 km, 100 Hz, obtained from the CERL FFP, CFFP, FFLAG FFP, and the FAST PE.

4. PE solutions

As noted earlier, computational time is excessive for this long range case using the FINITE PE. The FAST-PE, however, runs in just a few minutes. Details of the fine structure depend upon the height at which the calculation is truncated but the general form is the same as that in Fig. 10.

C. All cases for the FFP and PE

In this section the numerical techniques are used to calculate the transmission loss for the full range of atmospheric conditions described by cases 1 to 4. In the preceding section, results showed that three of the FFP solutions and the

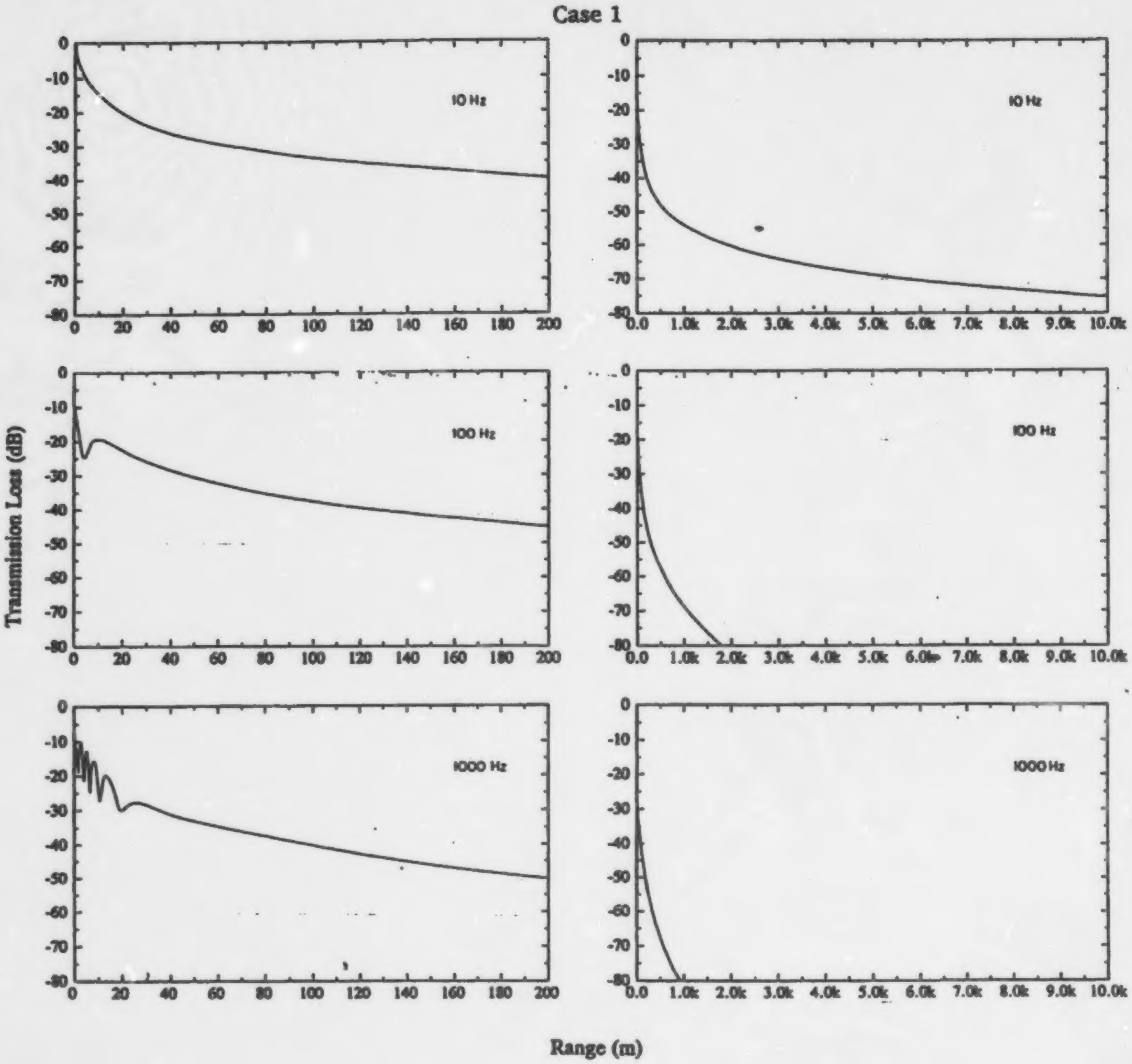

FIG. 11. Transmission loss for case 1 for the FFP and PE. The curves obtained from the two models are indistinguishable.

two PE methods agree with the analytical solution Eq. (10) for case 2, to within the accuracy of implementation (The results from the SAFARI FFP differed because of the assumption of an elastic ground surface) Although not shown here, the FFP and the PE also agree with the analytical solution Eq. (11) for case 3 and the analytical solution Eq. (12) for case 1. Therefore detailed comparison here are restricted to the FFP (except SAFARI) and the PE. In the FFP input parameters were adjusted to obtain an accurate prediction over the entire range of interest for each case, while minimizing run time. The PE used accurately propagates the phases for angles under 45° from horizontal. Consequently, very high angles modes in case 2 at 10 Hz, 10 km have phase errors in the PE solution. We note that case 1 is the most difficult to implement with the FFP's. Case 2 is most difficult for the PE due to the large number of trapped modes. The larger number of modes make the sampling in wave number space less sensitive for the FFP's, since the total solution is the sum of many contributions. Sampling errors of a few modes will not alter the total solution significantly. The FINITE-PE is generally prohibitively slow at longer range or high frequencies, though it needs much less parameter "tuning" than the FFP to obtain convergence.

1. Case 1

Case 1 is a model for sound propagation near the ground in a homogeneous atmosphere and the results are shown in Fig. 11. In case 1, spherical spreading dominates the solution, with a 6-dB enhancement of the field at low frequen-

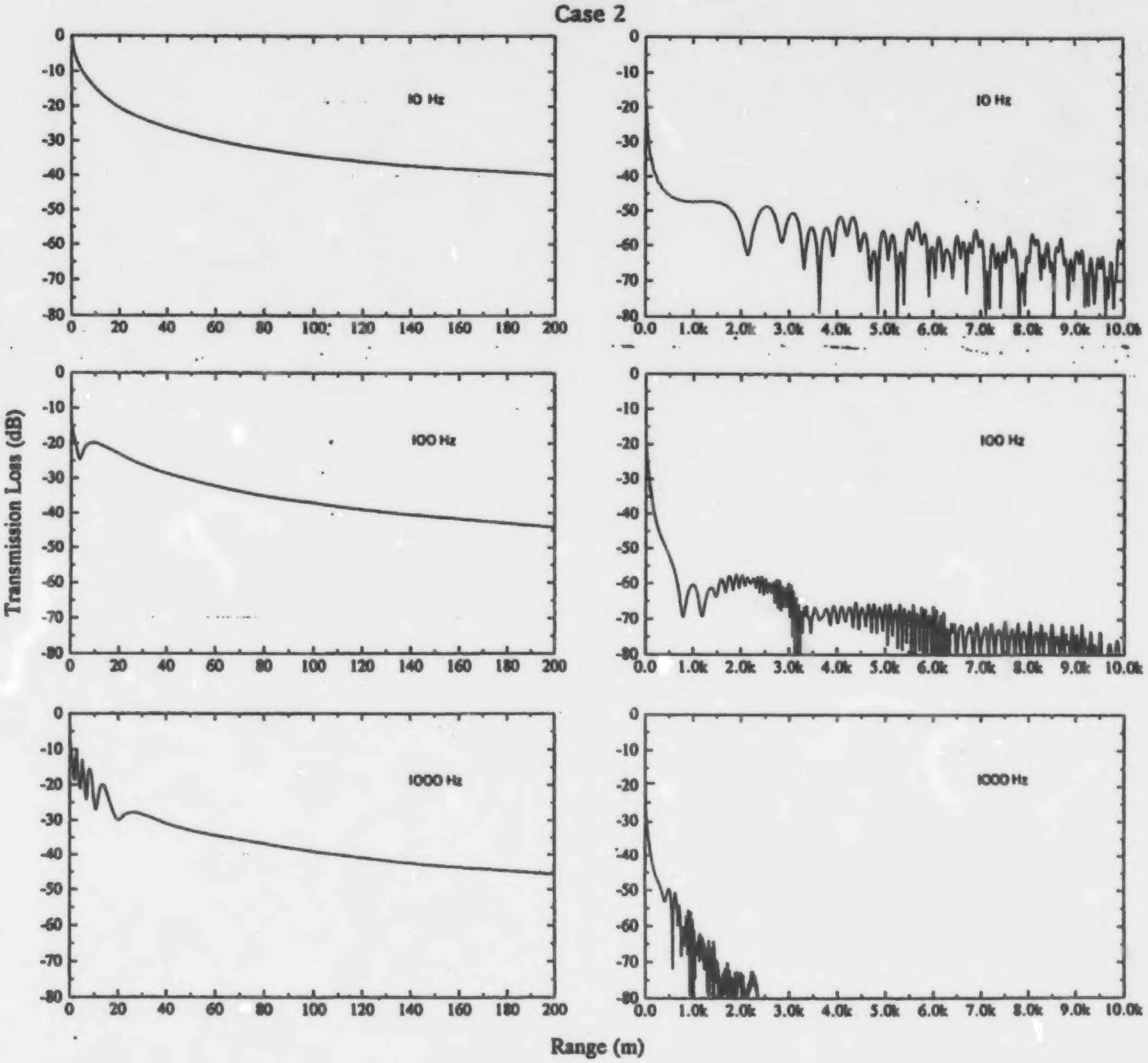

FIG. 12. Transmission loss for case 2 for the FFP and PE. The curves obtained from the two models are indistinguishable.

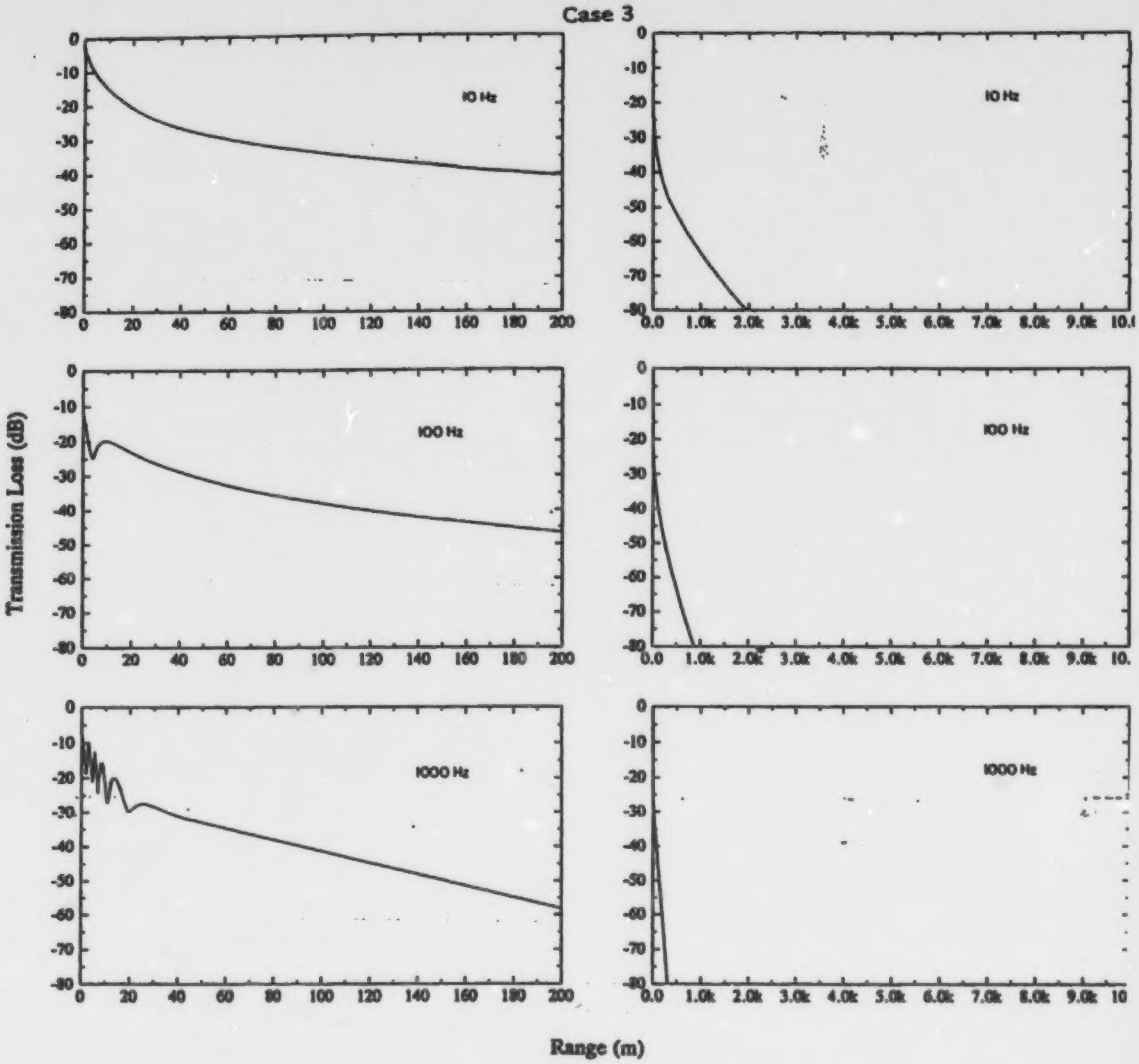

FIG. 13. Transmission loss for case 3 for the FFP and PE. The curves obtained from the two models are indistinguishable.

cies. There is negligible attenuation of the wave at 10 Hz from atmospheric absorption in the atmosphere. There is also negligible ground attenuation from the finite-impedance ground surface at 10 Hz. At 100 Hz, the atmospheric attenuation is 0.18 dB/km. A ground shadow appears at around 850 m and the signal decays at 46 dB per decade of distance (spherical spreading amounts to 20 dB per decade of distance). At 1 kHz, the atmospheric attenuation is 5.4 dB/km. Beyond 200 m a ground shadow occurs and the field decays at 56 dB per decade of distance, including spherical spreading, thus greatly exceeding the decay rate from atmospheric absorption. Although case 1 is the most difficult for the FFP's, when properly implemented, curves obtained from the FFP's and the PE's are indistinguishable. The analytical solution for this case is Eq. (12) and this solution agrees all the numerical results.

2. Case 2

Case 2 models sound propagation near the ground downward refracting situation and was considered in d in the previous section for all the models. The curves tained in the case of the FFP and the PE are indistinguish and a complete set of curves are shown in Fig. 12.

3. Case 3

Case 3 models sound propagation near the ground i upward refracting environment. At short range (under 20

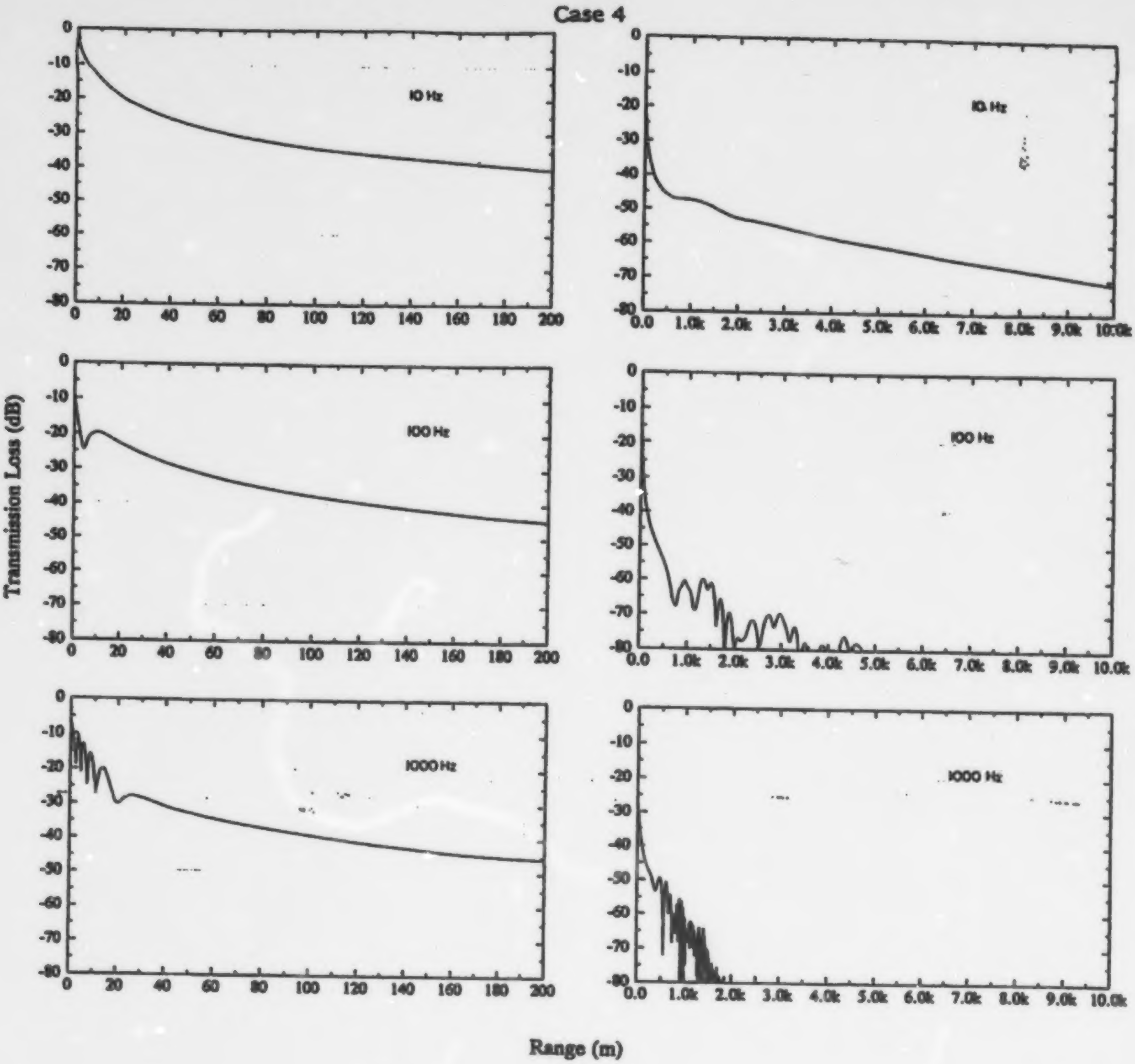

FIG. 14. Transmission loss for case 4 for the FFP and PE. The curves obtained from the two models are indistinguishable.

the predicted curves show very little variation from case 1 except for an increase in TL for 1000 Hz beyond about 130 m. At longer ranges, all curves rapidly decay in the shadow zone formed by the sound speed profile. The results of the PE are indistinguishable from the FFP. A complete set of curves are shown in Fig. 13.

The analytical solution for this case within the shadow zone is the residue series given by Eq. (11) and calculations using this expression, while not shown, agree with the results in Fig. 13. We note, however, that despite agreement between the calculations, the large attenuation predicted at the longer range is not supported by experimental data (for example, see the results shown in Ref. 30).

4. *Case 4*

Case 4 models sound propagation near the ground in a profile that traps energy near the ground, and refracts sound waves away from the ground at altitudes above 100 m. Above 300 m, the profile is constant. At short range (under 200 m) there is no difference between predictions for this situation and case 2 (downward refraction).

At longer ranges, higher angle modes of propagation interact with the upward refracting portion of the sound speed profile and "leak" energy out of the waveguide formed at the ground. At 100 Hz the curve shows less energy in the signal beyond 1.5 km than in case 2. At 1000 Hz, essentially all of the energy is trapped in the waveguide, and

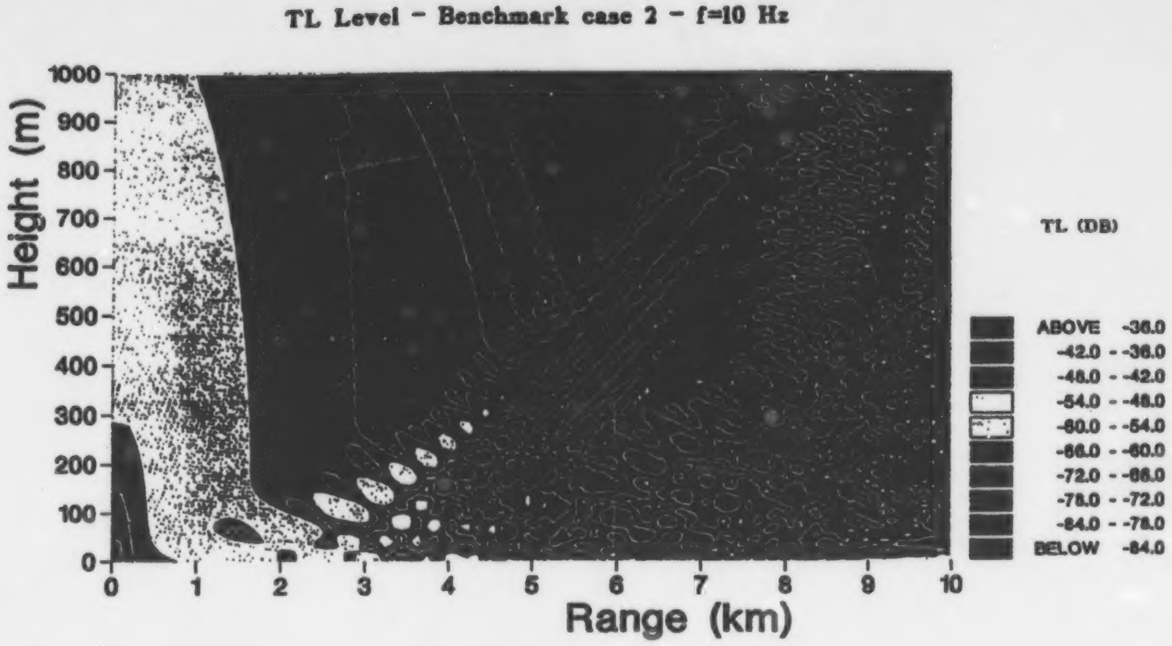

FIG. 15. Contour plot for case 2, 10 Hz.

there is no difference in the results from case 2. The complete set of curves are shown in Fig. 14. There is no analytical solution for this case.

D. Contour plot

For illustrative purposes a contour plot of transmission loss is shown in Fig. 15 for case 2, $R=10$ km, $f=10$ Hz which can be compared directly with the ray diagram in Fig. 16.

V. SUMMARY

Benchmarks were calculated using analytical models, ray tracing models, the FFP solution and the PE solution. The analytical models included two residue series for cases 2 and 3, respectively, and the result of a steepest descent integration for case 1. The ray tracing included a model restricted to a single bounce, a multiple bounce model and a Gaussian beam summation. Four different implementations of the FFP were considered. In one FFP (SAFARI), the ground is assumed to be a nonporous elastic layered interface. Two FFP's (CERL-FFP, CFFP) considers the ground to be a rigid semi-infinite porous surface while the fourth FFP (FFLAGS) assumed a porous elastic layer above a nonporous elastic substrate. The PEs considered included a Crank–Nicolson version (FINITE PE) and a fast Green's function method (FAST PE).

For all cases, results show that the FFP and the PE agree with the analytical solution, where an analytical solution is available, to within the accuracy of implementation. Any differences between the various implementations of the FFP and the PE can readily be attributed to different assumptions in the models. For example SAFARI predicts less transmission loss than the other versions because it assumes a nonporous ground.

The results from the ray tracing models depend on how many physical mechanisms are included and to what level o detail they are considered. For example a ray model tha assumes a single bounce at all distances predicts larger transmission loss at long ranges for a downward refracting atmosphere than the other models. In the absence of upward refraction, for the cases considered, the ray trace algorithm give reasonable agreement with the more accurate technique (FFP and PE).

None of the models considered here include the effect of turbulence, rough ground, or terrain features. These effect are all present to some degree in experimental data. For thi reason, the results of the calculations presented here may no compare well to experimental data especially in refractiv

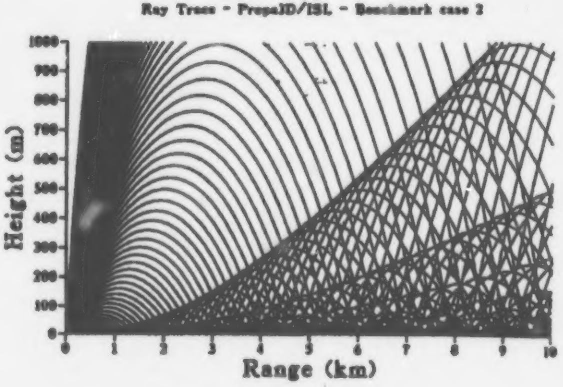

FIG. 16. Ray diagram for case 2.

shadow zones. The benchmark calculations presented here should be used to test theory and algorithms in the absence of these complications which are always present in the real world. Then the user can proceed to include other effects with a confidence that refraction, diffraction, and ground reflection have been properly accounted for.

ACKNOWLEDGMENTS

The authors are rigorously listed in alphabetical order with authors from the same institution grouped together. The editing of the manuscript and preparation of the figures was coordinated by the National Research Council of Canada. NATO DRG Panel 3 is acknowledged for sponsoring and providing the frame work for this investigation. Atlas Elektronik GmbH acknowledges MoD-Bonn FRG, RÜ T III/4, Mr. H. Wolff. Work at the National Research Council was supported in part by DND/DREV. Work at the Open University, England, was supported in part by the U.S. Army (WES) through its European Research Office.

[1] J. E. Piercy, T. F. W. Embleton, and L. C. Sutherland, "Review of noise propagation in the atmosphere," J. Acoust. Soc. Am. 61, 1403–1418 (1977).

[2] R. Raspet, G. E. Baird, and W. Wu, "The relationship between upward refraction above a complex impedance plane and the spherical wave evaluation for a homogeneous atmosphere," J. Acoust. Soc. Am. 89, 107–114 (1991).

[3] R. Raspet, G. Baird, and W. Wu, "Normal mode solution for low frequency sound propagation in a downward refracting atmosphere above a complex impedance plane," J. Acoust. Soc. Am. 91, 1341–1352 (1992).

[4] S. W. Lee, N. Bong, W. F. Richards, and R. Raspet, "Impedance formulation of the fast field program for acoustic wave propagation in the atmosphere," J. Acoust. Soc. Am. 79, 628–634 (1986).

[5] K. E. Gilbert and M. J. White, "Application of the parabolic equation to sound propagation in a refracting atmosphere," J. Acoust. Soc. Am. 85, 630–637 (1989).

[6] L. B. Felsen, "Benchmarks: An option for quality assessment," J. Acoust. Soc. Am. 87, 1497–1498 (1990).

[7] H. A. J. M. van Hoof and K. W. F. M. Doorman, "Coupling of airborne sound in a sandy soil," Laboratory for Electronic Developments TNO (1983). The Wezep soil is also measurement No. 12 in M. J. M. Martens, L. A. M. vander Heijden, H. H. J. Walthous, and W. J. J. M. van Rems, "Classification of soils based on acoustic impedance air flow resistivity and other physical soil parameters," J. Acoust. Soc. Am. 78, 970–980 (1985).

[8] The expressions for k_b^2 and $\rho_b(\omega)$ are found in K. Attenborough, "Acoustical impedance models for outdoor ground surfaces," J. Sound Vib. 99, 501–544 (1985), however, λ is written here as a function of the pore shape factor ratio s_p defined by Eq. (21) in K. Attenborough, "On the acoustic slow wave in air-filled granular materials," J. Acoust. Soc. Am. 81, 93–102 (1987). A good appreciation of the role of the flow resistivity, tortuosity, and porosity of ground surface can be found in K. Attenborough, "Ground parameter information for propagation modeling," J. Acoust. Soc. Am. 92, 418–427 (1992) and H. M. Hess, K. Attenborough, and N. W. Heap, "Ground characterization by short-range propagation measurements," J. Acoust. Soc. Am. 87, 1975–1986 (1990).

[9] ANSI SI.26-1978, "Method for the calculation of the absorption of sound by the atmosphere" (Acoustical Society of America, New York, 1978).

[10] A. Berry and G. A. Daigle, "Controlled experiments on the diffraction of sound by a curved surface," J. Acoust. Soc. Am. 83, 2047–2058 (1988).

[11] K. Attenborough, S. I. Hayek, and J. M. Lawther, "Propagation of sound above a porous half-space," J. Acoust. Soc. Am. 68, 1493–1501 (1980). Typographical corrections can be found in the Appendix in K. B. Rasmussen, "Sound propagation over grass covered ground," J. Sound Vib. 78, 247–255 (1981).

[12] Anon., "Advanced Sound Propagation in the Atmosphere," University of Mississippi (1991). ASOPRAT includes the CERL FFP as a default in shadow zones. Only the ray trace part is described here.

[13] A. L'Espérance, P. Herzog, G. A. Daigle, and J. Nicolas, "Heuristic model for outdoor sound propagation based on an extension of the geometrical ray theory in the case of a linear sound speed profile," Appl. Acoust. 37, 111–139 (1992).

[14] V. Cerveny, M. M. Popov, and I. Psencik, "Computation of wave fields in inhomogeneous media-Gaussian beam approach," Geophys. J. R. Astron. Soc. 70, 109–128 (1982).

[15] Y. Gabillet, H. Schroeder, G. A. Daigle, and A. L'Espérance, "Application of the Gaussian beam approach to sound propagation in the atmosphere: Theory and experiments," J. Acoust. Soc. Am. 93, 3105–3116 (1993).

[16] F. R. DiNapoli, "A fast field program for multilayered media," Naval Underwater Systems Center, Tech. Rep. 4103 (1971).

[17] H. W. Kutschale, "The integral solution of the sound field in a multilayered liquid–solid half-space with numerical computations for low-frequency propagation in the Arctic Ocean," Tech. Rep. No. 1 (CU-1-70, ONR Contract N00014-67-A-0108-0016), Lamont–Doherty Geological Observatory, Columbia University, Palisades, New York (1970).

[18] H. W. Kutschale, "Rapid computation by wave theory of the propagation loss in the Arctic Ocean," Tech. Rep. No. 8, Lamont–Doherty Geological Observatory, Columbia University, Palisades, New York (1981).

[19] R. Raspet, S. W. Lee, E. Kuester, D. C. Chang, W. F. Richards, R. Gilbert, and N. Bong, "Fast-field program for a layered medium bounded by complex impedance surfaces," J. Acoust. Soc. Am. 77, 345–352 (1985).

[20] Y. L. Li, S. J. Franke, and C. H. Liu, "Numerical implementation of an adaptive fast-field program for sound propagation in layered media using the chirp *z* transform," J. Acoust. Soc. Am. 89, 2068–2075 (1991).

[21] A. Güdesen, "Application of the SAFARI model to sound propagation in the atmosphere," J. Acoust. Soc. Am. 87, 1968–1974 (1990). For a detailed discussion of the use of SAFARI in underwater acoustics, see H. Schmidt, "SAFARI User's Guide," SACLANTCEN Report SR-114, NATO (1988) and C. H. Harrison, "Ocean Propagation Models," Appl. Acoust. 27, 163–201 (1989).

[22] T. L. Richards and K. Attenborough, "Accurate FFT-based Hankel transforms for prediction of outdoor sound propagation," J. Sound Vib. 109, 157–167 (1986).

[23] S. Tooms, S. Taherzadeh, and K. Attenborough, "Sound propagation in a refracting fluid above a layered fluid-saturated porous elastic material," J. Acoust. Soc. Am. 93, 173–181 (1993).

[24] S. J. Franke and G. W. Swenson, Jr., "A brief tutorial on the Fast Field Program applied to Sound Propagation in the Air," Appl. Acoust. 27(3), 203–216 (1989).

[25] M. West, R. A. Sack, and F. Walkden, "The fast field program. A second tutorial: Application to long range sound propagation in the atmosphere," Appl. Acoust. 33, 199–228 (1991).

[26] G. D. Dockery, "Modeling electromagnetic wave propagation in the troposphere using the parabolic equation," IEEE Trans. Antennas Propag. 36(10), 1464–1470 (October, 1988).

[27] J. F. Claerbout, *Fundamentals of Geophysical Data Processing* (McGraw-Hill, New York, 1976), p. 206.

[28] F. D. Tappert, "The parabolic approximation method," in *Wave Propagation and Underwater Acoustics*, edited by J. B. Keller and J. S. Papadakis (Springer-Verlag, New York, 1977).

[29] M. K. Myers and G. L. McAninch, "Parabolic approximation for sound propagation in the atmosphere," AIAA J. 16, 836–842 (August 1978).

[30] M. J. White and K. E. Gilbert, "Application of the parabolic equation to the outdoor propagation of sound," Appl. Acoust. 27(3), 227–238 (1989).

[31] K. E. Gilbert and X. Di, "A Fast Green's function method for one-way sound propagation in the atmosphere," J. Acoust. Soc. Am. 93, 714–720 (1992). The software package that implements The Green's Function PE (GF-PE) is referred to as "FAST-PE" in this article.

[32] J. C. Craddock and M. J. White, "Propagation of acoustic waves past an impedance discontinuity: a parabolic equation approach," J. Acoust. Soc. Am. 91, 3184–3191 (1992).

[33] J. S. Robertson, M. J. Jacobson, W. L. Siegmann, and D. P. Santandrea, "Acoustical effects of a large ridge on low-frequency sound propagation in stationary and moving atmospheres," RPI Math. Rep. No. 181, Dept. of Mathematical Sciences, Rensselear Polytechnic Institute, Troy, NY 12180-3590 (November 1989).

[34] J. M. Noble, H. E. Bass, and R. Raspet, "Effects of large-scale wind driven turbulence on sound propagation," J. Acoust. Soc. Am. 87, S149 (1990).

[35] K. E. Gilbert, R. Raspet, and X. Di, "Calculation of turbulence effects in an upward refracting atmosphere," J. Acoust. Soc. Am. 87, 2428–2437 (1990).

Spatial coherence of a sound field in a refractive shadow: Comparison of simulation and experiment

David I. Havelock
Institute for Microstructural Sciences, National Research Council, Ottawa, Ontario K1A 0R6, Canada

Xiao Di[a)]
National Center for Physical Acoustics, University of Mississippi, University, Mississippi 38677 and Institute for Microstructural Sciences, National Research Council, Ottawa, Ontario K1A 0R6, Canada

Gilles A. Daigle and Michael R. Stinson
Institute for Microstructural Sciences, National Research Council, Ottawa, Ontario K1A 0R6, Canada

(Received 15 February 1995; revised 17 April 1995; accepted 1 May 1995)

The coherence of a sound field in a refractive shadow near the ground has been examined for microphone separations which are transverse or longitudinal to the direction of propagation. Single tone test signals at 1 kHz, 500, and 100 Hz were measured at a range of 700 m by a microphone array, spanning 270 m longitudinally and 15 m transversely. Estimates of the spatial correlation, based on 10-minute averages, indicate transverse coherence lengths less than 2 m and longitudinal correlation lengths less than 7 m for moderately strong upward refraction conditions. Numerical simulations were done which emulate the experimental conditions. The Green's-function method for the parabolic equation was used to generate two-dimensional sound fields within a refractive shadow. An upward refracting atmospheric model with homogeneous isotropic Gaussian turbulence was used. The coherence in the simulated sound fields compares well, qualitatively, with the experimentally measured coherence. Both simulation and experiment indicate that the longitudinal coherence length within a refractive shadow is dramatically less than is typically observed outside of a shadow. The reduced coherence will restrict the useful aperture size of beamforming arrays deployed in acoustical non-line-of-sight conditions.

PACS numbers: 43.28.Fp, 43.60.Cg

INTRODUCTION

Beamforming takes advantage of known signal phase relationships across an array of sensors to achieve coherent integration of the signal. Acoustic arrays have been used successfully for this purpose underwater where the signal fluctuations are relatively small, even at very long ranges.[1] In the atmosphere, signal fluctuation due to turbulence can be significant even at ranges of only a few hundred meters.[2,3] These fluctuations reduce the spatial coherence of the sound field and limit the effectiveness of beamforming. An important benefit of acoustic sensors for source localization and detection in the atmosphere is that they need not have line-of-sight contact with the source. When deployed in this mode of operation, such as behind a hill, the beamforming microphone array is often within an acoustic shadow. This paper investigates the coherence of sound fields within such shadows.

Acoustic shadows can also form in an upward refracting atmosphere, for which the sound speed decreases with increasing height above the ground. The ray paths for sound propagating from the source curve upward generating an envelope, or shadow boundary, separating an acoustic shadow region near the ground from the overhead skywave,[4] as illustrated in Fig. 1. A refractive shadow generated in this manner is analogous to the acoustic shadow caused by a large hill masking a sound source from a receiver. In both cases, energy arrives within the acoustic shadow region by diffraction at the shadow boundary and by scattering from turbulence in the overhead skywave.

The sound energy diffracted at the shadow boundary decreases rapidly within the shadow region, with higher frequencies penetrating less into the shadow than do lower frequencies. Sound scattered from turbulence in the skywave propagates deeper into the shadow region. The scattered sound energy dominates the diffracted energy deep within the shadow region, where sound-pressure levels (SPL) are typically several tens of decibels higher than predicted from diffraction theory.[2,5] The randomness of the scattered sound field leads to reduced spatial coherence deep within the shadow region. An understanding of the spatial coherence within an acoustic shadow, and its effects on beamforming capabilities, is a critical performance element for acoustic detection systems in the atmosphere.

Most studies of sound fields both within and outside of shadow regions have concentrated on measurement and prediction of the mean SPL. Little is known about the statistics of the sound field within an acoustic shadow region other than the mean SPL. Experiments by Daigle *et al.*[2] report the spatial coherence within the shadow region at a propagation distance of 200 m and suggest that a characteristic distance for loss of coherence, transverse to the direction of propagation and deep in an acoustic shadow, is twice the signal

---

[a)] Present address: Dept. of Acoustics, Penn State University, University Park, PA 16801.

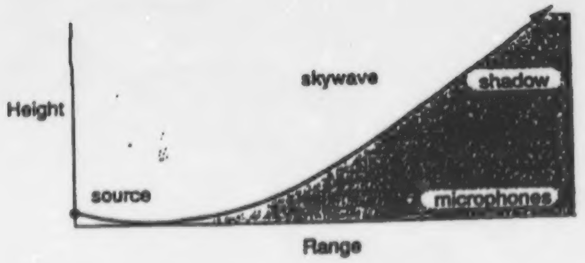

FIG. 1. Refractive shadow. During upward refraction conditions an acoustic shadow is generated near the ground. An array deep within the shadow receives signal energy due mainly to scattering from the skywave.

wavelength for wavelengths less than the coherence length of the turbulence. No corresponding results are reported for longitudinal coherence within a shadow but it is noted that the asymptote of the transverse coherence approaches the longitudinal coherence between the source and receiver. Outside of the shadow region, the coherence length along the propagation path is predicted to be very long,[6] although direct measurements to confirm this are limited. Daigle *et al.*[7] shows very high coherence in the presence of turbulence between source and receiver at a range of 100 m for frequencies below 2 kHz.

Only recently has it been possible to predict the sound field within an acoustic shadow near the ground for an upward refracting turbulent atmosphere with an efficient propagation code.[8–11] The parabolic equation method,[5] in particular, the fast Green's-function method for the parabolic equation[10] (GF-PE), has been shown to provide SPL estimates which agree reasonably well with experimental measurements. Since the PE methods are based on a solution to the wave equation, albeit in the forward direction only, the propagation aspects of the calculations should be physically accurate; however, the atmospheric models used in these numerical predictions have a less well established physical basis and therefore require validation with measured data.

In this paper the effects of atmospheric turbulence on the spatial coherence of a sound field within a refractive shadow are investigated by examining spatial correlation statistics obtained by both field measurements and simulations. By comparing high-order statistics, such as spatial correlation, from experimental measurements and simulation calculations, the physical accuracy of prediction codes are challenged to a greater extent than by comparison of SPL alone. Section I discusses the experimental setup used to measure the acoustic sound field in a refractive shadow. Section II describes the digital signal processing used to obtain estimates of the spatial correlation of the sound field. Various signal characteristics which are relevant to the analysis are discussed in Sec. III. The GF-PE acoustic propagation prediction code[12] and the processing parameters are discussed in Sec. IV. In Sec. V the experimental and simulation data are compared and some of the observed characteristics of the spatial coherence are discussed. A brief discussion of the significance of the observed coherence lengths to beamforming arrays is presented at the end of Sec. V.

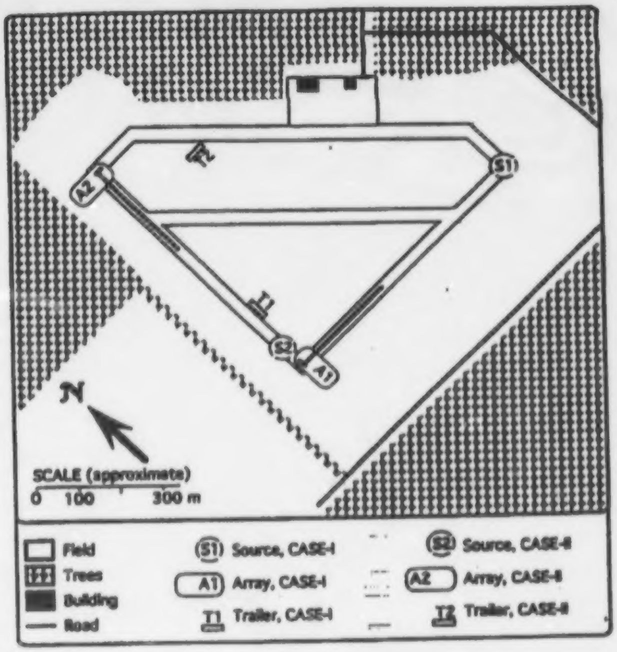

FIG. 2. Test site layout. The tests were conducted at an airfield which has runways of 700 m length. The locations of the source (S1, S2), array (A1, A2), and equipment trailer (T1, T2) are indicated for the two test cases (I and II, respectively).

I. EXPERIMENTAL MEASUREMENTS

Experimental determination of the spatial coherence in a sound field requires that correlation between pairs of microphones be measured for different sensor separations. To obtain measurements over a wide range of separations and complete the measurements quickly, before changes occur in the propagation conditions, many microphones are necessary for simultaneous measurement of the sound field; hence a large array is used. To obtain measurements deep within a refractive shadow the measurements were conducted at an airfield which provides a large expanse of flat ground. The hard surface of the runway simplifies the ground impedance effect. In this section the test site, meteorological conditions, microphone array configuration, and signal acquisition system are described.

A. Test site

The test site (Fig. 2) was an airport in a rural area about 50 km east of the city of Ottawa. There are three runways, each approximately 700 m long and about 30 m wide. Acoustic impedance measurements of the asphalt runways indicate that they can be considered to be acoustically hard up to 1 kHz. There are no hills or prominent structures in the vicinity except for the airport hangers which are distant enough to avoid significant reflections.

Based upon the prevailing wind direction for the day of each test, the runway which provided the best upwind propagation conditions was selected. The source and array were deployed at opposite ends of the runway. Two sets of test data are reported here; the north–south runway was used for the first set (case I) and the east–west runway was used for the second set (case II). The location of the array, source, and equipment trailer for each set is shown in Fig. 2.

B. Meteorological conditions

Simple meteorology was collected during the experiment to determine if upward refracting conditions existed. For the qualitative nature of this study detailed measurements were not necessary. Temperature and wind measurements were taken at the ground (10 cm) and at head height (2 m) with hand held thermo-anemometers (Alnor, model GGA-26). After the data were collected, the signal levels at the array were compared to those at the source. Significant losses in excess of those expected due to spherical spreading and absorption were interpreted as verification of upward refraction. (See Sec. III C.) The elapsed time for collection of the data for case I and case II was about 40 min each.

The case-I data were collected under *weak* upward refraction conditions. The temperature was 12 °C with about −0.5 °C/m vertical gradient (lapse). The sky was clear and the wind was light and intermittent, approximately 1 m/s, with the direction difficult to determine.

The case-II data were collected under *moderate* upward refraction conditions. The temperature was 4–5 °C at the lower level (10 cm) and about 2 °C at the higher level (2 m). Winds were 3–6 m/s from the west, providing direct upwind propagation. Combined lapse and upwind propagation conditions indicate consistent upward refraction.

C. The array

The microphones in the acoustic array were custom built, consisting of a ½-in. electret capsule mounted in a metal tube and permanently connected to a matched preamplifier. The electret capsule is a condenser-type transducer (Panasonic electret, model WM063T). The microphone tubes are 1 cm in diameter by 15 cm long and are fitted with 9-cm windscreens (B&K model UA0237). The preamplifiers are located approximately 2 m from the microphones and provide about 50-dB gain. Frequency response tests of the capsule and preamplifier combination indicated consistent and flat response within ±2 dB over the frequencies of interest. Various tests, including response under heating and tolerance to dirt, moisture, and mechanical shock, were performed to ensure that the microphones were tolerant of a wide range of outdoor environmental conditions. Although not suitable for extremely accurate measurements, the microphones are adequate for our purposes and have proven reliable and consistent.

The array was deployed in a "T" pattern, using 24 microphones as illustrated in Fig. 3, with the microphones on the ground. The array center, defined as the junction of the two straight segments of the array, was positioned on the centerline of the runway. The transverse arm, which was perpendicular to the centerline, is the short axis of the array. The longitudinal arm, which extends from the array center along the centerline toward the source, is the long axis of the array.

The transverse arm consists of 11 sensors extending 15 m with the spacing chosen to span the range of desired separations while remaining compact and minimizing the number of sensors required. The distribution of spacings between the transverse sensors is shown in Fig. 4.

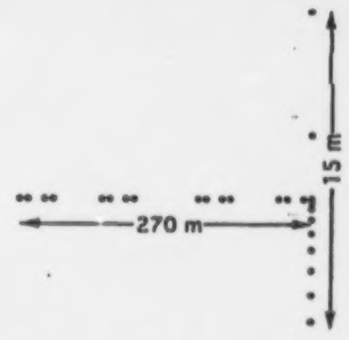

FIG. 3. Array geometry. A nonuniformly spaced array is used to obtain good selection of sensor separations. The longitudinal arm is 270 m long and the transverse arm is 15 m long. The array is deployed in a "T" pattern on the ground within a refractive shadow. (Not to scale.)

The longitudinal arm of the array consists of 16 microphones, one of which was shared with the transverse arm. It is longer than the transverse arm because preliminary simu-

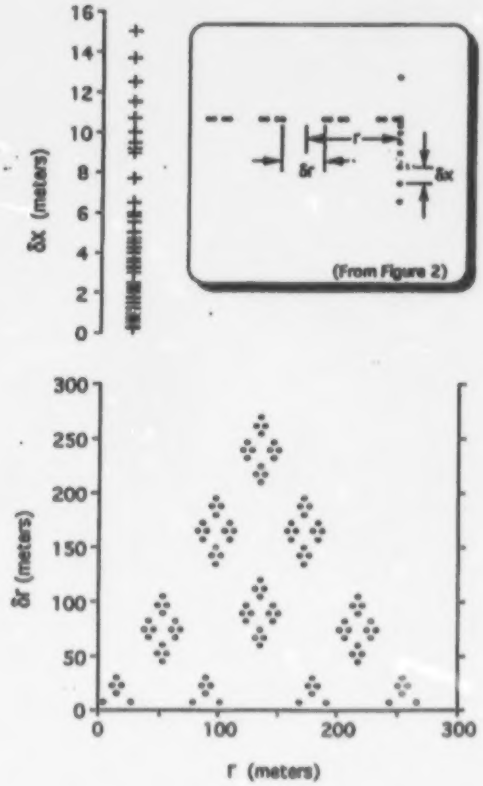

FIG. 4. Available sensor spacings. The separations (δx) between sensor pairs in the transverse arm of the array are indicated with crosses (+) adjacent to the upper axis. The available separations (δr) between sensor pairs in the longitudinal arm of the array depends upon the distance (r) between the sensors and the array center. All possible combinations or r and δr are indicated with solid circles (●) in the lower plot. The insert at the upper right shows an example of δx, δr, and r within the array geometry of Fig. 3.

TABLE I. The source signal levels and pairs of received signal levels, noise levels, SNR, and refractive losses are tabulated for weak/moderate upward refraction conditions for three frequencies. Calculation of the refractive losses is explained in the text.

Frequency (Hz)	Source level (dB)	Levels at array center (dB)			"Refractive losses" (dB)
		signal	noise	SNR	
1000	123	46/41	24/26	22/15	17/22
500	126	54/54	32/36	22/18	13/13
100	124	64/51	50/43	14/8	3/16

lations indicated that the longitudinal coherence would be greater than the transverse coherence. Microphone spacing was chosen so that similar separations were available at different ranges. The distribution of ranges and separations for all pairs of microphones in the longitudinal and transverse arms is illustrated in Fig. 4. The diamond patterns in the figure are a result of the symmetric spacing of the four clusters of four microphones in the longitudinal arm.

D. Acoustical source

The source was located 700 m from the array center, at the opposite end of the runway. It consists of a conventional loudspeaker and amplifier, a portable generator to provide electrical power, and a prerecorded set of test signals. The speaker had a single 15-in. (38 cm) driver housed in a single port enclosure with the center of the driver about 30 cm from the ground. An equipment rack was positioned 15 m away at 45° behind the speaker. The generator was located 15 m beyond the equipment rack. Noise from the generator was negligible at the array.

The source signals were 1000-, 500-, and 100-Hz pure tones, each prerecorded separately on digital audio tape. For each test, the amplifier output voltage was stabilized at a predetermined level corresponding to about 300 W of electrical power. The source output levels listed in Table I were measured at a height of 1 m above the ground at a range of 10 m in front of the speaker and were referenced to 1-m range relative to 20 μPa. A Brüel & Kjær $\frac{1}{2}$-in. microphone, preamplifier, and instrumentation amplifier, models 4133, 2804, and 2610, respectively, were used to measure the source levels.

E. Signal acquisition

The electrical signal from each microphone–preamplifier combination is amplified by a programmable gain amplifier for transmission over cables to the equipment trailer which is about 200 m away. The gain is adjusted remotely from the equipment trailer to maximize the signal levels while remaining within the voltage limits of the system. This manual gain adjustment increases the useful dynamic range of the system by about 20 dB.

At the equipment trailer, signals are bandpass filtered using a bank of analog filters. The low-pass component of the filter prevents aliasing while the high-pass component reduces the dominating low-frequency ambient noise. Although the analog filters are required for accurate digital representation of the signals, it is the subsequent digital filtering which ultimately affects the bandwidth and phase response of the system. Within the narrow frequency band of processed signals the magnitude response of the filters is essentially flat and the phase response is linear. The characteristics of the digital filters are described in Sec. II A.

The filtered analog signals are multiplexed using a high-speed, low noise solid-state switcher array and then digitized. The analog to digital converter has 12 bits of sampling resolution and a sampling rate of 8000 samples per second per channel was used. To ensure that signal level fluctuations did not cause clipping, peak signal levels were kept well below the maximum input level of the converter; peak digital signal levels were typically in the range of 6–10 significant bits.

Each single tone test signal was acquired for 10 min. The digitized data were stored on a hard disk drive and subsequently written to digital 8-mm tape for off-line storage. All digital signal processing, including narrow-band filtering, was done in the laboratory, after data collection.

II. SIGNAL PROCESSING

An overview of the digital signal processing is illustrated in Fig. 5. The energy (and information) in the received signals lies entirely within a narrow frequency band centered about the frequency of the source tone. For our experiments, this bandwidth is always less than 100 Hz; hence much of the 4000-Hz bandwidth of the acquired digital data contains only noise. Discarding the unnecessary frequency bands by applying a narrow-band filter improves the signal-to-noise ratio. Bandshifting the filtered signal so that the important

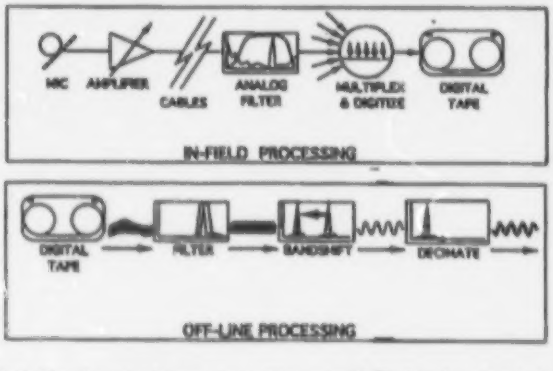

FIG. 5. Signal processing sequence. The processing of analog signals in the field and the subsequent off-line processing of digital data are depicted. The digitized data is narrow-band filtered, bandshifted, and decimated to improve the SNR and reduce the volume of data prior to calculating the spatial correlation.

frequency band is in the range 0–200 Hz, for example, *makes it possible to decimate* (subsample) the signal.[13] By ensuring no frequency components beyond 200 Hz remain after filtering and bandshifting, decimation can be done without aliasing effects by keeping only every 20th data sample. This greatly reduces the data volume and subsequent processing time.

Using the decimated signals, the correlation between complex time series data from pairs of microphones are computed. The complex correlation is calculated as the zero lag of the conventional cross-correlation function.[14] The magnitudes of the calculated correlation are plotted as a function of the separation of the corresponding sensor pairs to obtain correlation function curves. The shape of the correlation function curve indicates the coherence length of the signal at the array.

A. Filtering

The narrow-band filter improves the signal-to-noise ratio and prevents aliasing during decimation. The narrowest possible passband is desired but the bandwidth must be sufficient to span the frequency spreading of the signal caused by amplitude and phase fluctuations. The signal bandwidth is discussed in Sec. III A.

The Remez exchange algorithm[15] was used to design an equiripple finite impulse response filter of length 800 samples. The template for the design is the following idealized piecewise linear magnitude response function:

$$|H_{\text{ideal}}(\bar{f})| = \begin{cases} 1, & 0 \leqslant |\bar{f}-\overline{f_0}| < \dfrac{\kappa}{4} \ \text{(passband)}, \\ 2-\dfrac{4}{\kappa}(\bar{f}-\overline{f_0}), & \dfrac{\kappa}{4} < |\bar{f}-\overline{f_0}| < \dfrac{\kappa}{2} \ \text{(transition bands)}, \\ 0, & \dfrac{\kappa}{2} \leqslant |\bar{f}-\overline{f_0}| \ \text{(stopband)}. \end{cases} \tag{1}$$

In this ideal filter, $\bar{f}=f/f_s$ is the normalized frequency, where f_s is the sampling rate and f is the signal frequency in Hz. The (normalized) center frequency of the passband is $\overline{f_0}$, and the (normalized) bandwidth is $\kappa/2=1/80$. The center frequency is equal to the frequency of the source tone for the data being filtered. The filter is one sided because the bandshifting operation does not preserve the conjugate symmetry of the signal spectrum. Figure 6(a) and (b) shows the magnitude and phase response of the designed filter. The stopband signal attenuation is greater than 80 dB, the passband ripple is less than -80 dB, and the phase is extremely linear inside the passband. The filter is applied in the frequency domain using the overlap–add method.[13]

B. Bandshifting and decimation

A data sequence can be bandshifted (or heterodyned) in the frequency domain by shifting the discrete Fourier-transform coefficients in a cyclic manner. The bandshifted version of a discrete Fourier spectrum $X(k)$ is given by $X'(k)=X((k+\Delta k))$, where the double parentheses (()) indicate index evaluation modulo N, and N is the number of points in the discrete Fourier transform. The time series $x(n)$ and $x'(n)$ corresponding to the spectra X and X', respectively, are related by

$$x'(n)=x(n)e^{-j2\pi\Delta kn}. \tag{2}$$

Note that a real time series will generally become complex following bandshifting.

Applying the shift $\Delta k = [\overline{f_0} - (\kappa/2)]$ to the bandpass filtered data, based on Eq. (1), moves the nonzero portion of the spectrum left so that only zero-valued spectral components lie above the frequency κf_s. This ensures that decimation by $1/2\kappa$ can be performed without aliasing effects. The shift also positions the left edge of the left transition band of the filter at 0 Hz, thus eliminating any dc component.

Decimation of the bandshifted data is done in the time domain. The decimated sequence $x_d(n)$ is obtained from the bandshifted sequence $x'(n)$ as $x_d(n)=x'(n/2\kappa)$, for $0 \leqslant n < 2\kappa N$. The processed time series has a sampling frequency

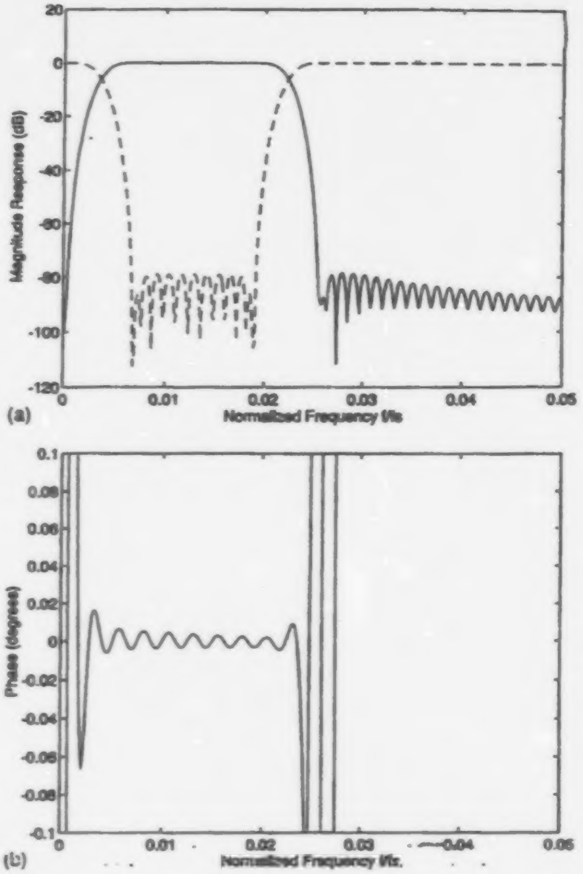

FIG. 6. Narrow-band filter description. The magnitude response (a) shows the stopband attenuation to exceed 80 dB (solid curve) and the passband ripple (dashed curve—unity minus the magnitude response) to be less than −80 dB. The phase response is plotted in (b), with time delay removed, showing negligible phase variations in the passband.

of $2\kappa f_s=400$ Hz and a bandshifted signal frequency of approximately $\kappa f_s/2=100$ Hz with a bandwidth of $\kappa f_s/2=100$ Hz.

The 1-kHz and 500-Hz test data were each filtered, bandshifted, and decimated as described above. The 100-Hz test data have a narrower bandwidth and so they were processed twice. The second iteration results in a sampling frequency of 20 Hz and a bandshifted signal frequency of approximately 5 Hz with a bandwidth of 5 Hz.

C. Complex correlation

Following decimation, the real part of the processed time series was saved in a file and the imaginary part was discarded. The real and imaginary parts of the time series are related by the Hilbert transform,[13] due to the one-sided bandpass filter. To compute the complex correlation, the complex time series was recovered again from the real data using the discrete Hilbert transform. This transform was implemented in the frequency domain by applying the transfer function H_{Hilb} to the N-point FFT of a frame of data, where $N=2048$:

$$H_{\text{Hilb}}(k)=\begin{cases}1, & k=0,N/2,\\ 2, & 1\leq k<N/2,\\ 0, & N/2<k<N.\end{cases} \tag{3}$$

Inaccuracies arise at the ends of each frame due to the lack of N-point periodicity in the time series. Accordingly, only the middle 75% of each frame was kept. The frames were appropriately phase shifted and overlapped to generate seamless complex time series data. Based on simulation tests performed using synthetic signals with randomly modulated phase, similar to the measured data, the rms phase errors introduced by this procedure are less than 0.1 rad, indicating a reasonably accurate reconstruction.

The complex correlation C_{ij} for a pair of sequences $x_i(n)$ and $x_j(n)$ (representing the signals from the ith and jth sensors, respectively) is defined as

$$C_{ij}=\frac{\langle x_i^* x_j\rangle}{(\langle|x_i|^2\rangle\langle|x_j|^2\rangle)^{1/2}}, \tag{4}$$

where $\langle\ \rangle$ indicates averaging over the entire data sequence, the asterisk indicates complex conjugation, and $|\ |$ indicates absolute value. The magnitude of C_{ij} is unaffected by constant phase and magnitude differences between the two sensors. Furthermore, the narrow-band filter eliminates any dc offset, so C_{ij} is equivalent to the zero-lag point of the well-known cross correlation for complex stochastic processes. The errors in the magnitude of the complex correlation due to phase estimation errors mentioned above are only 1%.

The correlation C_{ij} is similar to the mutual (or transverse) coherence function evaluated at the separation distance between sensors i and j, as commonly used in optics. The correlation is defined for a separation in any direction but only the directions perpendicular (transverse) or parallel (longitudinal) to the line joining the source and receiver are considered here. Other authors[7] have defined longitudinal correlation as the correlation between the sound field at (or near) the source and that at a point distant from the source. As defined here, longitudinal correlation is between two points at any ranges. Notice that, since the direction of propagation for sound scattered into a refractive shadow is not well determined, the longitudinal correlation is not strictly along the direction of propagation but, rather, it relates to the source–receiver geometry. Transverse correlation, as defined here, has the accepted interpretation. It is related to the phase and log amplitude structure functions D_s and D_χ by[7]

$$|C_{ij}|=e^{-1/2(D_\chi+D_s)}. \tag{5}$$

The magnitude of the correlation as a function of separation generally decreases monotonically, approaching an asymptotic value C_∞, which need not be zero. Indeed, if the signals at sensors i and j are each correlated with the source signal, then they must be correlated with each other to some degree; hence C_∞ will only approach zero as the sensor signals decorrelate from the source.

The coherence length ρ is defined as the separation at which the correlation has dropped to $(1-C_\infty)/e$.

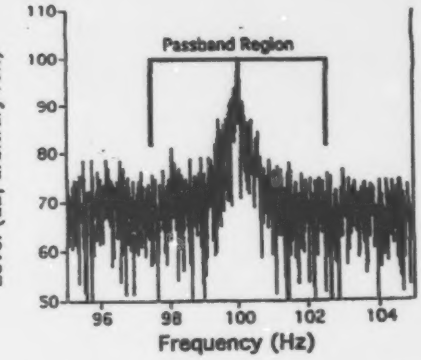

FIG. 7. Signal spectrum. A segment of the magnitude spectrum of the 100-Hz case-II test data. The passband of the narrow-band filter is indicated, showing that the bandwidth of the received test signal is passed by the filter. The bandwidths of other test data were similarly contained within the filter passband.

III. SIGNAL CHARACTERISTICS

In this section several characteristics of the signals received at the array are discussed. The signal bandwidth is important for the filter design, as mentioned in Sec. II A. The signal-to-noise ratio (SNR) is examined to assess the extent to which noise will affect the correlation estimates. The signal losses between the source and receiver, beyond those expected due to free-field spherical spreading and atmospheric absorption, are referred to here as *refractive losses*. These losses include the effects of diffraction and turbulent scattering and indicate the "depth" of the refractive shadow.

A. Signal bandwidth

Fluctuations in the phase and amplitude of the signal due to atmospheric turbulence result in an increase in the received signal bandwidth. Figure 7 shows the portion of a high-resolution spectrum corresponding to the frequencies within the passband of the narrow-band filter. The spectrum was obtained using a 2^{17}-point discrete Fourier transform (approximately 327 s) of a 100-Hz signal under moderate refraction conditions (case II). Notice that a passband of 5 Hz generously spans the signal bandwidth.

To ensure an accurate examination of the effects of the signal fluctuations it is important that the narrow-band filter applied to the data be designed so as not to omit any of the signal bandwidth. The narrow-band filter was designed so that the width of the signal spectrum, as measured at the level of the background noise, remains well within the filter passband for all cases. Observed signal bandwidths ranged from 0.5% to 4% of the signal frequency.

B. Signal-to-noise ratio

It was pointed out by Bass *et al.*[16] that noise can alter the asymptotic value of the structure function if the SNR is not high enough. Similarly, noise can alter the complex correlation. Let C_s, C_n, C_{sn}, be the complex correlation for the signal in the absence of noise, for the noise alone, and for the signal and noise combined, respectively. Assuming the signal and noise are independent but have the same total power at each microphone, it is easy to see from Eq. (4) that

$$C_{sn}=\frac{RC_s+C_n}{1+R}, \tag{6}$$

where R is the SNR as a linear ratio of signal and noise power.

The SNR of the processed data was estimated from the spectra. A clipped version of the spectrum was generated in which the prominent spectral peak corresponding to the signal was eliminated. The clipped spectrum, $X^c(k)=F_{\text{med}}\{X(k-k_0),X(k),X(k+k_0)\}$, was obtained by applying a median filter F_{med} to a split sampling $(\{k-k_0,k,k+k_0\})$ of the original spectrum X. The split width k_0 was chosen to be greater than the width of the signal peak. The total noise power was then estimated as $N=\Sigma|X^c(k)|^2$ and the total signal power was estimated as $S=\Sigma|X(k)|^2-N$, with k ranging over the passband of the filter. Since the signal bandwidth was generally much less than the passband width, end effects were neglected. The resulting estimates of the SNR are shown in Table I. The lowest estimated value is 8 dB ($R=2.5$), which could result in errors in the magnitude of the complex correlation as large as 30%. All other cases allow only much smaller errors in the correlation.

To determine the SPL of the received signal from the observed digital data levels, the sensitivity of the overall system at 1 kHz was measured *in situ* during the field measurements. Variations between channels were small (within ±2 dB). The system sensitivity at 500 and 100 Hz was determined by adjusting for the response of the analog filters at these frequencies. The SPL estimates of the signal and noise at the array are shown in Table I.

C. Signal attenuation

The source output sound-pressure levels (unweighted) at 1 m relative to 20 μPa are shown in Table I. They were measured as described in Sec. I D. At a range of 700 m, signal loss due to spherical spreading is 57 dB. Atmospheric absorption, based on typical absorption curves[17] and rounded to the nearest decibel, is estimated to be 3 dB for the 1-kHz signal, 2 dB for the 500-Hz signal, and 0 dB for the 100-Hz signal. The difference between the SPL observed at the array and the SPL expected at the array after accounting for spreading and absorption losses is the *refractive loss*. They are listed in Table I. Refractive losses in excess of 20 dB are not uncommon, so the values obtained here support the conclusion that a weak refractive shadow existed during the case-I tests and a moderate refractive shadow existed during the case-II tests. The estimated uncertainty in the signal level is ±3 dB.

IV. THE GF-PE

The Green's-function method for the parabolic equation (GF-PE) is used to calculate transverse and longitudinal correlations of the sound field. The GF-PE is a significant improvement to the Crank–Nicolson range step method (CN-PE)[18] because it provides greatly improved computational efficiency, greater clarity in physical meaning, and more efficiently accommodates finite ground impedance. A good summary of the GF-PE method is presented in various papers[5,10,18,19] but the assumptions inherent in the PE method receive only cursory discussion there. Although details of these assumptions can be found in the literature pertaining to other areas of application it is felt important to review the approximations inherent in the GF-PE here since the method has only recently been applied to sound propagation in the atmosphere above a finite impedance ground and is being used here, for the first time, to simulate correlations in a turbulent atmosphere. In the first subsection we provide an overview of the PE method leading to the GF-PE formulation. In the second subsection, we describe how the GF-PE method is implemented to calculate correlations and the parameters used for the simulation are specified.

A. Mathematical formulation

In cylindrical coordinates (r,φ,z), the Helmholtz equation has the form

$$\left(\frac{\partial^2}{\partial r^2}+\frac{1}{r}\frac{\partial}{\partial r}+k^2+\nabla_T^2\right)\phi=0, \tag{7}$$

where

$$\nabla_T^2=\frac{1}{r^2}\frac{\partial^2}{\partial\varphi^2}+\frac{\partial^2}{\partial z^2} \tag{8}$$

is the Laplacian for the transverse coordinates (φ,z) and $k^2(\mathbf{x})=\omega/c(\mathbf{x})$ is the spatially varying wave number. If k^2 is range independent, the first three terms form Bessel's differential equation. To take advantage of this, a constant reference wave number k_0 is defined, so that $k^2-k_0^2$ is small, and a solution is sought in the form

$$\phi(r,\varphi,z)=U(r,\varphi,z)H_0^{(1)}(k_0r), \tag{9}$$

where the Hankel function $H_0^{(1)}(k_0r)$ is the forward propagating solution to Bessel's equation. The factor U is expected to be a slowly varying function of r since most of the variation with r is accounted for by $H_0^{(1)}$. The residual variation is due to the small quantity $k^2(\mathbf{x})-k_0^2$; thus U describes the variations in the sound field due to refraction and turbulence.

Applying the Helmholtz equation to $\phi=UH_0^{(1)}$ and using the asymptotic approximation $\partial H_0^{(1)}/\partial r \sim -(i+1/2r)H_0^{(1)}$, for $r \gg 1$, the following equation for U is obtained:

$$\left(\frac{\partial^2}{\partial r^2}+2ik_0\frac{\partial}{\partial r}+k^2-k_0^2+\nabla_T^2\right)U=0. \tag{10}$$

The standard *parabolic equation* can be obtained from this far-field version of the Helmholtz equation by simply neglecting the first term; however, a better approximation to Eq. (10), and a better appreciation of the approximations involved, is obtained through the following development.

The second-order differential operator in Eq. (10) can be factored as

$$\left[\frac{\partial}{\partial r}+i(\sqrt{Q}+k_0)\right]\left[\frac{\partial}{\partial r}-i(\sqrt{Q}-k_0)\right]+i\sqrt{Q}\,\frac{\partial}{\partial r}-i\,\frac{\partial}{\partial r}\,\sqrt{Q}, \tag{11}$$

where

$$Q=k^2+\nabla_T^2, \tag{12}$$

and the last two terms are the operator commutator for $i\sqrt{Q}$ and $\partial/\partial r$.

In the parabolic method, the second factor in the first term of Eq. (11) is equated to zero to obtain the *one-way wave equation*

$$\left[\frac{\partial}{\partial r}-i(\sqrt{Q}-k_0)\right]U=0. \tag{13}$$

The solution of this simpler equation is taken to be an approximate solution to the entire equation. The method omits contributions from the first factor, which represents backscattering, and it ignores the operator commutator, which may be nonzero when the wave number k is range dependent. Since scattering in a turbulent atmosphere is strongly in the forward direction, neglecting backscattering may be justified. The approximation of omitting the operator commutator is not as clear since atmospheric turbulence leads to complicated range-dependent effects. Omission of the commutator is justified, however, with the assumption that k varies smoothly with range.

The parabolic equation method can generally be traced to the one-way wave equation and evaluation of the operator $\sqrt{Q}$. The equation allows a "marching" solution whereby the known solution at r is used to calculate the solution at $r+\delta r$ using an exponential propagator;

$$U(r+\delta r,\varphi,z)=e^{i\delta r(\sqrt{Q}-k_0)}U(r,\varphi,z). \tag{14}$$

The range step δr must be chosen to be sufficiently small that variations in k are small. The implementation of the propagator is greatly simplified by isolating the variations in k as a distinct factor. Defining $Q_0=Q-\delta k^2$, where $\delta k^2=k^2-k_0^2$, and using a first-order expansion for the square root gives

$$\sqrt{Q}=\sqrt{Q_0}+\delta k^2/2k_0. \tag{15}$$

As is shown in the Appendix of Ref. 5, for small range steps this results in the so-called *split step approximation*, for which the propagator has the form

$$U(r+\delta r,\varphi,z)=[e^{i\delta r\,\delta\bar{k}^2/2k_0}][e^{i\delta r(\sqrt{Q_0}-k_0)}]U(r,\varphi,z). \tag{16}$$

where $\delta\bar{k}^2$ is the average value of δk^2 at the two points (r,φ,z) and $(r+\delta r,\varphi,z)$. For smoothly varying k and small δr, $\delta\bar{k}^2$ and δk^2 are essentially the same. The split step approximation assumes the commutator of δk^2 and $\sqrt{Q_0}$ is small.

Equation (16) separates the exponent into range-dependent and range-independent parts. The range-dependent part is further separated into deterministic and stochastic parts, $k(r,\varphi,z)=k_d(z,\varphi)+\delta k_s(r,\varphi,z)$, where $k_d=\eta_d k_0$ is the deterministic (range-invariant) wave-number profile and $\delta k_s=\mu k_0$ is the stochastic component. Substituting into the operator expression of Eq. (16), and neglecting the small term μ^2, gives the propagator in the form

$$[e^{i\delta r\eta_d\mu k_0}][e^{i\delta r(k_d^2-k_0^2)/2k_0}][e^{i\delta r(\sqrt{Q_0}-k_0)}], \tag{17}$$

where the first factor is the stochastic component and the last two factors constitute the deterministic component.

For larger range steps, $\Delta r=N\delta r$, the above propagator can be applied repeatedly. If, as was assumed for Eq. (16), the commutator operators are ignored, then the exponential operators can be rearranged to obtain

$$U(r+\Delta r,\varphi,z)=\left[\prod_{n=1}^{N}e^{ik_0\delta r\,\eta_d\mu_n}\right][e^{i\Delta r(k_d^2-k_0^2)/2k_0}]$$
$$\times[e^{i\Delta r(\sqrt{Q_0}-k_0)}]U(r,\varphi,z), \tag{18}$$

where μ_n is the refractive index at range step n, i.e., at $r+n\,\delta r$. This form of the propagator allows large range steps and requires only that the index of refraction μ_n be integrated across the entire step. It will be useful to combine the first two factors in Eq. (18) into an operator S which accounts for the wave-number variations.

To apply Eq. (18) it is necessary to evaluate the operator $\sqrt{Q}$ and each implementation of the parabolic equation method is generally characterized by its particular choice of evaluation technique. The Green's-function method for the parabolic equation uses a spectral decomposition of the propagator, leading naturally to a Green's-function implementation which, besides being relatively easy to evaluate, can directly incorporate boundary conditions such as a finite ground impedance. Details of the spectral decomposition of $\sqrt{Q}$ are described in Ref. 10. The result is a three-term expression for the propagator. According to the formalism developed in Ref. 10, the first term is the direct wave, the second is the reflected wave, and the third is the surface wave. For the calculations considered here, this method is implemented with the assumption of azimuthal symmetry (no φ dependence); accordingly, $\nabla_T^2=\partial^2/\partial z^2$ and the φ dependence will henceforth be omitted from the notation:

$$\begin{aligned}U(r+\Delta r,z)&\\ =S\Bigg\{&\frac{1}{2\pi}\int_{-\infty}^{\infty}dk'\,Ae^{ik'z}\int_0^{\infty}dz'\,U(r,z')e^{-ik'z'}\\ &+\frac{1}{2\pi}\int_{-\infty}^{\infty}dk'\,RAe^{ik'z}\int_0^{\infty}dz'\,U(r,z')e^{+ik'z'}\\ &+B\int_0^{\infty}dz'\,e^{-i\beta z'}U(r,z')\Bigg\},\end{aligned}\tag{19}$$

where

$$S=e^{i\Delta r(k_d^2-k_0^2)/2k_0}\prod_{n=1}^{N}e^{ik_0\delta r\,\eta_d\mu_n},\tag{20}$$

$$A=e^{i\Delta r\sqrt{k_0^2-k'^2}},\tag{21}$$

$$R=\frac{(k'Z_g-k_0)}{(k_0Z_g+k_0)},\tag{22}$$

$$B=\frac{2ik_0}{Z_g}\,e^{ik_0z/Z_g}e^{i\Delta rk_0\sqrt{1-Z_g^{-2}}}.\tag{23}$$

In Eq. (19), S accounts for the variations in k, A arises from the Green's function, R is the plane-wave reflection coefficient at the ground, and Z_g is the normalized ground impedance. For an infinitely hard ground, as is assumed for the calculations in this study, the reflection coefficient R is unity and the third term vanishes.

The so-called phase screen[19] is contained in the factor S as $e^{i\Phi}$, where $\Phi=\Sigma k_0\delta r\,\eta_d\mu_n$, which is applied at each range step Δr. This phase screen is the only stochastic component in the formulation.

B. Implementation of the GF-PE

The GF-PE has been implemented as a computationally efficient code.[12] The integrals appearing in the first two terms of Eq. (19) are Fourier transforms which are implemented as fast Fourier transforms (FFT). The integral in the third term, however, is implemented as a discrete Fourier transform. Since the FFT implementation truncates the height variable z, the procedure requires an artificial absorption layer to prevent undesired reflections from the upper boundary. The absorption layer is defined between z_1 and $z_{\max}$ where $z_{\max}$ is the truncation height. Within the absorption layer, the imaginary part of the wave number is smoothly increased using

$$k_d(z)=k_d(z_1)+i\alpha\left(\frac{z-z_1}{z_{\max}-z_1}\right)^2,\quad z_1\leq z\leq z_{\max}.\tag{24}$$

For the simulation calculations, $\alpha=1\ \mathrm{m}^{-1}$ for all frequencies. The 100-Hz simulations used $z_{\max}=800$ m and $z_1=300$ m. For 500 and 1000 Hz, $z_{\max}=400$ m and $z_1=250$ m.

Since the parabolic equation method is a far-field method, the source must be propagated to some initial distance by another method before the GF-PE takes over. The usual approach, which was employed here, is to provide a Gaussian starting field of the form

$$U(r_0,z)=\sqrt{\sigma}\left\{e^{-(z-z_s)^2/\sigma^2}+\frac{Z_g-1}{Z_g+1}\,e^{-(z+z_s)^2/\sigma^2}\right\},\tag{25}$$

where z_s is the source height and $\sigma=2/k_0$.

The atmospheric model used in the GF-PE for this study is an upward refracting atmosphere with a two-dimensional (i.e., range r and height z) homogeneous isotropic Gaussian turbulence field. [The formulation of the GF-PE in Eq. (19) imposes azimuthal symmetry in the corresponding three-dimensional turbulence.] The index of refraction n is expressed as a range-independent deterministic part $\eta_d=k_d/k_0$ plus a fluctuating stochastic part μ, so that $n=\eta_d+\mu$ as in Eq. (17). The deterministic part of the index of refraction is generated by a logarithmic vertical sound-speed profile

$$\eta_d(z)=1-\frac{a}{c_0}\ln(z/0.006),\tag{26}$$

where z is the vertical height, a is the *refraction strength* parameter, and c_0 is the mean speed of sound (340 m/s). The value of $\eta_d(z)$ is held constant for $z<10$ cm.

The stochastic part of the sound-speed profile $\mu(\mathbf{r})$ is assumed to have a zero-mean Gaussian distribution. The variance μ_0^2 is the *turbulence strength* parameter. The random turbulence field has spatial correlation

$$\langle\mu(\mathbf{r}+\mathbf{s})\mu(\mathbf{r})\rangle=\mu_0^2e^{-|\mathbf{s}|^2/L^2},\tag{27}$$

where L is the *turbulence coherence length* parameter.

The wave-number power spectrum of the turbulence is defined as the (two-dimensional) Fourier transform of the correlation function of the turbulence field. The wave-number magnitude spectrum is the square root of the power spectrum. Each realization of the turbulence field was obtained by multiplying the wave-number magnitude spectrum by uniformly distributed random phase factors and taking the inverse Fourier transform. Thus the index of refraction fluctuations $\mu(\mathbf{r})$ for each realization were different in detail but had the same coherence length and root-mean-square amplitude.

There are three adjustable parameters in the atmospheric model, the turbulence strength $\mu_0^2=\langle\mu^2\rangle$, the turbulence coherence length L, and the refraction strength a. Since limited meteorological data were available during the acoustic measurements, exact values for these parameters could not be directly determined. Instead, parameter values were selected *ad hoc*, based on typical meteorological conditions for the region, to represent the sort of parameters expected during the measurements.

Two sets of atmospheric parameters are used. The first set corresponds to weak upward refraction and weak turbulence, with $a=0.5$ m/s and $\mu_0^2=2.0\times10^{-6}$. The second set corresponds to moderate upward refraction and moderate turbulence, with $a=2.0$ m/s and $\mu_0^2=8.0\times10^{-6}$. Both sets of parameters use a turbulence coherence length of $L=1.5$ m.

The GF-PE computes the complex sound field on a plane perpendicular to the ground, between the source and the receiver. The horizontal spacing (range step) of the computational grid for the GF-PE was 6.4 m in all cases. The vertical spacing, which varied with signal frequency, was 0.2, 0.05, and 0.05 m for 100, 500, and 1000 Hz, respec-

TABLE II. Correlation lengths. The correlation lengths (in meters) are determined from Figs. 8 and 9. Several longitudinal correlation lengths are smaller than the minimum sensor separation. The correlation length for case I, 100 Hz was indeterminate.

Signal (Hz)	Test case	Experiment		Simulation	
		trans.	long.	trans.	long.
1000	I	1	<7	1	35
	II	0.5	<7	1	13
500	I	4	40	3	45
	II	1	<7	2	20
100	I	>>15	>>300	>>15	>>300
	II	2	<7	3	50

tively. The source and receiver positions were modeled as being near the ground. The source height was 0.4, 0.3, and 0.3 m for 100, 500, and 1000 Hz, respectively, and the height of the array center z_0 was 0.0, 0.1, and 0.1 m for 100, 500, and 1000 Hz, respectively. (The source and receiver heights were adjusted to fit the vertical spacing resolution at each frequency.) The range from the source (i.e., the Gaussian starting field) to the array center x_0 was 704 m for all tests.

For computation of the spatial correlation, pairs of points were selected longitudinally and transversely, relative to the line joining the source and receiver, in a manner similar to the experimental measurements. Each longitudinal pair consisted of the point at the array center (x_0,z_0) and a point (x_0-x,z_0) at the same height as the array center but closer to the source. The transverse correlation is similarly computed using a point directly above the array center at (x_0,z_0+z). Notice that the simulated transverse correlation is vertical while the experimental transverse correlation is horizontal. It is assumed that the transverse horizontal and vertical spatial correlations are similar, based on earlier measurements.[2,20]

The correlation between two points in the complex sound field was calculated using Eq. (4) applied to 100 realizations of the GF-PE. For each realization a new random turbulence field was generated, with the same values for μ_0^2 and L, and used to obtain new values for the sound field at each point of the computation grid. It was observed that increasing the number of realizations made no significant difference in the results.

V. DISCUSSION OF RESULTS

In this section the spatial correlation curves obtained from the experimental and simulation data are compared. A summary of the transverse and longitudinal coherence lengths is provided in Table II.

A. General characteristics

The experimentally measured correlation data are shown as a function of sensor separation in a series of six graphs in Fig. 8. Data for transverse separation are displayed in the left set of graphs and data for longitudinal separation are displayed in the right set. The graphs at the top, middle, and bottom of the figure correspond to source frequencies of 1 kHz, 500 Hz, and 100 Hz, respectively. Each graph shows the correlation data from the case-I and case-II tests. Notice that the horizontal scale of the longitudinal coherence plots is different than that of the transverse coherence plots.

The simulation data are displayed in Fig. 9 with the same format and axis scales as the experimentally measured data. Detailed quantitative agreement between experiment and simulation is not to be expected since the parameters for the simulation were only inferred from general considerations. Indeed, the simulation data generally indicates a slightly higher correlation and longer coherence length. Nevertheless, good qualitative agreement is obtained and the simulation data successfully reveals many characteristics of the spatial correlation.

The correlation curves are generally smooth and monotonically decreasing to an asymptotic value; this is consistent with the typical shape of the structure function.[7] As predicted by theory, the asymptotic values of the transverse and longitudinal correlation should be equal. This is clearly seen in both the experimental and simulation data.

The case-I transverse and longitudinal correlations are consistently greater than the corresponding case-II correlations for both experiment and simulation. This indicates that stronger refraction conditions lead to reduced spatial coherence. Note in Table I that, although stronger refraction leads to somewhat reduced SNR, this alone does not account for the decreased correlation; rather, it is the increased significance of the effects of turbulence which reduces the spatial correlation.

The transverse coherence lengths are consistently and substantially less than the longitudinal coherence lengths, yet the longitudinal coherence lengths are much shorter than those observed for line-of-sight propagation. In fact, the observed longitudinal coherence lengths are shorter than were expected during the design of the array, resulting in a sensor geometry which provides inadequate resolution for the correlation curve at small separations.

B. Transverse correlation

For the measured data, the transverse correlation is determined along the ground by the microphone array, whereas, for the simulation, it is determined along a vertical line. Previous measurements suggest that this difference is not important[20] and the reasonably good agreement between experiment and simulation supports this.

A prominent feature of the transverse correlation curves for both the experimental and simulation data is the rapid decline at separations of only 1 or 2 m. This indicates that it will be difficult to effectively beamform in the transverse direction with an array of substantial length. For line-of-sight propagation through turbulence for long distances, theory indicates that the transverse coherence length is approximately equal to the coherence length of the turbulent medium itself. The observed coherence lengths are not inconsistent with this but there is a trend of greater coherence lengths for lower frequencies in both the experimental and simulation data. A similar trend was observed in the measurements of Daigle *et al.*[2]

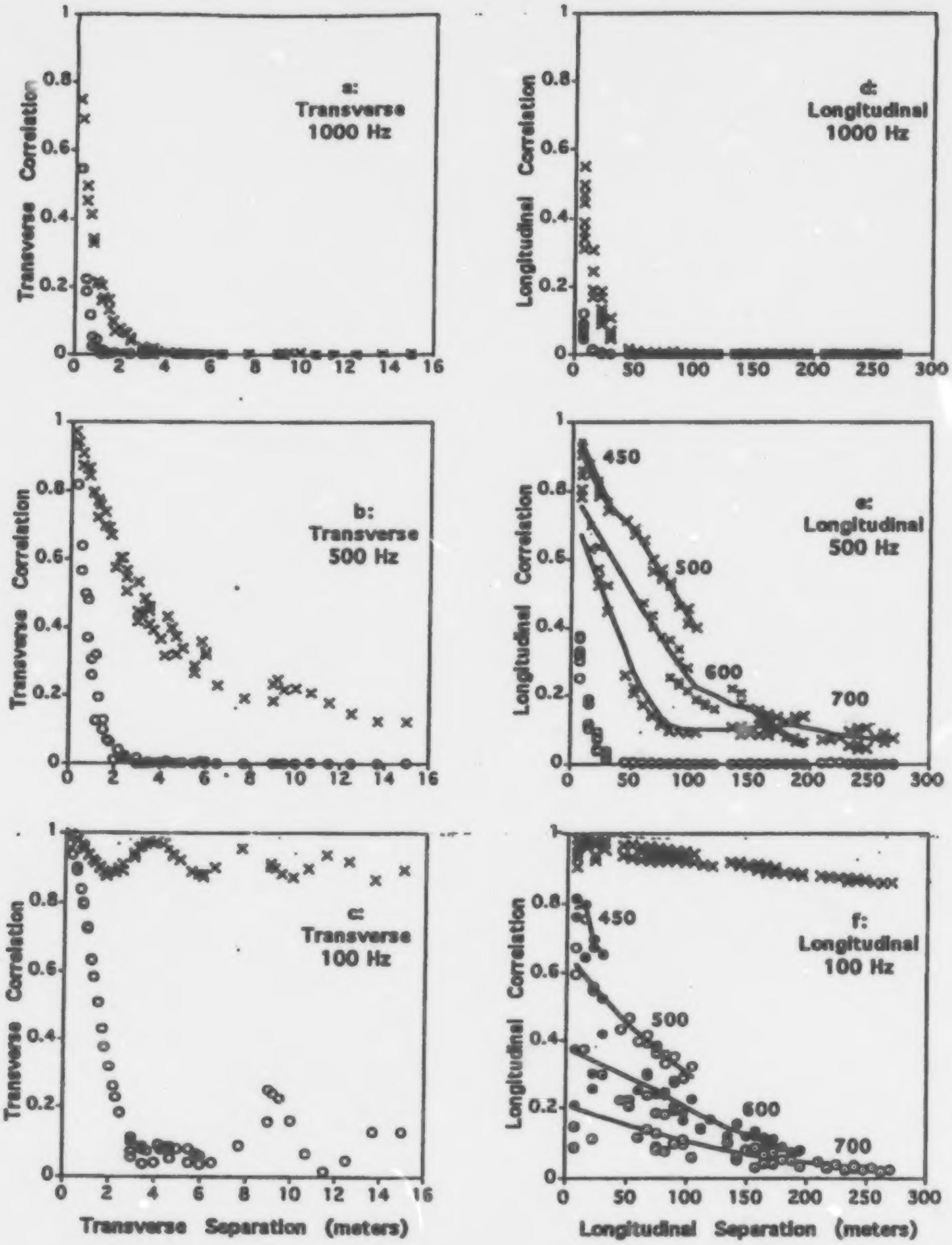

FIG. 8. Measured spatial correlation. Transverse correlation is shown on the left, longitudinal on the right. Correlation data for case-I tests (crosses ×) and case-II tests (circles ○) are shown for 1000 (top), 500 (middle), and 100 Hz (bottom). The horizontal scale of the longitudinal coherence plots is different than that of the transverse coherence plots. The smoothed curves in (e) and (f) are labeled with sensor ranges in meters, showing the range dependence in the correlation data. Data at different ranges are distinguished by various types of circles.

Distinct ripples are observed in the case-I experimental data at 100 Hz [Fig. 8(c)]. These ripples are due to coherent interference between the 100-Hz signal and the exhaust noise from the generator at the equipment trailer. The magnitude of the ripple is related to the SNR, as indicated in Eq. (6), and the spatial periodicity is related to the exhaust frequency and direction from the array. The hump in the corresponding case-II correlation curve at separations of about 10 m may be related to the same interfering source. The ripples in the correlation curves for the simulation data, on the other hand, are thought to be numerical artifacts.

C. Longitudinal correlation

The longitudinal coherence length, for both the experimental and simulation data, is dramatically less than is observed for line-of-sight propagation outside of a shadow, where longitudinal coherence lengths are much greater than

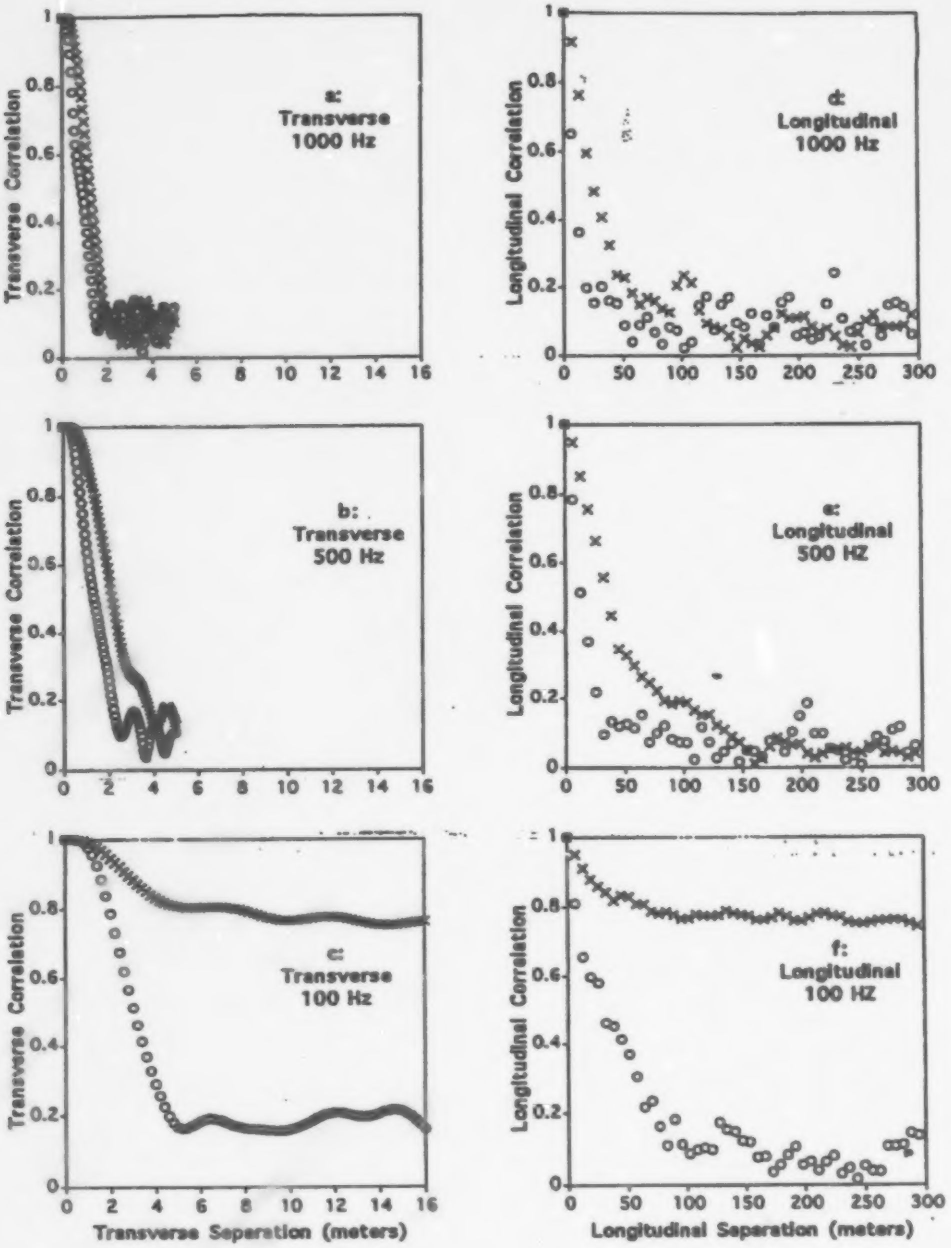

FIG. 9. Simulation spatial correlation. Correlation data from the simulated propagation model are displayed in the same format and scale as the measured correlation data of Fig. 8.

100 m. When not within a shadow, the performance of a beamforming array can generally be improved by using a geometry which has elements aligned along the anticipated direction of propagation (endfire array); however, with the longitudinal coherence length greatly reduced within a refractive shadow, this technique will be less effective. A severe constraint is thus imposed on the available coherent aperture of an array in an acoustic shadow.

The longitudinal coherence lengths for the case-II experimental data were generally less than the smallest sensor spacing of 7.5 m. This differs from the simulation data, for which the coherence lengths increase from about 20 to 50 m with decreasing frequency. The presence of ambient noise in the experimental data does not account for the difference since the SNR was sufficiently high to avoid a substantial bias in the correlation estimates. The difference may be due to the simple atmospheric model used in the simulation, which assumed a constant, range-independent vertical velocity profile, whereas in reality the profile fluctuates considerably with time and range (see Ref. 9, for example) thereby increasing the longitudinal variability in the sound field and reducing the longitudinal correlation.

D. Range dependence of correlation

The array geometry was chosen so that variations with range in the longitudinal correlation could be examined. Two of the test tones exhibited such an effect, the 500-Hz tone with weak refraction strength [case I, Fig. 8(e)] and the 100-Hz tone with moderate refraction strength [case II, Fig. 8(f)].

The striations observed in the experimental data (overlaid with smoothed curves) are not seen in the corresponding simulation data. This is because the experimental correlation curves are computed using *every* two-sensor combination in the longitudinal arm of the array, whereas, for the simulation, the correlation is only computed between the sensor at the array center and the other sensors. Since the longitudinal arm of the array (Fig. 3) consists of four widely spaced identical clusters of microphones, the experimental data has several sensor pairs with the same separation, whereas, for the simulation data, no two sensor pairs have the same separation. To clarify the range dependence in the longitudinal correlation, the experimental data is grouped, as seen in Fig. 8(e) and (f), to provide four fitted curves as follows.

We label the four microphone clusters 1–4 starting at the cluster closest to the source. For each cluster, a subset of the correlation data is selected by requiring that the first sensor in the correlation pair lie within the cluster and that the second sensor must be closer to the source than the first. Constructed in this way, the data subsets corresponding to clusters 1–4 have 6, 22, 38, and 54 members, respectively. Each curve in Fig. 8(e) and (f) is fitted to the correlation data of one of these subsets. The clusters which are closer to the source have fitted curves which have higher correlation than those further from the source. The vertically aligned points in other longitudinal correlation plots from the experimental data have the same ordering effect; sensor pairs closer to the source have greater correlation values than those further away.

To examine range dependence in the simulation, the longitudinal correlation was calculated as though the array center was at 500 m for the 500-Hz tone with weak refraction (case I). The correlation curve for this closer range is plotted with the corresponding curve for the array center at 700 m in Fig. 10. An increase in correlation at the shorter range is observed but the difference is not as great as is seen for the experimental data in Fig. 8(e).

The range dependence observed in the experimental data indicates that the coherence length decreases progressively within the shadow. At some distance, adequately deep within the shadow region, this loss of correlation is expected to reach a limiting value. Other longitudinal correlation curves, such as the 1-kHz curves in Fig. 8(d), show no range dependence, suggesting that a limiting value has been reached for those cases. For the 100-Hz signal [Fig. 8(f)] the range dependence is observed in the curve for stronger refraction yet the upper curve, corresponding to weaker refraction, shows very little range dependence. This suggests that the sound field at the array is governed by diffraction rather than by scattering for weak refraction at this frequency. This supposition is supported by the long transverse and longitudinal coherence length and the low refractive losses in Table I.

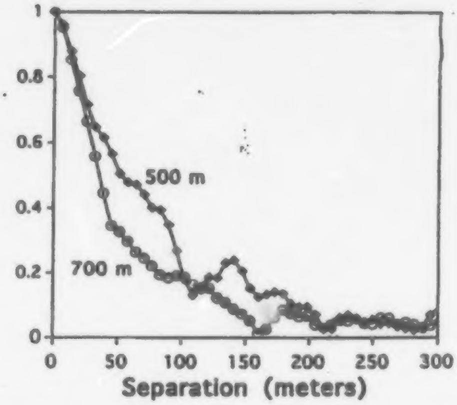

FIG. 10. Range dependence in the simulation correlation. The longitudinal correlation data for ranges of 700 (open circles O) and 500 m (solid diamonds ◆) show only minor differences. The experimental data shows a greater variation in longitudinal correlation with range.

E. Implications for beamforming

An example of the effects of turbulence on beamforming can be seen in Fig. 11, where two beam response patterns are shown for data integrated over about 10 s. A frequency domain implementation of the conventional delay and sum beamformer was used. The solid upper curve shows a strong, stable beam response pattern. It is obtained from the transverse arm of the array with the case-I 100-Hz signal, which has a coherence length much longer than the (transverse) array length. The signal arrives broadside to the transverse array and is integrated with excellent coherence. The dashed lower curve shows no discernible peak in the beam response. It is obtained with the case-II 1000-Hz signal, which has a coherence length much shorter than the array size. Since the SNRs for these two signals are essentially the same, it is the differing spatial coherence lengths which are responsible for the different beamformer results.

An array deployed for endfire beamforming operation

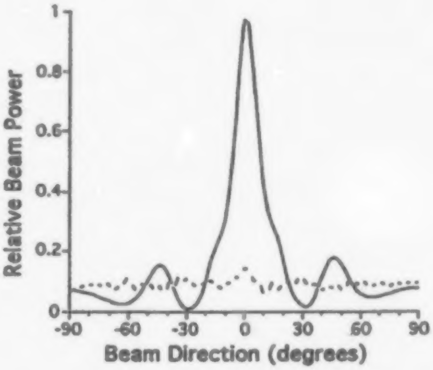

FIG. 11. Beamformer response. The significance of spatial coherence length is illustrated by comparing the beamformer output for two examples of real signals, one of which is coherent across the array (solid line) and the other not coherent (dashed line). The SNR of the two signals are nearly the same, yet the latter produces no distinct peak. In each case, coherent integration was performed for a time interval of 10 s.

outside the shadow region can take advantage of the longer longitudinal coherence length. Within the shadow this may not be possible since the longitudinal coherence length is much shorter. The measurements and simulations indicate that at 100 Hz, coherence may extend no further than two wavelengths. An array with such a small aperture will have limited array gain or bearing accuracy.

The lack of correlation is based on long-term averages. For beamforming, where short-term averages are more important, the low coherence associated with a deep shadow may not be sustained and opportunities may arise for intermittent signal coherence across a larger array. Furthermore, fluctuations in the arrival angle of the signal wavefront may result in reduced (long-term) correlation at the array. In this case, a large aperture array may succeed at coherent detection, but wide variations in estimates of the direction of arrival may be experienced.

VI. SUMMARY

Experimental and simulation results on spatial coherence near the ground within an acoustic shadow region have been brought together to provide new insights into the sound field coherence. A large array of 24 microphones was deployed at an airfield to obtain the measured data and the fast PE with an homogeneous isotropic Gaussian turbulence model was used to simulate sound propagation through an upward refracting atmosphere. The agreement between the measured and simulated correlation demonstrates the ability of the propagation model to predict higher-order statistics of the sound field.

It was found that stronger refraction conditions lead to reduced spatial coherence. The transverse and longitudinal coherence lengths were observed to be less than 0.5 and 7 m, respectively. The transverse coherence length was consistently less than the longitudinal coherence length, yet the longitudinal coherence lengths were much shorter than those expected outside of a shadow region. The coherence length tends to increase with decreasing frequency and to decrease with greater distance into the shadow region. The short coherence length within a shadow region may limit the useful aperture of beamforming arrays; however, there may be opportunity for intermittent signal coherence across a larger array, allowing for short-term coherent integration of signals.

ACKNOWLEDGMENTS

Part of the work reported here was carried out while the second author worked in the Institute for Microstructural Sciences under a secondment agreement between the National Research Council of Canada and the University of Mississippi. Financial support was provided in part by Defense Research Establishment Valcartier. The cooperation of the Gatineau Gliding Club and the use of their property for field trials is gratefully acknowledged.

[1] For example, estimated rms fluctuations in the phase of a 4-kHz signal propagating 35 km (Cobb Seamount experiment, 1976) is 1.6 cycles. Similar estimates for a 406-Hz signal propagating 1250 km from Eleuthera to Bermuda have been estimated to be about four cycles.

[2] G. A. Daigle, T. F. W. Embleton, and J. E. Piercy, "Propagation of sound in the presence of gradients and turbulence near the ground," J. Acoust. Soc. Am. 79, 613–627 (1986).

[3] J. M. Noble, "The effect of large-scale atmospheric inhomogeneities on acoustic propagation," J. Acoust. Soc. Am. 92, 1040–1046 (1992).

[4] J. E. Piercy, T. F. W. Embleton, and L. C. Sutherland, "Review of noise propagation in the atmosphere," J. Acoust. Soc. Am. 61, 1403–1418, 1977.

[5] K. E. Gilbert, R. Raspet, and X. Di, "Calculation of turbulence effects in an upward-refracting atmosphere," J. Acoust. Soc. Am. 87, 2428–2437 (1990).

[6] V. I. Tatarskii, *The Effects of the Turbulent Atmosphere on Wave Propagation* (Keter, Jerusalem, 1971).

[7] G. A. Daigle, J. E. Piercy, and T. F. W. Embleton, "Line-of-sight propagation through atmospheric turbulence near the ground," J. Acoust. Soc. Am. 74, 1505–1513 (1983).

[8] W. E. McBride, H. E. Bass, R. Raspet, and K. E. Gilbert, "Scattering of sound by atmospheric turbulence: A numerical simulation above a complex impedance boundary," J. Acoust. Soc. Am. 90, 3314–3325 (1991).

[9] A. L'Espérance, Y. Gabillet, and H. Schroeder, "Outdoor sound propagation: Experimental study of atmospheric turbulence and simulation with FFP," Proceedings of InterNoise '92, Toronto, Canada, July 1992, pp. 139–142.

[10] K. E. Gilbert and X. Di, "A fast Green's function method for one-way sound propagation in the atmosphere," J. Acoust. Soc. Am. 94, 2343–2352 (1993).

[11] K. Attenborough, S. Teherzadeh, H. E. Bass, X. Di, R. Raspet, G. R. Becker, A. Güdesen, A. Chrestman, G. A. Daigle, A. L'Espérance, Y. Gabillet, K. E. Gilbert, Y. L. Li, M. J. White, P. Naz, J. M. Noble, and H. A. J. M. van Hoof, "Benchmark cases for outdoor sound propagation models," J. Acoust. Soc. Am. 97, 173–191 (1995).

[12] The software implementation of the GF-PE method is referred to as the "fast-PE."

[13] A. V. Oppenheim and R. W. Schafer, *Digital Signal Processing* (Prentice-Hall, Englewood Cliffs, NJ, 1975).

[14] A. Papoulis, *Random Variables and Stochastic Processes* (McGraw-Hill, New York, 1965).

[15] *IEEE Programs for Digital Signal Processing II*, IEEE (Wiley, New York, 1979), Algorithm 5.1.

[16] H. E. Bass, L. N. Bolen, R. Raspet, W. McBride, and J. Noble, "Acoustic propagation through a turbulent atmosphere: Experimental characterization," J. Acoust. Soc. Am. 90, 3307–3313 (1991).

[17] H. E. Bass, L. C. Sutherland, A. J. Zuckerwar, D. T. Blackstock and D. M. Hester, "Atmospheric absorption of sound: Further developments," J. Acoust. Soc. Am. 97, 680–683 (1995).

[18] K. E. Gilbert and M. J. White, "Application of the parabolic equation to sound propagation in a refracting atmosphere," J. Acoust. Soc. Am. 85, 630–637 (1989).

[19] X. Di and K. E. Gilbert, "The effect of turbulence and irregular terrain on outdoor sound propagation," in *Proceedings of the Sixth International Symposium on Long Range Sound Propagation*, Ottawa, Canada, 12–14 June 1994, pp. 315–328.

[20] G. A. Daigle, J. E. Piercy, and T. F. W. Embleton, "Incoherence in the propagation of sound near the ground," J. Acoust. Soc. Am. 70, S54 (1981).

BLASTO - Airblast Prediction Program for IBM-PC Compatible Computers.
Version 9 for MS-DOS 5 or above. Copyright 1994, JWR, Inc.

By Jack W. Reed March 7, 1994

GENERAL INSTRUCTIONS

INTRODUCTION:

If you began with the BEGIN A: C: batch command, as directed by the introductory letter, all needed files have been copied from the diskette into your hard-disk in a sub-directory named BLASTO. This should be your current working directory, as well as your directory whenever you operate or exit any BLASTO calculations.

After practicing BLASTO, and becoming familiar with its operation, you may eventually wish to "clean up" the provided data file examples, so they contain only your own localized operational data. It is suggested that these provided archive data files be preserved by renaming them, possibly to *.SAV files, or to a storage subdirectory. Later, if you should encounter difficulties, these tested source data files may be restored and run, to see whether your trouble has developed in BLASTO or in your local data files. These archive data files are named TESTS.DAT, RAOBS.DAT, SHOTPTS.DAT, TARGETS.DAT, TERRAIN.DAT, and PANES.DAT.

ARCHIVE FILES:

File TESTS.DAT archives explosion parameters for every previously analyzed event. It allows recall of information from earlier calculations; they can be re-run as is, or depending on needs, run in different weather conditions, at different shot points, etc.

File RAOBS.DAT is an archive collection of previously entered upper air radiosonde balloon (raob) weather reports. This file can easily become too large for rapid memory or editor access. Each raob report is typically 3000 bytes, so one should consider house-cleaning when about 20 raobs are listed. Thus, a periodic transfer of weather data should be made to an inactive hard disk storage subdirectory, a tape backup, or to diskettes.

File SHOTPTS.DAT is a collection of all shot point locations which have been entered, and TARGETS.DAT is a collection of all neighboring targets for which analyses have been made. Since individual entries in these archives are relatively short records, and because only a limited number of shot points are likely and the test site neighborhoods are probably a fixed few, these files should rarely need size reduction. Nevertheless, in keeping with safe computer practice, ALL changing data files ought to be backed up to diskettes or tape rather frequently.

File PANES.DAT contains census populations for neighboring communities. As loaded, it describes the communities around White Sands Missile Range, NM. Approximation may be made that there are about 19 window panes per capita, based on a survey of San Antonio, Texas, following the Medina explosion in 1964. Other surveys have shown about 4.7 persons per single-family detached house, while many residents may live in multi-family structures or mobile homes. Nevertheless, this factor may be useful for checking numbers of houses read from aerial photographs of target communities. A current GDM (Glass Damage Model) assumes 40 "typical" panes per single-family detached dwelling, based on records from Las Vegas, Nevada, for 1988. This "typical" pane is defined as 2-ft x 2-ft SS (single-strength) glass. In San Antonio and Las Vegas, if each actual pane had been replaced by this "typical" pane, the same total numbers would have been broken by the Medina and PEPCON accidental explosions.

Finally, file TERRAIN.DAT contains terrain cross-section elevation data, for determining airblast blocking by mountainous or hilly orography. Separate tabulation is needed for each shot point on a test site, but once entered, the terrain should remain unchanged and this file should require little maintenance. For test sites in flat country, this file is not used.

OPERATION:

Enter the batch command, BLAST, to review six operating modes that have been set up. This returns control to the working directory where selection is made for one of the following commands:

1. Normal Mode Command: BLASTO

This assumes that all archive data files contain the necessary test, shot point, neighboring target, panes, terrain, and weather information to be used in calculations. If BLASTO is run with no weather data input, it produces an isotropic (non-directional) prediction of overpressures versus distance for a Standard explosion and five categorical weather (sound velocity - height) structures. In this case, no shot point, target, or terrain data are needed. It is used in planning to determine whether damaging overpressures can reach various target ranges, under some weather conditions. If damage is possible, then some weather information will be required to predict whether some neighborhood may be adversely affected by an event under those weather conditions.

Detailed instructions for interactive responses during a BLASTO run are provided separately in "INSTRUCTIONS FOR BLASTO INTERACTIVE OPERATIONS". If any new archive input information is needed, it may be entered either with DOS EDIT or MS-DOS Batch commands shown in following modes.

If appropriate weather data are available, either in RAOBS.DAT or RAOB.DAT (make certain the correct coded entry, 2 or 3, is in the TESTS.DAT record), weather-dependent calculations will be made.

Results will be written to a file BLASTO.DAT which may be examined by using the DOS-EDIT (type: EDIT BLASTO.DAT). If results need saving, enter REN(ame) BLASTO.DAT "newname", otherwise they will be overwritten by the next BLASTO calculation.

2. New Test Entry Command: NTEST

This command produces a "blank form" for entering appropriate test information. A permanent model resides in file FORMA. It is initiated by entering this batch-processing command (type: NTEST), which brings a copy, FORMB, up on the screen using DOS EDIT. Form blanks have been filled merely to serve as a format guide for data entries. The editor keyboard should be in OVERTYPE mode (block cursor) rather than INSERT mode (underline cursor); this may be changed by triggering the <Insert> key. When entries have been made, exit to the working directory.

3. New Upper-Air Weather Command: NEWX

Upper air weather reports are assumed to arrive by communications modem in some common code form. They should be copied into file WXCODE.INP for translation by the reformatting program WXCODE.EXE into WXCODE.OUT tabulations needed by BLASTO. This output is next appended to data archive RAOBS.DAT. Then BLASTO may be initiated, and further interactions will take place in normal mode. Make certain that the appropriate TESTS.DAT record shows a value of R=3 under the raob weather entry, and that the corresponding date/time is available for entry if it is requested by WXCODE.

When a weather listing is obtained by phone or on paper, including a series of records (lines) of height, temperature, wind direction, and wind speed, it is most conveniently over-typed into file RAOB.DAT (note singular RAOB), using DOS EDIT. When data entry is complete, be sure that its access is opened by entering R=2 in the appropriate TESTS.DAT raob entry. Then BLASTO is started and run in normal mode.

4. New Ground Zero Entry: NEWGZ

This command copies archive file SHOTPTS.DAT to a temporary file, XY, and oopens it with the DOS EDITor. A new GZ name and site, with appropriate coordinates, is typed at the bottom of the file, preserving the format shown by other entries. On completion, exit the DOS EDITor to the working directory.

5. New Neighborhood or Targets Entry Command: NEWTGT

This command also DOS EDITs a copy, XY, of archive file TARGETS.DAT. New target names and sites, with appropriate coordinates, are typed at the bottom of the file, preserving the format of other entries. Then DOS EDIT is exited to the working directory.

6. New Terrain Data Entry Command: NTERA

This command copies a permanent blank model FORMC to FORMD and DOS EDITs new data in the provided blanks. On completion, DOS EDIT is exited to the working directory, and file FORMD is appended to TERRAIN.DAT where it can be accessed by BLASTO. Then FORMD is erased, and control is returned to the working directory, where BLASTO may be started and run in the normal mode.

JWR, Inc.
5301 Central Ave. NE
Suite 220
Albuquerque, NM 87108
(505) 265-6550

Date : March 10, 1994
To : BLASTO Users
Subject : BLASTO Version 9

Dear Colleagues:

Here is my long-promised BLASTO update, Version 9 for DOS-5 and above. New capabilities are provided for:

- Underwater bursts, similar to existing underground bursts.
- 1992 WMO raob weather code changes with the added 925-mb mandatory level and possible omitted high altitude wind groups.
- Window damage probabilities at targets, dependent on incident overpressure.
- Automatic mode option for simply updating raob weather in a count-down.

The sole incompatibility with Version 8 is that two character spaces must be added to each entry in TESTS.DAT, following DOB units entry. This allows an entry of G for underground or W for underwater explosions. Even if you do not contemplate using such buried sources, these spaces must be added so that following data on each record line are in new, correct format. A TEST.UW file is included for appending to your existing TESTS.DAT file, with a single record that shows this shift.

Examples are provided in file PANES.DAT to show the entry format for window counts, housing counts, or census populations, whichever is available. Locations must be the same as ones listed in TARGETS.DAT if they are to be used. File PROBP.DAT provides a table of "typical" window pane break probability versus incident overpressure. This pane is 2 ft x 2 ft (0.3716 m^2) SS (single-strength) glass. If every pane in San Antonio (1963) and Las Vegas (1988) had been replaced by a "typical" pane, the same total number would have been broken. In other words, actual broken panes were weighted for their areas, thicknesses, types, and breakage probabilities, to produce an averaged exposure. Derived from the Medina Incident, this GDM (Glass Damage Model) worked very well for PEPCON analyses.

Old batch files, NTST.BAT, NT.BAT, NEWGZ.BAT, GZ.BAT, NTGT.BAT, TG.BAT, NTERA.BAT, and TR.BAT, for entering new test, GZ, target, and terrain data, should be replaced by new commands NTST.BAT, NEWGZ.BAT, NTGT.BAT, AND NTERA.BAT. DOS-EDIT is used in these new batch commands, and it exits to the originating batch command. This is unlike the old Ace Editor, which exited to the directory and required a second batch command to install a modified file.

Updated instructions are provided in the new *.TXT files.

I am sure that you will use at least some of these new features.

Sincerely,

Jack W. Reed

JACK W. REED
Certified Consulting Meteorologist

BLASTO - Airblast Prediction Program for IBM-PC Compatible Computers.

Copyright, 1994, JWR, Inc.

By Jack W. Reed March 7, 1994

INSTRUCTIONS FOR BLASTO INTERACTIVE OPERATIONS

BLASTO begins by displaying the current date/time followed by an entry of test data for automatic re-entry if desired, from file TAUTO.DAT. The default response is Y(es), assuming that only weather input is to be up-dated or changed. In this event, the next message would ask for the new raob.

```
BLASTO ANALYSIS DATE:  3/7/94, TIME: 1346 MDT

BLASTO CALCULATIONS FOR WEATHER-DEPENDENT
    EXPLOSION AIR BLAST PREDICTIONS

1-KG HE SURFACE  AUTOMATIC MODE:  Y(ES)=DEFAULT  N(O)
```

If new test parameters are to be used, enter N(o). Then a list of available tests will be displayed, including all explosion or test names which have been entered into an archive file, TESTS.DAT. They can be recalled and used either unchanged or with altered parameters.

```
    1 MINOR SCALE              4 DISTANT IMAGE            7 1-KG HE SURFACE
    2 MISTY PICTURE            5 MINOR UNCLE              8 1-LB HE SURFACE
    3 MIZERS GOLD              6 1-KT NE DNA STD
```

If listed here, type desired test number and <Enter>; otherwise, enter a zero to get the next page of test info, if available. If a desired test or explosion name is not found in this list, its description must be entered, by editing TESTS.DAT or using the NTEST command. EXIT from BLASTO for this purpose, or any other, can be ordered at any time - by keying <Control><C> simultaneously.

When a test number has been entered, a two-line, coded description of this event will be displayed, and the first line will be presented for change - if needed - following its format model.

```
MISTY PICTURE            PHETS GZ                     5 14 87 1000 MDT  1503. 1
  4685.000 4 3     .00 3     .00 3      .0 3  851.40 3  19.0 2 3 1 1

NAMENAMENAMENAMENAMENAMELOCLOCLOCLOCLOCLOCLOCLOCMM/DD/YY TTTT ZZZ HHHHH. U
MISTY PICTURE            PHETS GZ                     5 14 87 1000 MDT  1503. 1

DOES THIS LINE NEED CHANGING? Y(ES) OR N(O)=DEFAULT.
```

A Y(es)<Enter> response will open a line for entry of any changed values immediately below the old values. Name, location, month, day, year, time, and time zone entries are evident from the format line. HHHHH. U represents elevation above sea level in coded units, U. We suggest that a small copy of the table of various and acceptable BLASTO units be posted for easy reference. The value U=1 indicates that the stated elevation is in meters, U=2 indicates kilometers, etc. N(o)<Enter> or default <Enter> response will bring up the second line of test information for similar correction or change.

```
WWWWWW.WWW N XHHHHH.HH U DDD.DD U G AAAAA.A U PPPP.PP U TTT.T U R M Z
  4685.000 4 3     .00 3     .00 3 G       .0 3  851.40 3  19.0 2 3 1 1

 DOES THIS LINE NEED CHANGING? Y(ES) OR N(O)=DEFAULT.
```

Changed Note

A Y(es)<Enter> response will again open a line for any changed values immediately below the old values. This format line shows yield, W, in N weight units of X explosives (either nuclear, TNT, or ANFO); height-of-burst, H, in length units, U; depth-of-burst, D, in length units, U; DOB media G-ground or W-water; and for distributed charges, such as overburdened HEST explosive sheets, etc., the area, A, of the sheet in U units of length. Ambient air pressure, if known, is P, in pressure units, U. If pressure is not known, P=1.0 instructs BLASTO to use the U.S.Standard pressure-altitude tables at elevation H. The temperature entry, T, in U units, is optional and not yet used by BLASTO; it will be used if BLASTO is later modified to calculate shock time-of-arrival. The next coded entry, R, indicates whether or not an upper-air radiosonde observation (raob) is available for weather-dependent directional predictions. No weather data is shown by 1, 3 tells BLASTO that the upper air report is in the archive file RAOBS.DAT, and 2 says that a new raob has been typed into file RAOB.DAT.

Entry M, allows selection between 1 for the AFWL-75 explosion model or 2 for the DNA-81 explosion model. Finally, if Z=1, terrain blocking will be assumed where hills or mountains rise above the thickness of a calculated weather effects channel. Otherwise, a blank assumes a flat plane, perfect reflector at GZ elevation for propagation predictions.

A N(o)<Enter> or default <Enter> response to the previous question, or completion of changes, raises a query of whether currently entered info should become the new Automatic Mode entry. Here the default is Y(es), assuming that you will want to re-run this case with changed weather. If not, enter N(o), and existing test info in TAUTO.DAT will be preserved.

The question asks whether the later Defense Nuclear Agency 1-kt Standard explosion model (1981) or the earlier Air Force Weapons Laboratory 1-kt Standard explosion model (1975) shown in the ANSI Standard S2.20-1983 should be used. Generally, the later model is recommended and used as the BLASTO default selection, but for comparison with the ANSI curves or earlier test analyses, the AFWL-75 model is also made available to BLASTO. Any entry will override the M value in TESTS.DAT.

```
USE DNA-81 EXPLOSION MODEL?
TYPE Y(ES)=DEFAULT, OR N(O)
```

Any interactive response that is unacceptable, caused by typographical error or misunderstanding, will generate a request for a corrected response.

Next, the availability of upper air weather information is considered. In the second line of the selected TESTS.DAT, R=3 generates the following list of archived radiosonde reports in file RAOBS.DAT. This is also the point of entry when the Automatic Mode is selected at the beginning.

```
 1 MINOR UNCLE ZER   6/10/93    TIME: 1509 UTC
 2 MIN-UNC TROPOSP   6/10/93    TIME: 1509 UTC
  ................
6   MISTY PICTURE  05/14/87    TIME: 1011 MDT
```

If the desired raob is in this list, enter its number; otherwise, enter zero for further listings if available in file RAOBS.DAT.

```
YOU HAVE SELECTED RAOB NUMBER          2
```

If there are no specified shot point and target locations for the event, yet there was an applicable weather report, BLASTO will calculate predictions for each direction, around the clock, at 30-deg azimuth increments. Then the answer to the following question would be 2; there is no default value.

```
ARE TEST AND NEIGHBORHOOD COORDINATES AVAILABLE?
1 = YES, 2 = NO, 3 = ?, 4 = ONE DIRECTION ONLY,
5 = A DIRECTION, DISTANCE, & UNITS CODE
```

For one-time-only evaluation (input not archived), responses of 4 or 5 allow, respectively, calculations for one specified azimuth, or one target at a given azimuth and distance.

An answer of 3 would start a search through archive files SHOTPTS.DAT and TARGETS.DAT to determine whether there were location entries corresponding to the LOC(ation) entry selection from TESTS.DAT. A response of 1, yes, would immediately display named data from SHOTPTS.DAT as follows:

```
  1 WHITE SANDS            M-U GZ
  2 WHITE SANDS            M-P GZ
  3 WSMR                   GZ

IS THE SHOT POINT IN THIS LIST? 1=YES, NO=2(CONTINUES LIST)

ENTER DESIRED SITE NUMBER.
```

On entry of a site number, the site record is displayed for change or correction as needed, maintaining the format as shown. Coordinates may be in global longitude-latitude (xxx-deg, xx-min, xx.xxxx-sec) shown by units code 7, in decimal degrees with units code 8.

```
ENTER ANY CORRECTIONS UNDER PROVIDED VALUES.
  WHITE SANDS             PHETS GZ              1062826.4280 W 333716.0188 N 7
```

Alternatively, local coordinate units specified by length unit codes 1-6 may be used as shown in the following line. In this case, be sure that the same local coordinate system zero reference point is also used for targets.

```
   MODEL                   E                    -15.0         -15.0      2
```

A choice is next allowed for the set of directions which will be analyzed:

```
            SELECT     1: 30-DEG INCREMENTED DIRECTIONS ONLY,
                       2: INCREMENTED & TARGET DIRECTIONS, OR
                       3: TARGETED DIRECTIONS ONLY.
```

If the choice is 2 or 3, to make target direction analyses, archive file TARGETS.DAT is reviewed and a listing is presented of those targets connected with the test site entry (LOC) in TESTS.DAT, as follows:

```
                                                    LOCAL GRID
      TEST SITE        TARGET                     X              Y
   -----------------------------------------------------------------------
    1 WHITE SANDS      MDR/4                  -43.5428       69.9425
    2 WHITE SANDS      MCDONALD RANCH         -42.5056       72.4571
      ................
   15 WHITE SANDS      GRANTS                -166.5840      238.6981

    HOW MANY TARGETS SHOULD BE ADDED? DEFAULT=0
```

A non-zero response will stop BLASTO, and return to the working directory. Then, typing command NEWTGT <Enter> will bring up the existing target list to edit or amend the file TARGETS.DAT.

When the target table is completed, there is an opportunity given to enter an up-dated surface weather report of wind and temperature at a revised date/time.

```
IS A SURFACE WEATHER OBSERVATION UPDATE AVAILABLE?  Y(ES) OR N(O)=DEFAULT:
```

Ordinarily, upper air radiosonde ascensions are only made twice daily, at internationally uniform times of 0000 UTC (Universal Time Coordinate, formerly called Z-time or GMT-Greenwich Mean Time) and 1200 UTC. Since these are early morning and early evening hours in the United States, surface temperatures and winds will not usually be representative of midday test conditions. Consequently, an opportunity has been provided in BLASTO to enter updated surface temperature and wind values, by interactive response to BLASTO query. Updated conditions are only used for the immediate weather-dependent propagation calculation; they do not change the original radiosonde report in RAOBS.DAT. They will, however, be recorded in final output tables. Official hourly reports from the National Weather Service may be used as well as local field measurements. Even predicted values may be used, which can be derived from local diurnal wind roses and temperature curves or from local forecasters.

Since the sun only heats the ground surface (air is practically transparent to solar radiation) where air warming is accomplished by conduction and convection, upper air conditions are little changed during a diurnal (daily) cycle. Only the "boundary layer" is modified, with effects often limited to roughly 500-m height. Consequently, an updated surface temperature and wind observation is generally adequate for midday corrections to blast prediction. Upper conditions do not need updating unless strong mountain-valley wind details are critical for avoiding blast nuisance. In those cases, pilot balloon winds may be required during a test count-down. Otherwise, for ordinary operations, BLASTO automatically uses the surface temperature entry, assumes an adiabatic lapse rate with altitude (for turbulent mixing), and adjusts upper raob temperatures accordingly.

If the answer to the above question is 1 (Yes) the entry is requested as in the following dialogue, shown with some typical responses:

```
ENTER DATE TIME OF OBSERVATION - MO/DY/YR TIME UTC:
12/13/91 1500 UTC <Enter>
ENTER NEW TEMPERATURE, INCLUDING DECIMAL POINT -
TTT.T U,  U= C OR F
17.3 C <Enter>
 ENTRY ERROR, TRY AGAIN
 17.3 C <Enter>
ENTER NEW WIND OBSERVATION, NO DECIMALS -
DIR/SP
332/14 <Enter>
```

This will cause the surface level raob report to be changed along with all the weather-dependent refraction effects on airblast propagation. NOTE: Surface weather updates DO NOT change the RAOBS.DAT file entry, so they must be re-entered each time you want to run with updated surface values.

Finally, a choice is offered for output units in sound velocity versus height tables. Ordinarily, only metric unit tables would be prepared, but in case the customer wants it, or the blast predictor gets a better feel from the situation expressed in ft/sec sound velocities at altitudes in feet, an output alternative or addition is allowed.

```
SHOULD DIRECTED SOUND VELOCITY TABLES BE PRINTED IN SI METRIC UNITS?
IF O.K., TYPE Y(ES)=DEFAULT, OTHERWISE TYPE E(NGLISH) OR B(OTH),
FOR OUTPUT UNITS.
```

After about a minute, more or less depending on PC speed, the program will be finished with the message:

```
Stop - Program terminated.
```

Control will be returned to the working directory and tabulations of results will reside in file BLASTO.DAT. A hard copy may be produced by the command PRINTOUT, or it can be inspected on the screen with DOS EDIT(or). Remember to REN(ame) BLASTO.DAT "newname", where "newname" is the file named as you wish to save it. Otherwise, results will be lost, over-written by the next BLASTO calculation.

****

IF YOU HAVE TROUBLE RUNNING BLASTO, GIVE ME A CALL.

Jack W. Reed, (505) 265-6550 Phone (505) 255-2946 FAX

BLASTO - Airblast Prediction Program for IBM-PC Compatible Computers.
Version 9 for MS-DOS 5 or above. Copyright 1994, JWR, Inc.

By Jack W. Reed March 9, 1994

WELCOME TO BLASTO

You have received this BLASTO program on either: one 3.5" diskette or two 5.25" diskettes, in low density configuration with no file compression. BLASTO requires about 500 Kb hard disk space to install and run. Everything is provided to run this program which, we hope, is sufficiently user-friendly for even novice PC users. It assumes only that you know an explosion weight-yield and its height above (or under) ground or water. For slightly greater accuracy, you may also want to know the ambient air pressure or the elevation above sea level. It will produce a table of distance versus overpressure coordinates for the explosion burst under six categories of weather conditions.

If you were not previously aware of it, weather conditions of winds and temperatures, both at the surface and aloft, can distort airblast wave propagation and cause a tremendous range of results at intermediate to long ranges from a given explosion yield. If you have the necessary weather information, BLASTO uses it to make weather-dependent overpressure-distance tables for various directions, with consideration of actual temperatures and wind vectors.

If you know the shot point and have a list of vulnerable neighboring targets (communities, buildings, houses, etc.), BLASTO will also make spot weather-dependent predictions for each of them. If you can also estimate the number of windows at some (or each) targets, BLASTO will calculate breakage probability per "typical" pane, dependent on incident overpressure, and an expected number for broken panes. If there is a range of hills extending above the airblast weather-ducting layer at a particular time, BLASTO will partially shadow targets at greater distances.

BLASTO will not produce times of shock arrival nor wave shapes (pressure-time signatures). It will not take any explosive other than nuclear, TNT, or ANFO; other explosives must be stated as TNT equivalents. Also, BLASTO is not reliable (except for nuclear explosions) at very high overpressures, above about 200 psi (1.4 MPa). Finally, BLASTO does not do Windows(C) or graphics. Those must be provided by the user, if needed. At JWR, Inc., we use an RPlot(C) graphics utility to produce overpressure-distance or sound velocity-height curves from BLASTO output tabulations.

To start using BLASTO, you must load the diskette files into your PC hard disk. We will assume that you call your hard disk drive "C:", and that you will place the diskette in a floppy disk drive called "A:". If you use other names for these drives, please substitute as necessary. BLASTO installation will create a directory named, you guessed it, BLASTO. It is suggested that you start in your root directory, C:\, but if you wish to hide BLASTO from your colleagues, you may wish to start in some other directory or drive. To load, place the diskette in the appropriate slot and type A: <Enter>. This should bring up the prompt A:\, to which you respond by typing:

```
BEGIN A: C: <Enter>
```

This batch command will create a BLASTO directory, move into it, and copy all files from the disk in drive A: into the BLASTO directory of drive C:. You are now ready to run BLASTO. First, we suggest that you print a hardcopy of file INSTRN.TXT, "Instructions for BLASTO Interactive Operations", and have it handy. Input data files are provided with examples that contain real weather, explosion, ground zero, target, and terrain data, for you to practice with and become familiar with BLASTO features. Then type BLASTO<Enter> and go for it. After this introductory session, we suggest that you hardcopy file README.TXT, "General Instructions". This should explain necessary steps for custom preparation of your particular, local problem.

If BLASTO will not load to your machine with these instructions, one of two things is wrong. The diskette was damaged in transit (it was carefully checked before shipping), or your machine is not set up to accept it. Try to load BLASTO on your neighbor's different make/model/setup PC; if it fails again, shipping damage is likely. Otherwise, check your setup indicators.

If problems ever arise, or if you just need coaching through some area, call me at my office (505) 265-6550, or at my home (505) 255-9991. My firm purpose is to make you an expert airblast predictor, capable of handling the problems that may arise at your facility. Then I can get to work and write some overdue reports; maybe even retire.

JWR, Inc.
5301 Central Ave. NE
Suite 220
Albuquerque, NM 87108
(505) 265-6550

Date : March 10, 1994
To : BLASTO Users
Subject : BLASTO Version 9

Dear Colleagues:

The enclosure announces BLASTO Version 9 for DOS-5 and above. New capabilities are provided for:

- Underwater bursts, similar to existing underground bursts.
- 1992 WMO raob weather code changes with the added 925-mb mandatory level and possible omitted high altitude wind groups.
- Window damage probabilities at targets, dependent on incident overpressure, along with expectations for broken panes.
- Automatic mode option for simply updating raob weather in a count-down.

I have not been vigorously following-up on how you are doing with BLASTO. Thus I am not sure whether you are still in the business, but assuming that your are, let me know and I will send this new version. A check for $10 would be appreciated, to cover costs of preparation and mailing, but DO NOT instigate $100 worth of paperwork on it. I'm still an outraged taxpayer.

If there are any new faces that you know of who could use this program, I would appreciate a referral.

I am almost certain that you can use at least some of these new features.

Sincerely,

Jack W. Reed

JACK W. REED
Certified Consulting Meteorologist

JWR, Inc.
5301 Central Ave. NE
Suite 220
Albuquerque, NM 87108
(505) 265-6550

ANNOUNCING BLASTO VERSION 9 (for DOS 5 or higher)
Weather-Dependent Airblast Predictions
(Copyright 1994 JWR, Inc.)
March 9, 1994

In common with other major and important projects, we are a couple years late with this promised, new and improved version of BLASTO. No excuses, just alibis. Keeping up with PC technology has taken far more time than ever was anticipated. In the good old days of computing, we only had to overhaul our codes every 3-5 years when major changes were made to mainframes or storage systems. Today, it seems that every month or so a new "essential" upgraded gadget or program facility hits the street. Then, when received, they invariably take a month or two to figure out how to install and get them working. We have so far managed to blow away our hard-disk boot in such a fashion that combined Microsoft and Norton tech services cannot fix. We sincerely hope that BLASTO instructions are not so hard to decrypt as typical commercial products.

So what is NEW with BLASTO? Several things. Underwater bursts can now be accommodated very similarly to underground explosions. An airblast attenuation model, based on U.S.Navy HYDRA Project tests at San Clemente, California, in 1961, is used. Everything published since then seems to be in agreement.

Recent analyses of damage claims from the PEPCON explosion, Henderson, Nevada, 1988, showed excellent agreement with the window damage patterns found after the Medina Incident, San Antonio, Texas, 1963. So, a log-normal probability relationship to predicted incident overpressure has been incorporated into BLASTO. With estimates of pane populations, based on Census Bureau populations, from housing counts from aerial photographs, or from actual window surveys, an expected number of broken panes can be calculated for each target, dependent on predicted incident overpressure. Hazard and injury from blast-broken glass must still rely on apocryphal reports and hand-waving correlations.

Finally, in result of field experiences at DNA Projects DISTANT IMAGE in 1991 and MINOR UNCLE in 1993, at White Sands, an automated alternative start-up procedure has been incorporated into BLASTO Version 9. When event parameters have been established, BLASTO can be run with only updated weather reports as they arrive during an event countdown.

Modifications also were required in the WXCODE component, which decodes number groups in radiosonde upper-air weather reports. The WMO (World Meteorological Organization) in 1992 added a mandatory level for reporting at 925-mb pressure, to accommodate air pollution forecasters concerned with low altitude details. Also, a minor rule change allows omitting wind code groups when direction tracking on a balloon has been lost, but temperature and pressure signals are still being received. These have caused the only real problems that have been encountered by the several agencies using BLASTO in real-time field tests.

As in Version 8 (1991), BLASTO produces explosion overpressure-distance tables, with or without input upper-air weather data. Required event inputs are explosion yield (weight) for nuclear, TNT (HE), or ANFO (ammonium nitrate-fuel oil) explosives. Other explosives must be converted to TNT equivalents. Correction is made for burst pressure-altitude, from either ground elevation, barometric reading, or Standard Atmosphere tables. Height-of-burst (HOB) effects are considered, when appropriate. Depth-of-burst (DOB) effects are also addressed, for either underground or underwater bursts. Sheets of confined explosives under ground may also be evaluated.

Weather-dependent propagations are calculated when upper-air measurements are provided, either in tabulations or phone-linked, coded weather reports. When shot point and target locations are specified, in either global, polar, or grid coordinates, wind vector influences are calculated for each target direction. If no targets were specified, directional predictions may still be made at 30°-incremented azimuths.

Finally, in rough terrain, where hills or mountains may block propagation of blast waves ducted by shallow atmospheric structures, appropriate barrier shadows are applied. This is unnecessary in flat country, but in many remote and mountainous test sites, an input tabulation of barrier heights and distances versus azimuth is provided.

Calculations are made in metric units, but in- and out-puts may be in American/Liberian units (England went metric), to accomodate those few remaining die-hard engineers. Eight units for length, six for yield and ambient pressure, five for wind speed, and three for temperature are allowed. Furlongs per fortnight are still unacceptable.

Also swimming against the flow, BLASTO is not available in a Windows version, nor does it incorporate graphics output. We regularly use RPLOT to graph overpressure-distance and sound velocity vs height curves from data in BLASTO output tables. We were never satisfied with graphs by Tandy DeskMate, Excell, or Quattro-Pro, but Harvard Graphics works fine for a price. So, you are on your own for graphics.

Finally, since we never liked to brief with plot-plan isobar patterns, BLASTO does not provide a separate airblast isobar coordinate output. Trouble comes with caustics or focused airblast, which does not have smooth, intelligible contours. We prefer to wave a red flag at test directors when caustics are indicated, because foci are not predictable for either distance or amplification except with log-normal statistical distribution functions. Advise on the odds and let decision-makers earn their pay.

In summary, you need BLASTO to easily and quickly provide:

* PLANNING PREDICTIONS: Input explosion yield, material, HOB or DOB, and air pressure or elevation produces overpressure vs distance and distance vs overpressure tables for Standard (calm, homogeneous atmosphere) propagations and for five categories of weather conditions: weak and strong inversions of sound velocity vs height, weak and strong gradients, and for focusing caused by dog-leg velocity-height structures. A map check will show which locations may be subjected to disturbance under some weather conditions. A session with a local meteorologist can establish how often troublesome temperature inversions or wind directions might occur. Some planned events might cause no trouble under any weather condition. Others could never be fired without flooding the switchboard with complaints. In between, an infinity of cases would require some degree of weather-watch and BLASTO for quick analyses of updated weather observations.

* OPERATIONAL PREDICTIONS: With shot point and potential target locations along with surface and upper air weather reports entered, BLASTO will calculate weather-dependent overpressures at each target. Rough terrain can be included that could block propagations from low altitude inversion airblast ducting. By adding target info - window or house counts, or census populations - overpressure-dependent window breakage probabilities and an expectation for total broken panes can be calculated by BLASTO. Can your project afford 1, 10, 100, or 1000 broken windows, economically or politically, in your neighborhood?

* POST-ANALYSES OF TESTS: Assume that a weather-dependent BLASTO forecast showed acceptable conditions. But there were complaints or claims of damage. A review of BLASTO output, directed sound velocities vs height, will show whether some small upper wind change could have caused airblast enhancement in the complainants direction. Weather is not constant, and forecasters have been known to err. On the other hand, some people can complain about anything, particularly if they hope to collect for their window broken by the latest wind storm.

* POST-ANALYSES OF ACCIDENTAL EXPLOSIONS: Most places in the United States have some record of surface weather conditions. Upper-air observations are made twice-daily at nearly 200 stations and conditions above the atmospheric boundary layer can be interpolated with reasonable accuracy. Explosion location will be known but actual explosive yield is rarely known. Several yield assumptions may be made for BLASTO to run with estimated-weather dependence. Window damage probabilities can then be compared with actual damage reports to converge on the needed yield. Final BLASTO calculation, with estimated weather and estimated yield, would also show whether individual damage claims were justified. After all, a claimed foundation crack, with no broken windows for blocks around, would hardly qualify for reimbursement.

If you still need convincing, get a BLASTO Trial Version and see how easy it is to run and how well its output provides the answers you need. This version does not contain many of the features described above, and it only runs with a short selection of sources and weather data, but we believe it provides a fair sampling of BLASTO capability.

JWR, Inc.
5301 Central Ave. NE
Suite 220
Albuquerque, NM 87108
(505) 265-6550

Program BLASTO 9.0

FOR WEATHER-DEPENDENT EXPLOSION AIRBLAST PROPAGATION PREDICTIONS.

Copyright 1994, JWR, Inc., Albuquerque, New Mexico

PRICE LIST (Effective 3/9/94)

If you have never used BLASTO, nor seen it work in demonstration, a trial version is available at only $10, for shipping and handling. If you find that BLASTO has what you need and you subsequently purchase it, that $10 will apply toward your purchase.

BLASTO is furnished on either 5.25" or 3.5" normal density diskettes, uncompressed, for an IBM-compatible computer with an MS-DOS-5 or higher operating system, a 640-kbyte RAM and 500-kb available hard disk memory. If you have only DOS-3, BLASTO will be provided with a full-screen Ace Editor for changing inputs through batch commands.

BLASTO may be copied for installation on another on-site PC, as required - for example - by forward area support; it may not be copied for use at other test sites or installations, such as ordnance disposal depots, etc. Loading and operating instructions are included.

Price, inclusive of taxes and delivery by regular airmail $1000.00

Updates thru 1995, as released, postpaid; each: $10.00

We do not provide 24-hour hotline service but, if you have problems with starting or running BLASTO, I will give them my personal attention, on my office phone (505) 265-6550 or at home (505) 255-9991.

Custom installation, demonstration, or tutoring may be arranged at $800 per day plus necessary travel expenses (at government approved rates), for a minimum of two days outside Albuquerque, or a minimum of one day in Albuquerque, with a rebate of $500.00 on the initial program purchase. Custom installation might include:

- Program loading and check-out with localized inputs.
- Review and consultation on local nuisance problems.
- Consideration of local air-mass and wind climatology.
- Recommendations for weather support that adequately addresses a specific problem situation.
- Background tutorial lectures on atmospheric airblast propagation and effects.
- Classroom instruction in operating BLASTO (user-furnished PC and projection facilities.)

In a worst-case scenario, a climatological assessment similar to one performed for large DNA explosion tests at White Sands [Sandia Report SAND86-1346, August 1986] would take a couple months effort, plus costs for copying five or ten years of radiosonde reports from National Climate Data Center archives in Asheville NC.

On the other hand, a two-day site visit should allow time to install and check out BLASTO, tutor hands-on operations by local staff, brief program managers on the airblast problem and what to expect from BLASTO, and review local climatological influences. If local electronic weather reports come in formats other than those translated by the included WXCODE program, a copy must be provided at least two weeks in advance of a visit, so that alternate decoding can be compiled.

BLASTO 9.0 includes weather-dependent window breakage estimates for single-family dwellings in a "typical" community (based on San Antonio, Texas, and Las Vegas, Nevada examples). If your potential targets seriously differ in architecture or composition, I will try to advise on normalizing them to a typical exposure.

Send me your requirements, or give me a call to discuss them, and I will provide a prompt proposal and cost estimate.

Sincerely,

Jack W. Reed
Certified Consulting Meteorologist

SOME BLASTO COMPONENTS

INPUT – GLASS DAMAGE MODEL

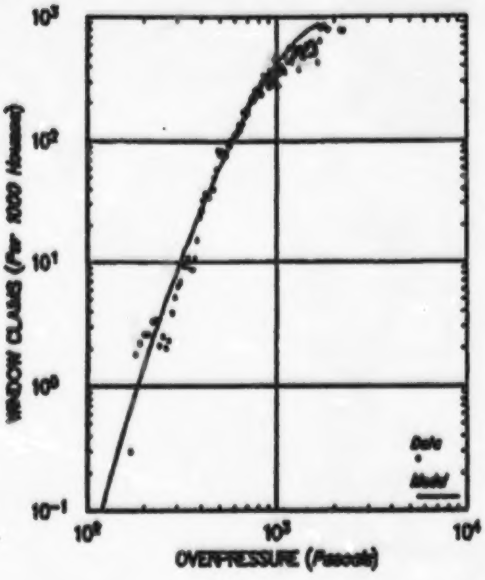

OUTPUT – OVERPRESSURE VS DISTANCE, SURFACE BURSTS

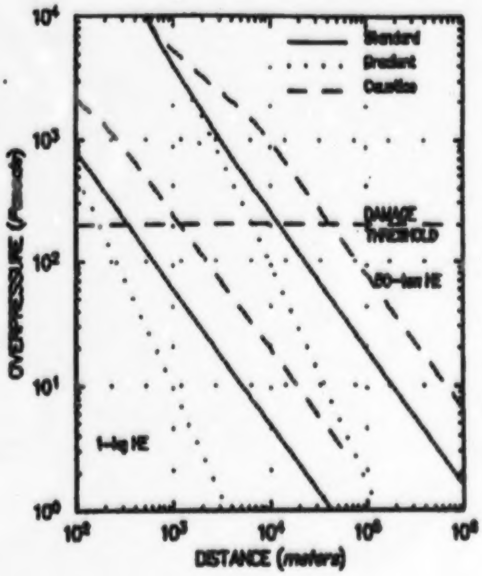

OUTPUT – SOUND VELOCITY VS ALTITUDE

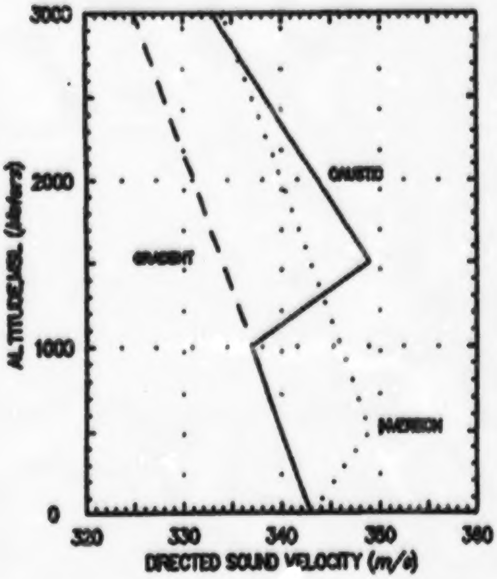

The Glass Damage Model (GDM) used by BLASTO shows good agreement with damage claims at the PEPCON (1988) AP Plant explosion.

Overpressure curves for extreme weather categories show 1-kg HE events may break windows to 1.2-km range. Fifty-ton shots could send damage to 40-km; inside 6-km damage could be expected under the best (inversion) of conditions.

Sound Velocity curves show altitude levels of blast ducting potentials from upper air temperatures and winds. All three curves could occur at once - in three different directions.

RECEIVED APR 2 2 1994

JWR, Inc.
5301 Central Ave. NE
Suite 220
Albuquerque, NM 87108
(505) 265-6550

Date : April 19, 1994

To : Combustion Dynamics Ltd.
132 4th Ave. SE #203
Medicine Hat, Alberta
T1A 8B5 CANADA

Subject : BLASTO Version 9.

Dear Colleagues:

Enclosed is the updated Version 9 of BLASTO for weather-dependent airblast predictions. We appreciate your continuing interest in this program.

You probably should install it in a separate drive or subdirectory, separated from your currently operating BLASTO Version 8 until you become familiar with its new features. You probably do not want it to overwrite many of your already installed *.DAT files. The new DIRECTRY file shows (by date) which files have been added or updated for Version 9. It might be even be easier if you copy your old BLASTO directory files into a newly created and named directory, and load V.9 into the BLASTO directory with the UPDATE.BAT (Batch) command. Then, when you are ready to go to work, append your old *.DAT files to the ones provided by Version 9. Unneeded lines can then be edited out.

There is one essential format change to your old TESTS.DAT file to be made to accommodate this new version. Two spaces must be entered after the Depth-of-Burst Units entry (for entering G or W to distinguish between underground and underwater bursts). For all tests these spaces must be in place to give proper format to the remaining entries on that record line.

If you are using the terrain barrier feature of BLASTO, you may be interested to know that I recently analyzed some 10-ton & 20-ton HE results from some tests at Alvdalen, Sweden, in 1989, in relatively rough terrain, and the barrier attenuation worked reasonably well. A change was suggested, however, that rather than making a discontinuous cut to Standard propagation at the terrain peak (with BLASTO), the subsequent overpressure-distance curve should decay with the square of distance. I found this relationship during large nuclear megaton-class tests at Christmas Island in 1962, then forgot it until my report was recently declassified. More details on weather and terrain from the Alvdalen tests are needed (which I expect to eventually get) before I again update BLASTO.

I would appreciate seeing some of your BLASTO applications, and hearing any comments you might have for further improvement.

Sincerely,

Jack W. Reed

JACK W. REED
Certified Consulting Meteorologist

JWR, Inc.
5301 Central Ave. NE
Suite 220
Albuquerque, NM 87108
(505) 265-6550

Date : August 15, 1995

To : BLASTO Users

Subject : Errors in Output Target Predictions Table.

Like Intel we are capable of error in spite of many checks. Fortunately, the problem just discovered is not devastating, affecting only calculations where "BOTH" incremental and target direction prediction outputs are requested. This creates garbage. We apparently confused some indexing when we added this bottom-line target predictions table to BLASTO.DAT output. The immediate fix is to refuse requests for "BOTH" incremental and target directions in the enclosed disk Version 9.1. They may be calculated by separate BLASTO runs with no troubles. You will find that "Selection #2" has been deleted from BLASTO capability until a fix is determined.

A couple other glitches in this final output table have also been fixed, along with some slight changes. When the trouble with "BOTH" is corrected we will send a new executable file to each user without charge. Our thanks go to Roy McCrory, Defense Nuclear Agency Field Command for discovering this problem. We either had or did not have targets in our many BLASTO applications, so we missed this error.

Two recently added output files are now produced, V(Z)FIG and RAYDAT. These lists are in formats needed by RPLOT Scientific Graphics (by Rsoft Inc., NYC) to quickly produce directed sound velocity versus height curves and crude ray paths. RPLOT requires entries in X,Y graph coordinates in that order, unlike most spread-sheet graphics programs. The ray path calculation program is under development, with quite a ways to go yet. The sound velocity grapher works well, and takes only a few minutes to produce figures, once a graph template is created.

What else is new here? Work for the Norwegian Defense Construction Service with Arnfinn Jenssen, is continuing toward its goal of determining airblast attenuation by terrain barriers and evergreen forests. And the Explosive Safety Board and Army Corps of Engineers - Huntsville are supporting a full review and reporting of airblast damage claims from the 1988 PEPCON disaster at Henderson, Nevada. Eventually, BLASTO can be extended beyond window breakage for single-family residences, to cover other types of structures and damage, as expressed in 1988 $U.S.

Thanks in advance for your understanding and patience in installing the enclosed and corrected BLASTO program.

Sincerely,

Jack W. Reed

JACK W. REED
Certified Consulting Meteorologist

26-28 August 1982, Norfolk, Virginia

BLAST PREDICTIONS FOR COYOTE CANYON EXPLOSIONS

Jack W. Reed
Ground Motion & Seismic Division 7111
Sandia National Laboratories
Albuquerque, NM 87185

INTRODUCTION

Tests of small explosions of up to 7.5 tons (6.8 Mg) of TNT have frequently been conducted on Kirtland Air Force Base with only occasional nuisance damage to, or complaints from, the neighboring community of Albuquerque. Provisions were made for weather checks, including observations, forecasts, and acoustic propagation calculations, to determine whether or not a planned event could be tested as well as estimates of the delays needed to await suitable propagation weather.

We have developed a set of yield limits that may be fired without seriously disturbing our neighbors (located as shown in Figure 1) and without any check on weather conditions (assuming unlikely strong propagations). Operations are conducted at two primary firing sites, located in Coyote Canyon, the 200 km^2 test field that extends 10 km south from Kirtland AFB - East, (formerly named Sandia Base). In addition, limits have been produced for keeping below the threshold of damage, as well as the threshold for general audibility. All such thresholds have been based on extensive experience, including recent results of USAF- and NASA-supported airblast propagation tests at Cape Canaveral, Florida, where detailed meteorological data acquisition systems were available [1]. Finally, an up-to-date blast

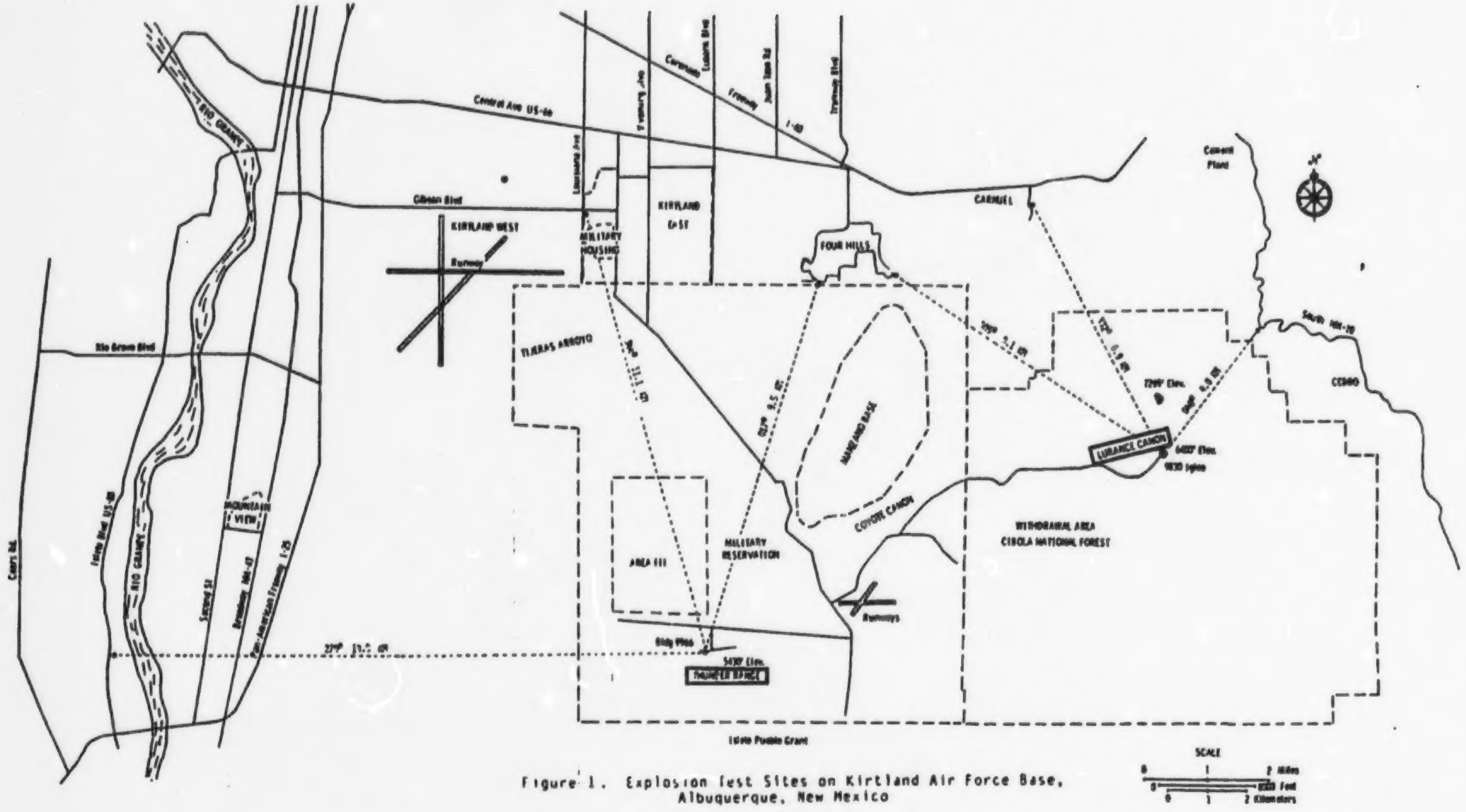
Central Ave US-66
Coronado Freeway I-40
Louisiana Blvd
Wyoming Blvd
Juan Tabo Rd
Tramway Blvd
Eubank Blvd
Gibson Blvd
KIRTLAND WEST
Runway
MILITARY HOUSING
KIRTLAND EAST
FOUR HILLS
CARNUEL
Cement Plant
N
South NM-14
CEDRO
TIJERAS ARROYO
MANZANO BASE
COYOTE CANON
MILITARY RESERVATION
AREA III
Runways
Bldg 9966
5430' Elev.
THUNDER RANGE
Isleta Pueblo Grant
LURANCE CANON
6420' Elev.
1830 hphm
7299' Elev.
WITHDRAWAL AREA
CIBOLA NATIONAL FOREST
Rio Grande Blvd
Isleta Blvd US-85
RIO GRANDE
Second St
Broadway NM-47
Pan-American Freeway I-25
MOUNTAIN VIEW
Coors Rd
277° 11.0 km
342° 11.1 km
022° 9.5 km
294° 5.1 km
336° 6.9 km
SCALE
0 1 2 Miles
0 5280 Feet
0 1 2 Kilometers

Figure 1. Explosion Test Sites on Kirtland Air Force Base, Albuquerque, New Mexico

prediction procedure, based on locally available weather observations and forecasts, has been developed for use by local USAF meteorologists.

BACKGROUND

Atmospheric Acoustic Refraction

Atmospheric acoustic refraction causes sound (or airblast) rays to bend upward, away from ground, when sound velocity decreases with height, as shown in Figure 2a, because higher portions of the wave travel in a slower velocity medium than lower wave portions. Conversely, when sound velocity increases with height (Figure 2c) emitted rays are bent toward ground, forming a sound duct and enhancing propagation. In the homogeneous atmosphere case (Figure 2b), with everywhere constant sound velocity, the hemispherical surface burst or spherical free air burst (FAB) explosion wave expands radially without distortion, and with characteristics that have been adequately defined by one-dimensional hydrodynamic models for explosions [2, 3].

Standard Explosion Definition

The standard 1-kt* nuclear explosion (NE), free-air burst (FAB), as computed by the USAF Weapons Laboratory (AFWL) [3], gives an airblast overpressure versus distance curve shown in Figure 3, using the distance scale at the top of the figure.

---

*The commonly used kiloton, abbreviated kt, was used rather than its SI equivalent, 4.2 TJ.

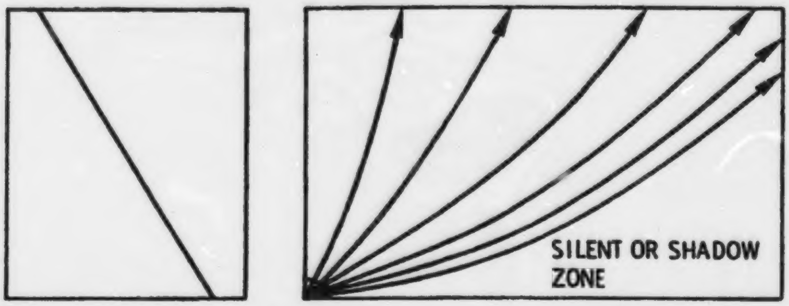
SILENT OR SHADOW ZONE

a. GRADIENT

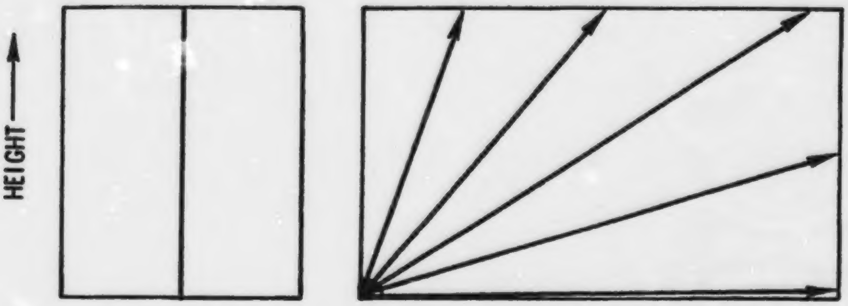

b. STANDARD

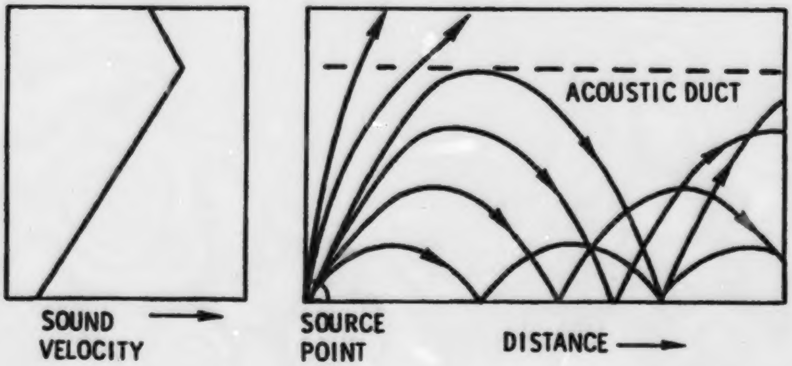
ACOUSTIC DUCT
SOUND VELOCITY
SOURCE POINT
DISTANCE

c. INVERSION

Figure 2. Atmospheric Refraction of Acoustic or Airblast Rays

The bottom scale has been adjusted to a 1 kg HE (TNT chemical high explosives) yield, following

$$R_1/R_2 = (W_1/W_2)^{1/3} \qquad (1)$$

where R is radial distance and W is explosion yield. Also included in the Figure 3 scale shift is the generally accepted factor of two converting NE to HE yield [4].

Height-of-Burst (HOB)

Height-of-Burst is an important factor in determining explosion airblast source strength [4]. The reflection-formed hemispherical Mach wave appears to come from an enhanced yield, as shown in Figure 4, up to a yield-scaled height referred to as the "optimum" HOB. This gives the "most bang for the buck," or maximum radial extent of specific over-pressure or damage (up to a level of a few tens of kilo-pascals).

Atmospheric Effects on Propagation

Refractive distortion of a blast wave by the atmosphere may enhance or attenuate propagation. In addition, a wave may actually be focused along a circumferential arc (caustic) around an explosion under more complex atmospheric conditions [5]. Specifically, when directed sound velocity decreases, then increases with height to a velocity aloft that is greater than the surface velocity, as shown in Figure 5, an annular portion of an explosion hemisphere wave is essentially reflected aloft and returned to the ground in an ensonified ring, beyond a so-called "zone of silence."

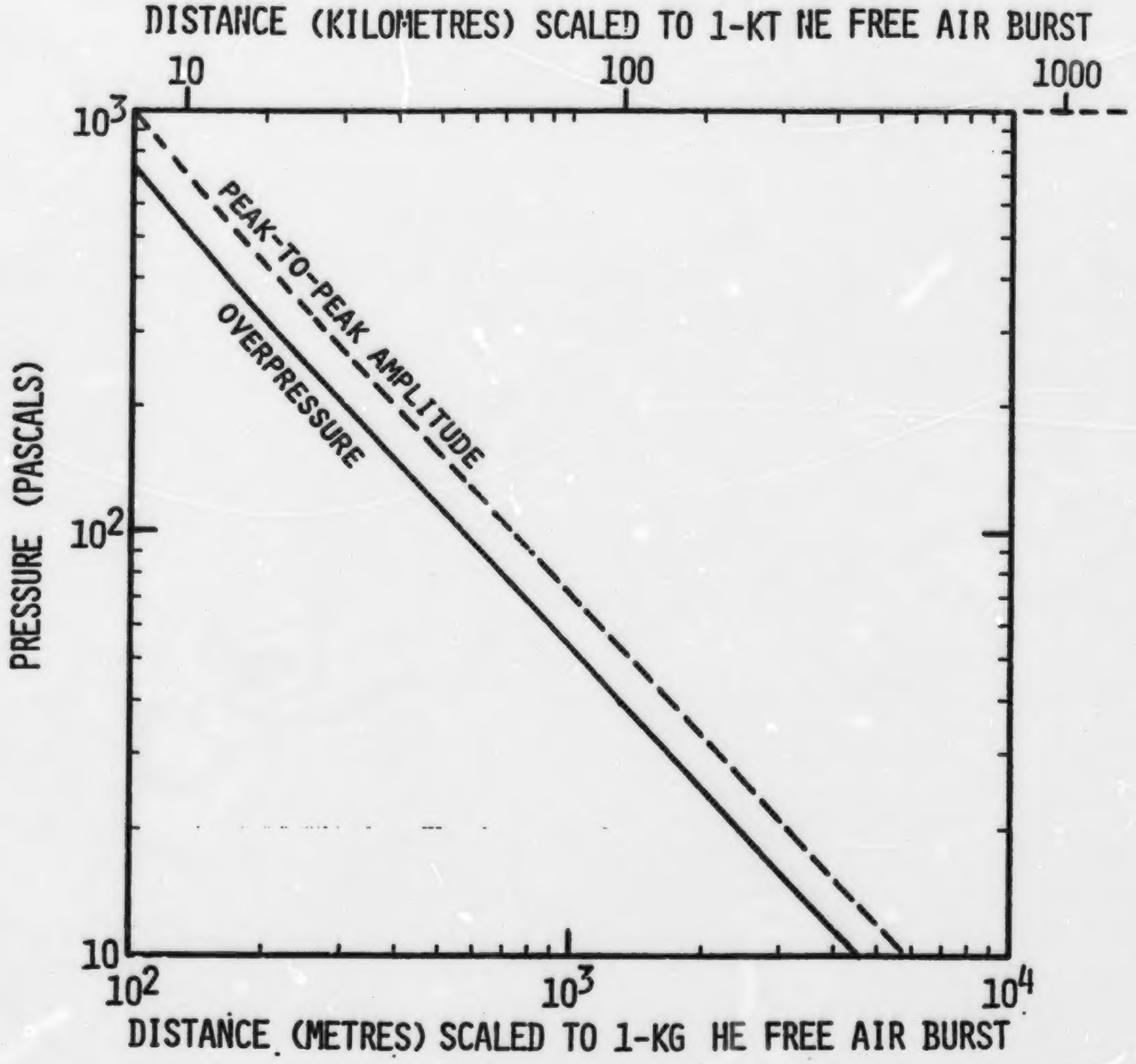

STANDARD EXPLOSION AIRBLAST PRESSURE-DISTANCE CURVES
FOR MEAN SEA LEVEL PRESSURE-ALTITUDE.

Figure 3

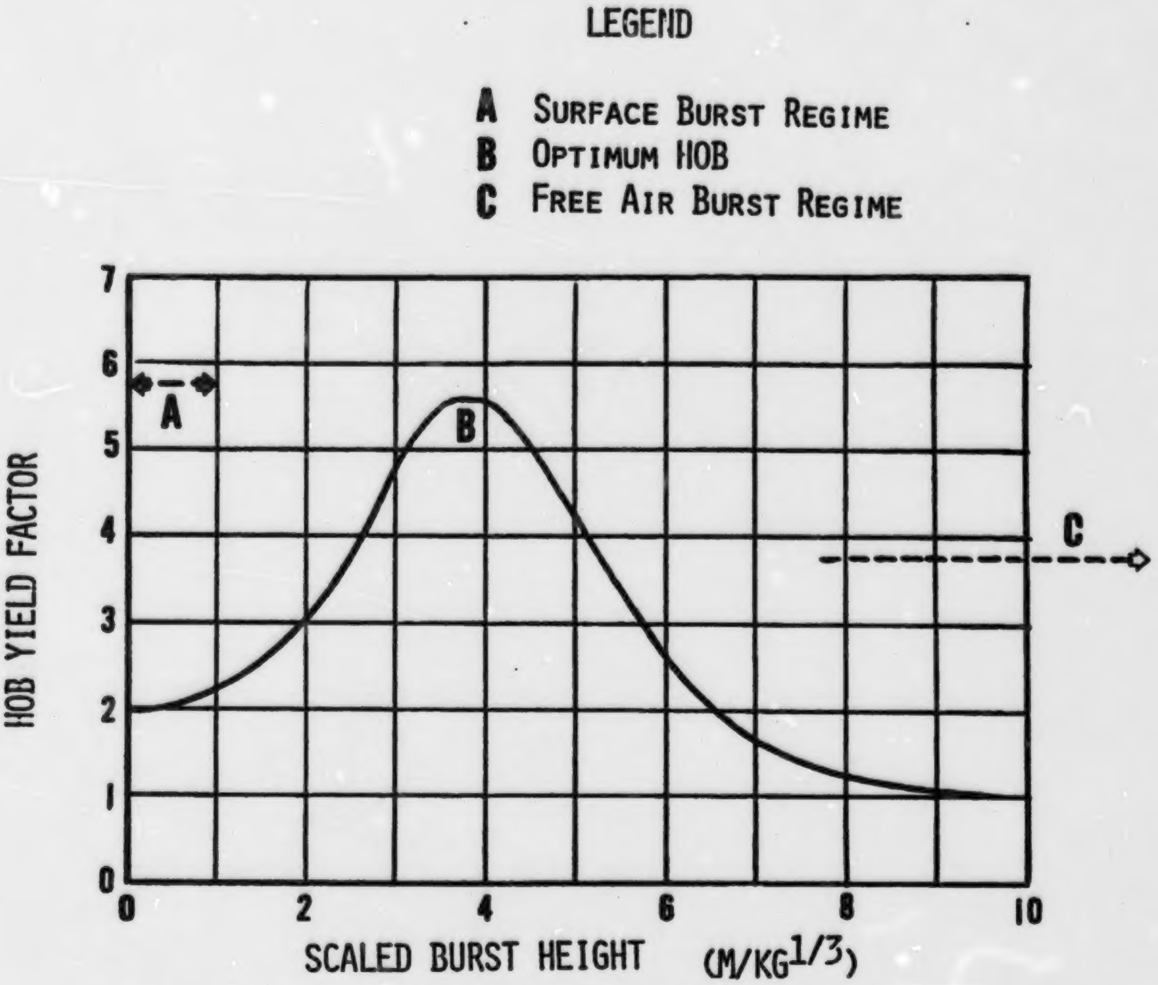

AIRBLAST HEIGHT-OF-BURST EFFECT ON APPARENT YIELD, BASED ON HIGH EXPLOSIVES MACH-STEM PRESSURES NEAR 8 M/KG$^{1/3}$ RADIUS.

Figure 4

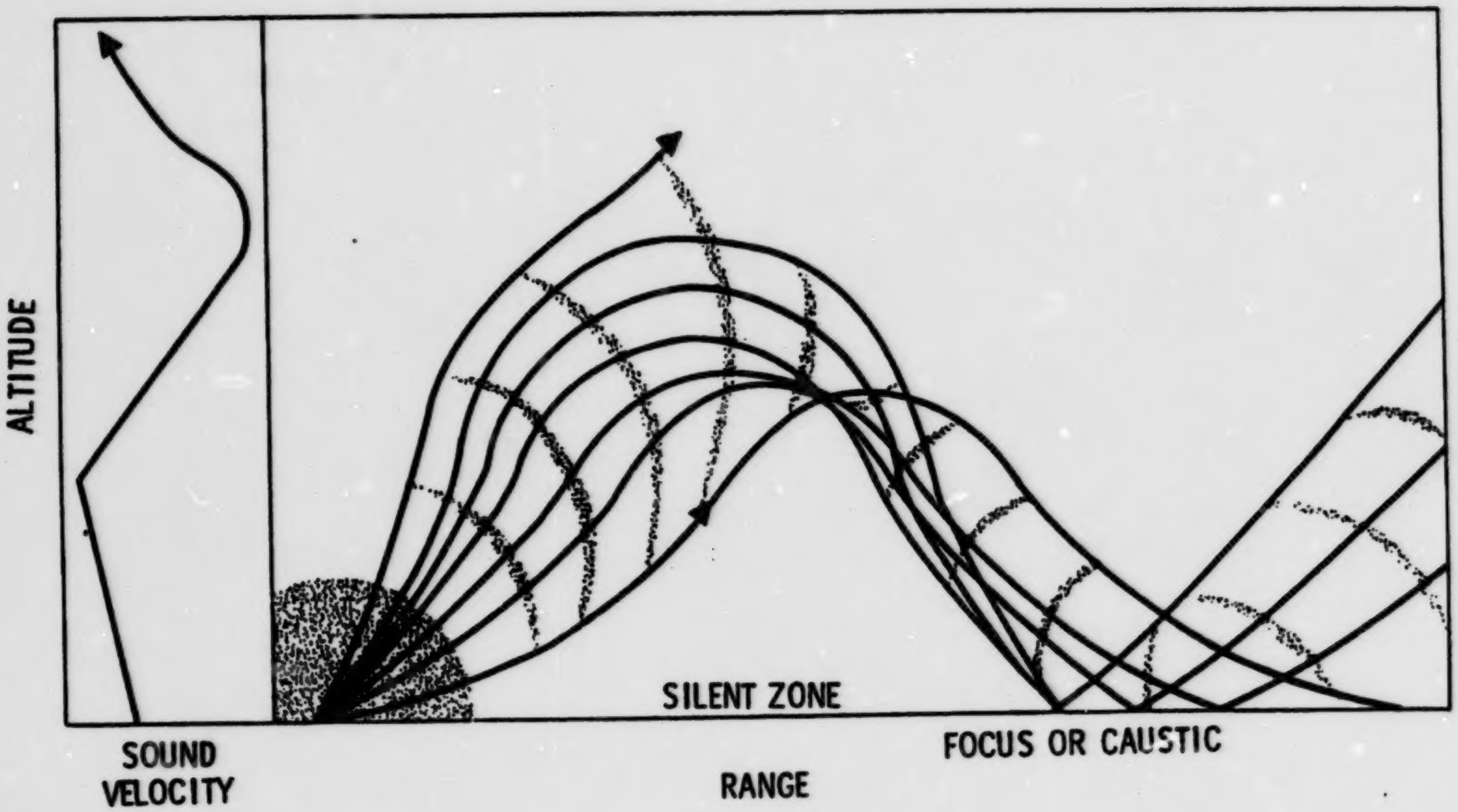

ALTITUDE
SILENT ZONE
SOUND VELOCITY
FOCUS OR CAUSTIC
RANGE

FIGURE 5. TYPICAL EXPLOSION RAY PATHS.

Observations of atmospheric nuclear tests recorded an extreme of 5X magnification above standard unrefracted incident amplitude propagation [6], caused by jet stream winds near 10 km MSL (mean sea level) altitude. Up to 3X recordings near 220 km range were caused by the relatively warm atmospheric ozonosphere layer near 50 km altitude with seasonally directed winds and propagations at that level. Sandia experiments in Nevada with 1134 kg HE explosions showed up to 8.3X amplitude magnification from jet stream winds that were calculated by caustic ray path programs to cause a caustic at about 60 km distance [7].

Current interest in hot-fueled motors (Class VII explosive fuels) for such vehicles as the Trident [8], MX and Shuttle, led to an extensive experimental study of boundary layer (to 1.5 km MSL altitude) propagation at Cape Canaveral, Florida. Several hundred explosions, with yields ranging from 2.3 kg to 1145 kg TNT, were fired in 1979, under a variety of weather conditions [1]. Airblast amplitude records were obtained that allow quantitative relation of propagation (amplitude versus distance functions) to weather (sound velocity change; positive for inversions, negative in gradient conditions).

Figure 6 shows an empirical family of amplitude-distance curves (scaled to 1 kg HE FAB) that was obtained over flat Florida palmetto, sand, and swamp. Sound velocity differences are shown for each curve, representing the maximum deviation from surface level sound velocity that was observed in the boundary layer by a nearby 150 m meteorological tower. Figure scales have been shifted to Albuquerque pressure-altitude (83 kPa).

Some statistics of propagation measurements under complex conditions are also shown in Figure 6. Complex cases include both clear dog-leg V(z) structures as well as what appear to be very nearly standard conditions (V(z) = constant). In near-standard cases there were occasional strong propagations caused by undetected sound velocity complexities.

Blast Noise Nuisance and Damage

Audible sounds generally range in frequencies from about 15 Hz to 20 kHz [5]. Low frequency explosion noises usually must reach about 20 Pa amplitude or 10 Pa overpressure (114 dB*) to be barely heard; 50 Pa overpressure (128 dB) usually arouses considerable attention from a typical community.

At long ranges, assumed for "distant" communities and low expected overpressures, the dominant frequency should be near 0.4 Hz from 1 kt NE and 30 Hz from 1 kg HE, except for added low frequency components caused by multi-path atmospheric propagations. On the other hand, it usually appears that much of what the public hears from distant explosions is the rattle of their houses in response to this low frequency pressure oscillation. Unfortunately, house-rattling often triggers a search for damage, and the years' accumulation of cracked

---

*Acoustic level $L = 20 \log_{10} (p/2 \times 10^{-5})$ decibels (dB), for pressure oscillation amplitude, p, in pascals.

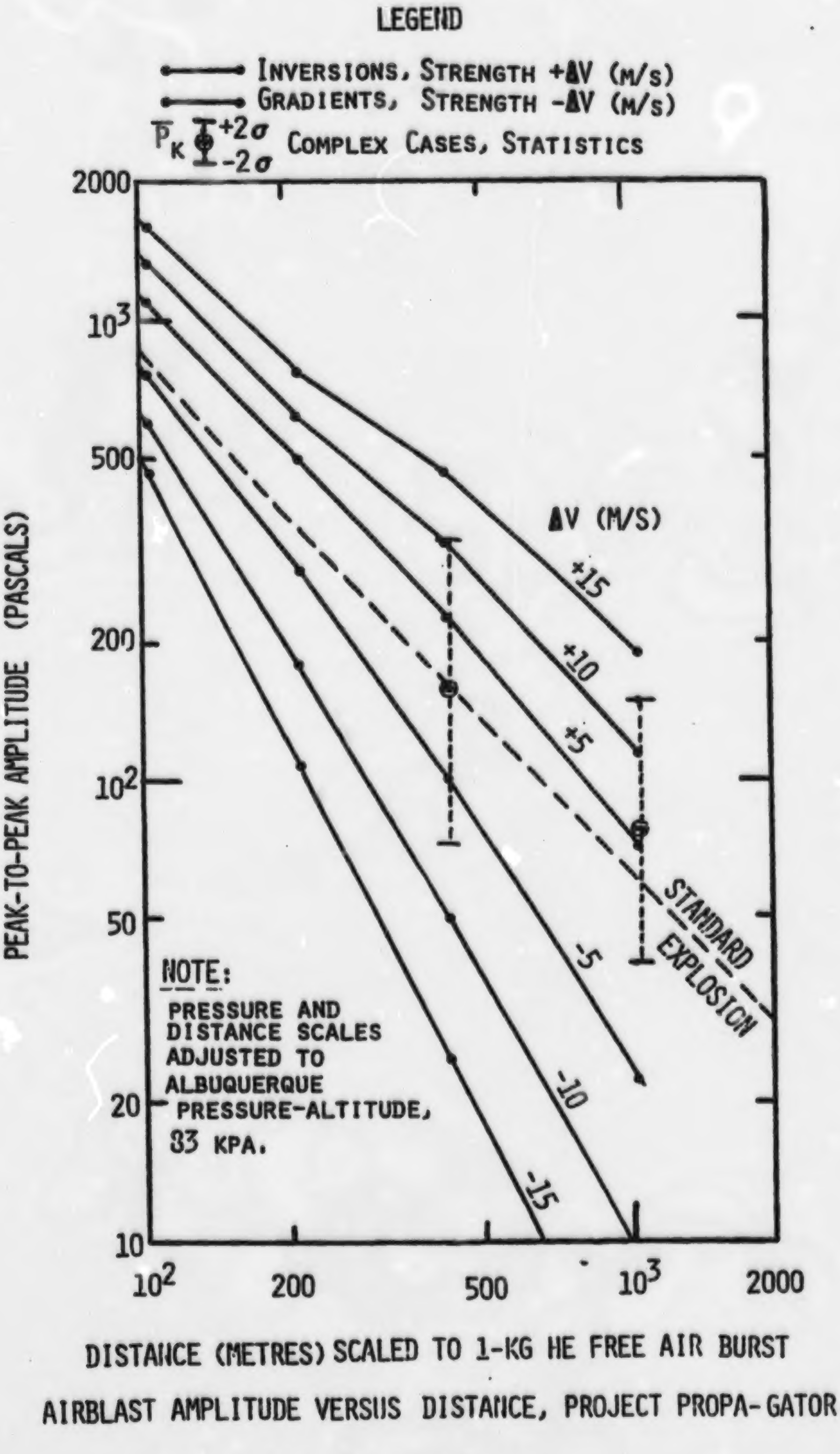

AIRBLAST AMPLITUDE VERSUS DISTANCE, PROJECT PROPA-GATOR.

Figure 6

plaster and windows is often claimed as the immediate consequence of an explosion.

Assessing true community damage from such weak explosion waves is quite complex. Experience with atmospheric nuclear tests has shown that a threshold for window damage appears to be about 400 Pa amplitude [9].

Window glass would seem to offer a relatively simple and sensitive structural component for airblast-damage correlations. Unfortunately, nothing is ever so simple as it seems, and to date, there is no satisfying and conclusive theoretical model for window damage response to airblast amplitude input. It appears that a simple empirical estimator, based on explosion test and accident results, gives the only satisfactory prediction [10]. As shown in Figure 7, the function relating breakage probability (on a community-wide basis of an assumed distribution of installations) to applied airblast overpressure, is the lognormal statistic

$$\Delta P_B = 7.5 \text{ x } (2.5)^{\pm} \text{ kPa}$$

YIELD LIMITATIONS, NO WEATHER CHECK

Acceptability Criteria

Cost effectiveness analysis would usually show that expenses of delaying an explosion test operation far exceed airblast damage costs, even under the worst weather conditions. Exceptions occur, of course, when someone is injured by falling or flying glass, or when community annoyance reaches such proportions

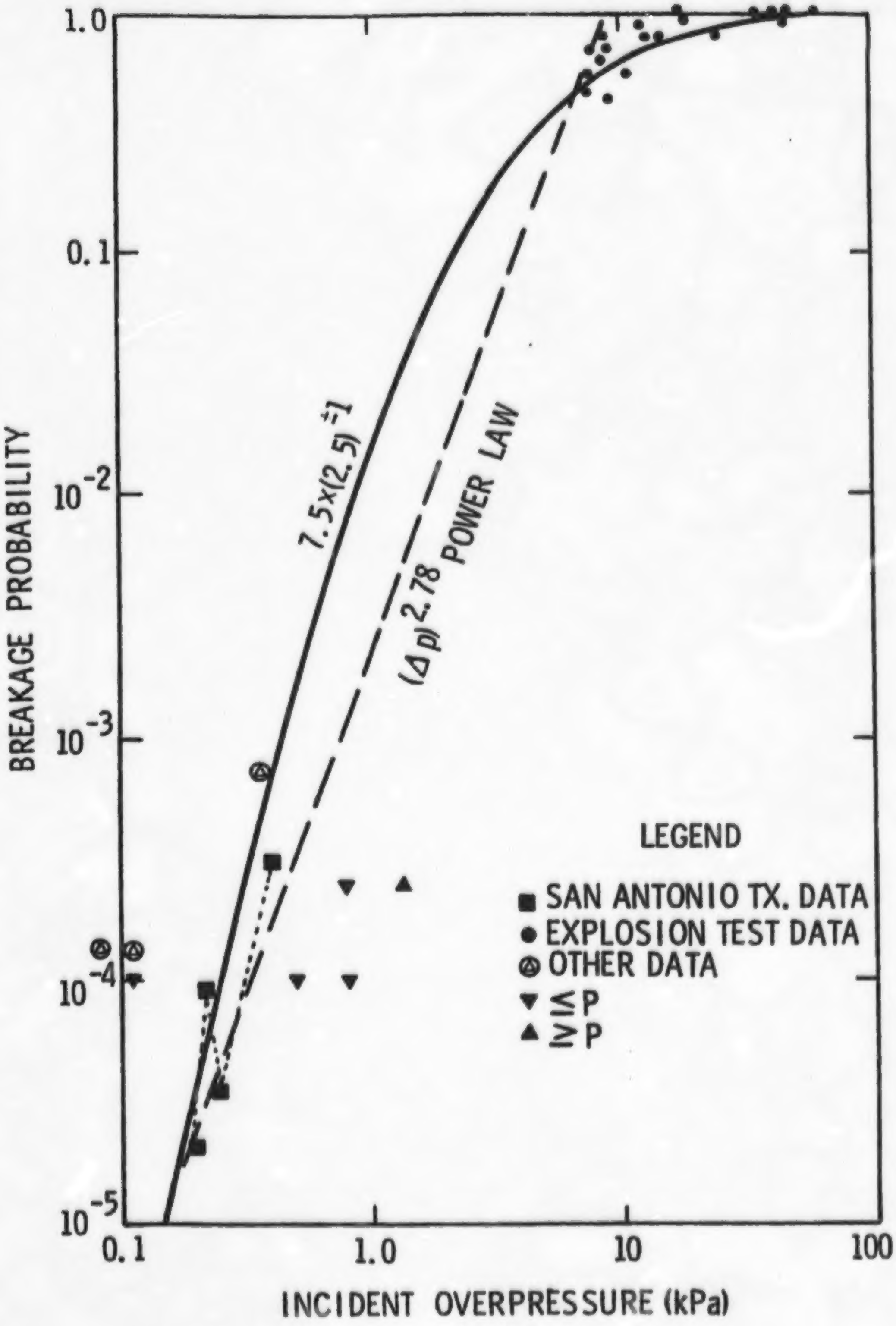

WINDOW BREAKAGE FROM AIRBLAST, THEORY & DATA

Figure 7

that political action is taken to suspend or radically change an operating program.

To avoid such consequences, limitations are commonly imposed and accepted by test managers to hold airblast noise levels down to mild rumbles, comparable to thunder. A recorded pressure amplitude of about 100 Pa corresponds to this noise level, at about one quarter the window damage threshold. Amplitudes of 20 Pa should pass unnoticed except by a forewarned and perceptive observer in a quiet ambience.

Relevant pressure-distance curves and data for establishing criteria are shown in Figure 8. Extreme propagation for 400 Pa damage has been adopted at a scaled distance of 1164 $m/kg^{1/3}$. Application of the 8.7X focus factor to long range gives the extreme range for minimal audibility (20 Pa) at 20 $km/kg^{1/3}$.

Operational decisions of whether or not a weather check is necessary may be made on the basis of generally accepting 100 Pa rumbings, while allowing that on rare occasions the rumble may be quite loud but not damaging.

Thus 100 Pa amplitude at 1950 $m/kg^{1/3}$ has been adopted, based on a $+2\sigma$ deviation from the average of complex condition propagations in Florida. With strong, simple inversions, $\Delta V = +10$ m/s, 100 Pa would carry just beyond 1 $km/kg^{1/3}$ on the average and $+1\sigma$ in the distribution would fall near 1.5 $km/kg^{1/3}$. Florida test inversions never exceeded $\Delta V = +10$ m/s. Stronger propagations will occur when there are complex conditions and focusing, but only 250 Pa would then be expected in the extreme cases of 8X

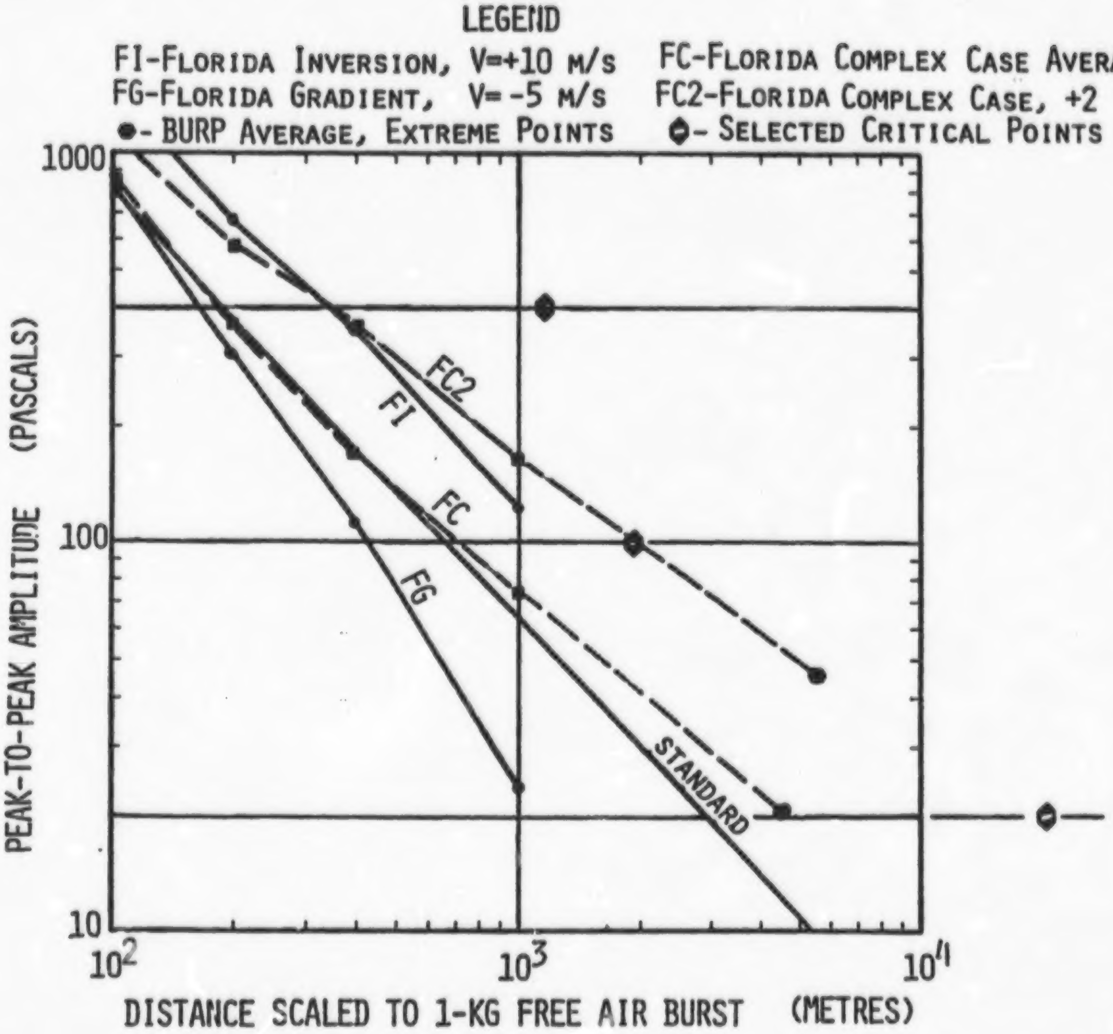

CRITICAL POINTS FOR COYOTE CANYON AIRBLAST PROPAGATION LIMITS.

Figure 8

magnification. No damage claims should arise from these rare incidents.

Calculated Limits for Various HOBs

Based on this criterion, that 100 Pa should extend to less than 1950 $m/kg^{1/3}$, explosion yield limits in Table I were calculated for critical target distances from two primary Coyote Canyon explosion test sites. Yield limits for not exceeding the 400 Pa damage threshold and the 20 Pa audibility threshold are also tabulated.

Table I shows that Lurance Canyon tests with surface bursts should be limited to 36 kg HE to hold propagation into Four Hills to less than 100 Pa amplitude under most weather conditions. Minor elevations of the charge can be accepted, up to 4 m, before HOB enhancement effects become significant. At optimum HOB, however, the limit is only 13 kg HE at 9 m above ground. Free air bursts, well above optimum HOB, could be 72 kg HE at 38 m or more, where FAB spherical wave formation is assured.

Thunder Range tests, at 9.5 km from the south boundary of Four Hills, should be restricted to 58 kg HE surface bursts. There have, in the past, been instances when minor airblast damage was caused by as little as 45 kg HE, as well as by rocket sled tests. Over thirty years of operation, such incidents have been so rare that they have been accepted by the community.

In general, it should take about four times the criteria yield limit, as well as extremely strong, focused propagations,

TABLE I.

Weather-Independent Explosion Yield Limits, Coyote Canyon Tests

Blast Location:	Lurance Canyon Igloo 9830	Thunder Range Bldg 9966
Critical Target:	Four Hills 8.1 km	Four Hills 9.5 km
Surface Bursts	36 kg	58 kg
Maximum Height	4 m	5 m
Elevated Bursts	13 kg	21 kg
Optimum Height	9 m	11 m

to cause damage at critical target communities. On the other hand, barely audible sound might be observed from yields of only a few grams of HE. Only if a great number of such small explosions were planned, as on a small-weapon firing range, would there be any chance for significant public annoyance from such small shots.

YIELD LIMITS WITH GOOD WEATHER CONDITIONS

Gradient Conditions

Table II shows explosion yields that could reasonably be contemplated for Coyote Canyon testing, assuming that a weather watch is available and test delays are acceptable while awaiting suitably attenuated propagations. These optimistic estimates were based on good gradient propagation conditions of $\Delta V = -5$ m/s. Stronger gradients were occasionally observed during Florida tests, down to -10 m/s, but they included a wind component that would not usually prevail over the necessary range of azimuths. Under clear skies and generally light wind conditions, with firing restricted to early afternoon during the greatest temperature lapse rate, there should be a number of days in any season when $\Delta V \leq -5$ m/s would be directed toward all heavily inhabited directions. Fortunately, prevailing daytime winds in Albuquerque are from the south through northwest so that most of the city is frequently upwind of both firing sites.

Maximum Yield Estimates

It appears that 4-ton (3.6-mg) HE surface bursts in Lurance Canyon and 5.8 Mg (6.4-ton) HE at Thunder Range could be fired

TABLE II. Explosion Yields for Very Good Conditions ($\Delta v \le -5$m/s)

	LURANCE CANYON			THUNDER RANGE		
	Four Hills	Carnuel	So. NM-10	Four Hills	La Blvd	Isleta Blvd
CRITERIA	8.1 km	6.9 km	4.0 km	7.5 km	11.1 km	14.8 km
MODERATE NOISE ($\le$ 100 Pa, 420 m/kg$^{1/3}$)						
Free Air Burst						
Max W (kg)	7173	4434	864	11572	18460	43756
Min Ht (m)	179	152	88	209	245	326
Surface Burst						
Max W (kg)	3587	2217	432	5786	9230	21878
Max Ht (m)	18	16	9	21	25	33
Optimum HOB						
Max W (kg)	1281	792	154	2066	3296	7814
Opt Ht (m)	43	37	21	51	59	79
Damage Threshold (400 Pa, 165 m/kg$^{1/3}$)						
FAB W (Mg)	118	73	14	190	304	722
Sfc W (Mg)	59	37	7	95	152	361
Opt HOB W (Mg)	21	13	3	34	54	129
Audibility Threshold (20 Pa, 1.1 km/kg$^{1/3}$)						
FAB W (kg)	399	247	48	644	1028	2436
Sfc W (kg)	200	123	24	322	514	1218
Opt HOB W (kg)	71	44	9	115	183	435

under select weather conditions. This conclusion is in accord with historical experience, except for those few occasions when peculiar and unsuspected local weather influences caused trouble. Conceivably, even 59 Mg HE could be fired in Lurance Canyon without actual damage in Four Hills. Until mountain shadow effects are better understood, however, this yield would appear to hazard the whole Tijeras Canyon and NM-10 South region. Such large and expensive tests would be better conducted at a larger test range.

WEATHER WATCH & PREDICTION PROCEDURES

Outline

When an explosion test is planned to exceed yield limits shown in Table I, a weather watch and airblast prediction is required to assure that propagations will not unduly disturb the community. The recommended evaluation procedure follows the chronological order of occurrences:

- Source definition
- Propagation conditions
- Target effects assessment

Calculation forms have been provided for test operator use, along with various useful conversion tables and nomographs.

Source Definition

Equivalent yield was probably already determined in reaching a decision that detailed weather-dependent predictions were needed. Nevertheless, this source strength should be systematically determined by following the steps of Table III. Airblast equivalent yield factors for common chemical explosives are available from several sources. An HOB yield enhancement factor should be estimated from the curve shown earlier in Figure 4. Results, in Lines 11-13, provide three points for plotting a standard pressure-distance curve for the indicated explosion.

Rather than attempting to reconstruct a yield-scaled family of propagation curves for various weather conditions, a background amplitude-distance pattern for 1 kg HE is shown in Figure 9 for use with a clear plastic overlay copy of Figure 10. The index arrow (at 1000 m or 1 km) is aligned under the overlaid distance scale at the kilometre distance given on Line 14 of Table III. This procedure, involving yield-scaling of distances, allows rapid evaluation for critical targets and weather threats, from a given explosion.

When the overlay has been aligned, the result shows the various weather-dependent propagation curves, with yield-scaled distances along the abscissa marked by ranges to specific local targets. Intersections of target distance lines (verticals) and propagation curves are used to establish limits on weather conditions to avoid exceeding pre-determined damage, noise, or audibility.

A number of notable incidents or test results have been shown by points on the Figure 9 background. Several incidents appear to show extreme propagations that exceeded results

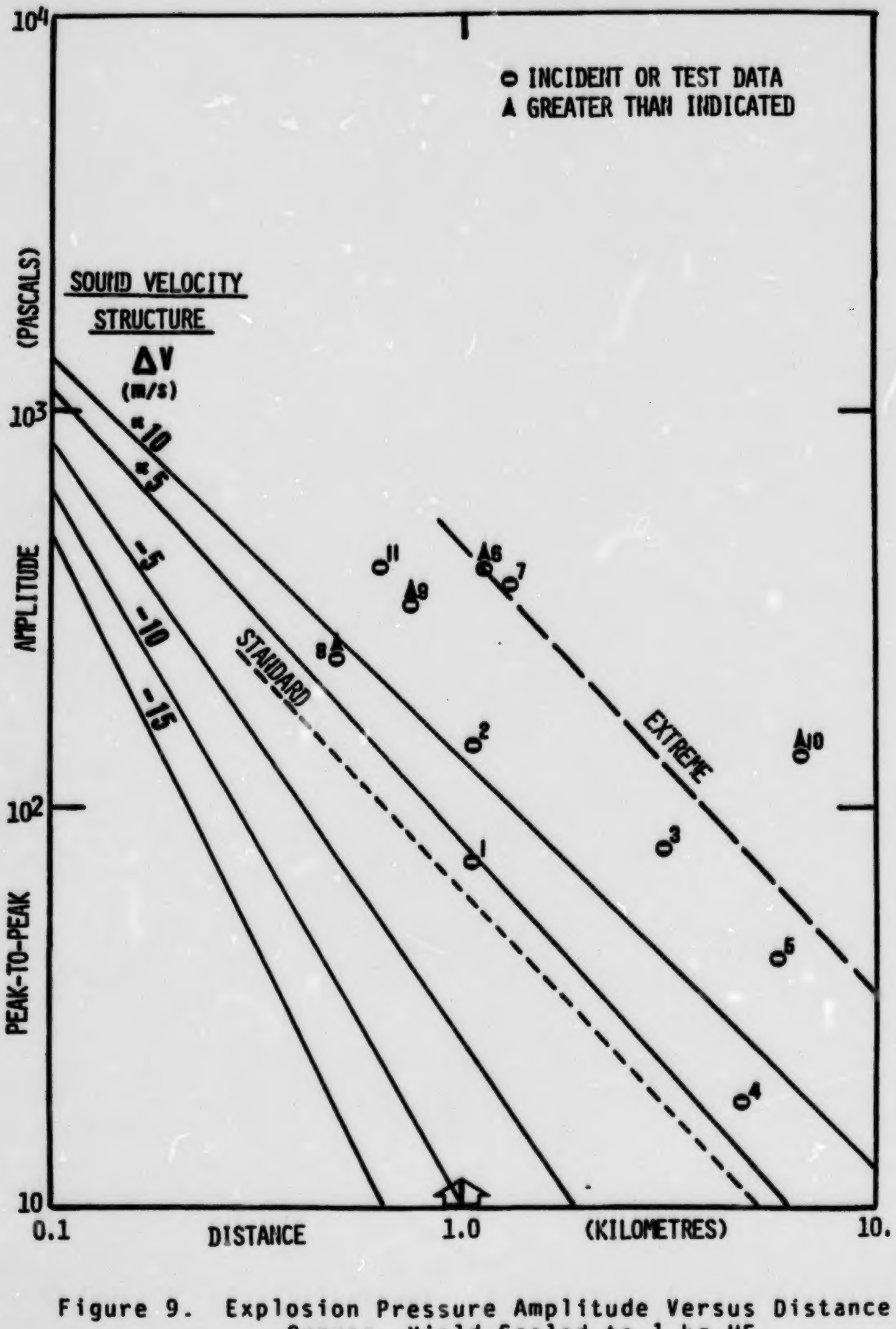

Figure 9. Explosion Pressure Amplitude Versus Distance Curves, Yield-Scaled to 1 kg HE

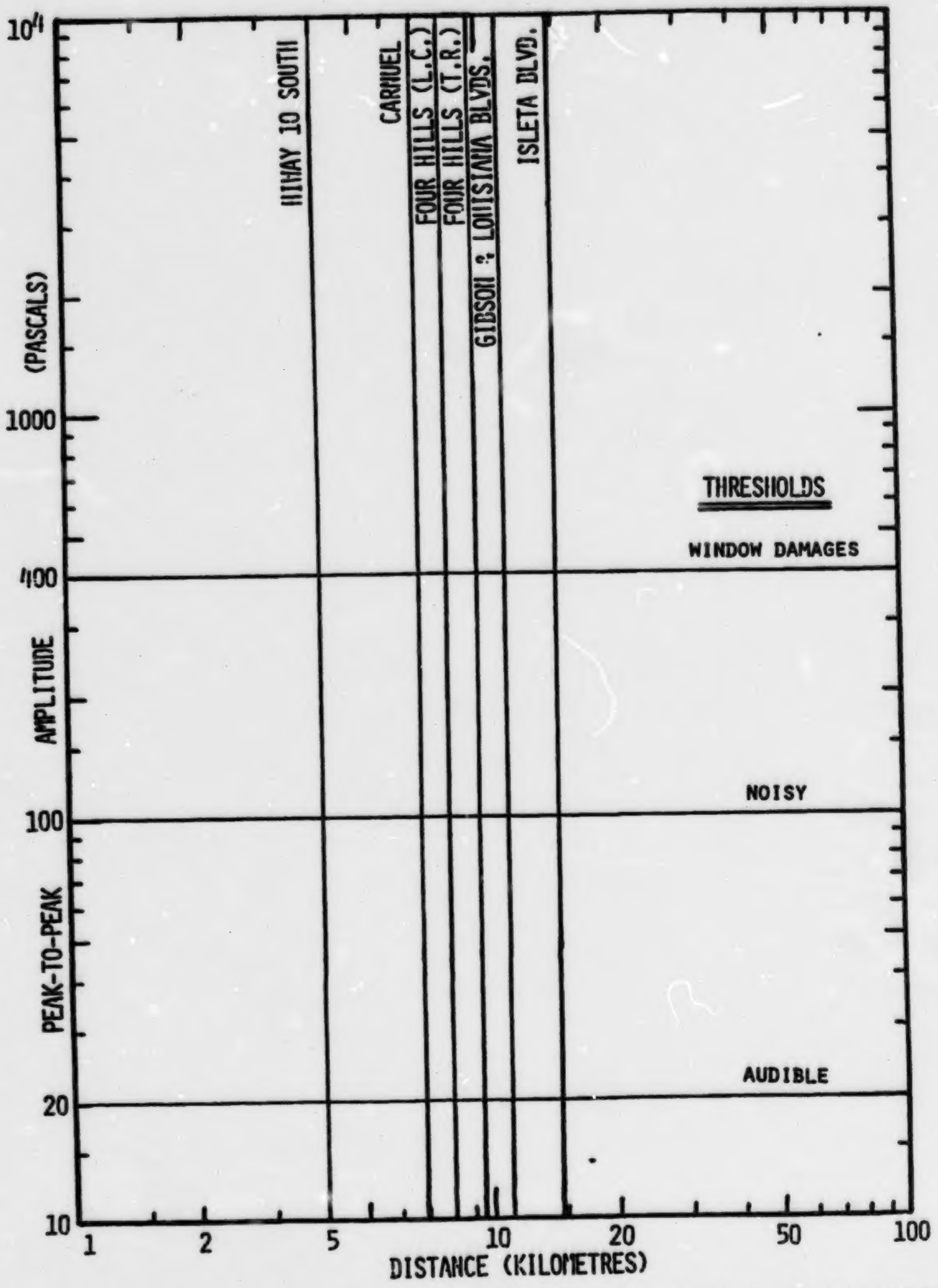

Figure 10. Target Distance Overlay for Amplitude-Distance Curves

obtained in experiments. As such, they indicate what could happen but not what might be expected to happen in a given situation. Except for the case shown by Point #10, extreme propagations appear to be bounded by the dashed line shown near 7X focus factor. In complex propagating conditions, either with a dog-leg sound velocity structure or near $\Delta V = 0$, and a yield that could conceivably cause damage to the community, a test delay should be recommended to await better weather. On the other hand, it may be necessary to proceed and fire some complicated or costly test explosions, with the remote chance of adverse response, even when the "Extreme" line is slightly exceeded. But if the amplitude of the exceedance is by about 50 percent or so, then there arises a real probability of injury caused by breaking or falling glass in any substantial population.

Well above the damage threshold level, and around 3 kPa overpressure (not amplitude), flying glass would have such density and velocity as to seriously threaten the safety of every resident [11]. This point is stressed here because there is a lingering remnant of misguided opinion that nearly 0.5-psi (3.5 kPa) is needed "to cause minor damage to the flimsiest structures." This conclusion, apparently originated by World War II bomb damage assessors and relevant only to the maintenance of building structural functions in war production, is still occasionally repeated with respect to sonic booms and mining activities [13].

Along similar lines, some obsolete analyses indicated 100X amplitude focusing potentials for atmospheric propagation [14]. All attempts to pin down the source data for this contention have been futile, but some clues have been obtained. Early (pre-1950) laboratory experiments made overpressure-distance measurements with small HE charges that showed $\Delta p \sim R^{-1.4}$, rather than $\Delta p \sim R^{-1.1}$ as now estimated for "standard" long range propagation. Similar rapid pressure-distance decays were later obtained from 0.4 g HE experiments [15]. Measurements at very long range from much larger explosions were apparently used to infer large magnification (referenced to the more rapid distance decay rate) in caustic zones. References to the new standard, however, should bring these amplifications down to or below the "Extreme" level shown in Figure 9.

Weather Observations and Calculations

Having established the explosion source strength and its potential for propagating unacceptable airblast amplitudes into some part of the surrounding community, the next step is to determine actual (or forecast) weather conditions and their capacity for causing airblast enhancements of unacceptable magnitude in critical directions. Surface and upper air observations of temperature and winds, as needed for this assessment, are entered in Table IV.

It is assumed that no humidity correction is needed for

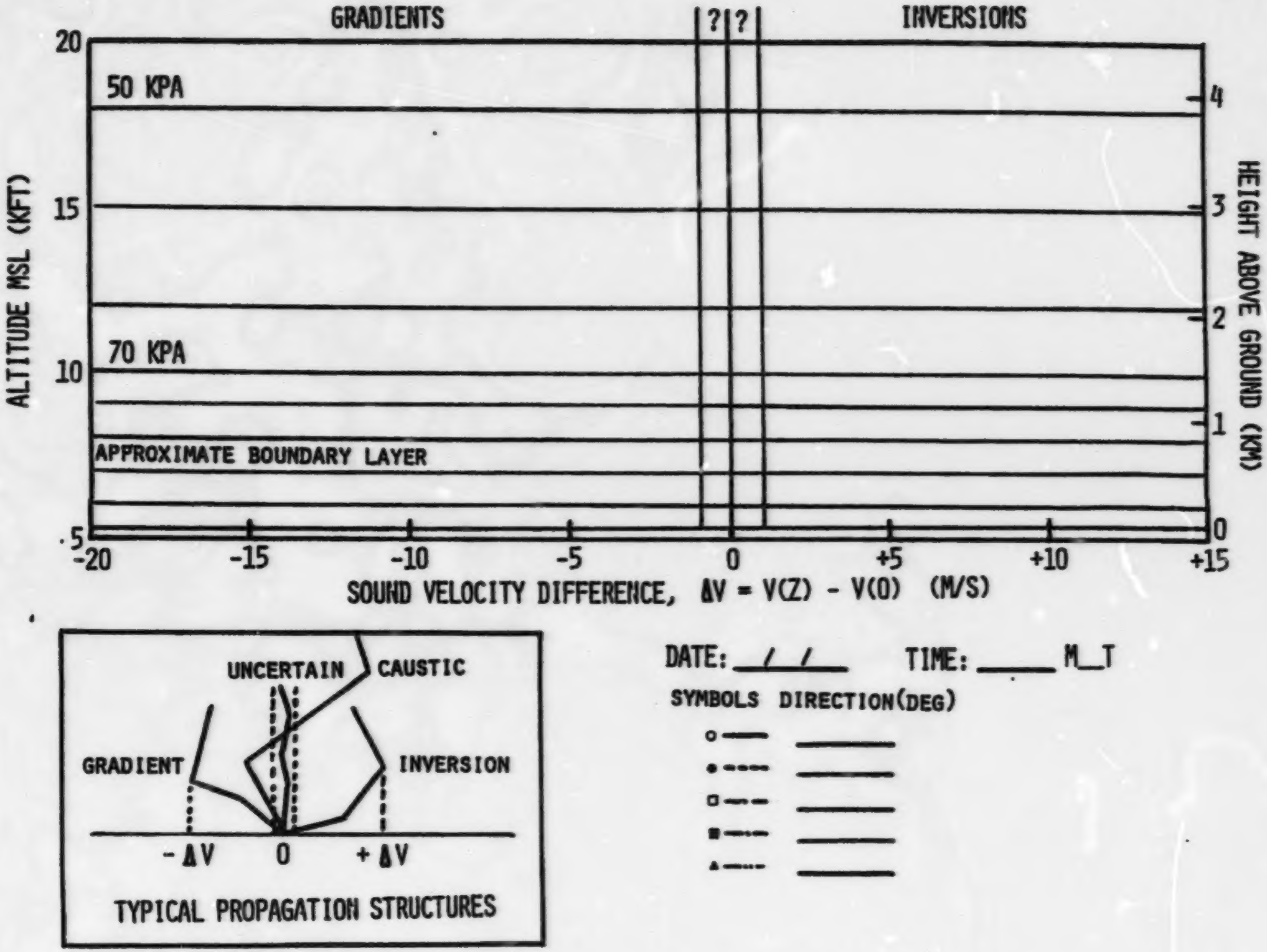

.SOUND VELOCITY VERSUS HEIGHT PLOTS.

Figure 11

TABLE III

EXPLOSION SOURCE STRENGTH CALCULATION

1.	Type of chemical explosive		________
2.	Total explosive weight, W	________lb	________kg
3.	Explosive yield equivalence factor (1.0 for TNT), k_e (see Table IV)		________
4.	TNT equivalent weight, $W_e = k_e \times W$	________lb	________kg
5.	Yield scaling factor, $W_e^{1/3}$	________$lb^{1/3}$	________$kg^{1/3}$
6.	Charge center height above ground, Z	________ft	________m
7.	Yield-scaled height of burst, $HOB = Z / W_e^{1/3}$	________$ft/lb^{1/3}$	________$m/kg^{1/3}$
8.	HOB yield enhancement factor, k_h (see Fig. 4)		________
9.	Apparent airblast yield, $W_a = k_h \times W_e$	________lb	________kg
10.	Apparent yield scaling factor, $W_a^{1/3}$	________$lb^{1/3}$	________$kg^{1/3}$
11.	Standard explosion 400 Pa distance, $R_A = 189.34 \times w_a^{1/3}$		________m
12.	Standard explosion 100 Pa distance, $R_B = 667.69 \times W_a$		________m
13.	Standard explosion 20 Pa distance, $R_C = 2884.04 \times W_a^{1/3}$		________m
14.	Index (Fig. 10) distance on overlay (Figure 11), Repeat Line 10 number entry.		________km

ate: ___/___/___ Mo Day Yr   Time: ________ M T
________ GMT

lti-ude MSL ft)	Temperature (°C)	Wind		Sound Speed (m/s)	Directed Wind Components (m/s)				Directed Sound Velocities (m/s)				Sound Velocity Differences(m/s)			
		Direction (deg)	Speed (knots)		θ_1 ___°	θ_2 ___°	θ_3 ___°	θ_4 ___°	θ_1	θ_2	θ_3	θ_4	θ_1	θ_2	θ_3	θ_4

ate: ___/___/___ Mo Day Yr   Time: ________ M T
________ GMT

lti-ude MSL (ft)	Temperature (°C)	Wind		Sound Speed (m/s)	Directed Wind Components (m/s)				Directed Sound Velocities (m/s)				Sound Velocity Differences(m/s)			
		Direction (deg)	Speed (knots)		θ_1 ___°	θ_2 ___°	θ_3 ___°	θ_4 ___°	θ_1	θ_2	θ_3	θ_4	θ_1	θ_2	θ_3	θ_4

			AIRBLAST ASSESSMENT					WEATHER CHECK				
Target	Azimuth (deg)	Distance (metres)	Scaled Distance (m/kg$^{1/3}$)	Acceptable ΔV(100) (m/s)	Damage ΔV(400) (m/s)	Audible ΔV(20) (m/s)	Complex F(400) (σ)	Complex V-Structure ? (yes/no)	OK? (yes/no)	ΔV (m/s)	OK? (yes/no)	REMARKS
LURANCE CANYON TESTS												
Cedro	070	5400										
NM-10 South	040	4000										
Cement Plant	010	7400										
Carnue	330	6900										
Four Hills	300	8100										
Gibson & Louisiana	290	15800										
Mountain View	260	22700										
THUNDER RANGE TESTS												
Four Hills	020	9500										
Gibson & Louisiana	340	11100										
Old Airport Terminal	320	12500										
Mountain View	290	11600										
Isleta Blvd	270	14800										

sound speed calculation in dry Albuquerque air. Altitude, temperature, and wind reports are entered directly from provided surface weather observation (zero level) and upper air balloon rawinsonde reports. Airblast propagation is usually dominated by the atmospheric layer of depth less than about one-fifth, possibly one-fourth, of the horizontal distance of concern. Most concerns with Albuquerque and Coyote Canyon tests thus involve only about 3 km of atmosphere up to 4.5 km MSL, and typically the first seven levels of a winds-aloft report. Space is provided in the table for ten balloon data levels, should further information be desired.

Sound speed in air, C, may be calculated from absolute temperature, T in kelvins, by

$$C = 20.0555\ T^{1/2}\ \text{m/s},$$

or read from prepared tables.

Selection of azimuthal directions for evaluation depends on target locations and directions as well as wind direction. One calculation should be made down-wind from the strongest wind in the lower two or three rawinsonde levels. Experience is useful in determining the fewest directional calculations that are necessary to establish the existence of a propagation problem.

The directed wind component, U, along azimuth, θ, is resolved from the reported wind speed, W, and direction, D. Note that meteorological observing practice is to report winds according to the direction from which the wind blows. This convention, a reversal from usual vector description, is defended to allow allusion to "cold north" and "warm south" winds, rather than vice versa.

Space is provided for analysis along four azimuthal bearings. Directed sound velocity at each level is obtained by simple addition of the directed wind component and sound speed. Sound velocity difference is obtained by subtracting the zero-level (surface) directed velocity from the upper level directed velocity. Difference curves are next plotted versus height on Figure 11. The apparent curve structure and, where applicable, the magnitude of the maximum boundary layer sound velocity difference provide the input to a propagation prediction from the yield-adjusted Figure 9/10 overlay.

Community Impact

Evaluation for community impact from the specified explosion and weather condition may be systematized by use of Table V. Values for the airblast assessment are read from the yield-adjusted Figure 9/10 overlay. The weather check, for complex structures as well as inversion or gradient intensities, is made from the directional curves drawn on Figure 11. YES-NO conclusions on acceptaility are entered as appropriate, along with any remarks.

REFERENCES

1. J. W. Reed, "Project PROPA-GATOR - Intermediate Range Explosion Airblast Propagation Measurements," 19th DOD Explosive Safety Seminar, Los Angeles, CA, Sept. 9, 1980.

2. C. D. Broyles, "IBM Problem M Curves," Report SC-TM-268-56(51), Sandia Laboratories, Albuquerque, NM, Dec. 1956.

3. C. E. Needham, M. L. Havens, and C. S. Knauth, "Nuclear Blast Standard (1 kt)," Report AFWL-TR-73-55 (Rev.), Air Force Weapons Laboratory, Kirtland Air Force Base, NM, Apr. 1975.

4. S. Glasstone, S. (Editor). The Effects of Nuclear Weapons, Washington, DC: Government Printing Office, 1977.

5. E. F. Cox, Sound Propagation in Air, Chap. 22, Handbuch der Physik. Berlin: Springer-Verlag, 1958, Vol 48.

6. J. W. Reed, "Climatology of Airblast Propagations from Nevada Test Site Nuclear Airbursts," Report SC-RR-69-572, Sandia Laboratories, Albuquerque, NM, Dec. 1969.

7. J. W. Reed, "Explosion Wave Amplitude Statistics for a Caustic at Ranges of 30 to 45 Miles," Report SC-RR-67 860, Sandia Laboratories, Albuquerque, NM, Feb. 1968.

8. J. W. Reed, "Predictions of Nuisance Damage and Hazard from Accidental Explosions during Trident Missile Test Flights," SAND 79-0626, Sandia National Laboratories, Albuquerque, NM, March 1980.

9. E. F. Cox, Air Shocks at Large Distances from Atomic Explosions, Operation Tumbler-Snapper Report WT-504 Sandia Laboratories, Albuquerque, NM, January 1953.

10. J. W. Reed, Distant Blast Predictions for Explosions, Minutes 15th ESB Seminar, DOD-ESB, Washington, DC, 18 September 1973.

11. E. R. Fletcher, D. R. Richmond, and R. K. Jones, Velocities, Masses and Spatial Distributions of Glass Fragments from Windows Broken by Airblast, Defense Nuclear Agency Report (Albuquerque, NM, Lovelace Foundation), in preparation.

12. J. W. Reed, B. J. Pape, J. E. Minor, and R. C. Dehart, "Evaluation of Window Pane Damage Intensity in San Antonio Resulting from Medina Facility explosion on November 13, 1963," Annals of the New York Academy of Sciences, 152:Art 1, October 1968.

Brüel & Kjær
Brüel & Kjaer Canada Ltd.

1313 Border Street, Suite 29
Winnipeg, Manitoba R3H 0X4

Tel.: (204) 694-2884
Fax: (204) 694-5025

July 29, 1994

Dr Paul Thibault
Combustion Dynamics Ltd.,
203, 132 - 4th Avenue SE
Medicine Hat AB T1A 8B5

Dear Paul,

Attached is a response I have sent to Dave Ritzel on the waveform information he had sent to me for comments.

I have included the costing of '2' Sound Level Meter Systems for your review, 1 on the unit we used, the 2236 and the other on our high end model the 2231 which I have configured with some options to allow its low frequency response to measure down to less than 1 hertz.

I look forward to further discussions with you on this matter.

Yours truly,
BRUEL & KJÆR CANADA LTD

Jim Ulicki

Jim Ulicki, C.E.T.
Technical Representative

JU/ck
att

ONTREAL
) Leacock Road
ointe Claire, Qué. H9R 1H1
el.: (514) 695-8225
ax: (514) 695-4808
elex: 05-821691

OTTAWA
1900 Merivale Road
Suite 212
Ottawa, Ontario K2G 4N4
Tel.: (613) 225-7648
Fax: (613) 225-9880

TORONTO
6155 Tomken Rd.
Unit 8
Mississauga, Ontario L5T 1X3
Tel.: (416) 564-5472
Fax: (416) 564-5226

RICHMOND
5520 Minoru Blvd.
Room 202
Richmond, B.C. V6X 2A9
Tel.: (604) 278-4257
Fax: (604) 278-3292

Brüel & Kjær
Brüel & Kjaer Canada Ltd.

29 - 1313 Border Street
Winnipeg, Manitoba
R3H 0X4
GST #R100672237

Tel.: (204) 694-2884
Fax: (204) 694-5025

QUOTATION

NUMBER
32-940711

DATE MO.	D.	Y.
07	29	94

Dr. Paul Thibault
COMBUSTION DYNAMICS LTD.,
#203, 132 - 4th Avenue SE
MEDICINE HAT, Alberta
T1A 8B5

COPIES TO

- PAGE 1 -
tel: (403) 529-2162
fax: (403) 529-2516

TOMER NO.	XXXXXXXX	PROVINCIAL SALES TAX	PROV.	CUSTOMER REFERENCE	TERMS OF PAYMENT	[redacted]
	GST EXTRA	N/A	AB	N/A	NET 30 DAYS	08 29 94

COLL.	SHIP VIA	F.O.B.	SALESMAN 1	DUTY	TE
X	BEST WAY	POINTE CLAIRE, QUE	JIM ULICKI, C.E.T.	INCL. ☒ EXCL. ☐	

QUANTITY	TYPE NO.	DESCRIPTION	PRICE	EXTENSION	DELIVERY
		2236 PRECISION SOUND LEVEL METER			
		(7Hz Low Limit Frequency)			
1	2236B	Precision Integrating Sound Level Meter with 512KB Memory including AO1386 PC Interface Cable and UA0237 Windscreen	$4,217.00		3-4 Wks
1	AO0408	Microphone Extension Cable - 3 Meters	$107.00		3-4 Wks
1	UA1254	Microphone Holder	$69.00		3-4 Wks
		2231 PRECISION SOUND LEVEL METER			
		(1Hz Low Limit Frequency)			
1	2231	Modular Precision Sound Level Meter	$7,680.00		3-4 Wks
1	ZI9101	Interface Module	$495.00		3-4 Wks
1	UC5265	Low Frequency Adaptor for 4155	$252.00		3-4 Wks
1	AO0027	Microphone Extension Cable - 3 Meters	$278.00		3-4 Wks
1	UA0588	Tripod Adaptor	$69.00		3-4 Wks
		OPTIONS			
	4231	Sound Pressure Calibrator	$873.00		3-4 Wks
	1550	Hardside Rugged Carrying Case	$325.00		3-4 Wks

THIS QUOTATION IS SUBJECT TO TERMS & CONDITIONS ON REVERSE SIDE

Overdue accounts are charged at 2% per month (24% per year)

Prices are in Canadian funds.

By Jim Ulicki

Brüel & Kjær
Brüel & Kjaer Canada Ltd.

29 - 1313 Border Street
Winnipeg, Manitoba
R3H 0X4
GST #R100872237

Tel.: (204) 694-2884
Fax: (204) 694-5025

QUOTATION

DATE
MO. D. Y.
07 29 94

NUMBER
32-940711

r. Paul Thibault
OMBUSTION DYNAMICS LTD.,
'203, 132 - 4th Avenue SE
1EDICINE HAT, Alberta
1A 8B5

COPIES TO

- PAGE 2 -
tel: (403) 529-2162
fax: (403) 529-2516

MER NO.	XXXXXXXX	PROVINCIAL SALES TAX	PROV.	CUSTOMER REFERENCE	TERMS OF PAYMENT	[redacted]
	GST EXTRA	N/A	AB	N/A	NET 30 DAYS	08 29 94

OLL.	SHIP VIA	F.O.B.	SALESMAN 1	DUTY	TERF
X	BEST WAY	POINTE CLAIRE, QUE	JIM ULICKI, C.E.T.	INCL. ☒ EXCL. ☐	

UANTITY	TYPE NO.	DESCRIPTION	PRICE	EXTENSION	DELIVERY
		N.B. 1) Overleaf prices include Duty. GST is extra 2) All instrumentation carrys a '1' Year Parts & Labour Warranty 3) All deliveries upon receipt of written order			

THIS QUOTATION IS SUBJECT TO
TERMS & CONDITIONS ON REVERSE SIDE

Overdue accounts are charged at 2% per month (24% per year)

Prices are in Canadian funds.

By Jim Ulicki

Brüel & Kjær
Brüel & Kjaer Canada Ltd.

1313 Border Street, Suite 29
Winnipeg, Manitoba R3H 0X4

Tel.: (204) 694-2884
Fax: (204) 694-5025

July 29, 1994

David V. Ritzel
Dept of National Defence
Explosive Effects Grp
Defence Res Estab Suffield
Box 4000
Medicine Hat AB T1A 8K6

Dear David,

After some delay, I have gathered some information concerning the time domain traces you had sent to me, and more specifically the differences observed between the Brüel & Kjær microphone and the PCB pressure transducer. My comments are as follows;

1. The system responses we are comparing are dependent on phase relation as well as the amplitude relation versus frequency. The upper and lower limiting frequencies of the transducer as well as the phase and amplitude characteristics must be similar or differences in traces will occur.

2. Attached is information on the phase response of several of our microphones which because of inherent design, provides a phase inversion at low frequencies. The exact transducer used on the 2236 SLM is not in this data, but similar in nature.

3. The -3dB down point of the microphone utilized on the 2236 is approximately 7Hz versus the PCB 106B50 which is close to .5Hz.

4. The magnitude of the Brüel & Kjær Peak response in your traces should be, in my calculation more towards 90 pascals versus the 40 you have showed. This is approximately half the PCB response which is likely partially related to point 3 above. This is an acoustical difference of 6dB (139dB PCB vs 133dB B&k) and I would expect that to remain fairly consistent.

$$\text{Pascals} = .00002\ (\text{Antilog}\ \frac{133}{20}\text{dB Peak})$$

2/.....

MONTREAL
90 Leacock Road
Pointe Claire, Qué. H9R 1H1
Tel.: (514) 695-8225
Fax: (514) 695-4808

OTTAWA
1900 Merivale Road
Suite 212
Ottawa, Ontario K2G 4N4
Tel.: (613) 225-7648
Fax: (613) 225-0880

TORONTO
6155 Tomken Rd.
Unit 8
Mississauga, Ontario L5T 1X3
Tel.: (416) 564-5472
Fax (416) 564 5226

RICHMOND
5520 Minoru Blvd.
Room 202
Richmond, B.C. V6X 2A9
Tel.: (604) 278-4257
Fax: (604) 278-3292

David Ritzel
Dept of National Defence
Explosive Effects Group
Defence Research Estab Suffield

5. The noise floor of the PCB 106B50 is considerably higher than the Brüel & Kjær as seen in the waveform. The stated noise floor (or resolution as PCB calls it) for the PCB is actually .03m PSI RMS which is equivalent to .2 pascals. The 2236 SLM has an RMS noise floor of .004 pascals using the linear weighting

In conjunction with this, the PCB unit can handle much higher pressures than the B&K as it is approximately 500 times less sensitive.

In summary, for the waveform analysis a much better comparison would be a different Brüel & Kjær microphone and preamp which would extend the frequency range down to similar characteristics. The phase differences would however remain. The Brüel & Kjær microphone in this test has a much higher signal to noise ratio and this coupled with a windscreen provides good isolation from wind during ambient conditions. The repeatability of the 2236 SLM using the peak detector is very high and for ease of measurements of pressures up to 280 pascals or 142dB, the 2236 will provide very good results. Lastly, I have included some technical documentation surrounding the windscreens we manufacture.

I hope this information is of assistance to DRES and you will consider Brüel & Kjær instrumentation for additional field trials in this area. We believe this, or one of our other meters would be useful in detection of community annoyance. It was very enjoyable meeting with you and the other DRES staff.

Yours truly,
BRÜEL & KJÆR CANADA LTD

Jim Ulicki, C.E.T.
Technical Representative

JU/ck
att

c.c. Dr. Paul Thibault
Combustion Dynamics Ltd.,

Dawn of a new era

Precision Integrating Sound Level Meter Type 2236

International version

Brüel & Kjær

A sound le

1

Precision Integrating Sound Level Meter Type 2236 has been designed with the world of environmental- and industrial-noise control in mind. Its ergonomic design heralds the dawn of a new era in sound level meter design. Just see for yourself.

Easy to use

Making measurements with the 2236 is simplicity itself. The pushkeys are self-explanatory and well laid out and give you direct access to all major functions. The display is clear and concise, and an interactive dialogue guides you every step of the way, ensuring fast and efficient usage. We've even taken the guesswork out of calibration: nothing could be easier, or more convenient, than using the pocket-sized Sound Level Calibrator Type 4231.

Measuring the L_{eq} and SEL from railway lines

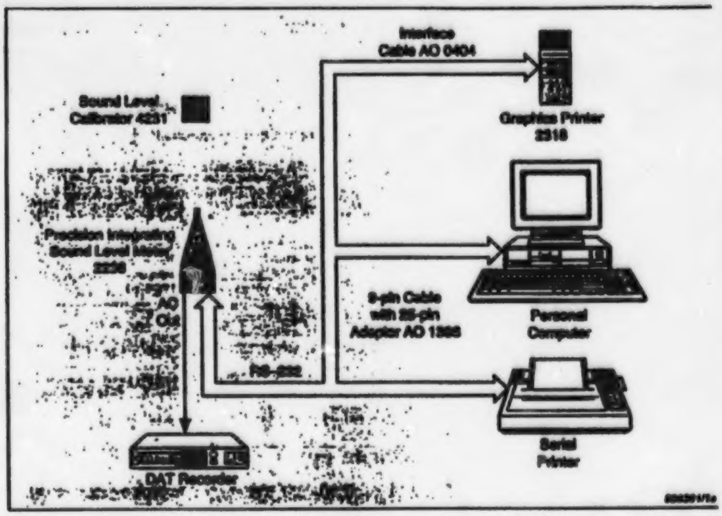
Interface
Cable AO 0404
Graphics Printer
2318
Sound Level
Calibrator 4231
Precision Integrating
Sound Level Meter
2236
AC
Out
RS-232
9-pin Cable
with 25-pin
Adaptor AO 1386
Personal
Computer
Serial
Printer
DAT Recorder

System set-up for printing, recording and transferring results from the sound level meter

Direct print and storage

You can print your results as soon as you've finished measuring, either on the lightweight Graphics Printer Type 2318, or on a standard serial printer. You can store results in the sound level meter's non-volatile memory, or transfer the results via the built-in serial interface to your personal computer in a spreadsheet compatible format, for additional analysis or graphical presentation using standard office software.

A front-end unit

The sound level meter also acts as a cost-effective front-end for a data acquisition system. While the sound level meter is measuring and displaying A-weighted parameters, the linearly-weighted output signal can be recorded, via the AC output, on a DAT recorder, providing a calibrated recording for further spectrum analysis and noise source identification.

el meter
ade just for you

Measuring the $L_{EP,d}$ for a particular worker. The filter versions can also be used to investigate the type of hearing protection required

Versatile

The sound level meter is available with an optional built-in 1/1-octave filter which enables you to perform frequency analyses according to national and international standards. Additionally, the sound level meter can be upgraded to include extra memory so that you can log results, for example, every second over an entire 24-hour period.

A complete measurement solution

Precision Integrating Sound Level Meter Type 2236 provides all the standardized international parameters you need for your chosen measurement task — whether measuring environmental noise, industrial noise or both. For example, it allows you to measure both L_{eq} and Peak, as required by the EC directive on exposure to noise at work (86/188/EEC), simultaneously. For environmental measurements, it can show L_Ns and noise distributions. Hand-held or tripod-mounted, it is a self-contained, precision instrument. To expand, just add a printer, a lap-top computer or DAT recorder, and a Sound Level Calibrator Type 4231 for a complete measurement solution.

A wealth of accessories

All accessories needed for measurement in the field (for example, a tripod, a calibrator or a printer) are available from Brüel & Kjær — your single-source supplier. We also supply a handy carrying case for transporting the sound level meter with essential accessories.

Carrying Case KE 0325 has space for the sound level meter, the calibrator, Tripod UA 1251 and Serial Printer WQ 1138

The Brüel & Kjær hallmark

Precision Integrating Sound Level Meter Type 2236 is just one of a long line of quality instruments from the company whose name is synonymous with sound level meters — Brüel & Kjær. As such, it comes with the Brüel & Kjær guarantee of quality which ensures that you will get years of reliable, accurate performance from a type-approved* sound level meter. And for regular calibrations and instrument checks, Brüel & Kjær provides a world-wide service back-up that is second-to-none.

In order to help you make better measurements, Brüel & Kjær also provides an extensive seminar and workshop programme run by local application specialists.

* Type approval is independent ratification of conformance to international standards

Product Data

Uses

- Investigation of hearing protection (filter set versions)
- Measuring industrial-noise according to national and international directives and legislation
- Measuring environmental-noise according to national and international directives and legislation

Features

- Type 1 sound level meter
- Simultaneous L_{eq} and Peak measurement with independent frequency weightings
- Calculates and displays two L_N values simultaneously
- Automatically logs L_{eq}, MaxL and MaxP
- 40 Records of manually stored results
- Back-lit display

Specifications 2236

Standards: Conforms with IEC 651 (1979) and 804 (1985) Type 1, and ANSI S1.4-1983 and Draft S 1.43 6th September, 1992 Type 1S
Optional $^1/_1$-octave Filter: 31.5 Hz to 8 kHz conforming with IEC 225 (1966) and ANSI S 1.11 – 1986 order 3 Type 1D
Measuring Range: 20 – 140 dB RMS (143 dB Peak) in five 80 dB ranges*
Noise Floor: Typically 18 dB(A) RMS
Time Weighting: S, F, I according to IEC 651 Type 1
Frequency Weighting: A (RMS only) and C according to IEC 651 Type 1, L (20 Hz to 20 kHz)
Detectors: RMS and Peak with independent frequency weightings
Display: LCD with back-light and battery low indicator
Parameters: MaxL, MinL, MaxP, Peak, SPL, L_{eq}, L_{Im}, SEL, IEL, L_{EM}, L_N, L_N and Overload in % of measurement time
Memory: 40 Records of Overall Results stored manually
Automatic Logging: L_{eq}, MaxL and MaxP every 1s or 1min.
Log Capacity: 21 600 (or 86 400) sets of results (for example, 6 or 24hrs of 1s logging) dependent on version
Outputs:
Serial Interface: Compatible with EIA-574 and EIA-232-E
Result Output Formats: Overall and Logged Results
DC Output: Displayed Parameter
AC Output: Preamp. output (L-weighted)
Clock: Real-time (calendar) and elapsed time
Electromagnetic Compatibility: FCC class B part 15J
Batteries: Four 1.5V LR6/AA size alkaline cells (lifetime > 8 hrs)
External Power Supply: 7 – 15 V DC
Size: 252 × 97 × 41 mm
Weight: ~ 460 g (incl. batteries)

* plus 10 – 90 dB RMS range with filter versions

Ordering Information

Type 2236 A Precision Integrating Sound Level Meter
Type 2236 B Precision Integrating Sound Level Meter (extended memory)
Type 2236 C Precision Integrating Sound Level Meter with $^1/_1$-octave filter set
Type 2236 D Precision Integrating Sound Level Meter with $^1/_1$-octave filter set (extended memory)

Accessories included:
4 × QB 0013 Four 1.5V LR6/AA size alkaline cells
Type 4188 Prepolarized Condenser Microphone Cartridge
KE 0323 Shoulder Bag
UA 1236 Protective Cover

Accessories available:
Type 4231 Sound Level Calibrator
UA 1251 Tripod
UA 0237 and UA 0459 Windscreens
AO 0408 and AO 0409 Microphone Extension Cables (3 m and 10 m)
KE 0325 Carrying Case with Insert for Type 2236, Type 4231, WQ 1138, UA 1251
ZT 0326 Octave Filter Set Ugrade

For output to PC, serial printer:
AO 1386 9-pole Cable with 25-pole Adaptor
WQ 1138 Serial Printer

For output to recorders:
AO 0403 LEMO to BNC Cable

For output to graphics printer:
AO 0404 9-pole to LEMO Cable
Type 2318 Graphics Printer

Services available with delivery of 2236:
EK 0102 Accredited calibration re. IEC 651 and IEC 804

Brüel & Kjær reserves the right to change specifications and accessories without notice.

Contact your local Brüel & Kjær representative for more information about Precision Integrating Sound Level Meter Type 2236 – the dawn of a new era.

Brüel & Kjær

WORLD HEADQUARTERS: DK-2850 Nærum · Denmark · Telephone: +45 42 80 05 00 · Telex: 37316 bruka dk · Fax: +45 42 80 14 05

Australia (02) 450-2066 Austria 0222/816 74 00 · Belgium 02-242 97 45 · Brazil (011) 246-8149/246-8166 · Canada (514) 695-8225 · Czech Republic 02-243 10458
Finland (0) 1481577 · France (1) 64 57 20 10 · Germany 04106/70 95-0 · Great Britain (081) 954-2366 · Holland 03402-39994 · Hong Kong 548 7486 · Hungary (1) 215 83 05
Italy (02) 57 60 4141 · Japan 03-5420-7302 · Republic of Korea (02) 554-0605 · Norway 66 90 44 10 · Poland (0-22) 40 93 92 Portugal (1) 65 92 56/65 92 80
Singapore 225 8533 · Slovak Republic 07-55686 · Spain (91) 368 10 00 · Sweden (08) 711 27 30 · Switzerland (1) 862 19 60 · Taiwan (02) 713 9303 · Tunisia (01) 232 478
USA: MA (508) 481-7737 GA (404) 981-6225 MI (313) 522-8600 IL (708) 358-7582 CA (800) 442-1030 WA (206) 883-2203/882-4359
Local representatives and service organisations world-wide

Printed in Denmark: K. Larsen & Søn A/S DK-2600 Glostrup

A personalised SLM to match your needs

Environmental- and industrial-noise measurements using Precision Integrating Sound Level Meter Type 2236

International version

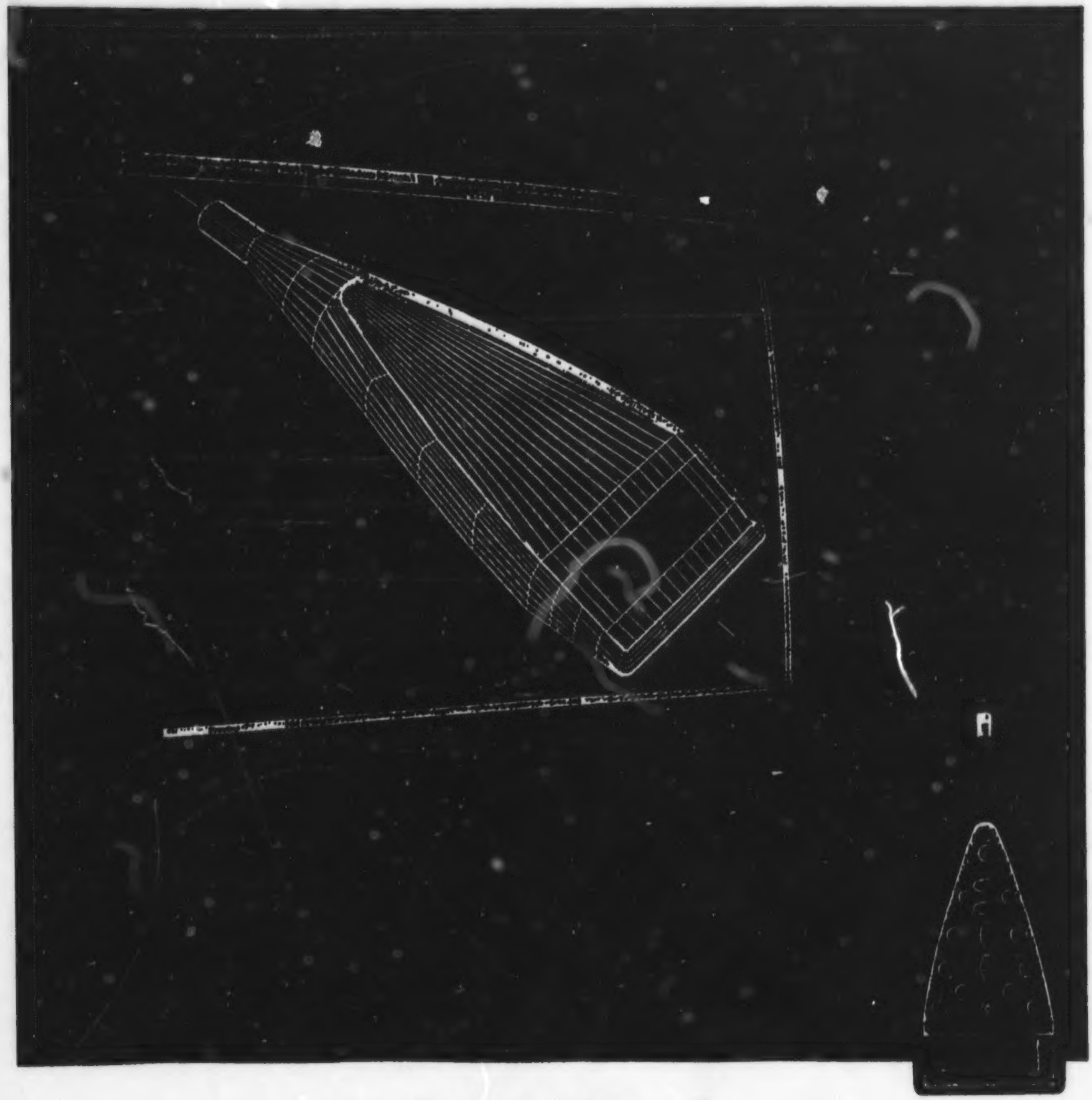

Brüel & Kjær

Precision Integrating Sound Level M

Easy to use

The Type 2236 has been designed with the world in mind. The principle of operation is simple and easy to learn. The pushkeys and display are self-explanatory and give you direct access to all major functions. Operation of the sound level meter is based on a two-way dialogue which guides you through its use. Calibration checks can be done quickly and easily with the pocket-sized Sound Level Calibrator Type 4231.

Safe results

Here are just some examples of how Brüel & Kjær has safeguarded the integrity of your measurements. When resetting, the sound level meter checks to see if you want to delete all previous results, thus ensuring that you don't accidentally lose vital measurements. Furthermore, the non-volatile memory protects the day's logged results against unexpected battery failure.

Measuring the L_{eq} experienced due to traffic noise

Measuring the $L_{EP,d}$ for a particular worker

Direct print and storage

You can print your results as soon as you've finished measuring, either on the lightweight Graphics Printer Type 2318 or on a standard serial printer. You can also transfer the results via the serial interface to your personal computer in a spreadsheet compatible format for additional analysis or graphical presentation in your preferred format.

A front-end unit

The sound level meter also acts as a cost-effective front-end for a data acquisition system. While the sound level meter is measuring and displaying A-weighted parameters, the Lin.-weighted output signal can be recorded via the AC output on a DAT- (Digital Audio Tape) or cassette-recorder, providing a calibrated recording for spectrum analysis and subjective evaluations.

Type 2236 — made just for you

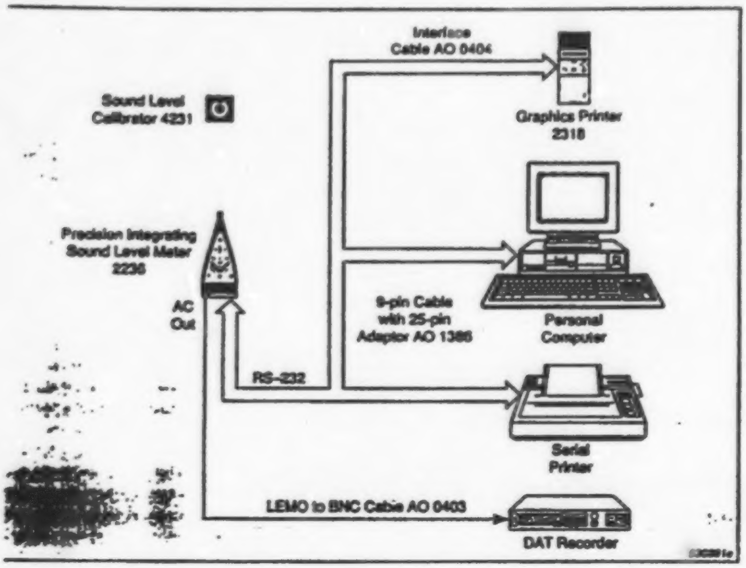
Interface Cable AO 0404
Sound Level Calibrator 4231
Graphics Printer 2318
Precision Integrating Sound Level Meter 2236
AC Out
9-pin Cable with 25-pin Adaptor AO 1386
Personal Computer
RS-232
Serial Printer
LEMO to BNC Cable AO 0403
DAT Recorder

System set-up for printing, recording and transferring results from Precision Integrating Sound Level Meter Type 2236

Reliable and sturdy

As you would expect of a high-quality precision instrument, this sound level meter withstands harsh measurement conditions. And, based on our experience, it will carry on doing this well into the next century. Even in poor lighting conditions, the display's back-light enables you to see the results and continue measuring. Naturally, like all Brüel & Kjær sound level meters, this one will be type-approved* so you are guaranteed a Type 1 sound level meter.

* Type approval is independent ratification of conformance to international standards

A complete measurement solution

recision Integrating Sound Level Meter Type 2236 provides all the relevant parameters, defined by international tandards, you need for your chosen measurement task – whether measuring environmental noise, industrial noise r both. For example, it gives you both L_{eq} and Peak as required by the EC directive on exposure to noise at work 86/188/EEC) – measured simultaneously. For environmental measurements, it can show any L_Ns of your choice. And, it as a serial interface *and* DC and AC outputs. Hand-held or tripod-mounted, it is a self-contained, precision instrument. o expand, just add a Graphics Printer Type 2318, a lap-top computer or DAT-recorder, and a Sound Level Calibrator ype 4231 for a complete measurement solution.

Upgradable

he Type 2236 is upgradable to an even more flexible meter with he addition of a built-in octave filter which will enable you to erform frequency analyses according to international and ational standards.

he Brüel & Kjær pedigree

he Type 2236 is just one of a long line of quality instruments rom the company whose name is synonomous with sound level eters – Brüel & Kjær. As such, it comes with the Brüel & Kjær uarantee of quality which ensures that you will get years of eliable, accurate performance. For regular calibrations and nstrument checks, Brüel & Kjær provides a world-wide service ack-up that is second-to-none.

In order to help you make better measurements, Brüel & Kjær lso provides an extensive seminar and workshop program run by ocal application specialists.

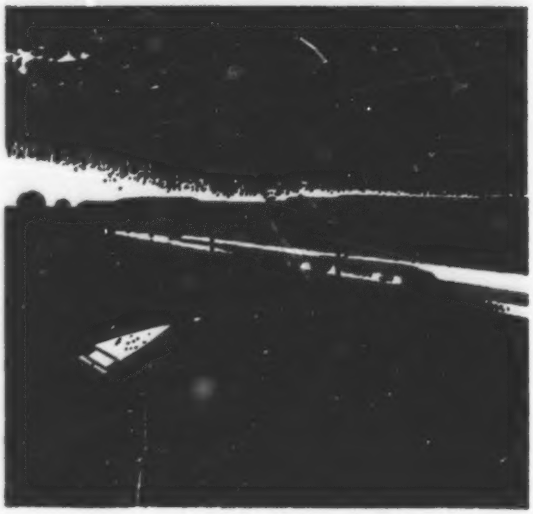

Measuring L_N from railway lines

Product Data

Uses

The international version is specially designed for measuring environmental- and industrial-noise according to international standards. For example, measuring the noise experienced by workers on a construction site according to the EC directive on exposure to noise at work (86/188/EEC).

Features

- Type 1 sound level meter
- Simultaneous L_{eq} and Peak measurement with independent frequency weightings
- Two L_N values
- Logs L_{eq}, MaxL and MaxP
- Stores up to 40 Records
- Back-lit display

Specifications 2236

Standards: Conforms with IEC 651 (1979) and 804 (1985) Type 1, and ANSI S1.4–1983 and Draft S 1.43, 6th September, 1992 Type 1S
Measuring Range: 20–140 dB RMS (143 dB Peak) in five 80 dB ranges
Noise Floor: Typically18 dB(A) RMS
Time Weighting: S, F, I according to IEC 651 Type 1
Frequency Weighting: A (RMS only) and C according to IEC 651 Type 1, L (20 Hz to 20 kHz)
Detectors: RMS and Peak with independent weightings
Display: LCD with back-light and battery low indicator
Parameters: MaxL, MinL, MaxP, Peak, SPL, L_{eq}, L_{Im}, SEL, IEL, $L_{EP,d}$, L_{95}, L_{5} and Overload in % of measurement time
Memory: 40 Records of Overall Results
Results Logging: L_{eq}, MaxP and MaxL
Logged every: 1s or 1min.
Log Capacity: 21600 sets of results (for example, 6 hrs of 1s logging)
Microphone Frequency Range: 8 Hz to 12.5 kHz ± 2dB
Outputs:
  Serial Interface: Compatible with IEA–574 and IEA–232–E
  Result Output Formats: Overall and Logged Results
  DC Output: Displayed Parameter
  AC Output: Preamp. output (L-weighted)
Clock: Real-time (calendar) and elapsed time

Electromagnetic Compatibility: FCC class B part 15J
Batteries: Four 1.5V LR6/AA size alkaline cells (lifetime > 8 hrs)
External Power Supply: 7–15 V DC
Size: 252 × 97 × 41 mm
Weight: ~ 500 g (incl. batteries)

ORDERING INFORMATION
Accessories included:
4 × QB 0013 Four 1.5V LR6/AA size alkaline cells
Type 4188 Microphone
KE 0323 Shoulder Bag
UA 1236 Protective Cover
Accessories available:
Type 4231 Sound Level Calibrator
UA 0801 and UA 1246 Tripod and Tripod Arm
UA 0237 and UA 0459 Windscreens
AO 0408 and AO 0409 Microphone Extension Cables
AO 1386 9-pole Cable with 25-pole Adaptor
AO 0403 LEMO to BNC Cable
AO 0404 9-pole to LEMO Cable
Type 2318 Graphics Printer
WQ 1138 Kodak Diconix 180si Serial Printer
ZT 0326 Octave Filter Set
KE 0322 and DS 0894 Carrying Case and Insert for Type 2236, Type 4231 and WQ 1138

el & Kjær reserves the right to change specifications and accessories without notice.

ontact your local Brüel & Kjær representative for more information about Precision Integrating Sound Level Meter
ype 2236 – a personalised sound level meter to match your needs.

rüel & Kjær

ORLD HEADQUARTERS: DK-2850 Nærum · Denmark · Telephone: +45 42 80 05 00 · Telex: 37316 bruka dk · Fax: +45 42 80 14 05
stralia (02) 450-2066 · Austria 0222/816 74 00 · Belgium 02-242 97 45 · Brazil (011) 246-8149/246-8166 · Canada (514) 695-8225 · Czech Republic 02-311 48 40/311 48 41
land (0) 1481577 · France (1) 64 57 20 10 · Germany 04106/70 95-0 · Great Britain (081) 954-2366 · Holland 03402-39994 · Hong Kong 548 7486 · Hungary (1) 215 83 05/215 89 29
y (02) 57 60 4141 · Japan 03-5420-7302 · Republic of Korea (02) 554-0605 · Norway 66 90 44 10 · Poland (0-22) 40 93 92 · Portugal (1) 65 92 56/65 92 80
gapore 225 8533 · Slovak Republic 07-55666 · Spain (91) 368 10 00 · Sweden (08) 711 27 30 · Switzerland (1) 862 19 80 · Taiwan (02) 713 9303 · Tunisia (01) 232 478
A: MA (508) 481-7737 GA (404) 981-6225 MI (313) 522-8600 IL (708) 358-7582 CA (800) 442-1030 WA (206) 883-2203/882-4359
al representatives and service organisations world-wide

d in Denmark K. Larsen & Søn A/S DK-2600 Glostrup

DRES

FACSIMILE COVER SHEET

Defence Research Establishment Suffield
P.O. Box 4000
Medicine Hat, Alberta, Canada
T1A 8K6

URGENT	
ROUTINE	✓

NO. OF PAGES (Incl Cover) 3

FROM	D. V. Ritzel/Gerry Rude	File No.	
	Explosive Effects Group		
	Military Engineering Section	Date	May 16, 1994
TELEPHONE	(403) 544 - 4767 / 544-4734		
TO	Jim Ulicki	FAX Tel	(403) 544 - 4704
	Brüel & Kjær	Telephone	(403) 544 - 4722
	Winnipeg, Manitoba		
FAX NUMBER	(204) 694-5025	*Secure Fax	(403) 544 - 4707

SPECIAL HANDLING INSTRUCTIONS

SUBJECT Comparative SLM Data from trials at DRES, 26 April, 1994

REFERENCES

COMMENTS Attached are traces from the third trial done while you were here on the 26th of April comparing B&K SLM with a standard DRES blast pressure gauge. I have included both long time traces (5 s) to show relative baseline noise, and short time scale (.2 s) to show waveform differences. We are most interested in your mechanical muffler or other techniques to eliminate baseline noise; However, on the short time scale, the B&K is very different than the DRES gauge.

ENCLOSURES

✓ I certify the enclosure(s) is/are unclassified/undesignated and are suitable for transmission by unsecure facsimile.

____ I certify the enclosure(s) is/are suitable for transmission by secure facsimile.

RELEASING AUTHORITY

Canada

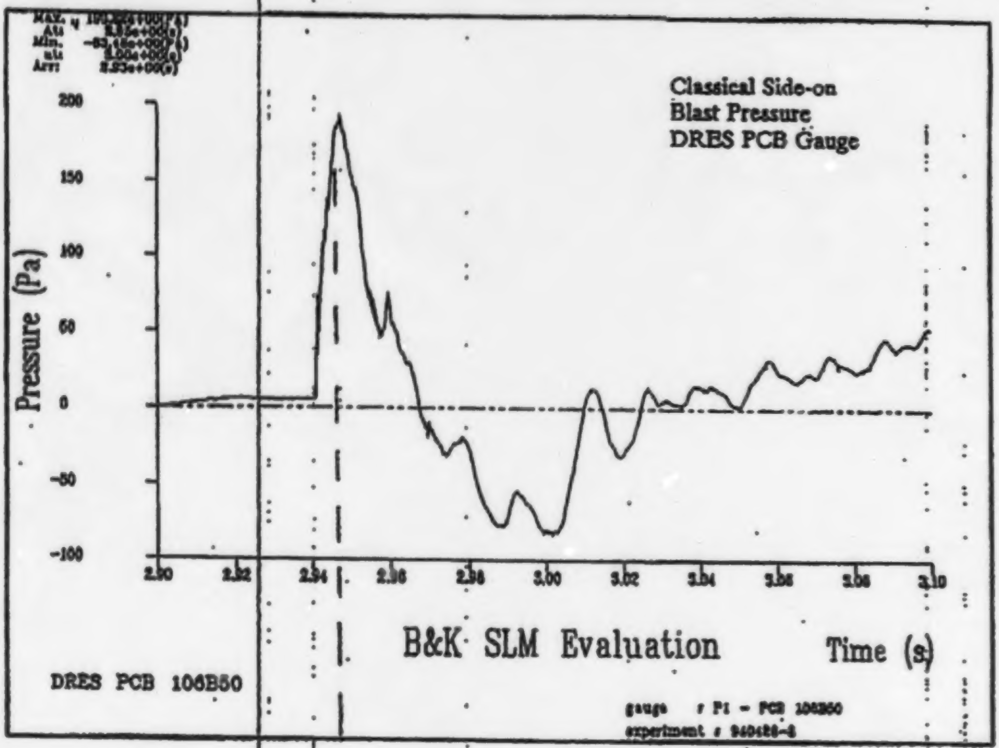

PAGE #1

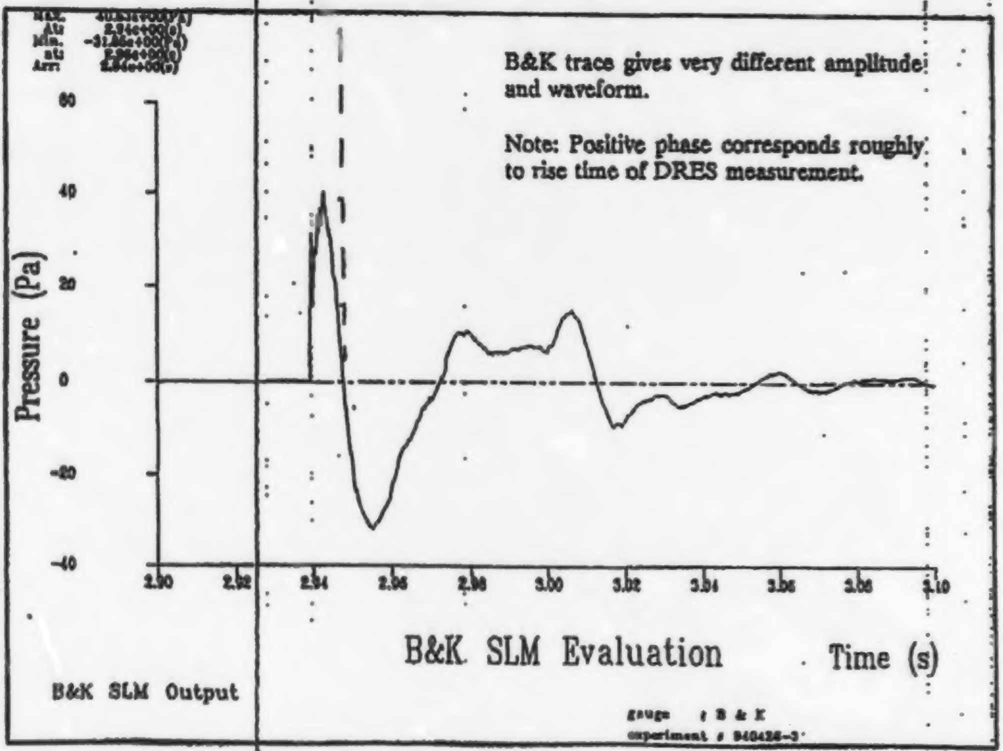

B&K trace gives very different amplitude and waveform.

Note: Positive phase corresponds roughly to rise time of DRES measurement.

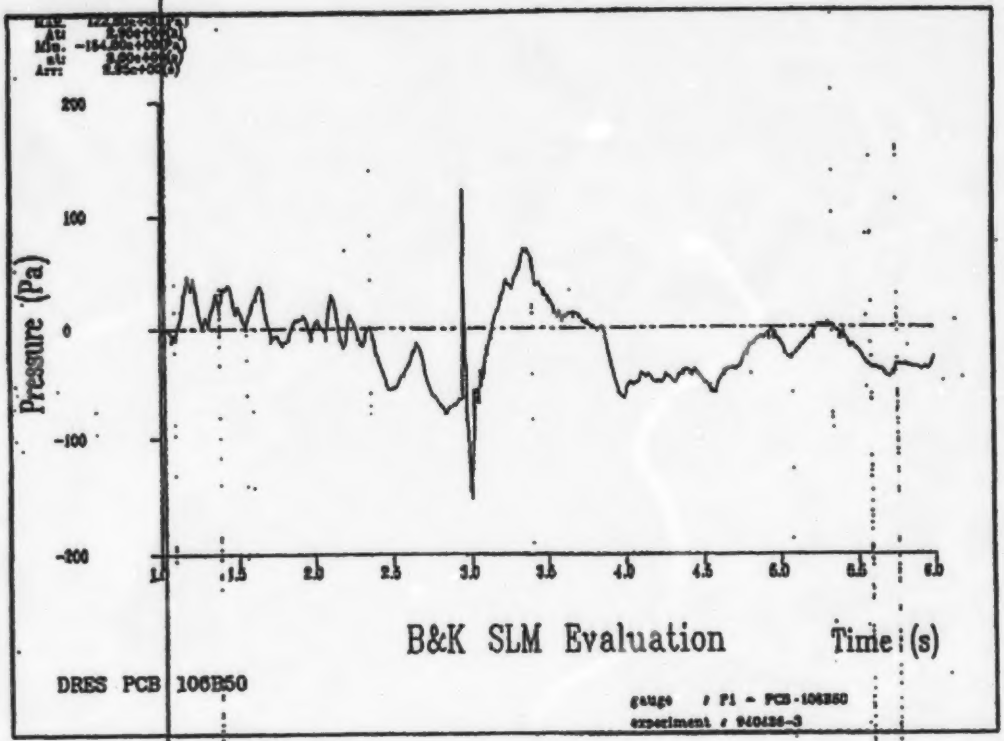
Max.
At:
Min.
at:
Arr:
200
100
0
-100
-200
Pressure (Pa)
1.0
1.5
2.0
2.5
3.0
3.5
4.0
4.5
5.0
5.5
6.0
B&K SLM Evaluation
Time (s)
DRES PCB 106B50
gauge # P1 - PCB-106B50
experiment # 940428-3

PAGE #2

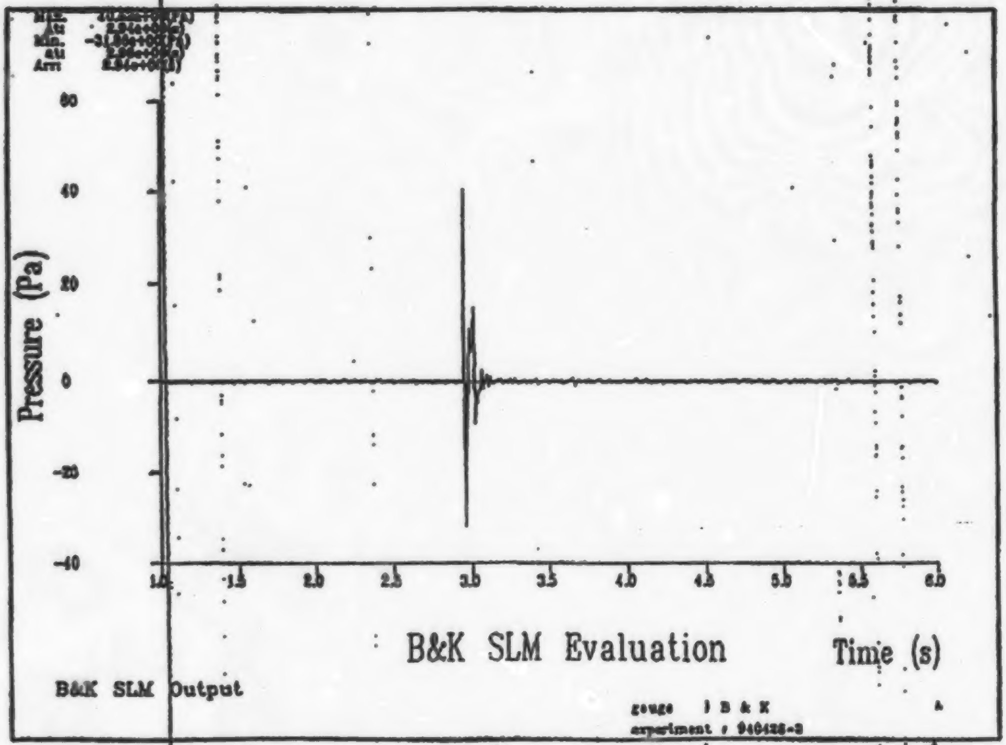
Max.
At:
Min.
at:
Arr:
60
40
20
0
-20
-40
Pressure (Pa)
1.0
1.5
2.0
2.5
3.0
3.5
4.0
4.5
5.0
5.5
6.0
B&K SLM Evaluation
Time (s)
B&K SLM Output
gauge) B & K
experiment # 940428-3

FAX coversheet

Telephone: 303-402-4728

Fax: 303-443-1628

Radian International LLC
Electronic Systems
5600 Airport Boulevard
Boulder, CO 80301

FAX # 902-492-0683

Phone # 902-492-1422

Date: June 26, 1998

Pages to Follow - 2 -

From: **Bill Bendel**
Senior Scientist
Radian International

To: **Paul Thibault**
President
Combustion Dynamics Ltd
Suite 301, 1888 Brunswick Street
Halifax, Nova Scotia
B3J 3J8

Message:

Dear Mr. Thibault:

Attached is the updated brochure on the LAP®-3000 System Lower Atmosphere Profiler which you requested.

Please call me should you have any additional questions or need a more firm quote (which would include installation, training, etc.) for your potential project.

Sincerely,

Bill Bendel

Wind and Temperature Profiling Technology from NOAA's Environmental Research Laboratories in Boulder, Colorado...

LAP®-3000 System
Lower Atmosphere Profiler

Now available at 915 and 1290 MHz.
Other frequencies from 850 to 1500 MHz by special order.

The Radian Electronics Division of Radian International LLC and Sonoma Technology Inc. have entered into a Cooperative Research and Development Agreement (CRADA) with the U.S. National Oceanic and Atmospheric Administration to commercialize the LAP®-3000 wind and temperature profiling system. The LAP-3000 system is a Doppler radar which reliably provides vertical profiles of horizontal wind speed and direction, and vertical wind velocity to 3 km above ground level (agl). When a Radio Acoustic Sounding System (RASS) option is added to the LAP-3000 system, it will provide virtual temperature profiles up to about 2 km agl depending on atmospheric conditions. This system can operate unattended and provide continuous real-time atmospheric wind and temperature data with high spatial resolution. Current users of the LAP systems include NOAA, NCAR, NASA, DOD, DOE, air quality districts, universities, utilities, and private industry.

Applications include:

- Atmospheric Boundary Layer Research
- Air Pollution Research
- Emergency Response
- Global Change Research
- Aviation Operations
- Mesoscale Meteorological Forecasting
- Battlefield Operations
- Forest Fire Management
- Urban Airshed Modeling
- Weather Modification
- Offshore, Shipboard, Airborne Platforms
- Arctic/Antarctic Research
- Optical Turbulence Measurements

RADIAN
INTERNATIONAL LLC
ELECTRONICS DIVISION

STI
Sonoma Technology Inc

Cooperative
Research &
Development
Agreement

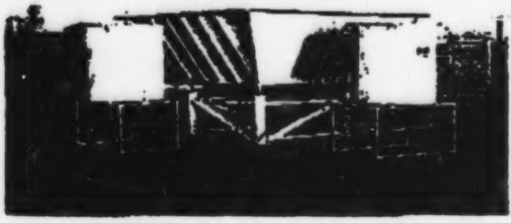

Fixed site LAP-3000 configuration with optional RASS and support stand.

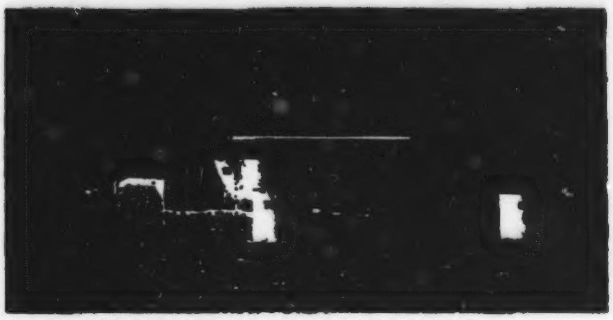

Mobile LAP-3000 configuration (deployed) with optional RASS.

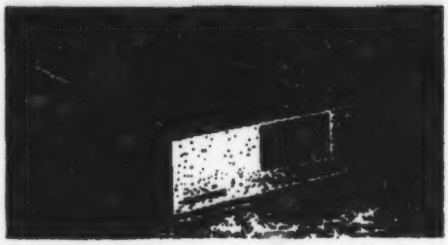

The profiler monitor, another option available for the LAP-3000 system, is a processor and data acquisition subsystem designed to monitor the health of the LAP-3000 system, assist maintenance personnel with fault diagnosis, and shut down the system should certain critical conditions exceed preset limits. Diagnostic documentation accompanies the profiler monitor.

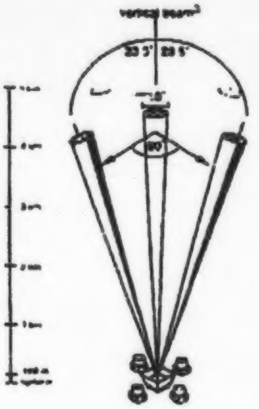

LAP-3000 Specifications
(915, 1290 MHz)

Minimum Height[1]	75-150 m
Maximum Height[2]	2-5 km
Spatial Resolution	
with 400 ns pulse	60 m
with 700 ns pulse	100 m
with 1400 ns pulse	200 m
with 2800 ns pulse	400 m
Wind Speed Accuracy	< 1 m/s
Wind Direction Accuracy	< 10°
Averaging Time	3-60 minutes
Power Output	500 W peak
Antenna	Electrically steerable micropatch phased array panels
Aperture	$2.7\ m^2$ (4 panels) $6.1\ m^2$ (9 panels)

Specifications for RASS
(~2 kHz)

Minimum Height[1]	75-150 m
Maximum Height[2]	1-2 km
Spatial Resolution	
with 400 ns pulse	60 m
with 700 ns pulse	100 m
with 1400 ns pulse	200 m
with 2800 ns pulse	400 m
Temperature Accuracy	1°C
Averaging Time	3-60 minutes
Acoustic Source	Four compression drivers, parabolic reflectors
Aperture	$1.2\ m^2$ x four

[1] Dependent on clutter environment and available radio frequency emission bandwidth

[2] Dependent on atmospheric scattering conditions

[3] Antenna pointing directions shown for standard 4-panel 915 MHz antenna

For more information contact:

RADIAN INTERNATIONAL LLC
ELECTRONICS DIVISION
Lower Atmosphere Profiler
1-800-RADARWP

Radian Electronics Division

5600 Airport Blvd.
Boulder, CO 80301-2340
(303) 443-2378
FAX (303) 443-1628

15508 Bratton Lane
Austin, TX 78728
(512) 244-0100
FAX (512) [illegible]

Sonoma Technology Inc.
5510 Skylane Blvd.
Suite 101
Santa Rosa, CA 95403
(707) 527-9372

International Sales
5801 Lee Highway
Arlington, VA 22207 USA
Telex: 892532 REPUBLIC
FAX: (703) 533-3190

LAP and the LAP logo are registered trademarks of Radian International LLC

© Copyright Radian International LLC [illegible] All Rights Reserved

** TOTAL PAGE.03 **

Wind and Temperature Profiling Technology from NOAA's Aeronomy Laboratory and Wave Propagation Laboratory...

LAP™- 3000a
Lower Atmosphere Profiler

Copyright 1992 by Image Control Studio

Radian Corporation and Sonoma Technology Inc. have entered into a Cooperative Research and Development Agreement (CRDA) with the U.S. National Oceanic and Atmospheric Administration to commercialize the LAP™ wind and temperature profiling system. The LAP-3000 is a Doppler radar which provides vertical profiles of horizontal wind speed and direction, and vertical wind velocity reliably to 3 km. When a Radio Acoustic Sounding System (RASS) option is added to the LAP-3000, it will provide virtual temperature profiles up to approximately 2 km depending on atmospheric conditions. This system can operate unattended and provide continuous real-time atmospheric wind and temperature data with high spatial resolution.

Current users of LAP systems include NOAA, NCAR, NASA, DOD, DOE, air-quality districts, universities, utilities, and private industry.

Applications Include:

- Atmospheric Boundary Layer Research
- Air Pollution Research
- Emergency Response
- Global Change Research
- Aviation Operations
- Mesoscale Meteorological Forecasting
- Battlefield Operations
- Forest Fire Management
- Urban Airshed Modeling
- Weather Modification
- Offshore, Shipboard, Airborne Platforms
- Arctic/Antarctic Research
- Optical Turbulence Measurements

RADIAN
CORPORATION

STI
Sonoma Technology Inc.

™

Cooperative Research & Development Agreement

Now available at 915 MHz and 1290 MHz

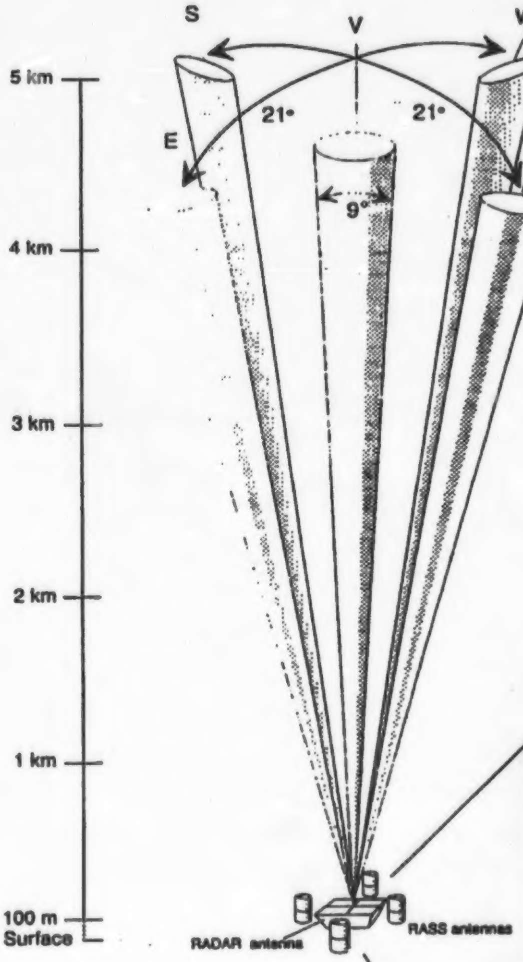

Nominal LAP-3000 Specifications

Lowest measurement height*:		
	Winds	100 m
	Temperature	100 m
Maximum measurement height*:		
	Winds	2 to 5 km
	Temperature	1 to 2 km
Minimum vertical resolution:		
	Winds	60 m
	Temperature	60 m
Wind speed accuracy:		<1 m/s
Wind direction accuracy:		<10 degrees
Temperature accuracy:		<1°C
Averaging time:		3 to 60 minutes
Radar frequency:		915 MHz or 1290 MHz
Power Output:		500 W (Peak)
RASS frequency:		~2-3 KHz

***dependent upon atmospheric conditions**

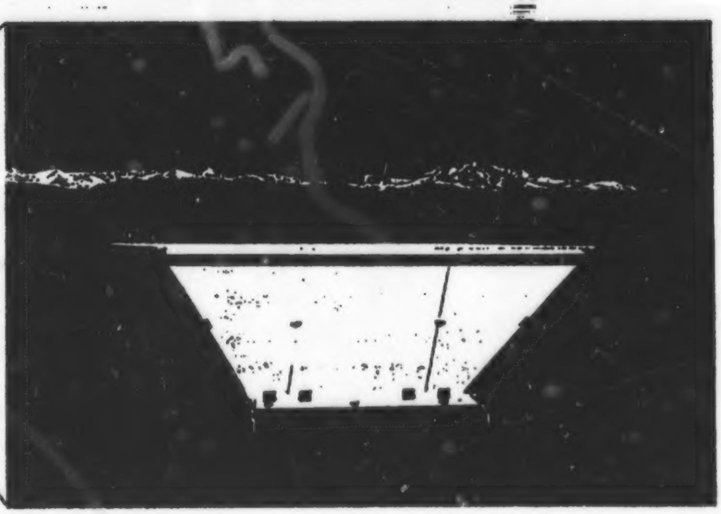

Typical patented LAP™-3000 micropatch antenna configuration consists of a single phased-array antenna and clutter screen (~2m×4m×4m)

For more information contact:

RADIAN CORPORATION
Lower Atmosphere Profiler
2990 Center Green Ct. S.
Boulder, CO 80301
(303) 443-2378
FAX (303) 443-1628

A company of The Hartford Steam Boiler Inspection and Insurance Co.

LAP and the LAP logo are trademarks of Radian Corporation.

6930245

LAP-3000 International Sales:

5801 Lee Highway
Arlington, VA 22207 USA
(703) 533-8555
Telex: 892532 REPUBLIC
FAX (703) 533-3190

STI
Sonoma Technology Inc.
5510 Skylane Blvd., Suite 101
Santa Rosa, CA 95403-1083
(707) 527-9372

Radian Corporation and Sonoma Technology Inc. have entered into a joint cooperation agreement for work under this NOAA CRDA.

The Lower Atmosphere Profiler Product Line

high performance atmospheric acoustic and radar profiling systems

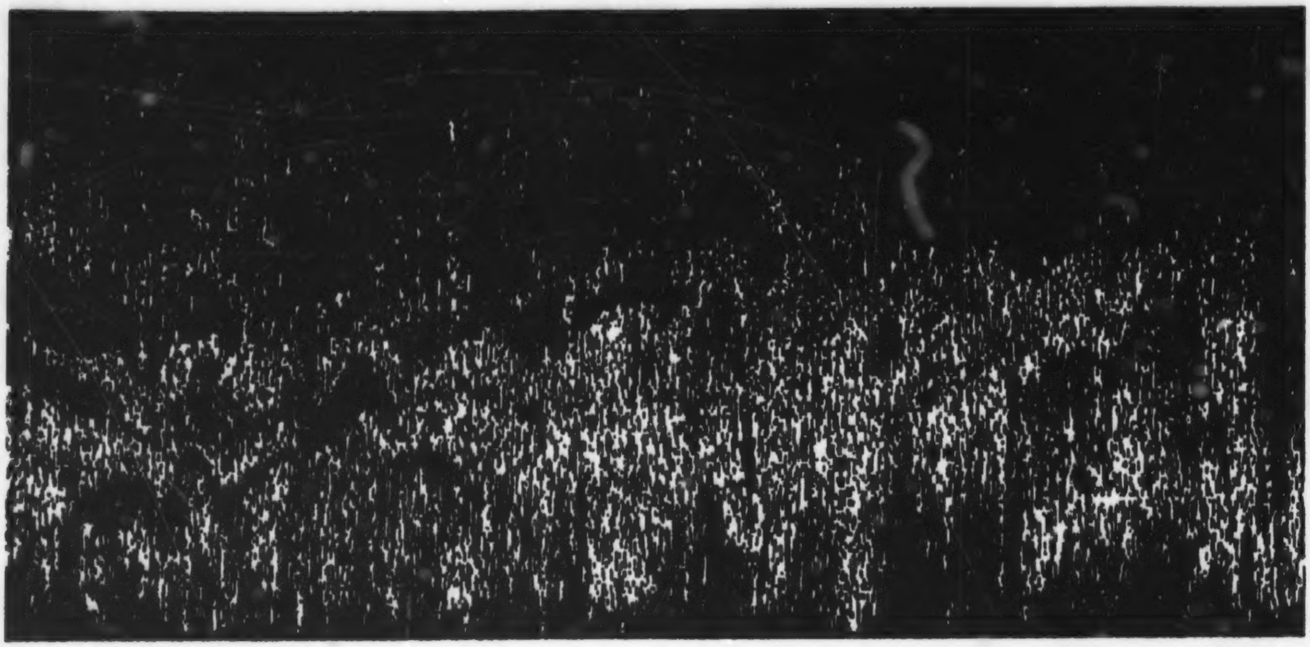

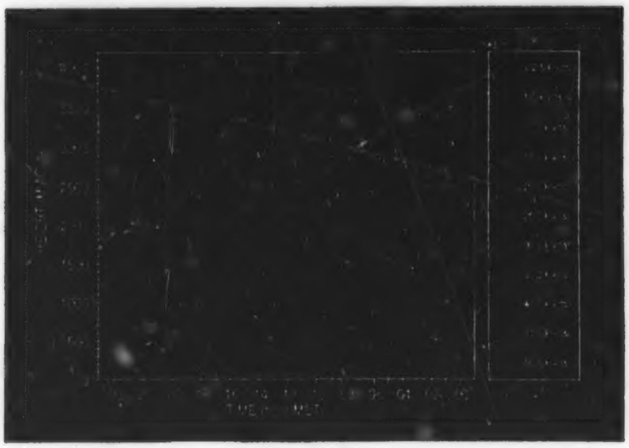

RADIAN
CORPORATION

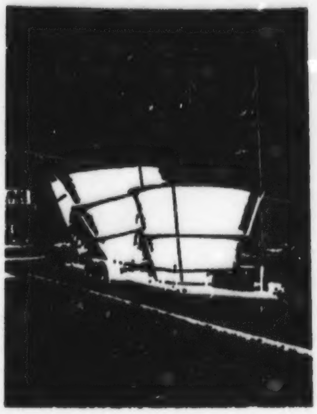

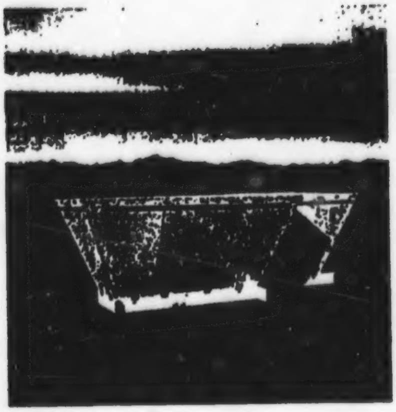

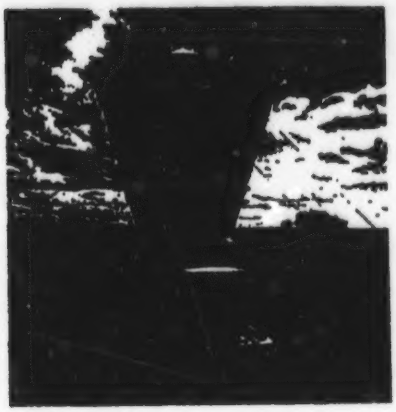

sonde®

r Acoustic Sounding System

hosonde acoustic profiler is
n over 10 years of Radian ex-
e in the design, manufacture,
pport of Doppler remote
heric sensing devices. Radian
lded over 100 sounding
s and is currently the leader
stic profiler technology.
hosonde systems can now be
red using a variety of host
nputer systems and acoustic
as; from highly portable
profilers" to maximum per-
ce, higher altitude systems.
na configurations range from
antenna monostatic to multi-
common volume monostatic
static geometries.

nde Applications

tine pollution and PSD
itoring
ustrial and optical site
luations
issions control strategies and
cial studies
ht operations
ersion detection and
racterization
clear and chemical dispersion
dels
undary layer research

LAP™-3000

Radar Profiling Systems

LAP-3000 radar profilers are a new family of economical, high-performance instruments that provide higher altitude coverage than is available with acoustic techniques. The LAP-3000 can be configured as a low-cost, single or multiple antenna radar profiler operating at 915 MHz, to provide atmospheric data through the boundary layer up to several kilometers above ground.

The LAP-3000 uses light weight microstrip antennas for mobile applications. This system is also adaptable to lower frequency operation—such as ~400 MHz and ~50 MHz—for even higher altitude coverage.

LAP-3000 Applications

- Airshed model 3-D wind measurements
- Aviation meteorology
- Laser range and optical telescope characterization
- Atmospheric research
- Shipboard and buoy data
- Test range support

RASS

Radar Acoustic Sounding System

A unique combination of both acoustic and radar systems, RASS allows the measurement of both wind and temperature profiles. Using modern digital techniques, the RASS can provide virtual temperature data up to high altitudes for applications that require more than just temperature structure.

RASS Applications

- Weather prediction
- Atmospheric research
- Fog prediction
- Radar ducting prediction
- Dispersion models
- Aircraft noise certification

Product Line Measured Parameters

- Vertical wind (w)
- Standard deviation of vertical wind (σw)
- Horizontal wind (u,v)
- Standard deviation of horizontal wind ($\sigma\theta$, $\sigma\phi$)
- Structure parameters (C_t^2, C_n^2, C_v^2)
- Inversion detection
- Mixing height
- Temperature
- Heat flux
- Optical image spread